2017

A Novel Induction Heating System Using Multilevel Neutral Point Clamped Inverter

Al Shammeri, Bashar Mohammed Flayyih

A Novel Induction Heating System Using Multilevel Neutral Point Clamped Inverter

Bashar Mohammed Flayyih Al Shammeri

Ph.D

January 17, 2017

This thesis is dedicated to

My mother, who sacrificed a lot for me and inspired me the meaning of

sacrifice and success

The memory of my father, who taught me the truth of life

My wife, who is the source of happiness in my life and my companion to the

way of success

My children, who make my life full of beauty

To all people who I love

RESEARCH DEGREES WITH PLYMOUTH UNIVERSITY

A Novel Induction Heating System Using Multilevel Neutral Point Clamped Inverter

by

BASHAR AL SHAMMERI

A thesis submitted to Plymouth University

in partial fulfilment for the degree of

DOCTOR OF PHILOSOPHY

School of Computing, Electronics and Mathematics

Faculty of Science and Technology

Plymouth University, UK

January 17, 2017

Acknowledgements

Author's Declaration

At no time during the registration for the degree of Doctor of Philosophy has the author been registered for any other university award without prior agreement of the Graduate Sub-Committee.

Work submitted for this research degree at the Plymouth University has not formed part of any other degree either at Plymouth University or at another establishment.

This study was financed by Iraq Ministry of Higher Education and Scientific Research and Al-Shuhadaa Establishment.

A programme of advanced study was undertaken, which included the extensive reading of literature relevant to the research project and attendance of international conferences on power electronics.

The author has presented papers in the following international conferences:

- Energycon 2014 IEEE International Energy Conference, Dubrovnik-Croatia. From 13th - 16th May 2014.

- The 11th IEEE International Conference on Power Electronics and Drive Systems (PEDS 2015), Sydney, Australia on 9th - 12th June 2015.

- The IEEE Transportation Electrification Conference and Expo Asia-Pacific (ITEC2016), Busan, Korea on 1st - 4th June, 2016.

Word count of main body of thesis: 46588

Signed $\cdots\cdots\cdots\cdots\cdots\cdots\cdots\cdots\cdots\cdots\cdots$

Date $\cdots\cdots\cdots\cdots\cdots\cdots\cdots\cdots\cdots\cdots\cdots$

A Novel Induction Heating System Using Multilevel Neutral Point Clamped Inverter

Bashar Mohammed Flayyih Al Shammeri

Abstract

This thesis investigates a novel DC/AC resonant inverter of Induction Heating (IH) system presenting a Multilevel Neutral Point Clamped (MNPCI) topology, as a new part of power supply design. The main function of the prototype is to provide a maximum and steady state power transfer from converter to the resonant load tank, by achieving zero current switching (ZCS) with selecting the best design of load tank topology, and utilizing the advantage aspects of both the Voltage Fed Inverter (VFI) and Current Fed Inverter (CFI) kinds, therefore it can considered as a hybrid-inverter (HVCFI) category. The new design benefits from series resonant inverter design through using two bulk voltage source capacitors to feed a constant voltage delivery to the MNPCI inverter with half the DC rail voltage to decrease the switching losses and mitigate the over voltage surge occurred in inverter switches during operation which may cause damage when dealing with high power systems. Besides, the design profits from the resonant load topology of parallel resonant inverter, through using the LLC resonant load tank. The design gives the advantage of having an output current gain value of about Quality Factor (Q) times the inverter current and absorbs the parasitic components. On the contrary, decreasing inverter current means decreasing the switching frequency and thus, decreasing the switching losses of the system. This aspect increases the output power, which increases the heating efficiency. In order for the proposed system to be more reliable and matches the characteristics of IH process , the prototype is modelled with a variable LLC topology instead of fixed load parameters with achieving soft switching mode of ZCS and zero voltage switching (ZVS) at all load conditions and a tiny phase shift angle between output current and voltage, which might be neglected.

To achieve the goal of reducing harmonic distortion, a new harmonic control modulation is introduced, by controlling the ON switching time t_α to obtain minimum Total Harmonic Distortion (THD) content accompanied with optimum power for heating energy.

Contents

List of Figures

List of Tables

Abbreviations

BEM	Boundary Element Method
CFI	Current Fed Inverter
DFT	Discrete Fourier Transform
EMF	Electro Motive Force
FDM	Finite Differential Method
FEM	Finite Element Method
FFT	Fast Fourier Transform
FS	Frequency Spectrum
HVCFI	Hybrid Voltage-Current Fed Inverter
IDFT	Inverse Discrete Fourier Transform
IH	Induction Heating
IR	Inductance Ratio
MIF	Multilevel Inverter Family
MNPCI	Multilevel Neutral point Clamped Inverter
PDM	Pulse Density Modulation
PRI	Parallel Resonant Inverter
PWM	Pulse Width Modulation
RCF	Resonant Converter Family
SRI	Series Resonant Inverter
THD	Total Harmonic Distortion
VFI	Voltage Fed Inverter
ZCS	Zero Current Switching
ZVS	Zero Voltage Switching

Chapter 1

Introduction

The electromagnetic induction phenomena forms the heart of **Induction Heating IH** concept was first discovered by **Michael Faraday** in 1831 [1]. Since then, the IH technology began to be the best choice in many industrial [2], domestic [3] and medical applications [4], because of its advantages of: clean, rapid, contactless, superior control design, non contaminated and high efficiency heating process as compared with other traditional heating appliances like fuel heating furnaces.

The IH device consists mainly from an induction coil fed from a resonant IH power supply and surrounds the material load (or also called workpiece) to be heated. The basic concept of induction heating is similar to the transformer theory with the inductor as a primary and a single turn-short circuited secondary winding as the workpiece. Therefore, its current will be high and considerable losses are developed. When the coil is excited, it produces an alternating magnetic field. The variation in the field induces eddy currents along paths concentric with the axis. The magnetic field of eddy currents opposes the main field according to **Lenz law**. This energy dissipation mechanism is called Joule effect [5], and it concentrates near the surface of the workpiece. The current density varies exponentially inside the workpiece, and when it falls to about one third of its surface value is usually called **penetration (skin) depth phenomena** [2].

The most important factor in any IH application is maximizing the efficiency, which means gaining more output power with less energy losses through the system, in other words the proposed design must offer the condition of achieving optimum heating power transfer from power supply bank to the consumer load tank side of proposed induction heating configuration.

The aim of maximizing the efficiency requires decreasing the power losses of induction heating process, which implies reducing the undesired losses like switching losses of the supply inverter and mitigating other losses like parasitic components. These losses have a considerable effect on the overall system efficiency especially when talking about high power, current and frequency. Achieving these goals mean having more reliable IH configuration with less financial cost and best fitted design, which may be considered as an important indicator for successful industrial application.

The choice of power supply in any IH system have a great effect on the efficiency magnitude of delivered power from inverter to IH load tank set being chosen. The electrical specifications of power supply like power, voltage, current and operating frequency depend on many determinants, among them: planned application and mainly on the interaction between the selected DC/AC inverter type and the IH load tank used. While the AC/DC rectifier side is also important for controlling the input power, at this stage it will be considered as a DC power supply throughout the work.

The IH load includes mainly the heating coil and the material (workpiece) to be heated or melted depending on application, it may be modelled by a configuration set of resistance(s), inductance(s) and compensating capacitor(s), depending on the selected method of resonance, which need to be discussed later; therefore this chapter will focus on the most popular configurations utilized in different power supply designs and their recent improvements.

While later on, the chapter will focus on the main categories of load tank equivalent circuit being utilized in most IH systems, in order to choose one of them that offers the advantages of compact design and less cost, and at the end of the chapter there will be a general map to the proposed prototype configuration of IH power supply for both inverter and load equivalent, which can be effectively used as a novel design in IH system together with other well known resonant inverters mostly used, but with reduced switching losses and less harmonic distortion content and hence maximum heating power efficiency.

1.1   The State-of-Art of Previous Work

The IH principle has many advantages, among them better working environment, safety, security, fast heating rate, heat control and high efficiency, which inspires to use it in many applications, from small ones like domestic to the huge applications such as aircraft industries. These applications includes three main categories: domestic, industrial and medical. The reason of using IH in these applications can be summarized as follows:

- **Domestic Applications:** The IH is used in domestic industries, because it can be considered as a highly reliable technique that has the capability to build a low-cost design that operates under medium frequency with high efficiency, besides it has the ability to heat non-ferromagnetic materials [6–9].

- **Industrial Applications:** IH is highly utilized in large industrial plants like aircraft and automotive industries, because of its reliability in high power rating and the ability for optimizing the heat distribution under low-high switching frequency with high efficiency [10–14].

- **Medical Applications:** It is used, because of the local heating capability accompanied by the ability to control the magnetic field with low power and high switching frequency [15, 16].

The history of IH can be divided into two phases: **The first phase** began from the latest XIX century [17]. The IH concept was first discovered by **Michael Faraday**, he showed that currents are induced in a secondary circuit because of alternating magnetic field caused by AC current flowing in the neighbour primary circuit, then **James P. Joule** introduced the Joule Effect principle, which states that heat is induced in a conductor due to current flow through it. But, the first IH industrial product for melting metals was established in (1887) by **Sebastian Z. de Ferranti**. Then in (1891), **F.A. Kjellin** introduced the induction furnace in its early form. Later, **Edwin F. Northrup** presented the high frequency induction furnace in (1916), and at the same time, **M.G. Riband** produced high frequency spark-gap generators. Also, **Valentin P. Vologdin** presented machine generators and vacuum tubes as an IH generators. During the WWII period and later, the aircraft and automotive industry accelerated the IH technology development.

The second phase of IH revolution is using the power semiconductors especially the thyristors in IH systems, accompanied by the appearance of bipolar junction transistor (BJT), metal oxide semiconductor field effect transistor (MOSFET) and the insulated-gate bipolar transistor (IGBT), which made the IH concept widely spread in many applications.

As a consequence, at the 80s decade, the IH domestic applications was widely spread, and since latest of the 80s and during the XXI century, the interest in using IH concept in medical applications increased, because of its accuracy and local heating capability for hyperthermia treatment [18].

In all of the above applications, the converter is the main device that provides them with the required frequency, voltage, current, and power. The converter consists mainly from two parts: **part one** is the AC/DC rectifier, which could be as a non-controlled diode bridge or controlled stage using thyristors [13]. In order to control the input power of the diode bridge, the DC/DC buck converter stage is inserted to the design [19], and

to increase the power factor of the configuration, a power factor correction (PFC) circuit is sometimes added [20].

The DC/AC inverter is the most important component which forms **part two** of IH system [21]. The most efficient and predominant categories of IH inverters are the series resonant voltage source and the parallel resonant current source [22]. The Load topology utilized in the series inverter is the series resonant second order tank [11, 23], while the load configuration utilized in the parallel inverter is the parallel resonant second order tank [24], whilst; the series-parallel LCL (or also called LCL) topology gathers the advantages of both the series and parallel resonant designs with adding extra protection from short circuit fault [10, 14].

Depending on the number of switches in the design, the most popular topologies utilized in the IH systems are the H-bridge [25], half-bridge [26, 27] and the single switch [28], as shown in Fig. 1.1, Fig. 1.2 and Fig. 1.3 respectively.
Therefore, an introduction to some of the previous induction heating systems will be provided as a literature review, demonstrating the prevalent designs of various components of IH unit for power supply converter and various models of IH load tank circuit equivalent.

Edgerley et al. (1988) [29] stated that the main converters used in the induction heating systems are of the AC-DC-AC types, achieving an efficiency of more than 90 %, as shown in Fig. 1.4.

Dede et al. (1991) [30] presented a medium power inverter which is designed for high-frequency induction heating applications with automatic tracking control circuit, which means that both resonant and inverter frequencies are almost the same at every moment. The power delivered to the load is regulated by a feedback loop that controls the duty cycle of the input chopper, as shown in Fig. 1.5.
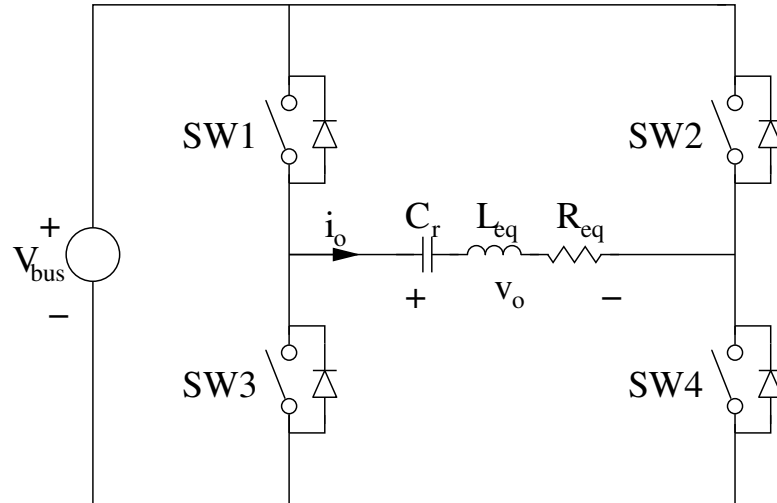
Figure 1.1: H-Bridge Series Resonant Inverter
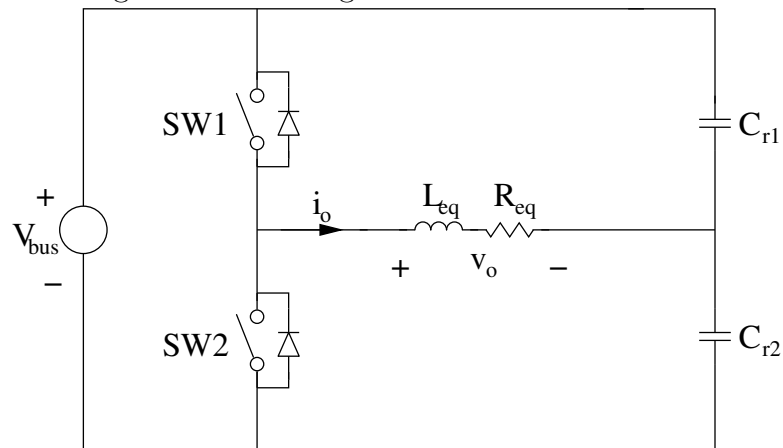
Figure 1.2: Half-Bridge Series Resonant Inverter
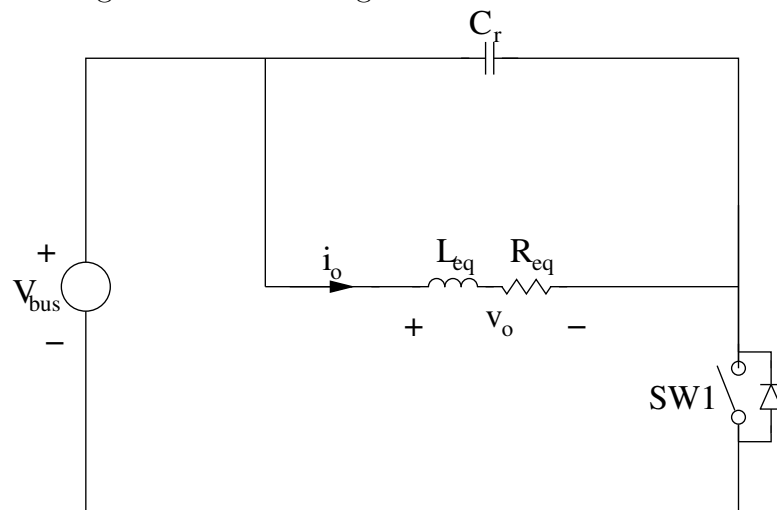
Figure 1.3: Single Switch Resonant Inverter
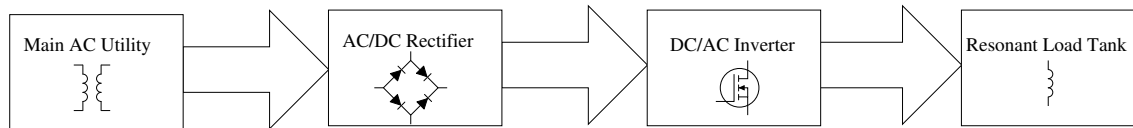
Figure 1.4: AC-DC-AC Power Supply Unit
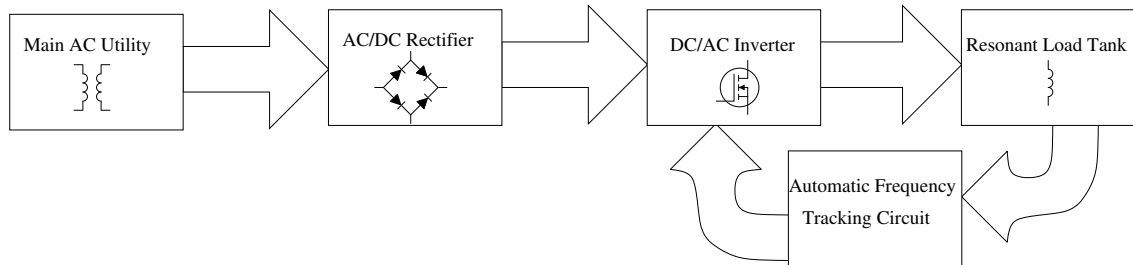
Figure 1.5: Power Supply Unit With Automatic Frequency Tracking

Dawson et al. (1991) [21] considered that the current fed inverter (CFI) and the voltage fed inverter (VFI) are the most common categories being used in IH systems, with introducing a comparative analysis between both types suitable for induction heating and melting applications.

Grajales et al. (1993) [31] described the development and implementation of a phase-shift controlled series-resonant inverter (PSC-SRI) for induction heating applications. While this design supposed to develop a phase-shift control strategy to provide output power regulation to obtain zero voltage switching (ZVS) by varying the switching frequency, the phase shift (between output current and voltage) depends mainly on the output current peak change, with increasing the peak, the phase shift decrease and more power transferred to load and vice versa.

Fujita et al. (1996) [32] presented a voltage-source inverter with a series resonant circuit for induction melting applications, with pulse density modulation (PDM) control while achieving zero-current-switching (ZCS) , and zero-voltage-switching (ZVS) operation in a wide range of output power, with no variation in the operating frequency.

He stated that the different kinds of **IH control systems** are as follows:

1. **Frequency control**.

2. **Pulse-width-modulation**.

3. **Phase-shift control**.

4. **Duty control**.

The authors stated that these control methods may result in an increase of switching losses and electromagnetic noise of IH configuration.

Ho et al. (1996) [33] described a simple novel control strategy for induction heating using PWM (pulse-width-modulation) gate signal driving circuitry for easy dead time setting for full H-bridge voltage fed inverter. The most outstanding advantage of this method is achieving a zero voltage switching (ZVS) operation, and less components architecture, while the disadvantage aspects are increasing the switching losses and the harmonic distortion content.

Kamli et al. (1996) [27] presented a half-bridge resonant-type IGBT inverter suitable for heating materials at high frequency. The inverter is operated at unity power factor irrespective of load variations, with improved current gain and overall system efficiency, and practically no voltage spikes in the devices at turn-off. This system is designed for relatively limited power of up to 6 KW.

Dorland et al. (2000) [34] developed a full-bridge insulated gate bipolar transistor (IGBT) power supply induction furnace system. The inverter topology includes LLC design with VFI. This design suffers from high compensating capacitor value which means more system capital cost and from the probability of short circuit occurrence, which requires more control care should be taken.

Khan et al. (2000) [35] showed that the lose of frequency resonance tracking would cause a very small power transfer from IH supply to workpiece load with remarkable

switching losses developed. Therefore, the IH system necessitate operation under automatic frequency control (AFC), which ensures high conversion efficiency due to zero voltage switching (ZVS) and maximum power transfer to the load at all times.

Chen et al. (2001) [36] discussed the voltage surge phenomena in a full H-bridge VFI and series RLC load equivalent with and without achieving ZVS mode. The authors stated that large voltage surges are formed under non-ZVS mode with compared to ZVS. The extra energy loss is produced in the line inductance due to reverse recovery process occurred in the body diodes of the configuration.

Chudjuarjeen et al. (2004) [37] stated that the full H-bridge current-fed IGBT inverter is selected to work at a frequency a little higher than circuit resonant frequency, in order to achieve zero current switching mode condition (ZCS) and thus decreasing the switching losses, which provides a good protection from voltage spikes.

Tanimatsu et al. (2005) [38] presents one stage power conversion AC-DC-AC converter with low pass filter (LPF) after the utility AC input source as a power factor correction (PFC) circuit and full ridge rectifier. The boost stage consists from Dc link filter, smoothing capacitor and snubbing capacitor. The chosen topology of inverter is half-bridge, one of its switches operates under high frequency with the aid of the boost snubbing capacitor mentioned above, as shown in Fig. 1.6.
The main advantages of this design is reducing the circuit components, compact size, less cost, unity power factor and decreased AC input main current harmonics, with efficiency achieved exceeded 86%.

Jingang et al. (2006) [39] investigated the characteristics of three types of three-order resonant circuits which were used in induction load-matched systems for voltage-source induction heating inverter (VFI). The authors concluded that the load type of LCL (or also called LLC) is of most advantages, as shown in Fig. 1.7.
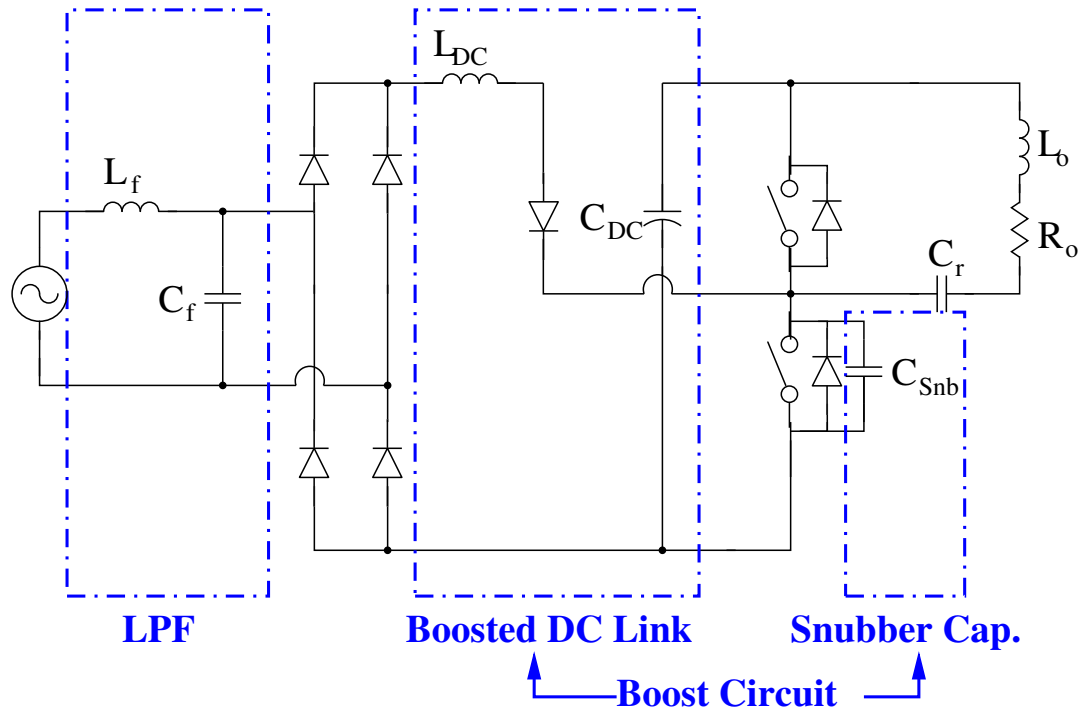
Figure 1.6: One Stage Boost Series Half Bridge Converter

The authors stated that the load equivalent resistance of the super high frequency induction heating systems is usually much less than the resistance while the inverter is working at rated power. Therefore, the load should be matched to the inverter source. The mostly used traditional way for load matching is the electromagnetic coupling high frequency transformer. This solution suffers from two aspects, first: complicating the design and second: increasing the cost.

Finally, they suggested to use the static electricity induction load matched of LLC design to replace the high frequency powerful transformers, which achieves high efficiency and lower cost. This method can be utilized in many applications like quenching, welding, metal finishing, crystal heating, and domestic applications like electric water heaters, electric cookers, and so on.

Wang et al. (2007) [40] proposed a novel dual-LLC resonant tanks zero voltage soft switching converter for super high-frequency solid-state induction heating power supplies.

(a)   (b)   (c)
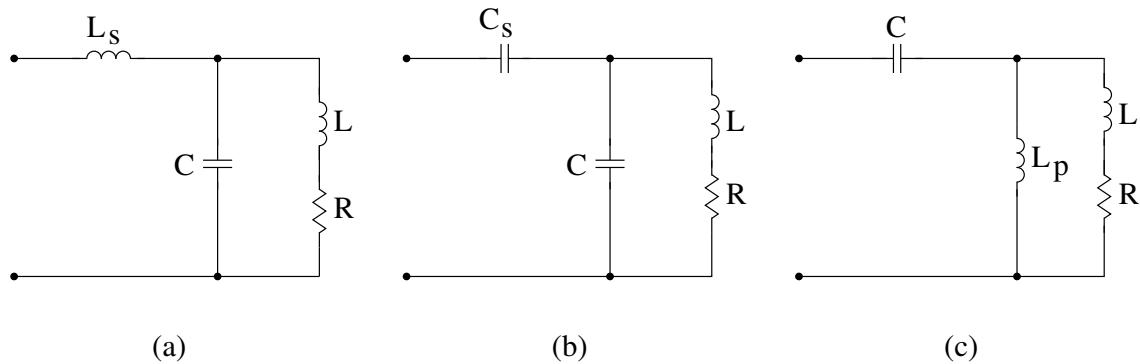
Figure 1.7: Three Order Resonant Load Tank Topologies (a) LLC (b) CCL (c) CLL

Although the proposed converter is capable of absorbing the inductive and capacitive parasitical components in the circuits and devices, but the proposed configuration suffers from complicated design of adding extra sets of inductances, which may increase the reactive power losses of the configuration and might itself act like parasitic inductance too, especially when working under high power in real IH systems, which will increase the reactive power losses on account of decreasing the active power delivered to the IH load tank and less efficiency of maximum transferred power is often produced.

Huerta et al. (2007) [10] investigated the characteristic of LLC load in a full bridge VFI inverter with discovering some advantage aspects of the configuration compared to the VFI of the so called Series Resonant Inverter (SRI) topology, see Fig. 1.8. These advantages can be summarized as follows:

1. High gain of load output current (i_o) with respect to small secondary transformer current (i_s), which means high heating power with less switching losses.

2. Short circuit immunity, where the LLC topology has steady state inductive properties operating in parallel resonant frequency ω_p (will be discussed later in Chapter 3) when short circuiting is occurred.

The authors also stated that the optimal operational condition of LLC load topology depends mainly on the harmony between parameters of 'Inductance Ratio', (β) and the Quality factor (Q) ratio, for which when the β ratio increases, the (Q) ratio also increases
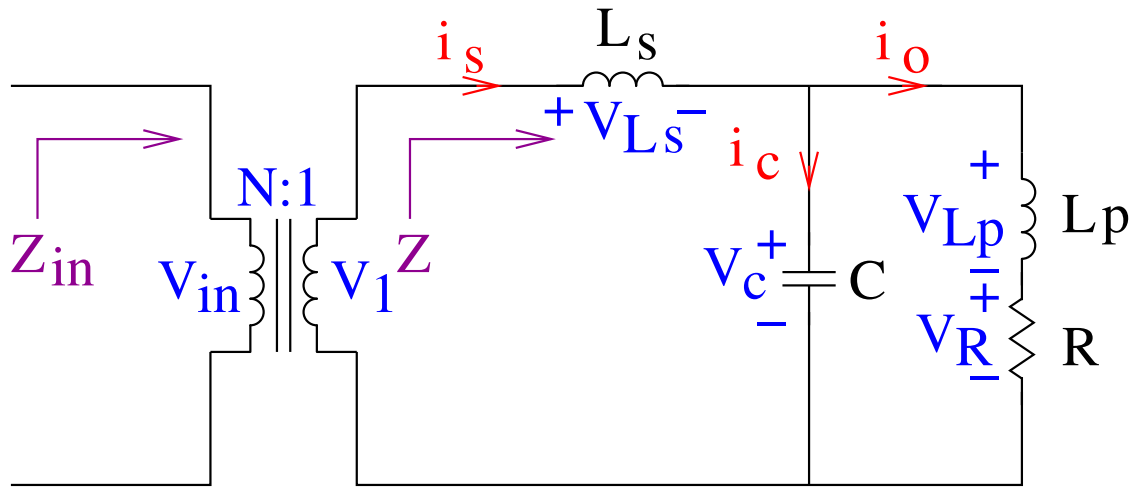
Figure 1.8:   *LLC*-Topology of Heurta Configuration

and thus, more current gain obtained and as a consequence better heating power achieved with optimum efficiency could be reached, as shown in Fig. 1.9, these parameters will derived and discussed later in Chapter 3.

Kubota et al. (2008) [41] presents a novel induction heating topology for ferromagnetic metals. The IH power supply uses power factor control, as a new control method to achieve soft switching below and above the Curie Point using a group of stray inductance-capacitance set to damp down the switching current. Due to the usage of these stray components, an extra parasitic losses formed in the configuration which give rise to the formation of voltage surges during the operation of inverter switches.

This appears clearly through comparing between the theoretical and experimental results, which shows the big difference between both signals, because of the selection of ideal state switching status and the assumption of neglecting the values of stray inductances and capacitances as compared to the heating unit parameter.

Hisayuki Sugimura et al. (2008) [42] developed a resonant high frequency PWM controlled power frequency converter with ZVS mode using the bidirectional switches inverter. The authors stated that the high frequency AC effective output power is linearly directly proportional to the square root of the series load resonant inverter operational
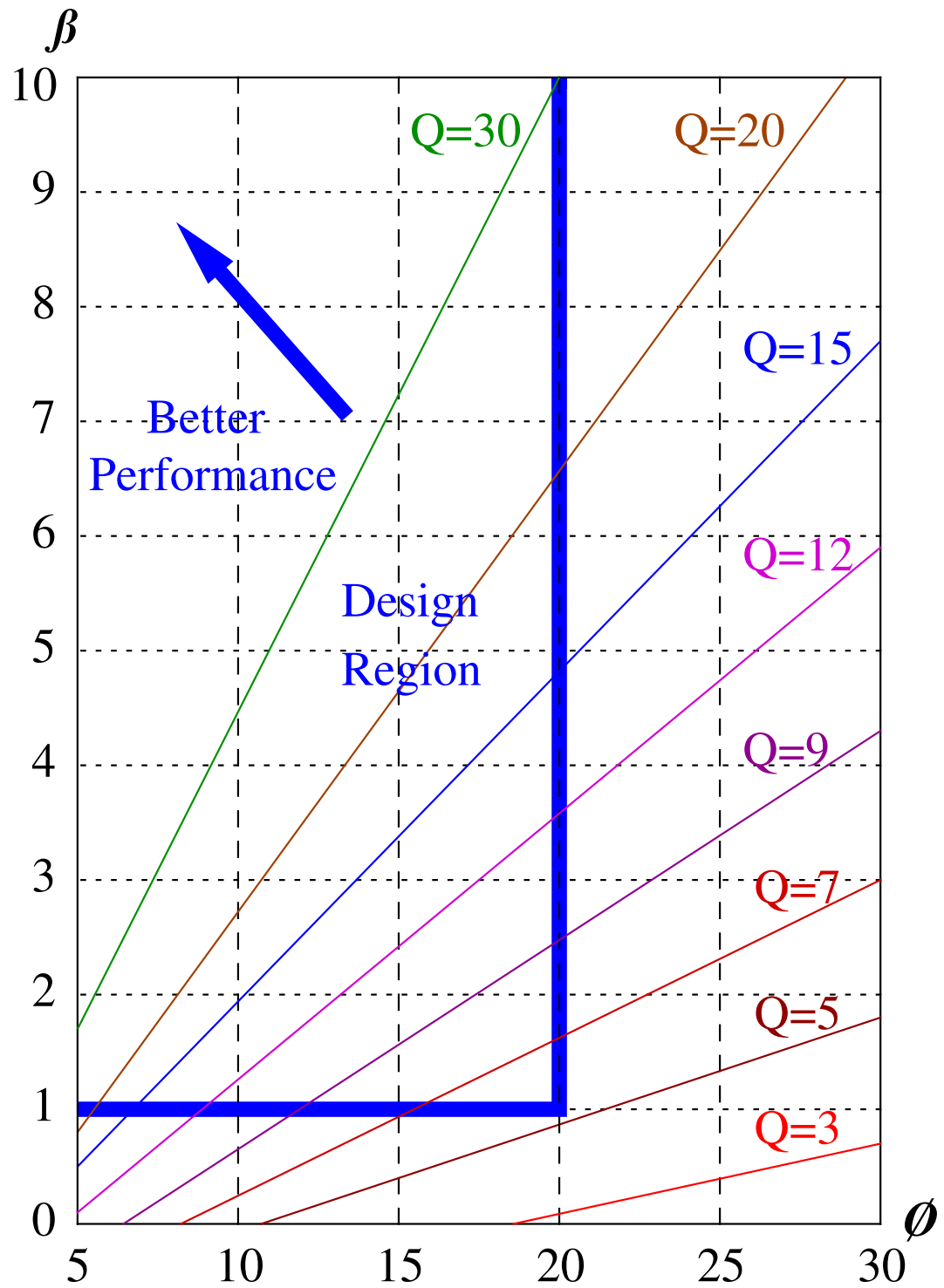
Figure 1.9: Optimum Condition of LLC Topology Operation [10]

frequency.

Lucia et al. (2009) [43] proposed and verified an asymmetrical duty cycle (ADC) modulation scheme, to improve efficiency of half-bridge series resonant inverter applied to domestic induction heating due to its switching frequency reduction and absence of additional hardware requirements, the prototype configuration is shown in Fig. 1.11 .

The authors stated that; the Duty cycle (D) reduction allows decreasing the switching frequency (f_s) and as a result the switching losses will be minimized also, while the minimum value of D and f_s determined by ZVS mode, as shown in Fig. 1.10 .

Ahmed et al. (2009) [44] introduced a multi-output (two-output) series-resonant high frequency inverter using a quasi-square wave control strategy, without using DC smoothing Capacitor filter link from the voltage grid of the AC utility power supply source. It allows the control of outputs, simultaneously and independently, up to their rated power using a simulated prototype.

Fuentes et al. (2009) [45] presented a high power factor full bridge induction heating system, which is formed by a AC mains source, two parallel phase shifted transformers, non-controlled rectifier with DC/DC buck converter as intermediate stage and a resonant inverter using IGBTs, as shown in Fig. 1.12 and Fig. 1.13.

The advantages of using the phase shifted transformers and the filters before and after the rectifier is to reduce the input current harmonics, and to serve as a power factor correction (PFC), which achieve a power factor of more than 0.94.
The authors used the parallel resonant inverter, because of the possibility of getting a very high current gain in the heating coil of the resonant load tank with respect to smaller current flowing in the inverter switched (IGBTs), as the relation between coil current and inverter current is expressed by Q, as follows:
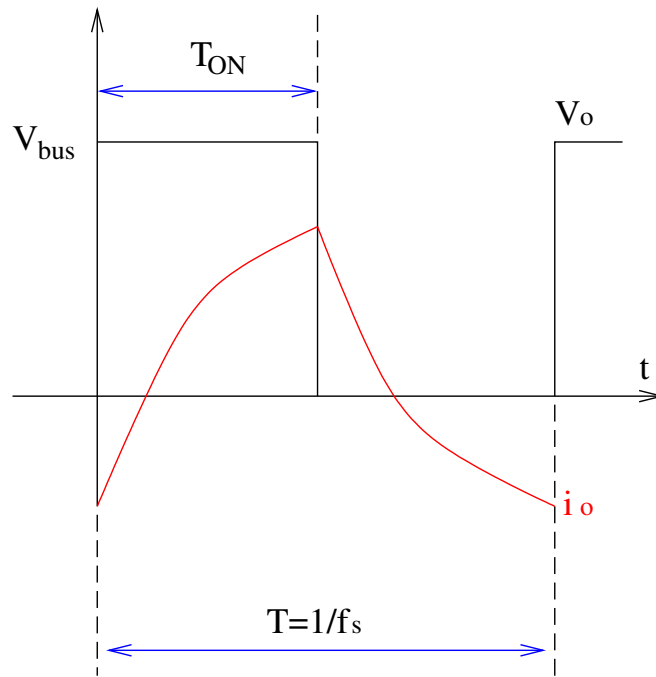
Figure 1.10: Duty cycle control
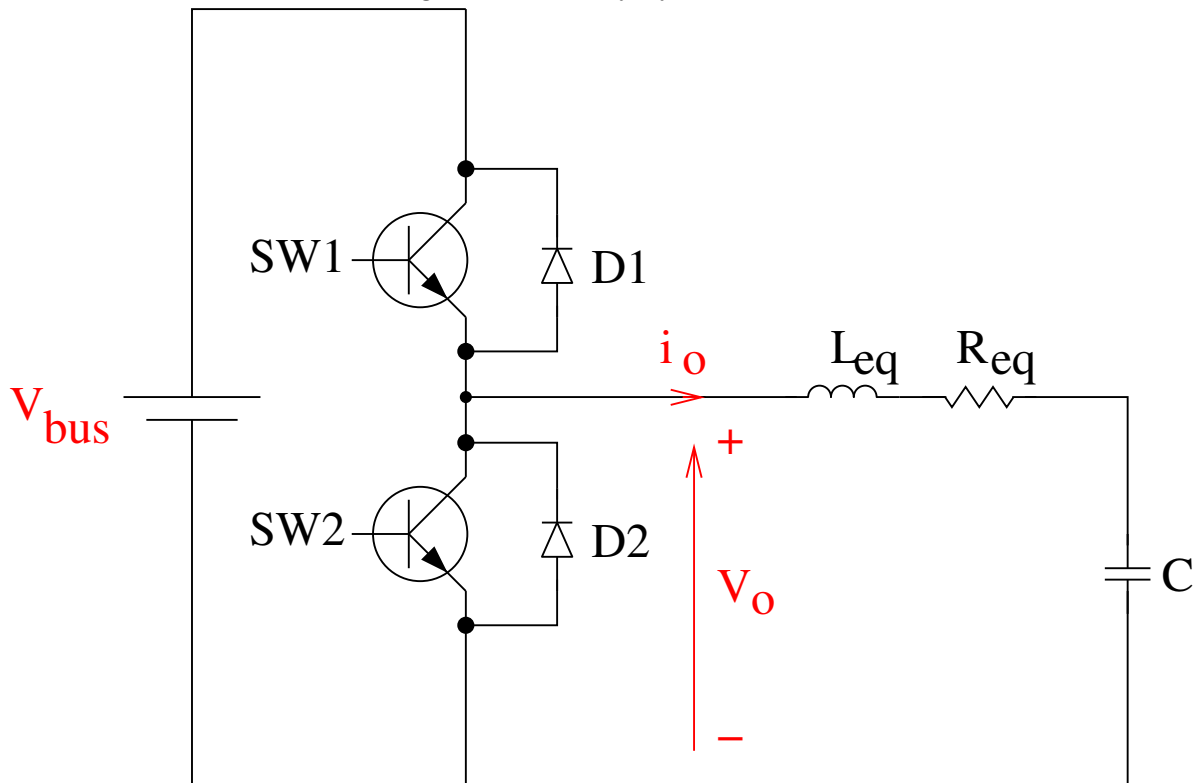
Figure 1.11: Half bridge configuration
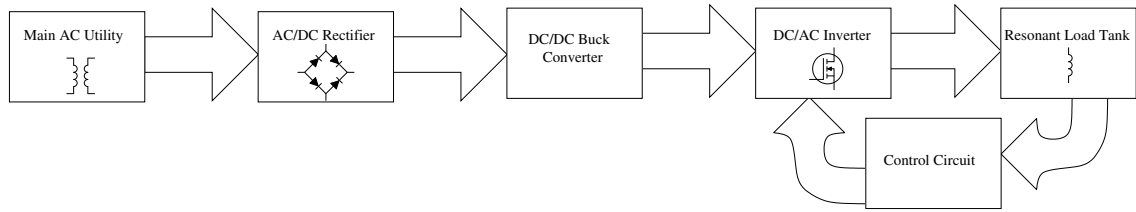
Figure 1.12: Power Supply Block Diagram
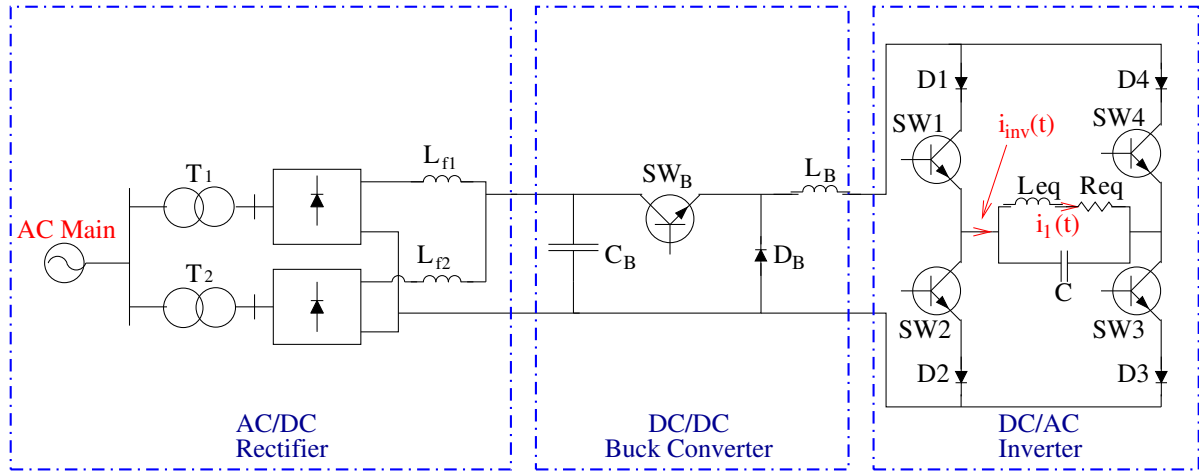
Figure 1.13: IH System with DC/DC Buck Converter

$$i_l(t) = Q.i_{inv}(t) \tag{1.1}$$

where, $i_l(t)$ is the heating coil current, $i_{inv}(t)$ is the inverter current and Q is quality factor which have a typical value of (15-20).

Therefore, having a huge coil current create a very high variable magnetic field links the workpiece which in turn induces a high eddy currents in the load and as a consequence a big heating energy is formed inside the load material. On the other hand, small switching current means decreasing the switching losses of the inverter which means increasing the efficiency of the configuration.

Because of the disadvantage of using the controlled rectifier as a current source and power controller of decreasing the power factor due to firing angle of the rectifier switches, the designers used a non-controlled rectifier and a buck converter as a current source to control the input power.

16

However, adding an intermediate stage of DC/DC buck converter between the source and the inverter might create a problem of imbalance in the design, because the output voltage of the buck converter could be very high that might damage the inverter switches. Therefore, a special care should be taken to the specification of the rectifier-DC/DC buck converter and inverter set.

Besides, using more capacitance and inductance in the buck stage increase the parasitic losses of the configuration and that may produce voltage surges in the inverter and might damage the switches. Therefore, a lot of attention should be considered especially when used with high power applications.

Qinghua Xiao et al. (2010) [46] proposed a series IGBT inverter with capacitive PWM control circuit to achieve the frequency tracking, in order to make the power factor of the inverter close to or equal to a quasi-resonant state.

The authors stated that heating coil current produces an alternating magnetic flux ϕ, which will induce electromotive force (EMF) in the workpiece according to **Faraday's Electromagnetic Equation**, which can be calculated as follows:

$$e = -N\frac{d\Phi}{dt} \tag{1.2}$$

Where N is heating coil turns, therefore, as the flux considered as sinusoidal, then the EMF will be as:

$$\Phi = \Phi_m Sin(\omega t) \tag{1.3}$$

Therefore, the EMF will be expressed as:

$$e = -N\Phi_m \omega Cos(\omega t) \tag{1.4}$$

And the valid value will equal to:

17

$$E = \frac{2\pi f N \Phi_m}{\sqrt{2}} = 4.44 N f \Phi_m \qquad (1.5)$$

As a result, the induced EMF and the heating power are related to frequency and magnetic field intensity. As the heating coil current increases, the magnetic flux increases as well and therefore higher EMF induced inside the workpiece and as a consequence higher eddy current created in the load, which means higher heating power formed in the workpiece.

Esteve et al. (2011) [11] analyses a high frequency voltage-fed inverter with a series-resonant load circuit for industrial induction heating applications, which is characterized by a full bridge inverter made of insulated-gate bipolar transistor (IGBT) and a power control based on pulse density modulation (PDM). This power control strategy allows the inverter to work close to the resonance frequency for all output-power levels. In this situation, zero-voltage switching and zero-current switching conditions are performed, and the switching losses are minimized.

The authors compared two cases of frequency variation control (FVC) and proposed pulse density modulation control (PDM) and showed that operation under nearly the resonant frequency may not achieve full optimal operational point. Therefore, special techniques like PDM is needed to perform better efficiency, by finding the appropriate modulation index values.

Jittakort et al. (2011) [47] proposed a class D current source resonant inverter (CSRI) with interleaved DC/DC buck converter for induction heating power supplies for non-ferromagnetic load. The output power is controlled by adjusting the pulse width of the buck converter stage.

The authors stated that for non-ferromagnetic loads, the effect of temperature on material properties especially the relative permeability is not so significant that can be

neglected and thus, no need for automatic frequency control to catch resonant state, because the resonant frequency is fixed during heating cycle. Therefore, choosing the control category depends widely on the properties of material of application, i.e. ferromagnetic or non-ferromagnetic.

Sarnago et al. (2012) [48] revealed that using the boost circuits at the rectification stage increases the system efficiency to approximately 94%, by reducing the rectifier losses to the minimum and increasing the output voltage, accompanied by decreasing the current levels for the same output power. The authors summarized the main boost DC link stage topologies for domestic applications, as follows:

- **Topology 1 of Boost Rectifier:** It is defined as the traditional or classical design of boost circuit that is consisting from one switch, one diode, DC link inductance and capacitance. It has the advantage of serving as a power factor correction (PFC) circuit, and increasing the DC link voltage, as in the Fig. 1.14.

- **Topology 2 of Boost Rectifier:** It includes more electrical storage components (i.e. inductors and capacitors), through using one switch also, four diodes, three DC link capacitors and two DC link inductors. On one hand, the advantage of this design is reducing the switching losses, but on the other hand it increases the conduction losses as it posses more diodes, as shown in Fig. 1.15.

- **Topology 3 of Boost Rectifier:** This configuration is characterized by replacing the DC link inductor by a high frequency power transformer and keep using one DC capacitor only, but with increasing the number of switches to four, therefore; the conduction losses are reduced, but the switching losses are increased because of using more switches, which will also complicate the control of the design, as in Fig. 1.16.
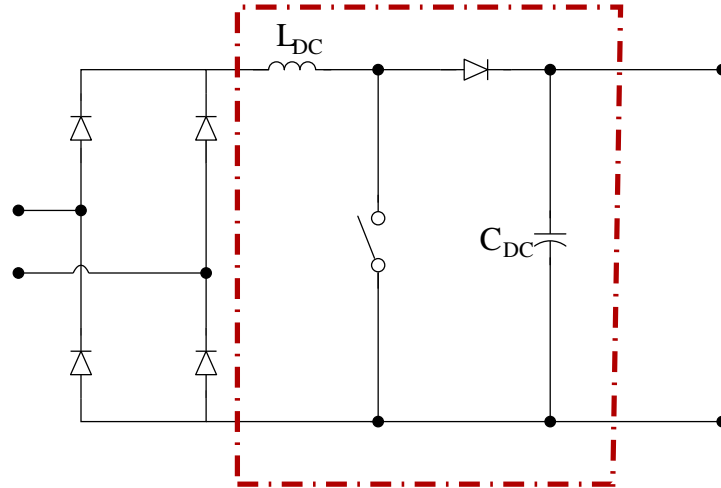
Figure 1.14: Classical AC/DC Rectifier Boost
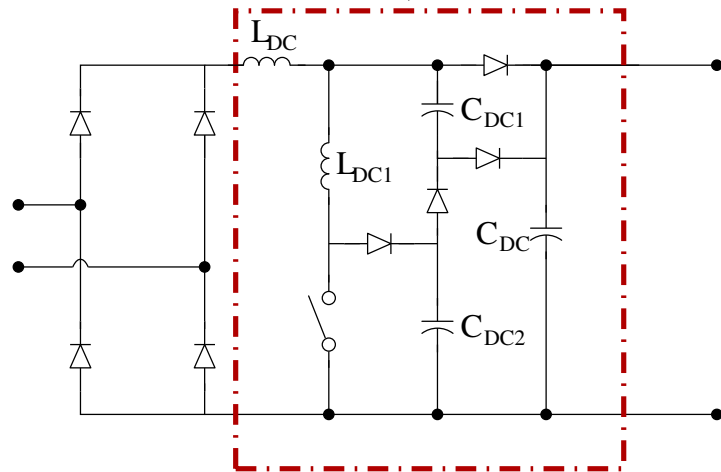
Figure 1.15: Improved AC/DC Rectifier Boost with less Switching Losses
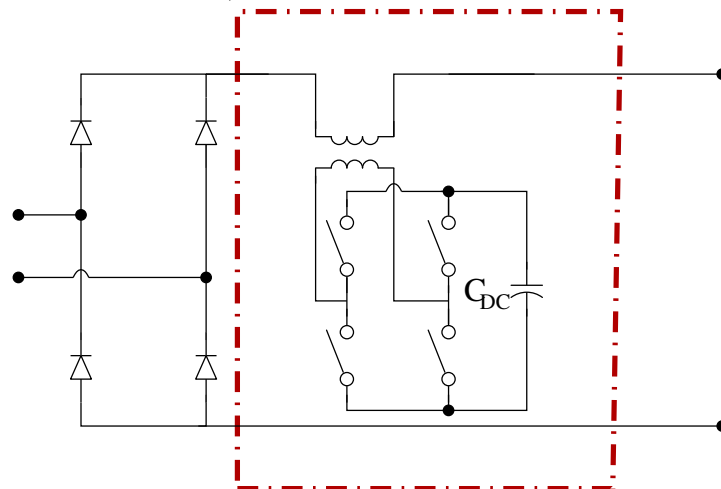
Figure 1.16: Improved AC/DC Rectifier Boost with less Conduction Losses

Yilmaz et al. (2012) [13] investigated the variable-frequency operation of the coreless induction melting furnace (IMF). It has shown the following: The major power quality problem of an IMF as a load on the power system is the injection of various current harmonics to the grid. The harmonic problem cannot be mitigated by passive filtering solutions; therefore the author suggested new technologies should be exercised in the IH system , such as active power filters, and/or PWM rectifiers.

While this solution will probably mitigate the harmonics to a considerable level, but the using of active filters will increase the capital cost considerably, besides the usage of PWM rectifiers will complicate the control circuit and increases the switching losses of the IH system and lowers the power factor of the system.

1.2   Thesis Aim and Organization

While, there are a certain number of resonant inverters types that can be employed in induction heating generators, but the mostly predominant utilized categories are the **'Voltage Fed Inverters (VFI)'** or also called **'Series Resonant Inverters (SRI)'** and the **'Current Fed Inverters (CFI)'** or also called **'Parallel Resonant Inverters (PRI)'** and the **'Hybrid Voltage-Current Fed Inverters (HVCFI)'** that takes the advantage aspects of both kinds.

Depending on the equivalent load tank set being used, the VFI configuration uses a load tank composed of a load of equivalent resistance and inductance connected in series with a compensating capacitor, while the resonant load tank in the CFI consists of a resistance and inductance equivalent set connected in parallel with a compensating capacitor.

The compensating capacitor existence here is very important to resonate the load circuit. Each of the two kinds has its own advantages and drawbacks that will be discussed later (in Chapter 2), but quickly it can be pointed that the VFI has a simple load tank connection with the inverter output current is the same as the load tank current which

needs a power transformer that matches the inverter with the load to have desired design.

The equality between the two currents means in order to raise the output heating current, it is necessary to increase the inverter current which certainly increases the switching losses and the heat in the switches. This situation requires a heat sink protection added to the inverter switches. Besides, the VFI design suffers from short circuit (S.C.) occasion especially when coil turns touch the workpiece. This problem will increase the output current suddenly in load circuit and may in turn damage the inverter switches.

These drawbacks are less existed in the CFI, as in CFI configuration the parallel load topology can be describes as the $L - R$ equivalent in parallel with C which can be called LRC topology . The CFI topology in spite of being better treated than the VFI as being in parallel, but it still suffers from S.C. problem, as for any reason even for a very small time the load became a capacitor, the capacitor inrush current will increase the output current suddenly and acts like a S.C., which may damage the inverter also. The topology needs power matching transformer which will increase the losses and decrease the efficiency.

The main advantage feature of the CFI configuration as compared with the VFI configuration, is the separation between the inverter current and the output load current by a certain gain, usually the inverter current is less than the output current by about a value of **Quality Factor** Q, which means better heating current and power, and at the same time less switching current and as a consequence less switching losses. While the main advantage of the VFI is the supplement of constant voltage delivery from the AC/DC power supply to the resonant load through the DC/AC inverter.
While, both kinds needs a power transformer to match the resonant load with the inverter, which means more cost.

Later on, a third kind of **Hybrid Voltage-Current Fed Inverter (HVCFI)** have

appeared to overcome these problems. This topology utilizes the same VFI source using a voltage source capacitor, while it posses the same CFI resonant load tank topology of $L - R$ equivalent in parallel with C and the whole set is in series with another inductance L_s forming the well known LLC topology. This configuration have overcome the problem of S.C. problem through adding an extra inductance, which performs as a mandatory path of inductance at any time, which can mitigate this problem a lot even when Inrush current problem occurs.

Although each kind have its own characteristics that can be applied to certain kind of application, i.e. depending on high frequency or low frequency and high quality factor or low quality factor, but the main general property of IH system is its variable characteristics of IH load tank during the heating cycle, especially when heating loads like ferromagnetic metals and particularly effect on the inductance and resistance of heated workpiece as exposed to high temperature.

This implies unbalance in the system even though a tracking mechanism of frequency have been applied, especially when the IH configuration working under high power. This load change injects undesired harmonic noise content to the IH system, which causes parasitic losses in the form of heating power. Therefore, In order to mitigate this harmonic distortion content and absorb these parasitic inductance components, a new techniques of IH power supply configuration should be employed to find better performance of IH system with a better harmonic distortion immunity design.

Since its starting and predominance at the $1980s$ decade, the **Multilevel Neutral Point Clamped Inverter (MNPCI)** topology has made revolutionary change in the utilization of the power electronics in high power applications such as metros, tractions and AC motor drive with pulse width modulation (PWM) control technique as a wide range variable speed-drive system [49].

Depending on its advantage aspects like high power factor, lower current harmonic distortion and low voltage stress on the inverter power switches, i.e. reduced losses and energy dissipations and hence, higher efficiency and lower capital cost, which is very important factor in any induction heating system application [50–52], these merits give a great inspiration to use it in IH system design as a novel IH inverter topology that has not been used in this field before.

This dissertation introduces a novel induction heating power supply using multilevel neutral point clamped inverter. The research is divided into two main phases. The first phase is the verification of the new configuration design as a successful IH power supply. During this stage, an experimental prototype of MNPCI converter with resonant load tank is built. The design uses a parallel LLC topology with fixed values to represent the resonance state of workpiece, inductor and capacitor set. The analytical analysis is carefully made to describe the total impedance and the condition of maximum power transfer of the design. A modified parallel LLC design is introduced together with all corresponding analytical derivations.

The second phase is the proposal of MNPCI power supply with variable parallel LLC topology. This stage tend to match the changeable characteristics of IH system during heating cycle. The system works in soft switching mode of ZCS and ZVS mode with minimum switching losses. The optimization condition of heating power is verified through reducing the harmonic distortion content to the minimal possible level.

This thesis is organised into five chapters: **Chapter** 1, is the introduction and literature review of the DC/AC power converter topologies that are commonly utilized in IH system. These inverters belong to the resonant power converters family. This Chapter tried to clarify these various categories and then stating their general designs and principles of each type. Then some critical feedback is stated to understand the advantages and the disadvantage aspects, in order to benefit from those in the design of proposed

configuration.

In **Chapter** 2, the general basis of electromagnetic induction effect phenomena is clarified in details, its formation, procession, advantages, methods of modelling and its employment in induction heating applications are also discussed in this research. The most widespread categories of IH converters are illuminated. With keeping their aspects of advantage and disadvantage properties in mind, their design restrictions must be avoided and the vantages should be taken to achieve the best possible future converter design with maximum possible efficiency.

Chapter 3, introduced the **Multilevel Neutral Point Clamped Inverter (MN-PCI)** as a novel inverter component in IH system. At the beginning the theory of multilevel inverters is discussed in details, then its significance, design, load topology are also studied carefully. The power transfer from proposed inverter to the load equivalent circuit is analysed using two cases of load tank topologies. Then the control circuit used is stated and finally the experimental results that verifies the prototype design are analysed.

Chapter 4, is concerned with the optimal control of IH-MNPCI configuration. The control map direction is achieving minimum total harmonic distortion and as a consequence obtaining maximum heating energy delivered to the load. The prototype used here is of variable load parameters of LLC topology in order to match the IH process properties. All configuration parameters are stated with their values to suit the corresponding application. All calculations of average power transfer and the harmonic analysis of the proposed configuration are derived in details. The results are analysed and illustration curves are given to clarify the control strategy.

And finally, **Chapter** 5 is about the conclusions obtained from this research work and suggestions for future plan to develop this technique are given.

1.3   Contribution to Knowledge

The main knowledge contribution of the dissertation can be summarized as follows:

- **A new design of induction heating power supply configuration with two categories of LLC topologies**

  A Novel induction heating power supply topology using multilevel neutral point clamped inverter (MNPCI) is investigated and verified. The proposed converter topology decreases the switching losses by decreasing the DC link voltage to half its DC rail voltage value with the aid of operation under soft switching mode condition. Depending on the modified LLC optimum design being introduced, it shares the advantage features of both voltage fed and current fed inverters with the capability to absorb the undesired parasitic components in the design. The new design involves adding new circuit parameter that helps in controlling the power transfer from the MNPCI to the resonant load tank. All the analytical analysis made and the corresponding experimental work verifies the prototype configuration.

  This contribution was presented by the author and published in:
  - **B.M. Flayyih; M.Z. Ahmed; M. Ambroze, "A Novel Hybrid Voltage-Current Fed Induction Heating Power Supply System Using Multilevel Neutral Point Clamped Inverter ", Energycon 2014 IEEE International Energy Conference, Dubrovnik-Croatia. From 13th - 16th May 2014.**

- **An optimum power control of induction heating system by reducing harmonic distortion content**

  The development of IH system has become a pressing need to improve the power transfer from power supply to the IH load of the application required, and due

to variable characteristic of IH load workpiece during the heating cycle [40, 53], it is necessary to develop an IH system that operates using resonant inverters with switching frequency that changes according to changing load conditions during the IH application process, in order to keep tuning with natural resonant frequency of the system and keep working under optimal operational point [13].

A novel super frequency induction heating power supply using MNPCI with optimum control algorithm is introduced. The control strategy is to keep phase shift angle between voltage and current approximately zero at all load conditions to ensure maximum power transfer whatever the load parameters changes, that is necessary to reduce the switching losses and increase the efficiency. The load topology being used consists of variable LLC resonant tank with values chosen carefully to coincide with the design.

Afterword, an Optimum Harmonic Control of a proposed induction heating power supply with MNPCI is also introduced in this research. The proposed system achieves the soft switching mode for both current and voltage with low harmonic distortion and the capability to maximize the heating power by controlling the harmonics. The modulation strategy depends on changing the ON switching time (t_α) of the prototype to an optimized value that achieves natural switching with lowest possible harmonic distortion and thus, gaining highest heating power efficiency.

This contribution was also presented by the author and published in

  – **B.M. Flayyih; M.Z. Ahmed; S. MacVeigh, "A Comprehensive Power Analysis of Induction Heating Power Supply System Using Multilevel Neutral Point Clamped Inverter With Optimum Control Algorithm ", 2015 IEEE 11th International Conference on Power Electronics and Drive Systems (PEDS), From 9th - 12th June 2015, Sydney, Australia.**

This contribution is also presented by the author in:

– **B.M. Flayyih; M.Z. Ahmed; M. Ambroze, "An Optimum Harmonic Control of Induction Heating Power Supply System Using Multi-level Neutral Point Clamped Inverter", The IEEE Transportation Electrification Conference and Expo Asia-Pacific (ITEC2016), Busan, Korea on 1st - 4th June, 2016.**

Chapter 2

Induction Heating Principles and Applications

2.1 Introduction

E lectromagnetic effect was first defined by **Michel Faraday** (1831) [1]; he showed that currents could be induced in a closed or secondary circuit as a result of varying AC current in a neighbouring primary circuit. The essential feature was the change in flux links with the closed secondary circuit caused by an alternating current in the primary circuit, this flux will induce voltage difference in the secondary, i.e. current will flow. This current is called eddy current or Foucault current.

In induction heating equivalent, the primary circuit is the coil (inductor) which is supplied by alternating current and the secondary circuit is the workpiece which to be heated.

The induced voltage in the workpiece which is produced by flux fluctuations, gives rise to Foucault current, i.e. $(I^2 R)$ losses which form the main source of heating energy required to raise the temperature of workpiece [2].

When the coil is excited by an alternating current, it produces an axial alternating

magnetic field. The variation of magnetic field produces an electric field and currents along loop paths concentric with the axial, which causes the workpiece heat rise.

This chapter illustrates the main principles of induction heating (IH) with a literature review of IH basics, modelling and famous induction heating converter topologies.

But for better understanding the IH process, first of all, a quick definitions are introduced to the main concepts of induction heating in this chapter.

2.2 Key Definitions

This section quickly illustrates some of the widely prevalent topics in IH as a key to enter the basics of electromagnetic effect theory and its applications.

2.2.1 Eddy Currents

It is occurred when an alternating magnetic flux caused by an AC current flowing through primary coil links with a neighbouring secondary coil, it causes voltage potential produced in the secondary, which will induce currents flowing in loops, this phenomenon is called eddy currents, or sometimes called "**Foucault Currents**".

The eddy currents are exponentially variates inside the workpiece towards its center, therefore; it can be expressed by the following equation [2]:

$$i_x = i_o.e^{-\frac{x}{\delta}} \tag{2.1}$$

Where,

i_x: is the current density at distance x from workpiece surface.

i_o: is the current density at distance $x = 0$ (workpice peripheral).

δ: is the skin depth constant, given by Section 2.2.3.

2.2.2   Effect of Temperature on Eddy Current Losses

When eddy currents are induced in the workpiece due to variable magnetic flux in the inductor, a heating power is produced inside the material of the load, and the temperature of workpiece is increased in a form of heat. When the temperature rises, the material properties especially the resistivity (ρ) of load material begin to change gradually, as a consequence; the load resistance variates. This variable resistance characteristics will affect the eddy currents flow through the workpiece and as a consequence; the induced heating power changes, therefore; it is very important to declare the effect of temperature change on the power losses formed by eddy current in this section.

The linked flux with the workpiece is the main factor that induces the eddy currents. This flux is denoted by Φ, and its value is given by Equation 1.3. The electromotive voltage produced because of flux linkage can be taken from **Faraday Equation** given by Equation 1.2. The induced voltage through an inductive load is calculated as follows:

$$e = L\frac{di_e}{dt} = -N\frac{d\Phi}{dt} \tag{2.2}$$

And for a linear flux change, the Equation 2.2 is equal to:

$$\Delta\Phi = -LN\Delta I_e \tag{2.3}$$

In other words, the eddy currents change ΔI_e is directly proportional to the magnetic flux change $\Delta\Phi$, as follows:

$$\Delta I_e \propto \Delta\Phi \tag{2.4}$$

Whereas, the eddy current losses (P_e) produced by eddy current I_e is directly proportional to the switching frequency (f) and magnetic flux density (B_m), and reversely proportional to the resistivity (ρ), as follows [55–57]:

Resistivity (n.Ohm.m)
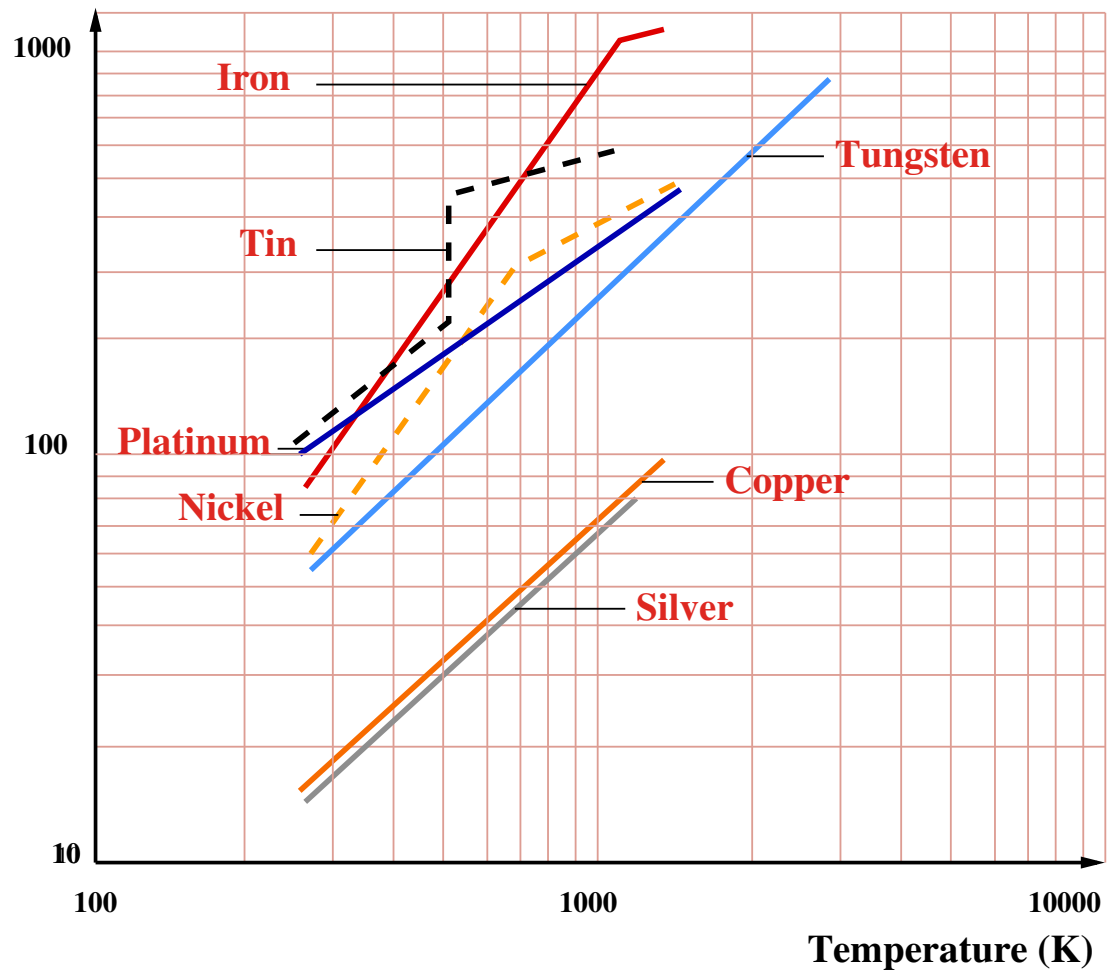
Figure 2.1: Change of Resistivity as a Function of Temperature for Some Metals [54]

$$P_e = \frac{K_e . f^2 . B_m^2}{\rho} \tag{2.5}$$

Where, K_e: is the coefficient of eddy current losses, and it depends on the material characteristics [56].

And, the value of magnetic flux density (B_m) in $Tesla$ (web/m^2) is equal to the following equation:

$$B_m = \frac{\Phi_m}{A} \tag{2.6}$$

Where, Φ_m is the maximum flux value.

And, A: is the cross sectional area of the workpiece.

Which means that when flux increases, the magnetic flux density increases, and hence; the eddy power increases as well.

Also, by observing the resistivity-temperature curve shown in Fig. 2.1, it can be concluded that the resistivity of metals (ρ) is directly proportional with temperature change (dT), which means:

$$\rho \propto dT \tag{2.7}$$

Where,

$$dT = T - T_o \tag{2.8}$$

Being, T: is the new temperature in ^oC or K.

And, T_o: is the ambient temperature, where $T_o = 20^oC$ or $293K$.

Thus, the resistivity (ρ) of metal given by Equation 2.5 above is a function of temperature. In order to represent this relationship, a coefficient called α_o factor is introduced,

as in the following expression [54]:

$$\rho = \rho_o \left[1 + \alpha_o \left(T - T_o \right) \right] \tag{2.9}$$

Where, α_o: is a constant coefficient that describes the variation relation between resistivity and temperature parameters, which can be found from the following equation:

$$\alpha_o = \frac{1}{\rho_o} \left(\frac{d\rho}{dT} \right)_{T=T_o} \tag{2.10}$$

Where,

ρ_o: is the resistivity at ambient temperature condition.

$d\rho$: is the resistivity change due to small temperature rise dT.

And, $d\rho$ is equal to the following mathematical expression:

$$d\rho = \rho - \rho_o \tag{2.11}$$

Therefore; when temperature of the metal increases, the temperature change term $(T - T_o)$ increases, causing the resistivity (ρ) in Equation 2.9 above increases as a result, which forces the eddy power P_e decreases, because $(P_e \propto \frac{1}{\rho})$, as can be seen from Equation 2.5 above. Therefore; the decrease in eddy power might reach 50% in some cases, depending on the new temperature, and on the rate of resistivity change of material versus temperature, as shown in Fig. 2.1.

2.2.3   Penetration (Skin) Depth

Generally, The induced Foucault currents density varies exponentially inside the work-piece, and when it falls to $(1/e = 0.368)$ -about one third- of its surface value is usually called penetration depth, at which most field and currents concentrates in this area, this phenomena is sometimes called **Kelvin Effect** [2].

The skin depth (δ) is related to electrical resistivity (ρ), reversely proportional with

Current Density Ratio
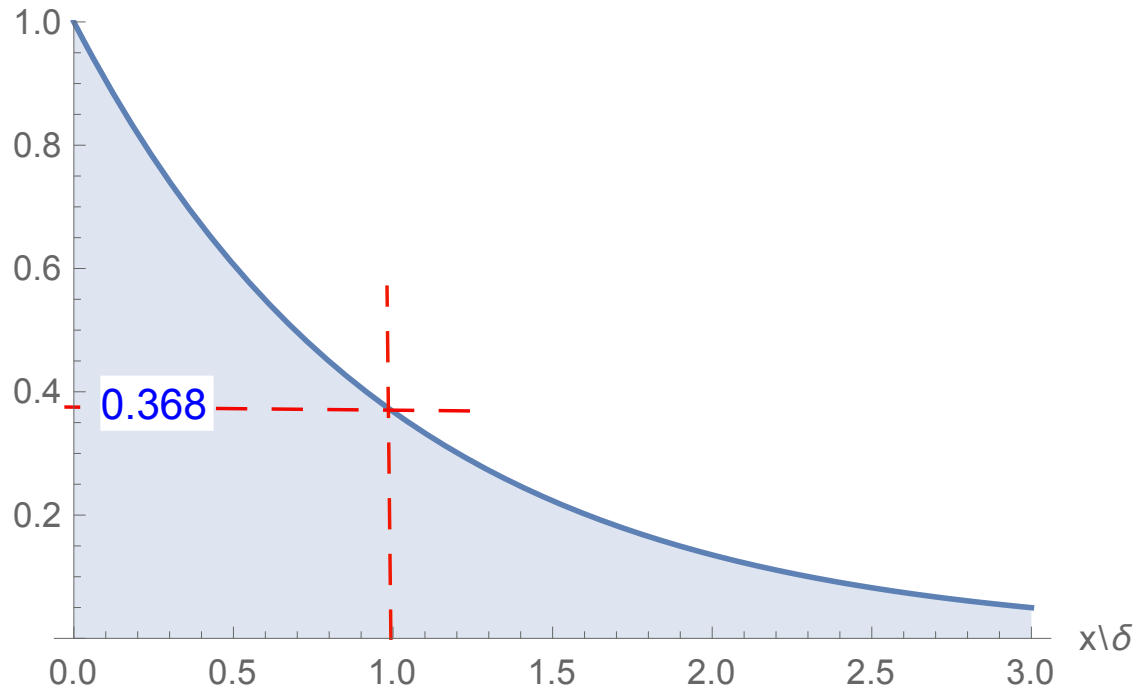
Figure 2.2: Skin (Penetration) Depth

magnetic permeability (μ) of the workpiece, and angular frequency (ω)

$$\delta = \sqrt{\frac{\rho}{\mu f \pi}} \tag{2.12}$$

and

-

$$\mu = \mu_o \mu_r \tag{2.13}$$

Where μ_o, is the absolute (vacuum) permeability equals $4\pi.10^{-7} H/m$ and μ_r, is the relative permeability.

-

$$\omega = 2\pi f \tag{2.14}$$

Current density falls off from surface towards the center of workpiece and the rate of decrease is higher when frequency increases. It is also dependent on two properties of material, i.e, resistivity and relative permeability, as shown in Fig. 2.2.
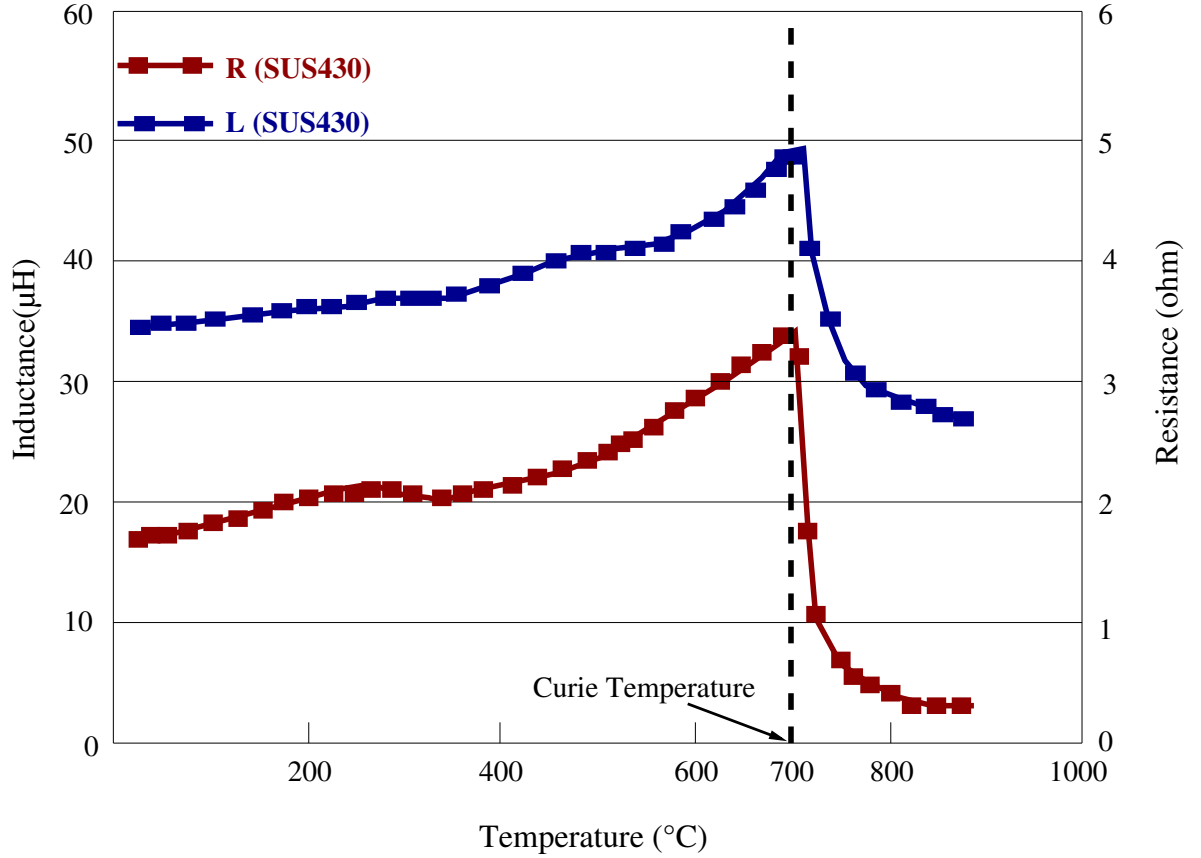
Figure 2.3: Inductance and Resistance Change as a function of Temperature for a Stainless Steel [41]

2.2.4   Curie Temperature

It is the point at which the electrical properties (like resistance and inductance) of ferromagnetic metal change rapidly during induction heating process, therefore; the material loses its magnetization characteristic and transforms into paramagnetised [58].

Therefore; the change in material properties is about 50% less than the optimum value of the resistance reached at the Curie point, and approximately 10% decrease from the maximum value of the inductance, as can be seen in Fig. 2.3 for a stainless steel metal. As a consequence, the IH system loses its resonant state and operate under hard switching mode, thus; the system losses jump quickly and may cause damage to the MOSFETs due to high switching current passing through at that moment , therefore; a special care should be taken to the IH system of more complex load circuit and more analysis should be done, in order to keep working under constant frequency [41, 59].

2.2.5   Joule Effect Phenomenon

IH process is based mainly on energy dissipation mechanism, which occurs when an AC current is flowing in the coil, it will induce an alternating magnetic field flux opposes the original coil magnetic field in direction and thus, produces a voltage potential in the workpiece.

This voltage potential will create currents in the workpiece called Foucault currents, which then have the same frequency as the original AC current but in opposite direction. These induced eddy currents will produce heat energy in the workpiece of I^2R, this phenomenon is so called "Joule effect".

While, other factor of heating energy dissipations of the hysteresis phenomena effect forms in best situation less than 7% of the entire energy losses in IH system [60] and may varies from material to another of workpiece. In consequence, the main energy dissipation mechanism is the Joule effect losses and the Foucault currents.

2.2.6   Quality Factor

One of the important parameters that characterizes the IH load is the quality factor (Q). Its value depends mainly on the load tank configuration, i.e. on series or parallel load topology.

It is defined as the ratio of reactive to active power of the IH system:

$$Q = \frac{|P_{rect}|}{P_{act}} \qquad (2.15)$$

2.2.7   Resonant Load Tank

It can be clarified as a resonant oscillatory circuit representation to the IH load side, formed mainly from a series equivalent to the workpiece-heating coil set represented by load resistance and inductance, to be connected with a compensating capacitor either in

(a) Series load tank   (b) Parallel load tank
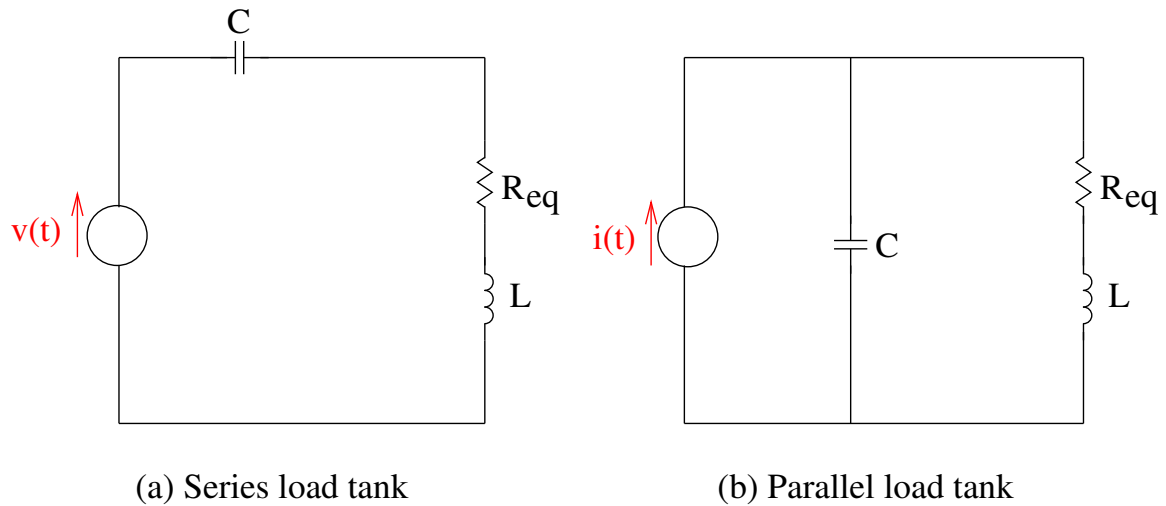
Figure 2.4: Series and Parallel Load Tank Configuration

series or in parallel, as can be shown in Fig. 2.4.

The main function of compensating capacitor is to resonate the load inductance, which helps the IH system to be operated under steady state condition. Fig. 2.4 shows there are two main types of resonant tanks:

- Series load tank: It is produced when connecting the series $(R - L - C)$ load tank set in series with a voltage source, as in Fig. 2.4-(a).

- Parallel load tank: It is formed when the parallel $(R-L//C)$ load tank is connected in parallel with a current source, as in Fig. 2.4-(b).

2.2.8 Inductor and Capacitor Response

In order to understand well the electromagnetic phenomena characteristic of any proposed IH load tank, it is very important to remember the response action of individual circuit components to sudden changes in voltage and current during cycle operation. For being most important storage components of IH load are the inductor and capacitor due to storage capability of current and voltage respectively, therefore this section recalls their electrical behaviour as follows:

Inductor Response:

Under steady state condition, the inductor current lags the voltage, as shown in Fig. 2.5 below.

Thus, the inductor voltage and current equations are equal to:

$$v_L = L\left(\frac{di_L}{dt}\right) \tag{2.16}$$

$$i_L(t) = i_L(t_1) + \frac{1}{L}\int_{t_1}^{t} v_L d\xi \tag{2.17}$$

Where, $t > t_1$ and ξ is the variable of integration.

It can be deduced from Fig. 2.5 and Equations (2.16) and (2.17), that even though the inductor voltage jump instantaneously, the inductor current can not change instantaneously but increases gradually until reaching its maximum steady state value and vice versa, when the voltage drops down suddenly, the current step down variation is gradually, therefore it stores magnetic field and usually considered as a current storage component especially at high frequency oscillation.

The time required for discharging the inductor current is called "Time Constant, τ", and its value for RL circuit can be calculated as follows:

$$\tau = \frac{L}{R} \tag{2.18}$$

Capacitor Response

In this case, the capacitor current leads the voltage under steady state condition, as shown in Fig. 2.6 below.

The inductor current and voltage are respectively equal to the following equations:
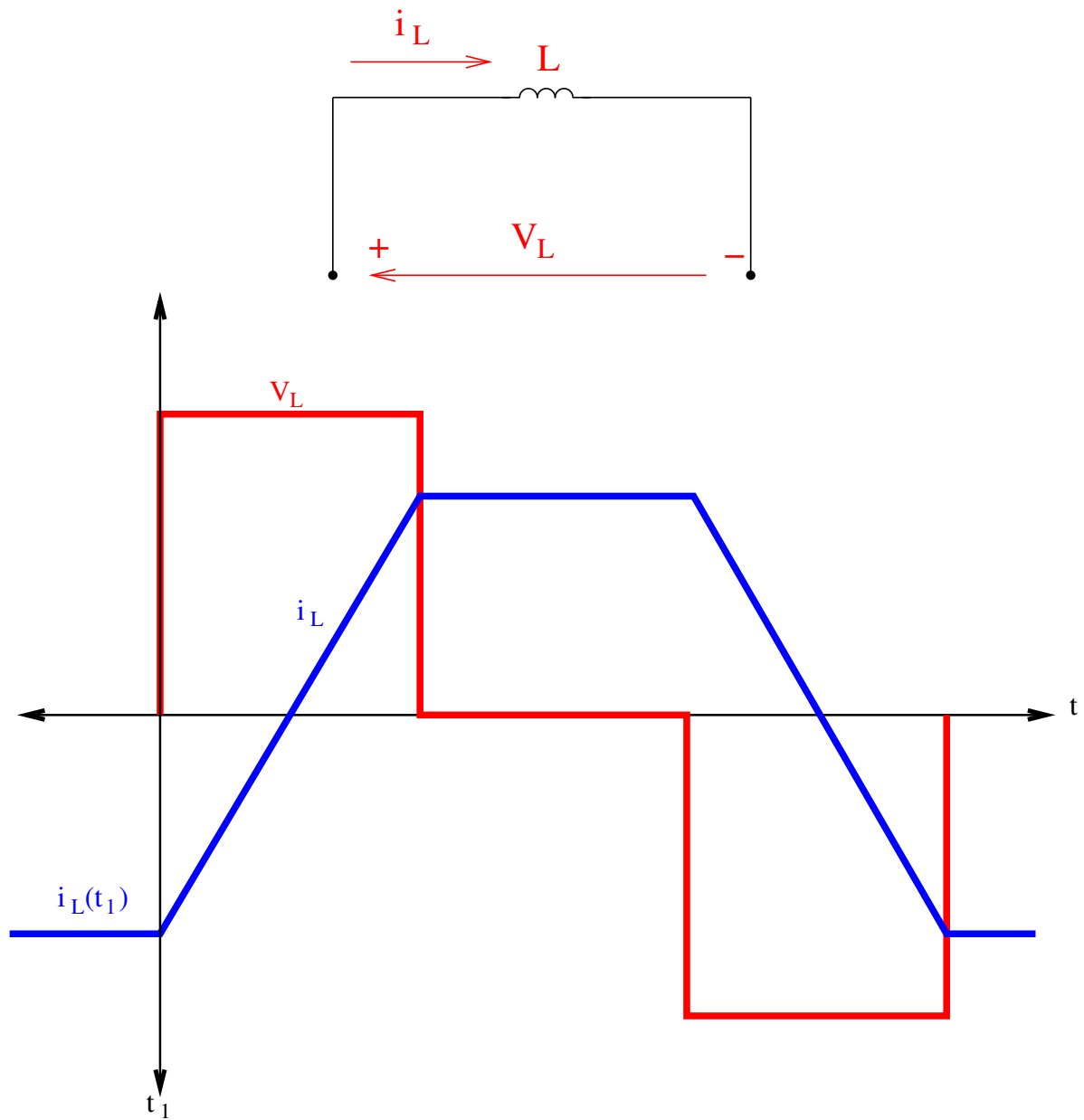
Figure 2.5: Inductor Current and Voltage Response

$$i_c = C \left(\frac{dv_c}{dt} \right) \tag{2.19}$$

$$v_c(t) = v_c(t_1) + \frac{1}{C} \int_{t_1}^{t} i_c d\xi \tag{2.20}$$

Where, $t > t_1$ and ξ is the variable of integration.

It can be revealed from Fig. 2.6 and Equations (2.19) and (2.20), that the capacitor voltage cannot alter instantaneously with sudden instant current pulse jump. This phenomena when happens at time instance of start charging the capacitor it is usually called 'Inrush Current', this current is very high and the capacitor during which three or more times its rated current, therefore; there should be a certain inrush protection circuit added to the circuit to prevent huge surge current from flowing even for a short time, which may cause damage to the sensitive components of the circuit like MOSFET switches if exceeded their current limitations.

When the current falls down suddenly, the voltage takes gradual step down, therefore the capacitor stores electric field and usually considered as a voltage storage unit.
The time required for discharging the capacitor voltage is also called "Time Constant, τ", and its value for RC circuit is evaluated as:

$$\tau = RC \tag{2.21}$$

2.2.9   Soft Switching Mode (SSM)

It can be defined as manipulating the output voltage and/or current signals to be at zero value during the moment of switching, so as to decrease the switching losses and therefore; gain higher energy conversion efficiency of proposed IH system.
It is usually accompanied by operation under resonant state condition of $L-C$ load tank circuits. The SSM is divided into two main categories:
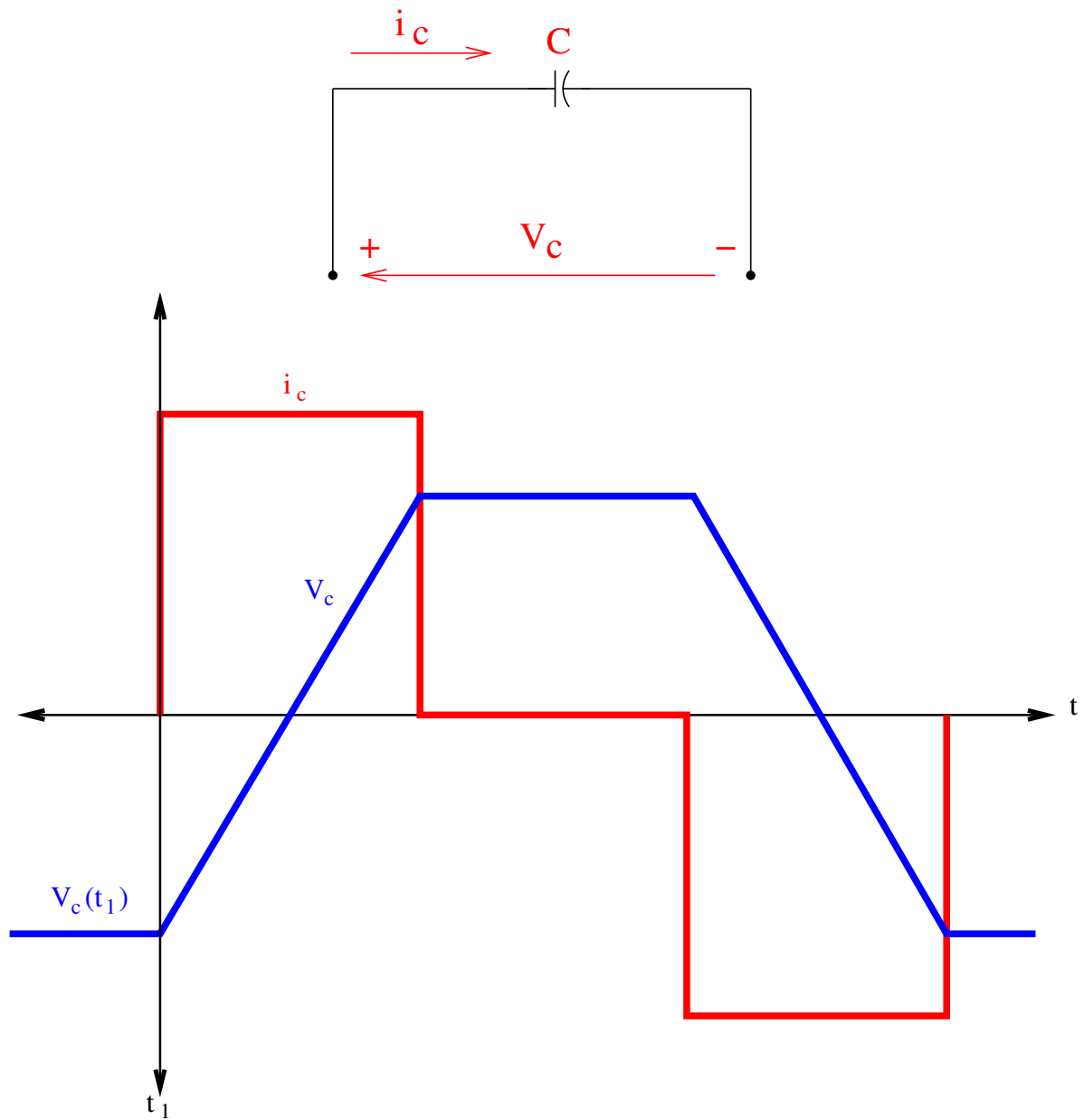
Figure 2.6: Capacitor Current and Voltage Response

- **Zero Voltage Switching (ZVS) Mode**

  It is referred to have the output voltage set at zero value prior to turn ON the circuit switch, in order to reduce the Turn-ON losses.

- **Zero Current Switching (ZCS) Mode**

  It is defined as having zero value of output current prior to turn OFF the circuit switch, to eliminate the Turn-OFF losses.

2.3   Advantages of Induction Heating

The principles of induction heating is utilized in a lot of applications like surface hardening, forming, annealing, metal melting and brazing, in which both magnetic and non-magnetic metals could be involved. Each application has its suitable resonant frequency. The induction heating process has a number of inherent benefits as compared with other fuel fired heating categories (e.g. gas- and oil-fired furnaces), can be stated as follows [61]:

1. Very fast melting rates; induction heating has an output production better than other fuel heating types.
2. It has a better environmental working conditions - as there will be no extreme heat losses from the heating process and no smoke, reek, dirt, or ashes.
3. Automatic stirring will be exposed on the molten metal- which gives the advantages of alloying processes and mixed melts, as the stirring assists in absorbing the materials to yield a homogeneous melt.
4. It provides safer operating conditions by reducing the danger occurred from open flames to the workers, and also reducing gas leaks as well.
5. Low running costs.
6. Low maintenance costs.
7. Low noise emissions.
8. Rapid start up from cold; no preheating required.
9. Better energy saving and improving production rates [62].
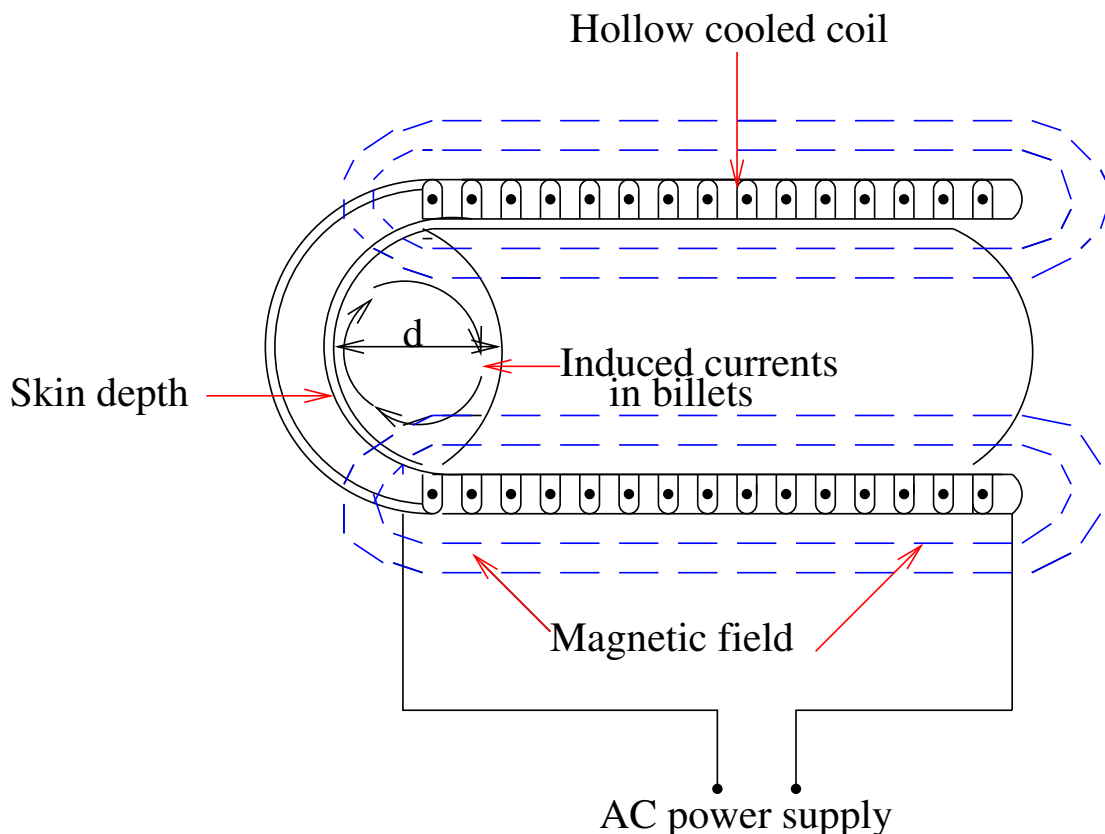
Figure 2.7: Induction Heating System Principles

2.4   Principles of Induction Heating

In its simplest form, the output of induction device consists of a hollow cooled coil being fed with an AC current from an IH power supply and surrounds the workpiece metal to be heated.

The basic concept of induction heating is similar to the well known transformer theory, but modified and based on a single turn, short circuited secondary winding. Since the secondary is considered short-circuited winding, its current will be very high and considerable losses will be developed. If the coupling between primary and secondary is considered to be ideal, then the primary current is related to the secondary losses.

When the coil is excited by an alternating current, it produces an alternating magnetic field, the variations in the field produces Foucault currents along paths concentric with the axis. The magnetic field associated with eddy currents opposes the exciting

field according to Lenz law; therefore the electromagnetic field alternates rapidly inside the workpiece, see Fig. 2.7.

In efficient induction heating system, it is proper to assume that $\delta \ll d$ (the diameter of the workpiece). Increasing the working frequency f will increase the power density, because P (workpiece supplied power) is proportional to $\sqrt{f}$ and this allows for much better induction heating process. [63].

In induction heating, the coil is constructed of hollow conductor to provide a path for cooling (liquid or gas); to remove the heat corresponding to the losses and radiated heat from workpiece to protect the coil and improve heated temperature. Therefore thermal installation is sometimes needed between the workpiece and the coil, which will increase the airgap in between and so, decrease the power factor.

In order to simplify the IH load set configuration, there should be a simple mathematical model to represent its electrical behaviour. Therefore, the inductor - workpiece load is modelled as an $(R - L)$ inductor-resistor equivalent set.

The electrical modulation of the IH load (inductor and workpiece) can be represented as an inductance, L, and an equivalent resistance, R_{eq}. This resistance represents the workpiece-inductor set resistance, and its value depends mainly on geometrical properties, material and resonant frequency of the inductor and the workpiece when operating under power supply inverter.

There are two kinds of IH load equivalent circuit model based on the inductance-resistance equivalent of the inductor-workpiece load. They are series and parallel models.
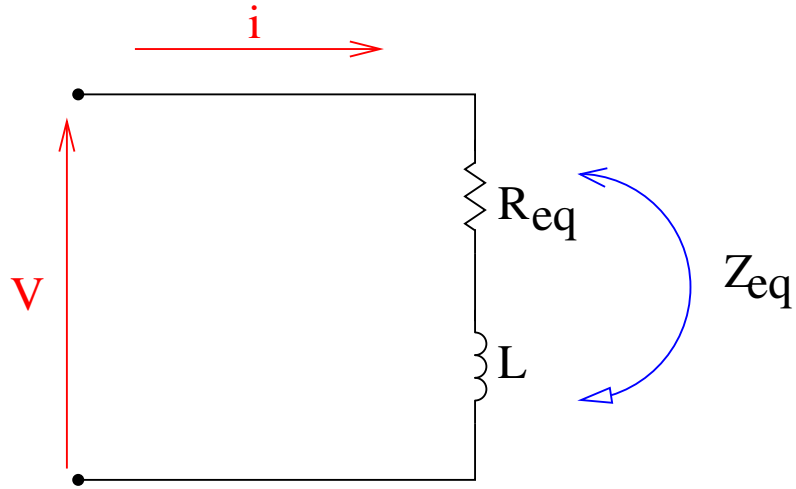
Figure 2.8: Series Model of IH Load

2.4.1   Series IH Load-Model

In series model case, the equivalent inductance, L and equivalent resistance,R_{eq} are in series, see Fig. 2.8; thus the IH load power is

$$S = I^2 Z_{eq} = I^2 \left(R_{eq} + j\omega L \right) \tag{2.22}$$

Thus, the quality factor, Q, can be expressed:

$$Q_{series} = \frac{|P_{reactive}|}{P_{active}} = \frac{\omega L}{R_{eq}} \tag{2.23}$$

2.4.2   Parallel IH Load-Model

In this model, the equivalent inductance, L, and equivalent resistance,R_{eq} are in parallel, as in Fig. 2.9, so the power will equal to

$$S = \frac{V^2}{Z_{eq}} = V^2 \left(\frac{1}{R_{eq}} + \frac{1}{j\omega L} \right) \tag{2.24}$$

so the quality factor,Q, will be as

$$Q_{parallel} = \frac{1/\omega L}{1/R_{eq}} = \frac{R_{eq}}{\omega L} \tag{2.25}$$

46
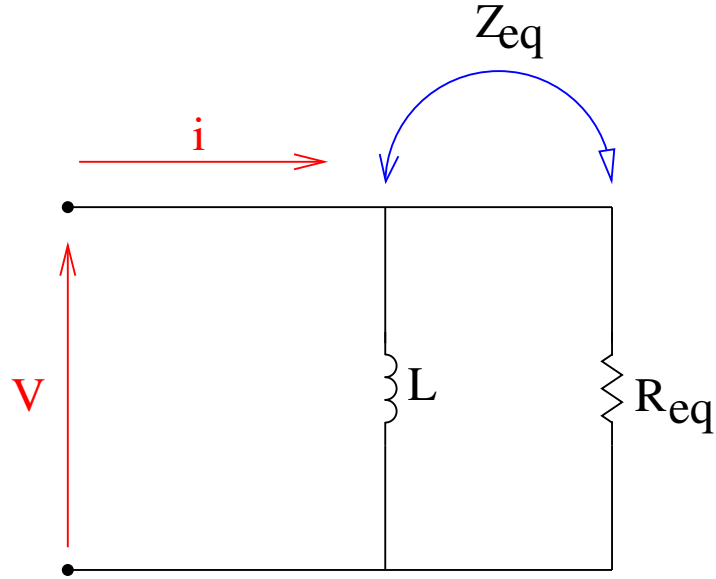
Figure 2.9: Parallel Electrical Model of Inductor-Workpiece

In this study, the model used is the series model as it is the most popular used model [62].

2.5   Induction Heating Modelling

In order to study the characteristics of electromagnetic effect on the workpiece-inductor IH load, a mathematical-model method is required. There are many methods solving this problem, but can generally classified under two groups: analytical and numerical methods. So, this section will illustrate the analytical method depending on the equivalent circuit of the IH workpiece-inductor load set.

Then, the numerical methods are briefly illustrated. These numerical methods serve the designers to have precise analysis when the workpiece shapes become too complex.

2.5.1   Analytical Methods

The basic assembly of an induction heater consists of a water cooled copper coil surrounding a workpiece. The coil can be designed by obtaining the values of the resistance and reactance and solving the equivalent circuit, this method was devised by Baker [64].
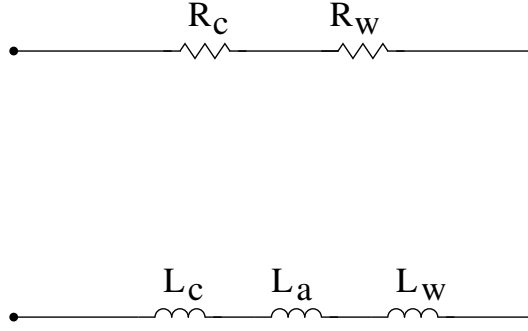
Figure 2.10: Series Model of Inductor-Workpiece System

In order to better comprehension to the IH cycle process, there is a need to a simple and accurate methods of load representation with some approximations [2, 63].

This approximation depends on the similarity between induction heating system and the transformer system behaviour, with suggesting Baker's series circuit [63]. This model is shown in Fig. 2.10, where the parameter R_w is the resistance of the workpiece, R_c is the resistance of the coil, L_a is the airgap inductance, L_w is the inductance of the workpiece and L_c is the inductance of the coil.

These methods used to calculate equivalent circuit of workpiece-inductor IH load, in which the equivalent resistance R_{eq} that affects the efficiency is calculated [65].

The magnitudes of the parameters in Fig. 2.10 for a long solenoid heating a solid state cylinder are as follows [37, 63]:

$$R_w = K\left(\mu_w \rho A_w\right) \tag{2.26}$$

$$R_c = K\left(k_r \pi r_r \delta_c\right) \tag{2.27}$$

$$L_a = K\left(\frac{A_a}{2\pi f}\right) \tag{2.28}$$

$$L_w = K\left(\frac{\mu_w q A_w}{2\pi f}\right) \tag{2.29}$$

48

$$L_c = \frac{R_c}{2\pi f} \tag{2.30}$$

Where

- K is a constant and is given by the following equation

$$K = \frac{2\pi f \mu_o N_c^2}{l_c} \tag{2.31}$$

  as being N_c is the number of turns of coil and l_c is coil length.

- A_w is the workpiece cross sectional area, which equals to

$$A_w = \pi r_w^2 \tag{2.32}$$

  being r_w is the radius of workpiece.

- μ_w is the workpiece relative permeability, which is adimensional parameter ($\mu = \mu_w \mu_o$, where $\mu_o = 4\pi 10^{-7} H/m$ for vacuum).

- p and q are non dimensional parameters of a solid cylinder [5]

- δ_c is the coil penetration depth, given by Equation 2.1 for the material of coil (copper).

- f is the frequency.

- k_r is a correction factor considering the space between coil turns, its value lies between 1 and 1.5 (usually 1.15 as a typical value) [66].

Considering this, then the electrical efficiency is expressed by the following formula

$$\eta_{electrical} = \frac{R_w I_c^2}{(R_c + R_w) I_c^2} = \frac{R_w}{R_c + R_w} \tag{2.33}$$

It should be noticed that in the case of continuous IH workpieces, the workpiece is put inside a refractory that eliminates the thermal losses (radiation and convection losses). Thus, thermal losses can be neglected [63].

This analytical method can introduce an approximate solution to better comprehension the IH load problem representation, which helps very much in IH converter setting specifications.

2.5.2   Numerical Methods

These categories of IH modelling need high performance computers with highly skilled simulation software. They are used for complex workpiece shape applications.

There are a lot of numerical procedures used to analyse the IH system problems. The most commonly used are: the Finite Element Method (FEM), the Finite Differential Method (FDM) and the Boundary Element Method (BEM).

Generally, there are two fundamental classifications for electromagnetic numerical solutions: differential and integral methods, as follows:

Differential Methods

They solve the IH problem utilizing the electromagnetic-differential mathematical expressions. FDM and FEM are the main differential methods. The basis of the FDM is the conversion of governing differential equations of the IH problem into a set of algabraic equations. These equations are solved at every point on a grid constructed over the required space domain [67].

While, FEM is another numerical technique solution of IH problems, in which the field region is subdivided into a finite number of discretesized subregions of finite elements. The elements can have complex shapes. The unknown quantities at each element are represented by suitable interpolation functions that contain node value for each element [68, 69].

Integral Methods

They solve the IH problem starting from an integral expressions. As an example of integral methods, the Boundary Element Method (BEM), in which the discretization of the full domain is avoided by the discretization of the surface only by making use of the fact that electromagnetic field attenuates rapidly as it penetrates into the side of conducting materials. Volume integral equations for homogeneous media may be simplified to boundary integral equations by application of the divergence theorem and the potential at any point is then defined in terms of the potential and its normal derivative on the boundary surface [70].

It should be pointed that, there is no unique IH numerical solution, but depending on problem situation, one or more numerical method can be used for each case [60, 71].

2.6   Induction Heating Converters

The IH converters belong to the Resonant converter family (RCF) group [72]. Their operation at resonant frequency mode permits them from having higher efficiency, which lets them to be widely used in high frequency applications, with higher current inductor ratings, which is very important aspect in the industry.

Generally, the IH inverters can be classified mainly into two categories, depending on their resonant load tank, voltage-fed inverters (VFI) and current-fed inverters (CFI), see Fig. 2.11 and Fig. 2.14. The VFI type supplies a series resonant load tank, whereas CFI based on parallel resonant load tank [60].

In this section, the basic principles of induction heating converters of both types will be introduced, which would be useful in in deciding the best design choice of proposed IH converter topology.
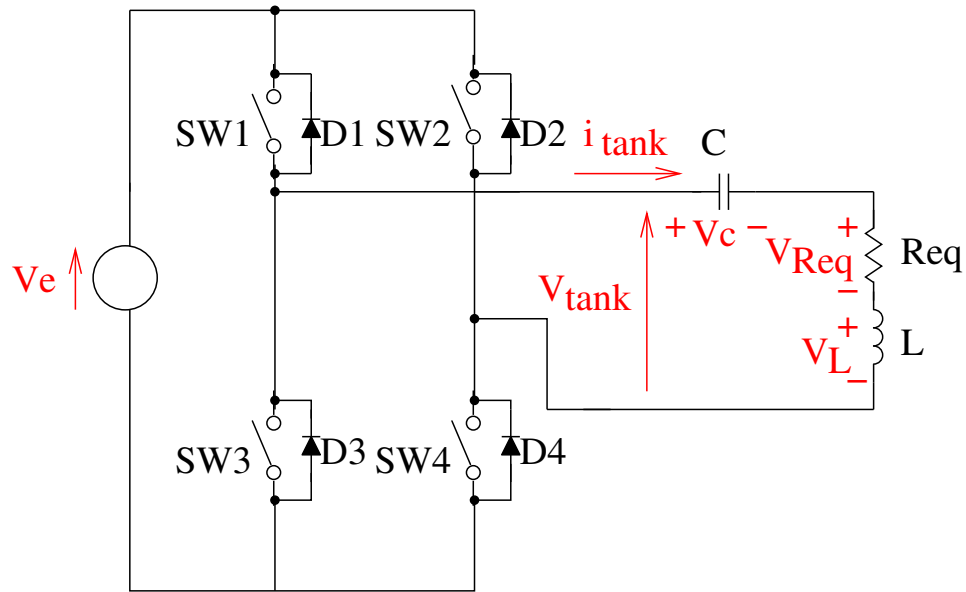
Figure 2.11: Voltage fed inverter topology

2.6.1 Voltage-Fed Inverters (VFI)

As stated previously, the VFI topology is based on series resonant load-tank. This tank acts like a current source with VFI supplied from constant voltage source. This needs that the VFI is fed from high capacitor to maintain constant voltage. Fig. 2.11 shows a typical VFI with series resonant tank.

In VFI, two switches of same leg of converter must not be switched together with the same turn ON time, because short circuit happens. The time interval between switching off of one switch and switching ON of other switch is called **Dead-Time(DT)**. It is essential to put anti-parallel diodes with each switch, to permit the current flowing during the time of the opposite diodes being switched OFF.

It can be stated that each of the two groups of switches SW1 & SW4 and SW2 & SW3 operate successively with a duty-cycle of 50 % and with a power control by changing the voltage of the source V_e as shown in Fig. 2.12.
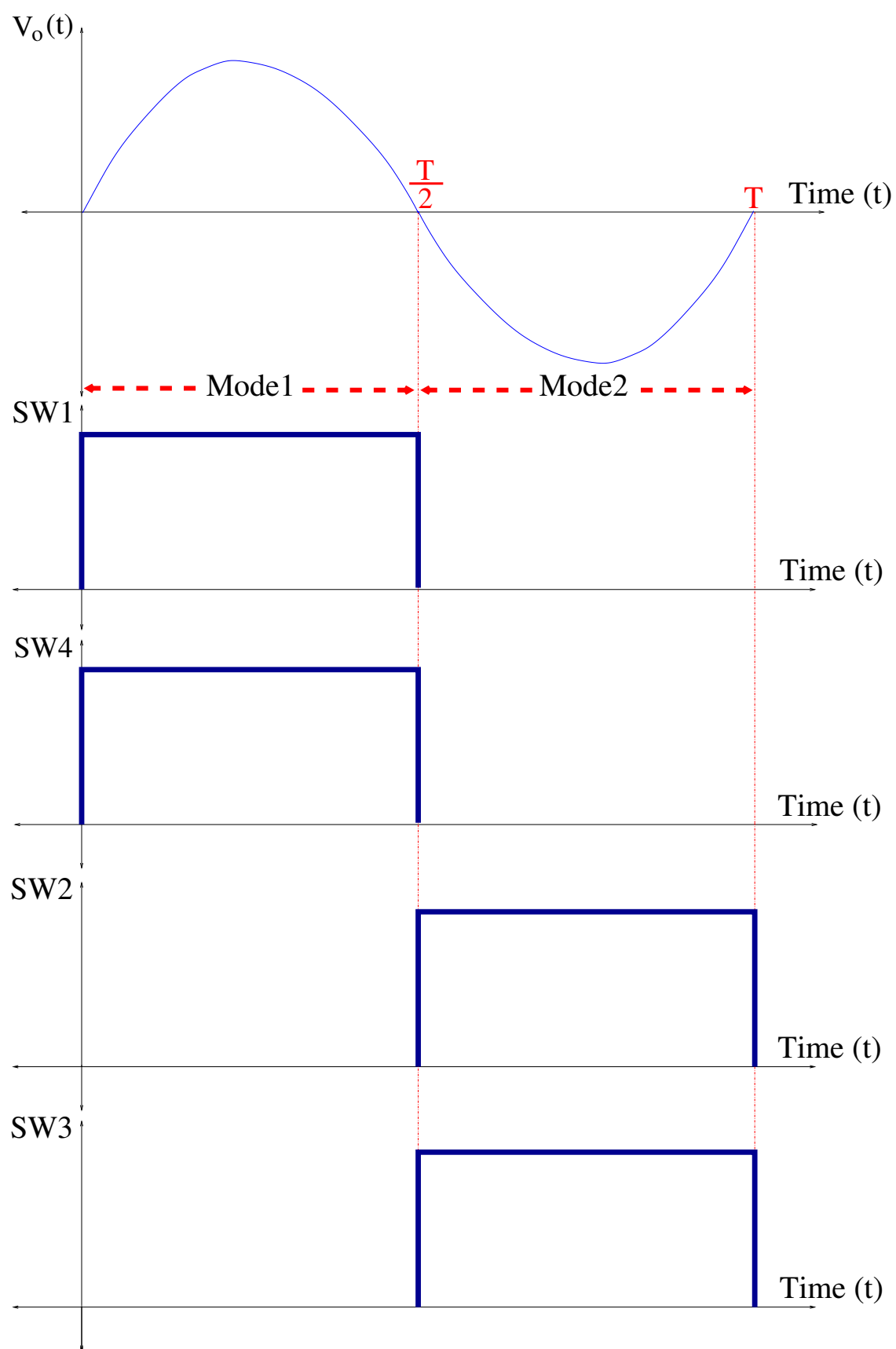
Figure 2.12: Output Voltage Duty Cycle of VFI topology
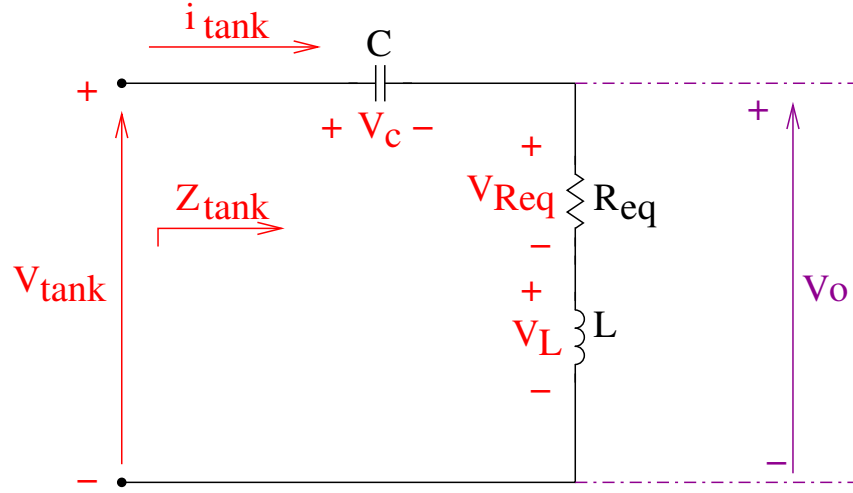
Figure 2.13: Load Tank of VFI Topology

Load Analysis of VFI Topology

By analysing the RLC series-load circuit of VFI in Fig. 2.13, the load tank voltages V_{tank}, can be given from the following formula:

$$V_{tank} = V_{R_{eq}} + V_L + V_C = R_{eq}i_{tank} + L\frac{di_{tank}}{dt} + \frac{1}{C}\int i_{tank}\ dt \qquad (2.34)$$

Where:

- The load-tank compensating capacitor voltage at resonant frequency, $V_c(\omega_r)$ is equal to

$$V_c(\omega_r) = X_C(\omega_r)I_{tank}(\omega_r) = \frac{1}{j\omega_r C}\left(\frac{V_{tank}(\omega_r)}{R_{eq}}\right) = -jQV_{tank}(\omega_r) \qquad (2.35)$$

Being, Q is the quality factor and ω_r is the resonant frequency of the circuit. Therefore, at resonant frequency, the capacitor compensator voltage is Q times the output converter voltage with 90° delay.

- The inductor voltage, V_L is expressed as

$$V_L(\omega_r) = X_L(\omega_r)I_{tank}(\omega_r) = j\omega_r L\left(\frac{V_{tank}(\omega_r)}{R_{eq}}\right) = jQV_{tank}(\omega_r) \qquad (2.36)$$

Which means that, the inductor voltage is Q times the output voltage of the

converter with 90° advance.

- In the case of equivalent resistance, the resistor voltage, $V_{R_{eq}}$ is equal to the converter output voltage as follows

$$V_{R_{eq}}(\omega_r) = R_{eq}I_{tank}(\omega_r) = R_{eq}\left(\frac{V_{tank}(\omega_r)}{R_{eq}}\right) = V_{tank}(\omega_r) \tag{2.37}$$

In spite of being the capacitor voltage is Q times higher, it has to be limited. As an example, having Q value of 10, means if there is output voltage of converter of 100 V, this leads to the need of 1000 V at the compensator capacitors, which means more capacitors connected in series to withstand this high voltage and as a consequence; design cost is increased dramatically.

Considering the VFI load tank design of Fig. 2.13, the load impedance Z_{tank} is equal to the following equation

$$Z_{tank} = R_{eq} + j\left(\frac{\omega^2 LC - 1}{\omega R_{eq}C}\right) \tag{2.38}$$

The absolute magnitude of the load impedance is equal to the following expression

$$|Z_{tank}| = \sqrt{(R_{eq})^2 + \left(\frac{\omega^2 LC - 1}{\omega C}\right)^2} \tag{2.39}$$

And, the phase shift of the load tank is equal to the following formula

$$\varphi = \arctan\left(\frac{\omega^2 LC - 1}{\omega R_{eq}C}\right) \tag{2.40}$$

From load tank impedance of Equation 2.38, one pole can be extracted representing the resonant frequency ω_r, as follows

$$\omega_r = \frac{1}{\sqrt{LC}} \tag{2.41}$$

Therefore; for maximum power transfer, the VFI should be switched at the resonant

frequency ω_r and the load tank impedance is given as follows

$$|Z_{tank}|_{\omega=\omega_r} = R_{eq} \tag{2.42}$$

Which means that the total resultant of inductor-capacitor set is completely under balance condition, i.e. the total impedance equivalent acts like a purely resistance.

Therefore; the maximum power transfer from VFI converter to the resonant load tank is equal to

$$P = \frac{V_L^2}{Z_{tank}} = \frac{V_L^2}{R_{eq}} \tag{2.43}$$

Quality Factor of VFI Topology

The quality factor of VFI is equal to the following expression:

$$Q = \frac{|P_{rect}|}{P_{act}} = \frac{\omega_r L}{R_{eq}} \tag{2.44}$$

The equation above shows that: if frequency and inductance are increased, then the quality factor is increased as a result, and vice versa with resistance. Therefore; better Q requires less resistance and more inductance and hence more frequency.

VFI and Matching Transformer

It is preferable in IH applications to have high current flowing through the inductance, in order to produce high heating energy in the workpiece. In VFI, the converter and the tank currents are the same. Keeping in mind that the value of equivalent resistance of the VFI load-tank is sometimes lower than one ohm, the converter voltage is going to be low and their currents are very high, which causes more losses and voltage drops in the VFI converters.

This was the main reason of the limit predominance of the VFI converters at their
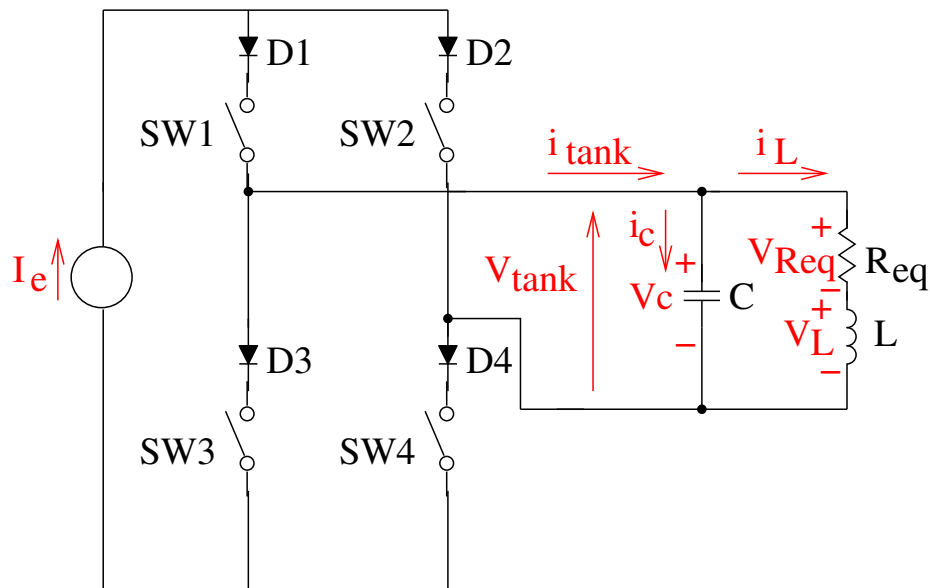
Figure 2.14: Current Fed Inverter Topology

early beginning, until the appearance of high performance matching-transformers. These transformers allow the usage of VFI topology in a lot of applications, but with the drawback of making the VFI converter more expensive with lowering their efficiency, because of their internal inductance that interferences with the load-tank inductance, with causing more parasitic components [39, 40].

2.6.2   Current Fed Inverters (CFI)

In the parallel resonant load-tank, both the inductor and equivalent resistor load-set are connected in parallel with the compensator capacitor. In contrary with series resonant load, the load tank acts like a voltage source and the converter behaves like a current-fed. This implicates that the converter is fed with a high inductance that preserves the current and acts like a current-source. A parallel load tank applied to a CFI converter are shown in Fig. 2.14.

In the CFI converters, the current path should not be opened and switches from same leg of converter should overlap. CFI switches must be unidirectional in current and bidirectional in voltage. The advantage of adding the diodes in Fig. 2.14 is to prevent the capacitor from discharging.

As the CFI converter is current-fed, it is assumed to be power-controlled using the source current, I_e therefore, the switches groups of (SW1 & SW4) and (SW2 & SW3) operate successively with a duty cycle of 50%, see Fig. 2.15. The equivalent resistor-inductor IH load set are also represented in series.

For better comprehension of the CFI operation, there should be an introduction to the mathematical derivation of the load tank impedance and the main factors that control the maximum power delivery from the CFI to the resonant load tank side in the following section.

Load Analysis of CFI Topology

Due to the parallel nature of the RLC resonant load tank of CFI topology, there is a serious difference in the mathematical derivations of the resonant load tank between the VFI and the CFI, which has more complicated calculations.

Therefore, with observing the load circuit of CFI topology of Fig. 2.16, the resonant load tank impedance can be also given as the admittance equivalent of the load, as in the following expression:

$$Z_{tank} = \frac{1}{Y_{tank}} = \frac{1}{(SC) + \left(\frac{1}{R_{eq}+SL}\right)} \tag{2.45}$$

Where, Y_{tank} is the resonant load tank admittance, which equals to the summation of total load admittance as follows:

$$Y_{tank} = Y_1 + Y_2 \tag{2.46}$$

Where, the transfer function $H_P(S)$ is equal to the load tank impedance and can be expressed as:
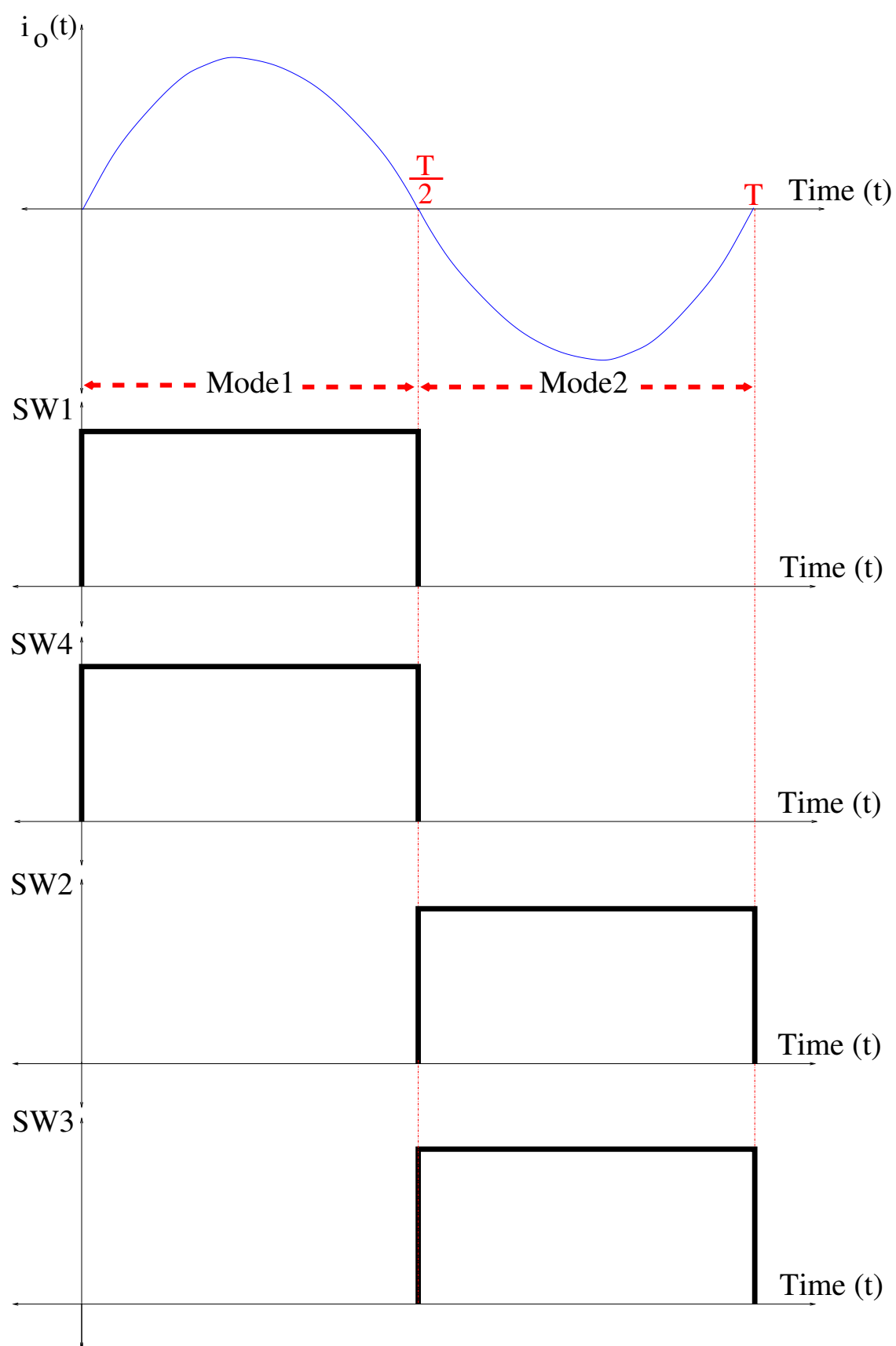
Figure 2.15: Output Current Duty Cycle of CFI Topology

$$H_P(S) = \frac{V_{tank}}{i_{tank}} = \frac{R_{eq} + SC}{S^2 LC + SR_{eq}C + 1} \tag{2.47}$$

In order to make $H_P(S)$ in frequency domain, therefore; Equation 2.47 is expressed as follows:

$$H_P(\omega) = \left(\frac{j\omega L}{(1 - \omega^2 LC) + j\omega R_{eq}C} + \frac{R_{eq}}{(1 - \omega^2 LC) + j\omega R_{eq}C} \right) * \left(\frac{(1 - \omega^2 LC) - j\omega R_{eq}C}{(1 - \omega^2 LC) - j\omega R_{eq}C} \right) \tag{2.48}$$

Then, after simplifying $H_P(\omega)$ into real and imaginary terms, the following expression is obtained:

$$H_P(\omega) = \left(\frac{R_{eq}}{(1 - \omega^2 LC)^2 + (\omega R_{eq}C)^2} \right) + j \left(\frac{\omega \left(L - R_{eq}^2 C - \omega^2 L^2 C \right)}{(1 - \omega^2 LC)^2 + (\omega R_{eq}C)^2} \right) \tag{2.49}$$

Therefore; the absolute magnitude of load impedance $|Z_{tank}|$ can be expressed as

$$|Z_{tank}| = \sqrt{ \left(\frac{R_{eq}}{(1 - \omega^2 LC)^2 + (\omega R_{eq}C)^2} \right)^2 + \left(\frac{\omega \left(L - R_{eq}^2 C - \omega^2 L^2 C \right)}{(1 - \omega^2 LC)^2 + (\omega R_{eq}C)^2} \right)^2 } \tag{2.50}$$

And thus, the phase shift angle of IH load is given from the following equation

$$\varphi = \arctan \left(\frac{\omega \left(L - R_{eq}^2 C - \omega^2 L^2 C \right)}{R_{eq}} \right) \tag{2.51}$$

With assuming the resonant frequency definition as the optimum of the transfer fuction $H_P(\omega)$ of Equation 2.49, only one pole representing the resonant frequency ω_r can be obtained, as in the following expression [5]:

$$\omega_r = \frac{\sqrt{C\sqrt{2LCR_{eq} + L^2} - C^2 R_{eq}^2}}{LC} \tag{2.52}$$

60
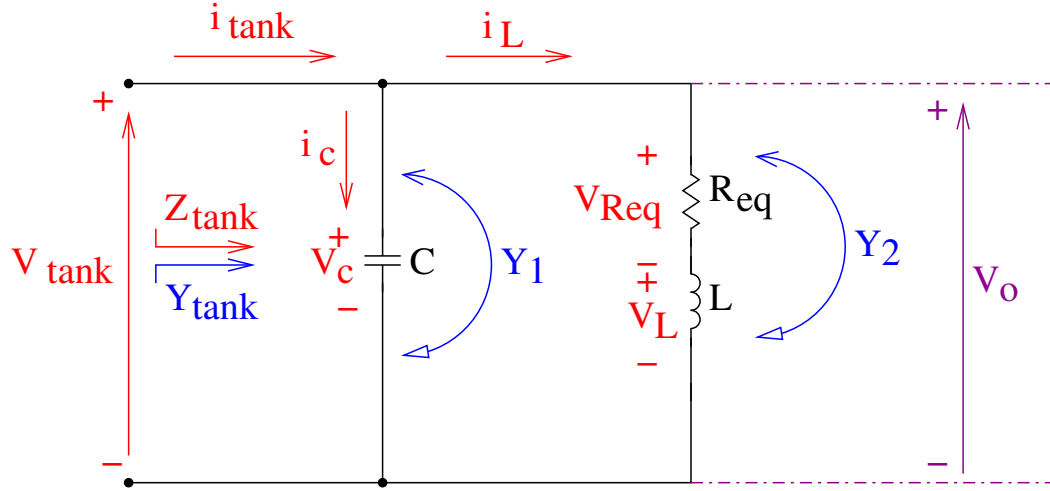
Figure 2.16: Load tank of CFI topology

Power Transfer of CFI Topology

The resonant load tank current and voltage of RLC circuit topology shown in Fig. 2.16, can be expressed as follows:

$$i_{tank} = i_C + i_L = C\frac{dV_{tank}}{dt} + \frac{1}{L}\int v_L \ dt \tag{2.53}$$

$$v_{tank} = v_L + v_{R_{eq}} \tag{2.54}$$

The inductor and capacitor currents, I_L and I_C at resonant frequency, ω_r are given by the following expressions: [5]

-
$$I_L(\omega_r) = -jQI_{tank}(\omega_r) \tag{2.55}$$

-
$$I_C(\omega_r) = (1 + jQ)I_{tank}(\omega_r) \tag{2.56}$$

So the inductor current at resonant frequency mode is approximately Q times the converter output current, but with a delay of 90° as the minus sign indicates., and the capacitor current is approximately Q times the output current with 90 degree advance as the plus sign indicates.

As the current in the inductance is the same as the current flowing in the equivalent resistance, then the power transmission to the load is as:

$$P = I_L^2 R_{eq} \tag{2.57}$$

The current delivered to the equivalent resistance is maximum at resonant frequency and as a result, the power is maximized too. Thus, the maximum power transfer from the CFI to the load tank at resonant frequency is as follows

$$P(\omega_r) = I_L^2(\omega_r) R_{eq} = (Q I_{tank}(\omega_r))^2 R_{eq} \tag{2.58}$$

Quality Factor of CFI Topology

The equation of quality factor of CFI is ratio of reactive to active power and can be given from the following formula:

$$Q = \frac{|P_{rect}|}{P_{act}} = \frac{\omega_r L}{R_{eq}} \tag{2.59}$$

The equation above shows that: if frequency and inductance is increased, then the quality factor is also increase, and vice versa with resistance. Therefore; having better Q requires less resistance and more inductance and hence more frequency.

2.7   Summary

Induction heating (IH) is a method of heating electrically conductive workpiece materials which depend on the heat losses generated from induced eddy currents of so called Joule effect phenomenon. Although there are also hysteresis losses, but it does not play any important role in the process. The penetration depth, δ is that important parameter that helps in determining the desired frequency of the IH process.

In IH systems, the inductor-workpiece load is modelled electrically by inductance and resistance that are connected together in series or in parallel models. The quality factor concept Q is defined as the ratio between reactive and active IH system power and can be used for comparison between the series and parallel models. Both model are useful with selecting the series mode as the most common mode.

Some methods of IH load modelling are introduced. At first, the analytical methods illustrated, which include equivalent circuit representation based on its electrical parameters, like coil resistance (R_c), workpiece resistance (R_w), coil inductance (L_c), workpiece inductance (L_w) and airgap inductance (L_a), with introducing the circuit efficiency. The analytical methods are used for non-complex shapes of IH workpieces.

On the other hand, the numerical methods used for complex shapes. Generally, there are two types of numerical equations: differential and integral methods.
The differential numerical methods include the FDM and FEM, while the integral numerical method includes the BEM.

There is no unique solution for all problems, but depending on the application, one or more methods can be used for each case.

The most commonly used topologies of inverters are the VFI and CFI. In VFI converter, the oscillatory circuit equivalent of the inductor and workpiece load set is con-

nected in series with the compensating capacitor and the VFI fed from a constant voltage source, which originally, would be a high value capacitor. Besides, the inductor voltage is Q times the VFI voltage.

While in the CFI converter, the oscillatory circuit equivalent is connected in parallel with the compensating capacitor and the CFI converter fed from a constant current source, which primarily represented by a storage inductor. The inductor current is Q times the CFI current.

In both VFI and CFI, the power transfer to the workpiece-load would be maximum at resonant frequency of the corresponding oscillatory circuit. Furthermore, approximately zero phase-shift between voltage and current can be achieved, which causes low commutation losses in the IH system, i.e. maximum efficiency can be reached as well. The comparison between the two topologies are shown in Table 2.1 below:

Table 2.1: A Comparison Between VFI and CFI Converters

Voltage Fed Inverter (VFI)	Current Fed Inverter (CFI)
The converter is fed from a capacitor which preserves the voltage	The converter is fed from an inductor which preserves the current
It needs short circuit protection.	It needs inrush current protection.
VFI converters are usually found in medium power applications.	CFI converters are usually found in high power application(>1MW).
The inductor voltage is Q times the converter output voltage.	The inductor current is approximately Q times the converter output current.
A matching transformer is essential between the converter and the load-tank.	A matching transformer is not required, usually.
Sometimes need high voltage capacitor for tank compensation.	Does not need high voltage capacitors but need more capacitors in parallel.
Converter switches must be unidirectional in voltage and bidirectional in current	Converter switches must be unidirectional in current and bidirectional in voltage.
The antiparallel diodes is essential with the converter switches.	The series diodes is essential with the converter switches.

Chapter 3

Induction Heating System Development Using Multi-Level Neutral Point Clamped Inverter

3.1 Introduction

T he multi-level converter topology was first patented in its initial form by Baker in 1975 [73]. However, at that time it was not so known the group of multi-level inverter family (MIF). The primary design was a cascaded inverter of separately connected DC-sourced H-bridge cells in series format, to synchronize an AC output voltage of staircase form. This cascaded topology was extended afterwards to include diodes which formed a diode-clamped multilevel inverter, this configuration was called Baker-clamped converter [74, 75].

This was the spark that motivated the appearance of the first famous diode-clamped multi-level topology, which consisted of three level inverter with a mid-point of zero voltage that separates two equal voltage levels. This inverter was known as a neutral-point clamped (NPC) topology at the 1980's decade [76]. Afterwards, the five level converter topology extensively appeared at the 1990's decade [77]. Then, the improvement in the

multi-level converter topology continued including a seven level configuration and even more levels, depending on the application being required [74, 78].

First, this chapter introduces the multilevel neutral point clamped inverter (MNPCI) as a proposed IH converter that can be efficiently used in IH power supply system, with discussing the topology theory. Then, it introduces a new experimental prototype of MNPCI with its control circuit, used in IH power supply unit. This circuit is built together with the improvement of the equivalent circuit derivation of the load-tank side components.

3.2   Multi-Level Converter Theory

In IH applications field, the need of higher level power equipments began to grow in recent years, which now reached the mega watt with relatively high voltage of (2.3, 3.3, 4.16, or 6.9) kV. Today, it is hard for a single power semiconductor switch to withstand directly these medium voltage grids, therefore; the idea of multilevel converter topology appeared, through splitting the rail voltage into two or more voltage so that their summation equals the main source voltage.

Generally, the multilevel converters consist of an array of power semiconductor switches and capacitors as voltage sources. The output of this kind of converters is an alternating sinusoidal AC voltage waveform for the single phase converter-leg (as can be seen later), and as a stepped voltage waveforms for three phase converter-legs [77].

The successive commutation modes of switches permits the addition of the voltage source capacitor stage, which reaches the higher voltage at the output, while the switches must withstand the reduced voltages only. This step-down voltage level will serves in decreasing the applied tension on the converter switches, i.e. better commutation environment and less switching losses and thus, better efficiency as well.
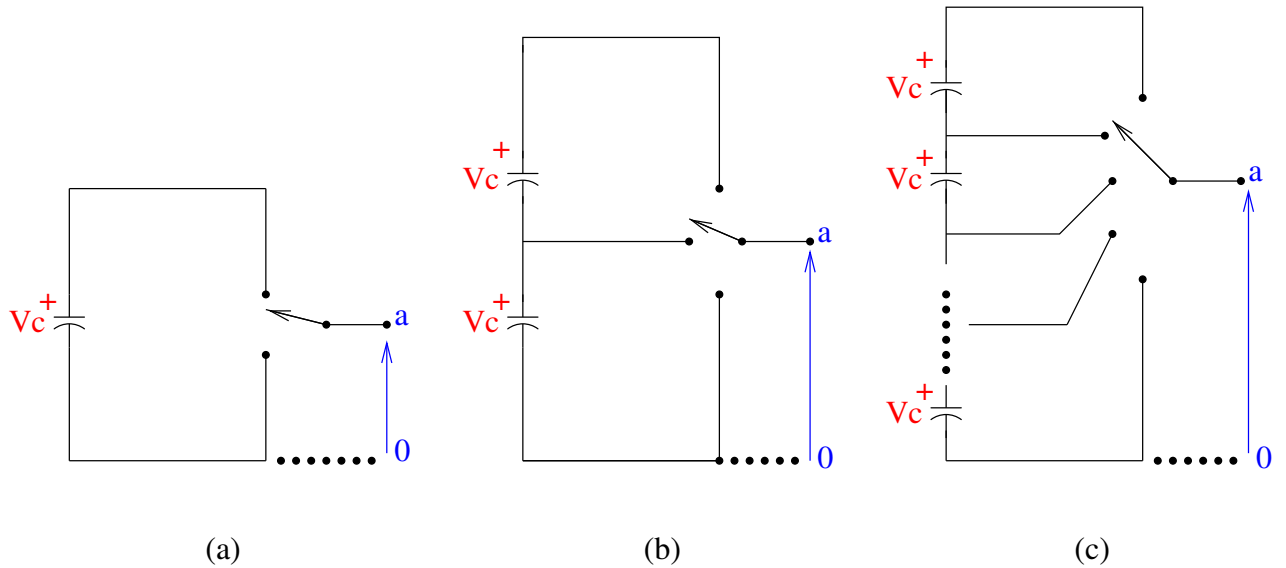
Figure 3.1: One Phase Inverter Leg With (a)Two Level, (b)Three Level, and (c) n-Level

Single phase inverters schematic diagram of one-leg with various multi-level category are shown in Fig. 3.1 above, in which the power semiconductor operation is explained by an ideal switch with multi-position regulation. The two-level inverter produces two voltage magnitudes with respect to the negative terminal of the capacitor (seeFig. 3.1(a)). While a three-level inverter gives three voltage values and so on. (see Fig. 3.1(b,c)).

The multi-level term starts its prevalence with the three-level converter introduced by Nabae [76]. His multi-level inverter design formed by increasing the number of levels in the inverter topology. The output voltage is a step signal that forms a shape of staircase waveform, which has a reduced harmonic distortion. However, the high number of levels cause disadvantages of control complexity and voltage imbalance problems especially with the neutral point. Therefore, a lot of attention should be considered to the control of neutral point balancing as the levels increase or the three phase topology being used as well [79].

3.3   Multilevel Neutral-Point Clamped Inverter Significance

There are many aspects of multi-level neutral-point clamped inverter (MNPCI) topology that can be detected from its extensive usage in a lot of high power applications with medium voltage such as laminators, mills, conveyors, pumps, fans, compressors, blowers and so on. Depending on these merits, this topology used in IH systems for the first time as a new power inverter. These advantages can be listed as follows [50]:

1. This topology-design can produce output voltages with extremely low distortion and lower dv/dt [51].

2. This converter draw input current of very low ripple distortion.

3. They produce smaller common-mode (CM) voltage, therefore they will reduce the stress applied on the semiconductor switches which reduces the switching losses , i.e. decreasing the undesired losses and increasing the power transfer to the load tank and hence, increasing the heating energy in the workpiece.

4. Due to low switching losses, this will decrease the heat sink requirements of the system, which in turn will decrease the overall capital cost of the IH process into a significant level.

5. They posses less stress in the motor bearings (if used as a motor drive application) [52].

6. They can operate with a lower switching frequency.

7. They have the capability to lower the harmonic distortion [76].
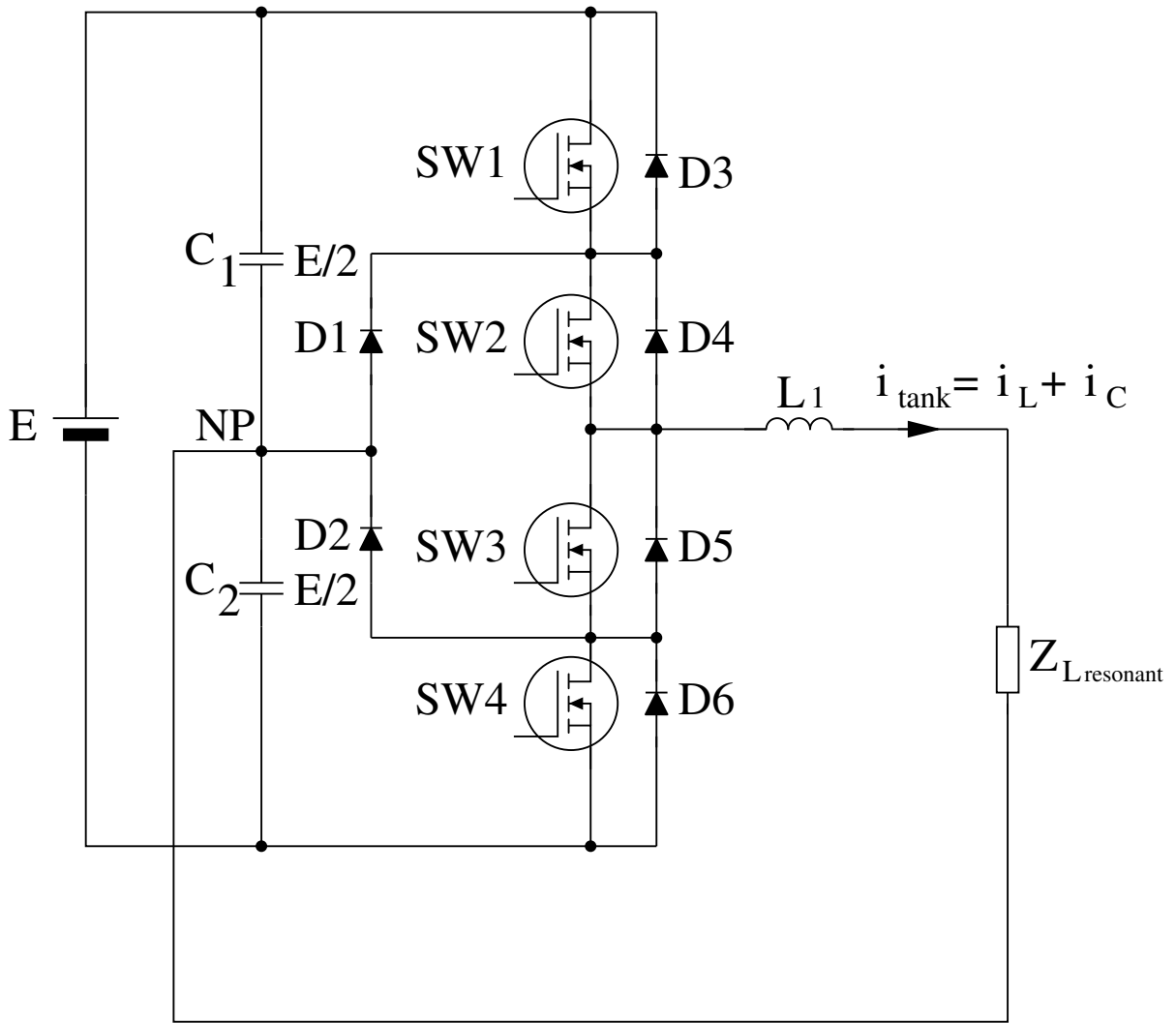
Figure 3.2: MNPCI Topology

3.4   MNPCI Topology Design

The proposed (MNPCI) as part of induction heating power supply is shown in Fig. 3.2 above. In this design, the DC-bus voltage split into three levels by two series-connected bulk capacitors, $C1$ and $C2$. The intermediate point between the two capacitors (NP) can be defined as the neutral point which is the main characterize of this topology.

The output voltage of proposed MNPCI configuration has three level values: ($\frac{E}{2}$, 0 and $-\frac{E}{2}$).

Generally, to accomplish these levels, there are three commutation states (as can be seen in Section 3.4.1) positive, negative and 0. For the $E/2$ level of positive voltage cycle,

SW1 and SW2 need to commutate; for the $-E/2$ level of negative cycle, SW3 and SW4 need to commutate; while for 0 voltage level, either of SW2 or SW3 must be switched ON separately.

The key-parameters that recognize this topology from the two level inverter is the presence of the clamped-diodes $D1$ and $D2$. The basic operation of these diodes is to clamp the switch voltage to half the level of the DC-bus input voltage.

During the positive cycle of output voltage, SW1 and SW2 are commutated both together, the voltage between the output point delivering the load with respect to the negative side of the source capacitor is E.

Within this cycle, $D1$ balances out the voltage shared between $SW3$ and $SW4$, with $SW3$ blocks the voltage across $C1$ and $SW4$ blocks the voltage across $C2$.

Therefore, it should be noticed that the output voltage of the inverter to the load-tank (Z) with respect to the neutral point is an AC voltage, while the voltage of the same Z-load delivering point with respect to the negative side of the source-capacitor is as a DC voltage. The difference between these two voltages is the voltage across the lower side capacitor, which would equal to $\frac{E}{2}$.

Therefore, if the output terminal changed from the delivering Z-load point to the negative source-capacitor point, then the inverter works as a DC/DC converter with three level DC voltages of (E, $E/2$ and 0).

3.4.1 Circuit Commutation

As stated before, the converter leg of Fig. 3.2 has three operating states: **Positive (P)**, **Negative (N)** and **0**. The clamping diodes $D1$ and $D2$ are connected to the neutral point. When the switches $SW1$ and $SW2$ are switched ON, the MNPCI inverter output terminal to the load Z is connected to the neutral point through one of the clamping diodes $D1$ and $D2$.

In order to analyse the circuit extensively, the converter topology operational modes are shown in Fig. 3.3, Fig. 3.4, Fig. 3.6 and Fig. 3.5, representing the converter states of **P**, **0** and **N**, respectively.

- In the **P** switching mode (Fig. 3.3), the upper side switches $SW1$ and $SW2$ are switched ON and the resulting inverter voltage is $+\frac{E}{2}$.

- While in the **N** switching mode (Fig. 3.5), the lower side switches $SW3$ and $SW4$ are switched ON and the inverter voltage will be $-\frac{E}{2}$.

- Whilst, when either of the inner switches of $SW2$ or $SW3$ are switched ON, the **0** switching mode of inverter voltage occurs (Fig. 3.4 and Fig. 3.6).

- Hence, the switch-groups of ($SW1$-$SW3$) and ($SW2$-$SW4$) operate in a successive complementary modes [80].

Considering that the load current i_L is constant during commutation due to load-tank Z, the DC source-capacitors ($C1$ and $C2$) are large enough and all the MNPCI inverter switches are ideal, the commutation can be analysed as follows [51]

- **Commutation when $i_L > 0$**

  With **0** switching mode, the switches ($SW1$ and $SW4$) are switched OFF and the voltage across each one is $\frac{E}{2}$. While the switches $SW2$ is turned ON and the voltage across it becomes zero. Furthermore, the clamping diode $D1$ is turned ON by load current, i_L.

  During this period, $SW3$ is switched OFF. If it has been switched ON, the load current path remains the same. When $SW3$ is OFF, the voltage across $SW3$ and $SW4$ becomes $E/4$.

  In **P** switching mode, the two upper high-side switches ($SW1$ and $SW2$) are switched ON. when the first switch $SW1$ is turned ON and the clamping diode $D1$ is turned OFF. If there is no transient state in between, the load current i_L is commutated from $D1$ to $SW1$, which may cause switch damage if it is followed instantly by the following commutation mode. Therefore, the presence of switches dead time and parallel diodes are essential to prevent interaction between modes which may cause switches damage. Since ($SW3$ and $SW4$) are switched OFF, the voltage across them is $\frac{E}{2}$.

- **Commutation when $i_L < 0$**

  In **0** switching mode, the Switch $SW3$ is turned ON, while the ($SW1$, $SW2$ and $SW4$) are turned OFF, and the clamping diode $D2$ is switched ON by the load current, i_L. The voltage across ($SW1$ and $SW4$) is $\frac{E}{2}$.

  In the case of $SW3$ is switched OFF during dead time, the diodes ($D3$ and $D4$) are turned ON and the voltage across switches ($SW1$ and $SW2$) will equal zero, because i_L can not change its direction instantly. The load current i_L is then commutated from $SW3$ to the diodes $D1$ and $D2$. While $SW3$ is turned OFF,

the voltage drop across $SW4$ will be of maximum value of $\frac{E}{2}$ due to the $D2$ being turned ON. Thus, the voltage drop across $SW3$ increases from 0 to $\frac{E}{2}$, whilst the voltage drop across $SW4$ is $\frac{E}{2}$.

In **P** switching mode, the upper high side switches ($SW1$ and $SW2$) are turned ON and no effect on the operation of the circuit, because even if they are switched ON, at that moment they do not carry load current due to the presence of diodes ($D1$ and $D2$) which have conducted the load current i_L.

The conclusion from the **MNPCI** converter operational states that, it **sustains** only **half** of the **DC link voltage** always during **P-0**, **0-P**, **N-0** and **0-N** modes.

It should be notified that **P-N** switching mode is **ignored**, because it involves all four switches commutate successively without any intermediate discharge time for current, which in turn will cause to double the switching losses and the MOSFET switches will be heated and that might cause damage them due to high heat, which absolutely need adding an extra heat sink components, which will increase the cost of the design, besides there is a possibility for short circuit to carry out in the four leg-switches.

Table 3.1 below, illustrates the MNPCI converter switching modes presented in Fig. 3.3,Fig. 3.4, Fig. 3.5 and Fig. 3.6.

The positive mode represents the two upper high-side switches are ON, in which the voltage drop across the output terminal equals $\frac{E}{2}$. This voltage is determined with respect to neutral point reference. While the negative status represents two lower (high-low) side switches are ON, with respect to neutral point and the output terminal drop voltage equals $\frac{-E}{2}$.
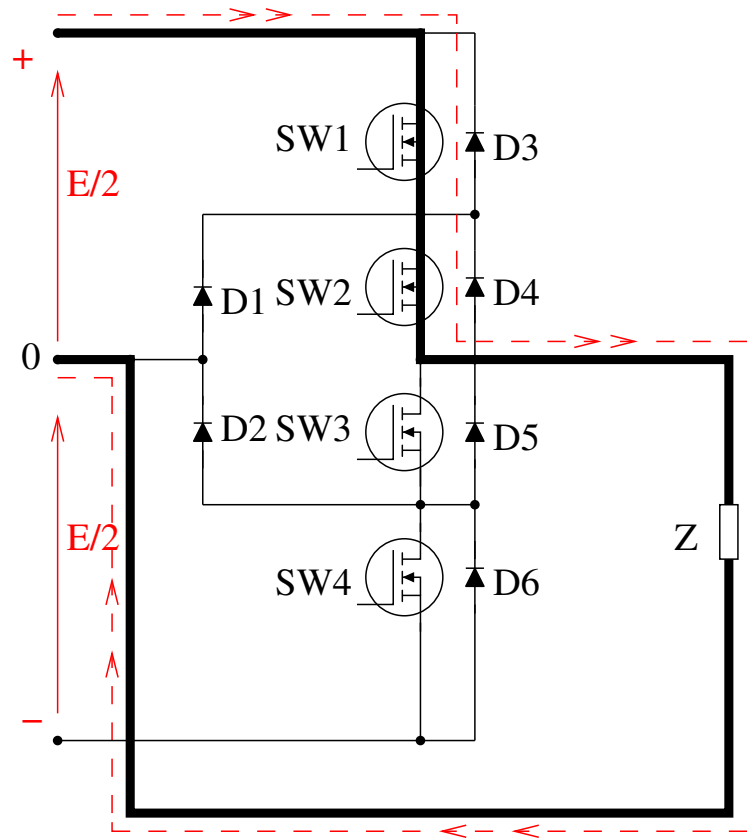
Figure 3.3: P-State of MNPCI Topology
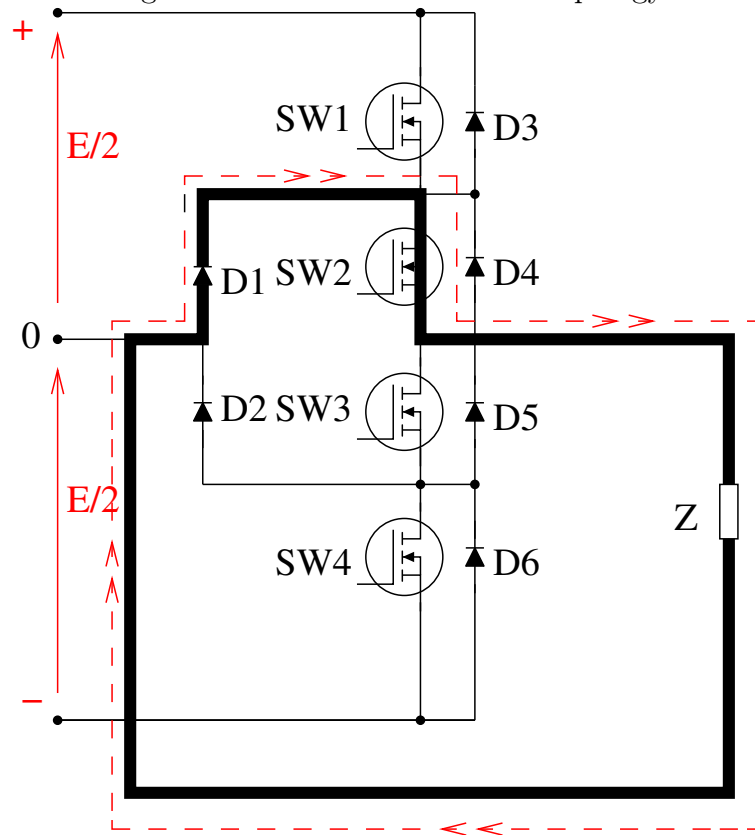
Figure 3.4: 0-State of MNPCI Topology (Complementary to Positive Mode)
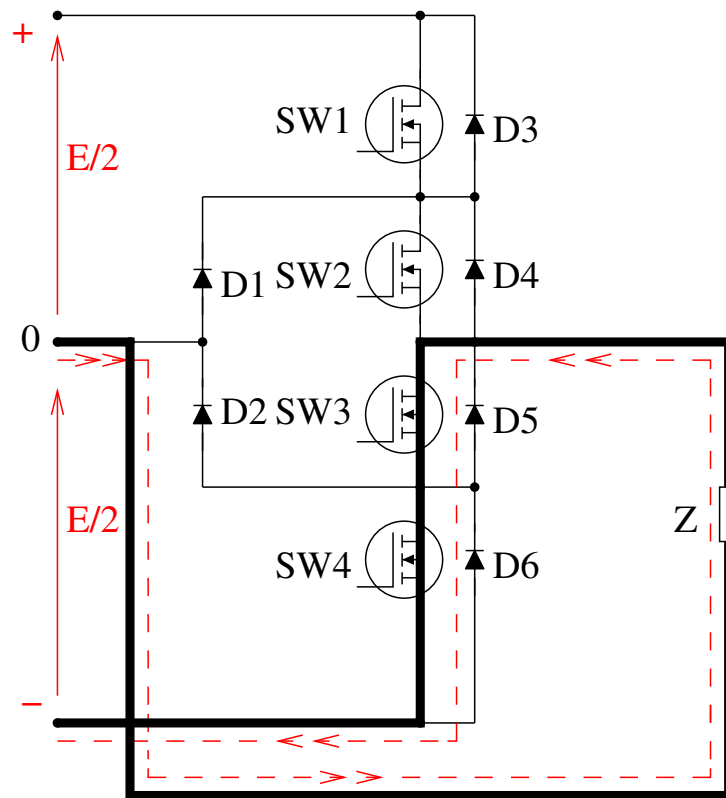
Figure 3.5: N-State of MNPCI Topology
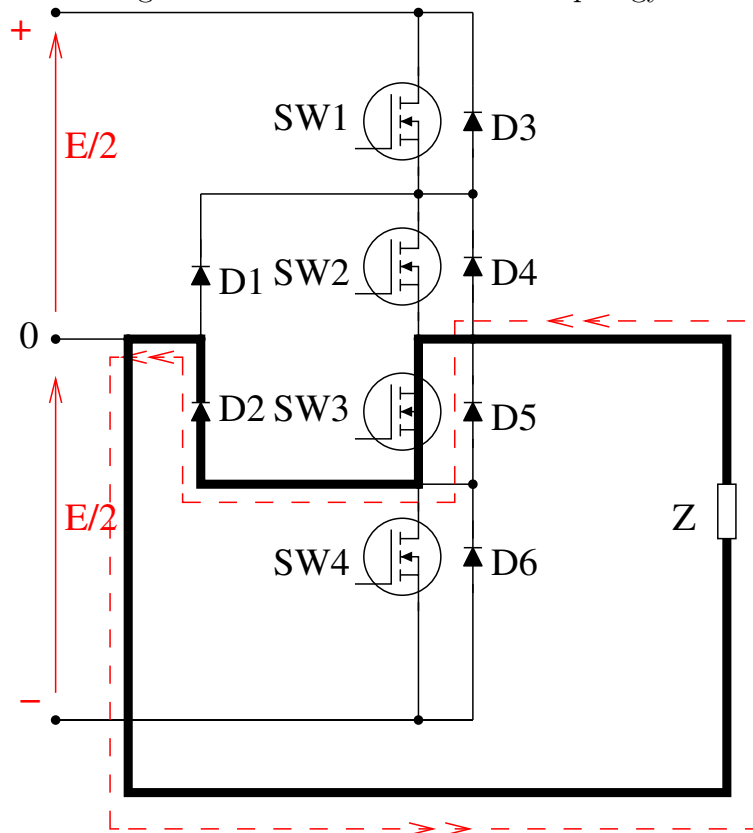
Figure 3.6: 0-State of MNPCI Topology (Complementary to Negative Mode)

Table 3.1: Multilevel Neutral Point Clamped Inverter Operational States

	SW1	SW2	SW3	SW4	Output voltage
P-Mode	1	1	0	0	$\frac{+E}{2}$
0-Mode	0	1	0	0	0
N-Mode	0	0	1	1	$\frac{-E}{2}$
0-Mode	0	0	1	0	0

3.4.2 Load Matching

There are some problems accompanied with the usage of classical series and parallel resonant load tanks, which led to the search of other load-match topologies. In the VFI topology, the current flowing in the converter switches is the same as that flowing in the load tank. This means the need of using load matching transformer in between, which increases the cost of the IH system and decreases the efficiency as well, besides there is a high risk for short circuit occurrence [39, 40].

While in the CFI, the current flowing through converter-switches is Q times lower than the current flowing through the inductor which is very good merit, because it lowers the inverter losses due to decreasing the switching current. But the CFI load topology still suffers from short circuit problem, especially for shunt capacitor if the inrush current phenomena takes place, furthermore; the cable connecting the coil with the load-tank will be with critical value; because of parasitic inductance factor which limits this distance in between. In order to avoid these restrictions, a better IH load system design of series-parallel set combination with three parameter-elements of R, L and C have been introduced [10, 81].

There are many types of three elements load-matching designs, but the most advantageous category is the LCL (or also so called LLC). This topology mixes the advantage aspects of both the VFI and CFI configurations. [39]
The aim of the following section is to provide an extensive idea about LLC topology design, its main characteristics, advantages and power derivations, then adding a new parameter of a current sensing resistance to its popular LLC design to form a modified
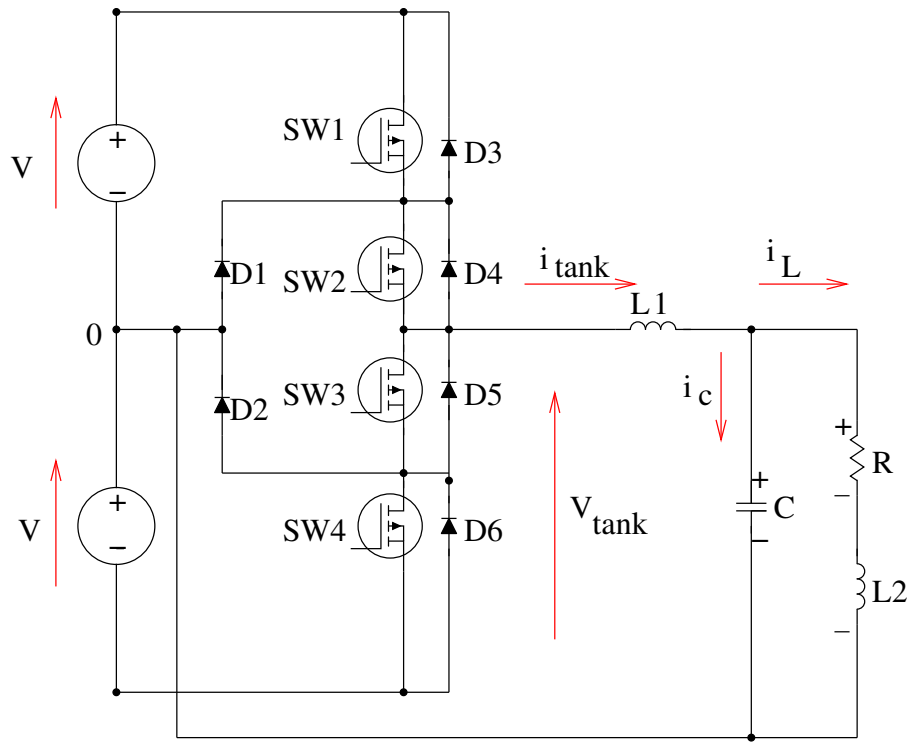
Figure 3.7: *LLC* Load-Tank Topology of MNPCI Configuration

LLC topology.

The typical *LLC* load-tank consists of a parallel tank, with an extra inductance in series L_1, as shown in Fig. 3.7 above. This equivalent load-design is considered as the natural development of combining both the parallel and series load-tank topologies.

Therefore by using the *LLC*, this topology uses the VFI converter configuration as it utilizes two bulk voltage source capacitors that supplies constant voltage delivery to load with only half the DC rail voltage, besides the current flowing in the converter semiconductors i_{tank} is lower than that flowing in the inductor by Q times just like CFI, besides it absorbs the parasitic components in the form of series inductance. As a consequence, the configuration benefits from both VFI and CFI topologies, therefore; it can be considered as a **hybrid VFI-CFI** topology (**HVCFI**) .

3.5   Heating Power

This section discuses the factors that affect the maximum power transfer to the resonant load tank of two main cases, the first one is the classical topology of LLC shown in Fig. 3.8, and the second is the modified topology with adding an extra series resistance to the resonant load-tank as a new parameter and see its effect on the maximum power delivery to the resonant load tank, as in Fig. 3.9.

3.5.1   Power Transfer of Classical LLC Topology

In order to have better comprehension to the operation of the MNPCI-load matched circuit design of Fig. 3.2, it is necessary to derive a mathematical formula which represents the system power transfer to the resonant equivalent load. This expression will help in analysing the electrical parameters which determine the power transmission to the load-tank.

First, from noticing the load-tank of Fig. 3.8, the equivalent impedance of the circuit Z, will equal to

$$Z = j\omega L_1 + \frac{1}{j\omega C + \frac{1}{R + j\omega L_2}}$$
(3.1)

By rearranging Equation (3.1) gives the following formula:

$$Z = \frac{R - \omega^2 R L_1 C + j(\omega L_2 + \omega L_1 - \omega^3 L_1 L_2 C)}{1 - \omega^2 L_2 C + jR\omega C}$$
(3.2)

The absolute magnitude of the total impedance Z of Equation (3.2) is going to be as follows:
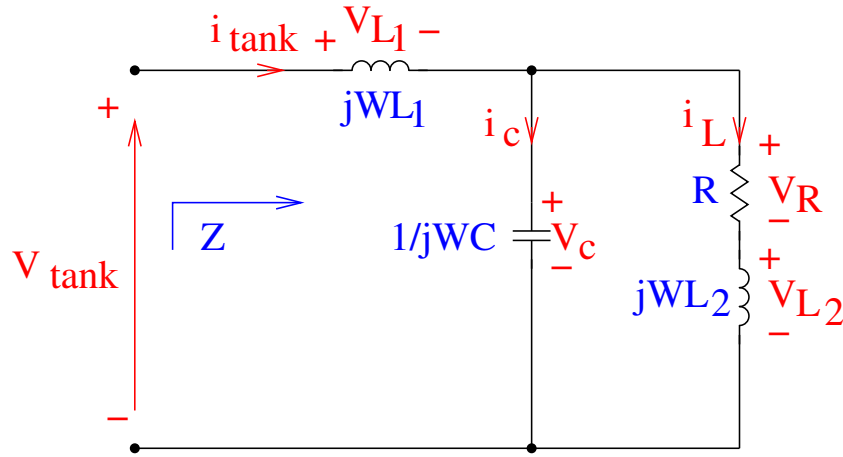
Figure 3.8: Classical LLC Load Tank

$$|Z| = \frac{\sqrt{(R - RL_1C\omega^2)^2 + (L_1\omega + L_2\omega - L_1L_2C\omega^3)^2}}{\sqrt{(1 - L_2C\omega^2)^2 + (RC\omega)^2}} \tag{3.3}$$

And, the phase shift angle is equal to:

$$\varphi = \arctan\frac{L_1\omega + L_2\omega - L_1L_2C\omega^3}{R - RL_1C\omega^2} - \arctan\frac{RC\omega}{1 - L_2C\omega^2} \tag{3.4}$$

From transfer function of Equation (3.2), two poles can be extracted. The first pole represents the parallel resonant angular frequency ω_p, due to the parallel inductance L_2 only.

And, the second pole represents the series resonant angular frequency ω_o, due to both series-parallel inductances of L_1 and L_2.

Considering that, the series resonant frequency takes into consideration the influence of both paralleled inductances, therefore; it expresses better representation to the circuit design at this operational point of the heating cycle [40].

Thus, the two corresponding resonant angular frequency formulas equal to the following expressions:

-

$$\omega_p = \frac{1}{\sqrt{L_2 C}} \tag{3.5}$$

-

$$\omega_o = \frac{1}{\sqrt{L_{eq} C}} \tag{3.6}$$

Where

$$L_{eq} = \frac{L_1 L_2}{L_1 + L_2} \tag{3.7}$$

In order to have maximum power transfer from the power supply to the induction load-tank equivalent, the switching frequency of the MNPCI converter should be switched at series pole ω_o (it is discussed and verified in the next section).

Therefore, by substituting ω_o into Z of Equation (3.2) above, and assuming that reactive power is minimum with respect to the maximum transferred power (P_{max}), due to resonant case, the following formula approximation is formed:

$$|Z|_{\omega=\omega_o} \approx \frac{R\left(1 - \frac{L_1}{L_{eq}}\right)}{\left(1 - \frac{L_2}{L_{eq}}\right)} = R\left(\frac{L_1}{L_2}\right)^2 \tag{3.8}$$

Therefore; the maximum power delivered to the load-tank at ω_o is approximately equal to:

$$P_{max} = \frac{V_{tank}^2}{Z} = \frac{V_{tank}^2}{R}\left(\frac{L_2}{L_1}\right)^2 = \frac{V_{tank}^2}{\beta^2 R} \tag{3.9}$$

Being,

$$\beta = \frac{L_1}{L_2} \tag{3.10}$$

Where,

V_{tank} is the root mean square value (r.m.s) of the fundamental voltage delivered to the load-tank.
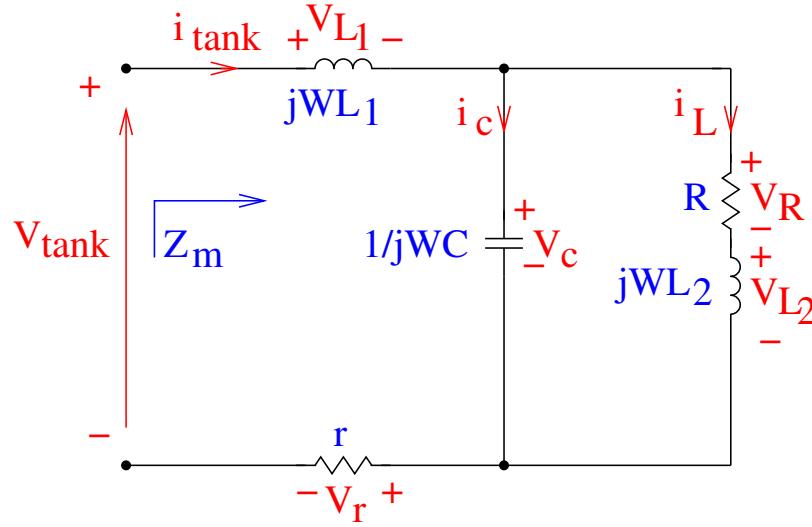
Figure 3.9: Modified LLC Load Tank

It can be deduced from Equations (3.9) and (3.10), that the maximum power transfer can be controlled by the square of the parameter β, which represents the ratio of series to parallel inductances under resonant condition. This factor can be utilized to alter the power transfer to the load-tank by modifying the value of L_1, therefore; it is convenient to call this control parameter β as **Inductance Ratio (IR)** of the induction heating system [10].

3.5.2   Power transfer of modified LLC topology

In high power IH systems, in order to achieve optimum power transferred to the load-tank, this needs a feedback from the load of the application to the controller circuit which would be connected to the driver of the converter-switches.

Usually, this controller requires a current transformer (CT) through which a feedback current can be monitored.

Although there are modern CTs with good properties used efficiently in many applications, but they still have some drawbacks, especially when used for high frequency applications [82]. Normally,they involve an internal transformer which will interference

with the inductance of the IH system and causes some deterioration change in the system impedance and increasing the cost which is undesirable, besides their complexity [83]. Thus, they will affect the resonant state of the system and thus, decreasing the efficiency of IH system [39, 40].

In order to avoid using traditional CTs in high power super frequency IH systems, a proposed current sensor circuit is introduced in this research, involving adding a small-value resistor connected in series with the load-tank.

For better comprehension of the new design, this section is investigating the effect of adding this current sensor on the control of maximum power transfer from the MNPCI converter to the proposed resonant load-tank of IH system.

Considering the new design of Fig. 3.9, the impedance Z with additional current sensing resistor r will equal to

$$Z_m = r + j\omega L_1 + \cfrac{1}{j\omega C + \cfrac{1}{R + j\omega L_2}} \tag{3.11}$$

By rearranging equation (3.11) into real and imaginary terms, Z_m equals to:

$$Z_m = \frac{(R + r - rL_2C\omega^2 - RL_1C\omega^2) + j\left(RrC\omega + L_1\omega + L_2\omega - L_1L_2C\omega^3\right)}{(1 - L_2C\omega^2) + jRC\omega} \tag{3.12}$$

Then, the absolute magnitude of new overall load Z_m of Equation (3.12) equals to:

$$|Z_m| = \frac{\sqrt{(R + r - rL_2C\omega^2 - RL_1C\omega^2)^2 + (RrC\omega + L_1\omega + L_2\omega - L_1L_2C\omega^3)^2}}{\sqrt{(1 - L_2C\omega^2)^2 + (RC\omega)^2}} \tag{3.13}$$

And the impedance phase angle, φ_m equals to:

$$\varphi_m = \arctan \frac{RrC\omega + L_1\omega + L_2\omega - L_1L_2C\omega^3}{R + r - rL_2C\omega^2 - RL_1C\omega^2} - \arctan \frac{RC\omega}{1 - L_2C\omega^2} \tag{3.14}$$

From transfer function of Equation (3.12), two pole-roots can be given, the first is due to parallel inductance only, this pole represents the resonant frequency at L_2 and expressed as:

$$\omega_p = \frac{1}{\sqrt{L_2C}} \tag{3.15}$$

And the second pole-root is the series resonant frequency that represents the effect of series-parallel inductances, L_1 and L_2 together with the effect of the sensing resistor r as well hence, the series resonant pole ω_o equals to

$$\omega_o = \sqrt{\frac{Rr}{L_1L_2} + \frac{1}{L_{eq}C}} \tag{3.16}$$

Being,

$$L_{eq} = \frac{L_1L_2}{L_1 + L_2} \tag{3.17}$$

As stated before, the series pole implies better representation to the circuit resonant state of the heating cycle, because it involves the effect of both inductances.

Considering that, the sensing resistor, r is always chosen to be very small with respect to equivalent load resistance R and close to zero value, in order to decrease the influence

on the maximum power transfer to the load tank of the system, therefore the series pole, ω_o could be considered approximately to be equal to:

$$\omega_o \approx \frac{1}{\sqrt{L_{eq}C}} \tag{3.18}$$

The factor of $\frac{Rr}{L_1L_2}$ inside the square root need to be chosen with appropriate values to be considered zero, in spite of this approximation; it still has the effect of shifting the resonant frequency even with a tiny value, which need to be focused on more carefully in order not to lose the circuit resonance.

Then, substituting ω_o into the impedance Z_m of Equation (3.12), and assuming that the reactive power dissipation is minimum with respect to the optimum power transfer to the load, due to resonant case (P_{max}) [10], therefore the impedance of Equation (3.12) at this resonant point will be the same as classic impedance of Equation (3.8), but with adding the extra series resistance, r.

Thus, the impedance Z_m at ω_o is approximately equal to

$$|Z_m|_{\omega=\omega_o} \approx r + R\frac{\left(1-\frac{L_1}{L_{eq}}\right)}{\left(1-\frac{L_2}{L_{eq}}\right)} = r + R\left(\frac{L_1}{L_2}\right)^2 \tag{3.19}$$

Therefore, the maximum power transfer from the MNPCI converter to the resonant load-tank at ω_o, is equal to the following formula:

$$P_{max} = \frac{V_{tank}^2}{Z_m} = \frac{V_{tank}^2}{r + R\left(\frac{L_1}{L_2}\right)^2} = \frac{V_{tank}^2}{r + \beta^2 R} \tag{3.20}$$

Where,

β is the Inductance Ratio IR (given from Equation (3.10)), and V_{tank} is the r.m.s value of the fundamental of resonant load-tank voltage.

It can be deduced from Equation (3.20), that, as soon as the value of current sensing resistor is kept with tiny value then its effect will be insignificant and the maximum power transfer to the load-tank will still modulated by varying only the modulation factor β, by varying the magnitude of L_1, but if load properties changed and the value difference between r and the equivalent resistor R become too close, then it will have a significant effect on the maximum power transfer and even the internal resistor of the load inductance will do, therefore; for precise and more generic case calculations, the analysis should not neglect its existence at all.

3.6   Determination of Optimal LLC Design

Depending on the equations being so far derived, the load behaviour characteristics of impedance, phase and power for LLC load topology are all shown in Fig. 3.10.
From these curves, it can be indicated that there are two frequency borders, forming three regions of frequency operation: the first two phases involves current lagging the voltage, these appear when the operational frequency is $\omega < \omega_p$ or $\omega \geq \omega_o$, in which, the power converter works in inductive mode.

While, in the third phase is when $\omega_p < \omega < \omega_o$, in which the converter works either in inductive or in capacitive mode where the current leads the voltage, depending on the application. For optimum case of the MNPCI converter operation, the best state of load resonant circuit is certainly the inductive mode [81], when $\omega \geq \omega_o$, as can be also deduced from power curve shown in Fig. 3.10.
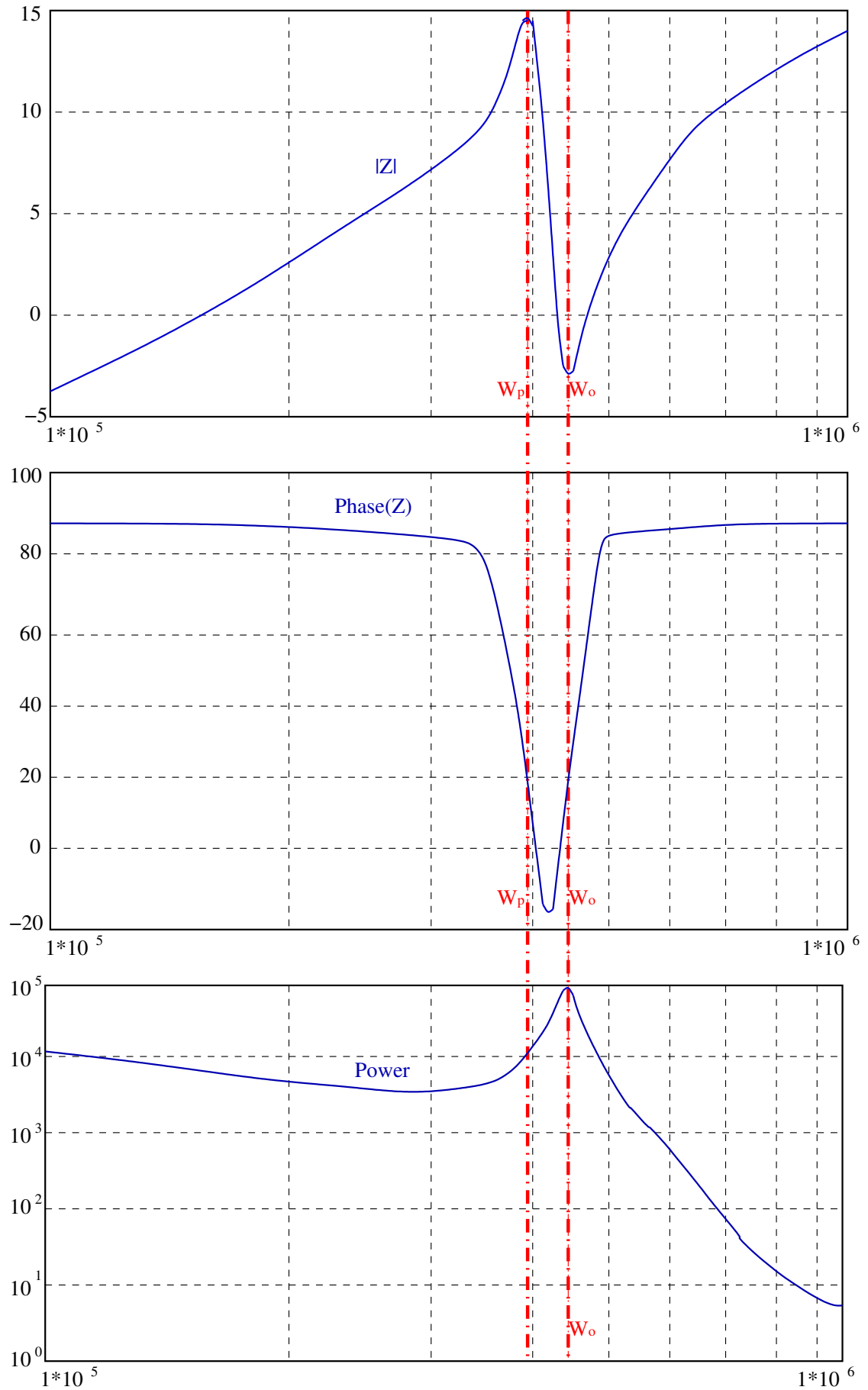
Figure 3.10: Characteristics of *LLC* Load-Tank Topology

The impedance-power graphs reveals that there are two peaks of load impedance curve, depending on the dual resonant frequency property of LLC circuit. The first is the maximal parallel impedance that occurs at f_1 resonant frequency (ω_p), in which the power is not at maximum value, and the second is the minimal series impedance which occurs at f_o resonant frequency (ω_o), in which the power is at maximum value.
This illustrates clearly that optimal mode condition of power transfer can only occurs at ω_o rather than ω_p frequency, which has less power efficiency.

According to the values of maximum and minimum impedances, it can be defined two limits of resonant frequencies 'f_1 and f_o' for different operational points of the IH system, having dual-range values of $([Q_{min}, Q_{max}]))$ respectively, in which the Q_{min} happens at maximum impedance, while the Q_{max} occurred at minimum impedance, as can be seen in the following couple equations:

$$Q_{max} = \frac{L_2 \omega_o}{R} \tag{3.21}$$

And,

$$Q_{min} = \frac{L_2 \omega_p}{R} \tag{3.22}$$

Where, it can be noticed that $\omega_o > \omega_p$ always.

Therefore; by observing Equations (3.21) and (3.22) above, it can be revealed that the current gain and hence the transferred power is optimum at Q_{max}, and vice versa when working under Q_{min} condition.

Now, by substituting ω_o given from Equation (3.6) in Equation (3.21) above, the Q_{max} is going to be as:

$$Q_{max} = \frac{L_2 \left(\frac{1}{\sqrt{L_{eq} C}} \right)}{R} \tag{3.23}$$

By substituting Equation (3.7) in Equation (3.23) above gives the following equation:

$$Q_{max} = \frac{L_2 \left(\frac{1}{\sqrt{\left(\frac{L_1 L_2}{L_1 + L_2} \right) C}} \right)}{R} = \frac{L_2}{R} \sqrt{\frac{L_1 + L_2}{L_1 L_2 C}}$$

$$= \frac{L_2}{R} \sqrt{\frac{\frac{L_1}{L_2} + 1}{L_1 C}} = \frac{1}{R} \sqrt{\frac{L_2^2 \left(\frac{L_1}{L_2} + 1 \right)}{L_1 C}}$$

$$= \frac{1}{R} \sqrt{\frac{L_2 \left(\frac{L_1}{L_2} + 1 \right)}{\left(\frac{L_1}{L_2} \right) C}} \tag{3.24}$$

Therefore; the Equation (3.24) in terms of inductance ratio β is equal to:

$$Q_{max} = \frac{1}{R} \sqrt{\frac{L_2 (\beta + 1)}{\beta C}} \tag{3.25}$$

Where, β is given from Equation (3.10).

With L_{eq} can be denoted by:

$$L_{eq} = \frac{L_1 L_2}{L_1 + L_2} = \frac{\frac{L_1}{L_2}}{\frac{L_1}{L_2} + 1} . L_2 = \frac{\beta}{\beta + 1} . L_2 \tag{3.26}$$

Therefore; as can be seen that β should be more than zero, but for better practical performance, its value must be $\beta > 1$. This fact can be seen clearly from observing the optimum condition curve of LLC topology mentioned earlier in Fig. 1.9.

By taking the square of both sides of (3.25) gives:

$$Q_{max}^2 = \frac{L_2}{R^2 C} \frac{\beta + 1}{\beta} \tag{3.27}$$

Then, the value of compensating capacitor C in terms of Q_{max} factor is equal to:

$$C = \frac{L_2}{Q_{max}^2 R^2} \frac{\beta + 1}{\beta} \tag{3.28}$$

By returning back to Equation (3.6), the value of C can be obtained as:

$$C = \frac{1}{4\pi^2 f_o^2 L_{eq}} \tag{3.29}$$

Through substituting Equation (3.26) in Equation (3.29) gives:

$$C = \frac{1}{4\pi^2 f_o^2 L_2} \cdot \frac{\beta+1}{\beta} \tag{3.30}$$

Referring to Equation (3.22), with substituting the ω_p value of Equation (3.5) in it, the following expression is formed:

$$Q_{min} = \frac{L_2\left(\frac{1}{\sqrt{L_2C}}\right)}{R} = \frac{1}{R}\sqrt{\frac{L_2}{C}}$$

Therefore;

$$Q_{min} = \frac{1}{R}\sqrt{\frac{L_1}{\beta C}} \tag{3.31}$$

Assume there is a series equivalent circuit of same load parameter magnitudes of L_2, R as shown in Fig. 3.11, and working at same max resonant frequency f_o, the value of ω_S is equal to:

$$\omega_s = \frac{1}{\sqrt{L_2 C}} = 2\pi f_o \tag{3.32}$$

Then, C_s equals the following formula:

$$C_s = \frac{1}{4\pi^2 f_o^2 L_2} \tag{3.33}$$

Therefore; by substituting Equation (3.33) in Equation (3.30), the following expression is produced:

$$C = C_s\left(\frac{\beta+1}{\beta}\right) \tag{3.34}$$
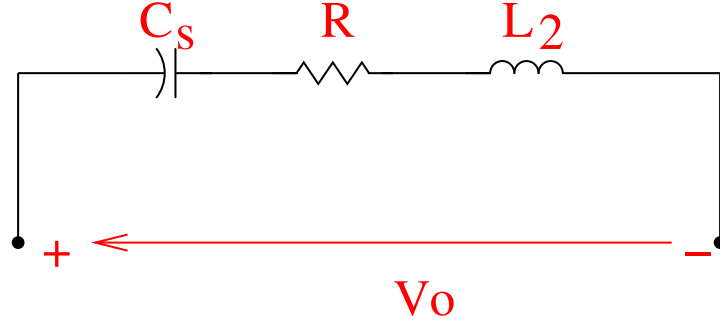
Figure 3.11: Series Resonant Equivalent Load Circuit

Equation (3.34) means that the value of compensating capacitor C is increased by a factor of $\left(\frac{\beta+1}{\beta}\right)$ than the series resonant compensator C_s, which is the main drawback of this design, because of increasing the cost, but on the other hand C value can be mitigated through increasing the capacitance voltage, which implies applying maximum voltage of V_c, to get minimum capacitance, as in the following equation:

$$i_c = C.\frac{dV_c}{dt} \tag{3.35}$$

Therefore; $C \propto \frac{1}{V_c}$, which means increasing voltage to V_{cmax} gives minimum possible capacitor C value.

3.7   Control Circuit

Generally, it can be seen from Fig. 3.12, that the induction heating power supply circuit diagram consists of four main parts.

The first part is the AC/DC rectifier source, which is not included for this moment in this thesis, but substituted by DC current source.

And, the second is the proposed MNPCI converter stage which is extensively discussed in the previous sections, with stating its various operational modes.
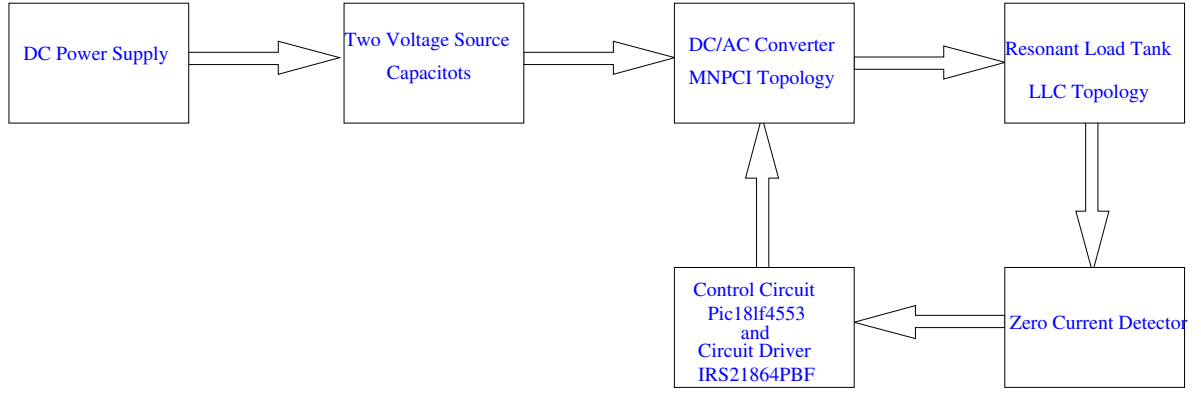
Figure 3.12: Induction Heating Power Supply Block Diagram

The third part is concerned with the resonant load tank. New LLC topology was already presented and analysed carefully to discover its effect on the resonance state of the proposed MNPCI-circuit and on the maximum power transfer from MNPCI to the load tank stage.

The last important partition is the feedback control circuit, which consists mainly from zero current detector circuit (ZCD) together with the processor (Pic18lf4553) and the MOSFET driver circuit (IRS21864pbf). The main function of the ZCD circuit is to ensures zero current switching mode (ZCS) to the driver circuit.

Therefore, the following sections will discuss the operation of the feedback control circuit in its various parts.

3.7.1 Zero Current Detector Circuit

In Section 3.5.2, there was an extensive analysis to the effect and advantages of adding the sensing resistor r on the resonant state of IH system and on the maximum power transfer from MNPCI power converter to the load-tank.

And, it was obvious that the IH circuit is still controlled by IR, β being clarified before. This will be a good starting point for better understanding the following section,

which will explain the main function of adding the current sensor to the resonant load-tank.

Considering this, in order to decrease the switching losses of the prototype design, it is very important to the MNPCI semiconductors to operate in soft switching mode, which requires the switches to commutate under zero current switching (ZCS) condition. To achieve this state, a zero current detector circuit is designed, as shown in Appendix C.

This design includes adding current sensing resistor r, which has a tiny value in series with the load tank (as in circuit of Fig. 3.9). The current i_{tank} will pass through r. This current is directed to flow into the differential amplifier (AD629), which will gives an output signal that is equal to the difference between the two signals on both sides of resistor r terminals.

Then, this signal enters to the A-B amplification stage, where the signal is amplified by a gain (G) that depends on the variable resistor R_v.

Thus, The gain is given from the following equation:

$$G = \frac{R_v}{10K} \tag{3.36}$$

After that, the signal will passes through the comparator (LM393). The output of this stage at point C of the diagram, that represents a positive square wave signal that matches exactly the positive portion of the current of the sensing resistor r as shown in Fig. 3.13.

This output signal will be as a trigger signal to the control stage of the MNPCI driver circuit, which is represented by the processor (Pic18lf4553). As soon as this signal matches the phase shift of the sensing current, it achieves a zero current switching (ZCS) condition of the MNPCI driver circuit.
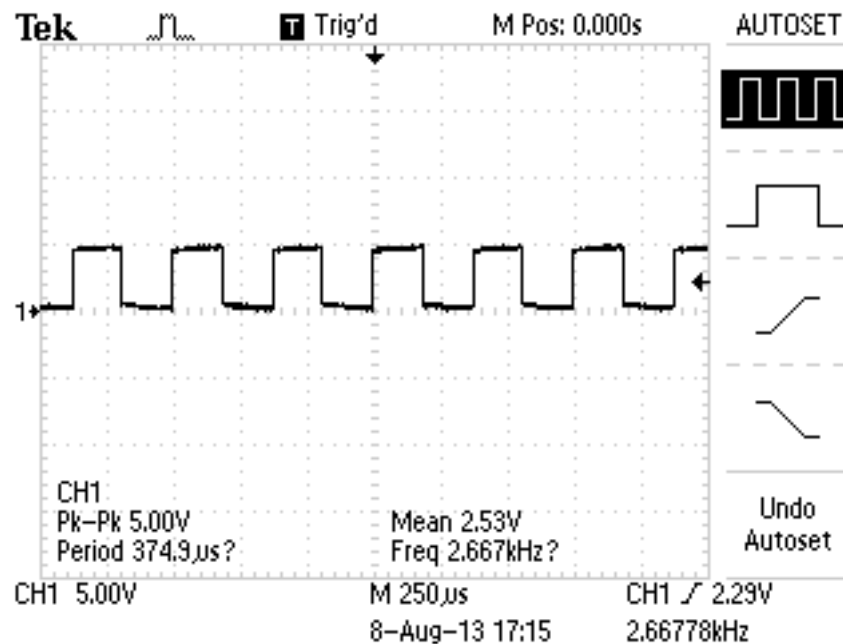
Figure 3.13: Output Signal of The Zero Current Detector Circuit

3.7.2   Processor and MOSFET Driver Circuit

So far, the first part of the feedback controller design is introduced. This part involves the zero current detector circuit. At this level, the performance of ZCS mode is achieved. This circuit design will act as a feedback triggering signal to the next level of the controller design, as shown in Fig. 3.14.

In this section, the second part of the controller topology will be introduced. It consists from two fundamental parts.

The first is the controller of programmable-microprocessor and the second is the MOSFET driver circuit.

The microprocessor being used in this topology is the high-performance controller of model **Pic18lf4553**.

According to its data sheet, This 40-pin microchip model has many properties that encouraged to choose it as a microcontroller to this design topology. Some of these advantage aspects is that it has high immunity from short circuit, because it withstand high current sink, and it is suitable for the switching frequency of the proposed prototype.
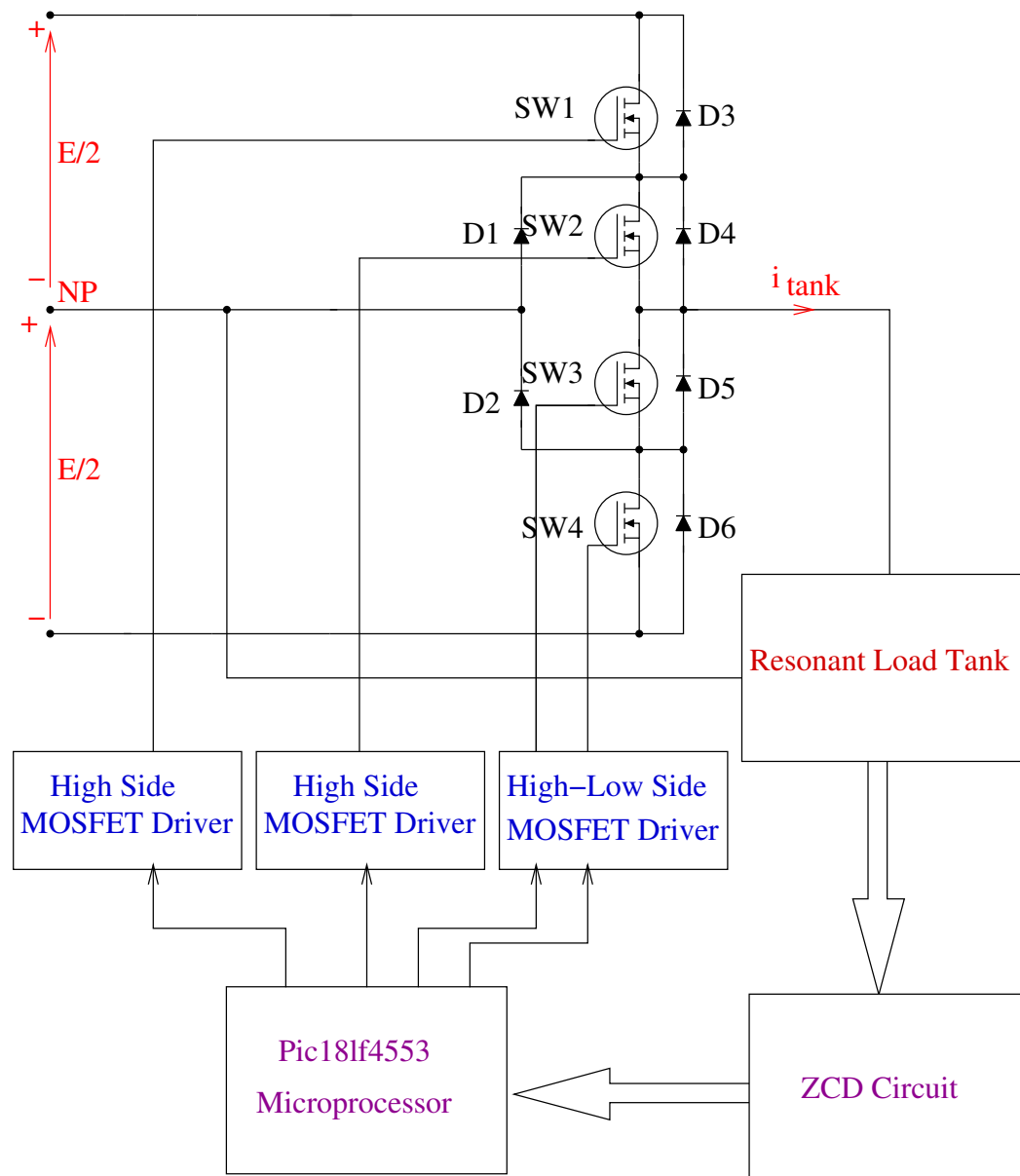
Figure 3.14: Microprocessor and MOSFET-Drivers Circuit Diagram
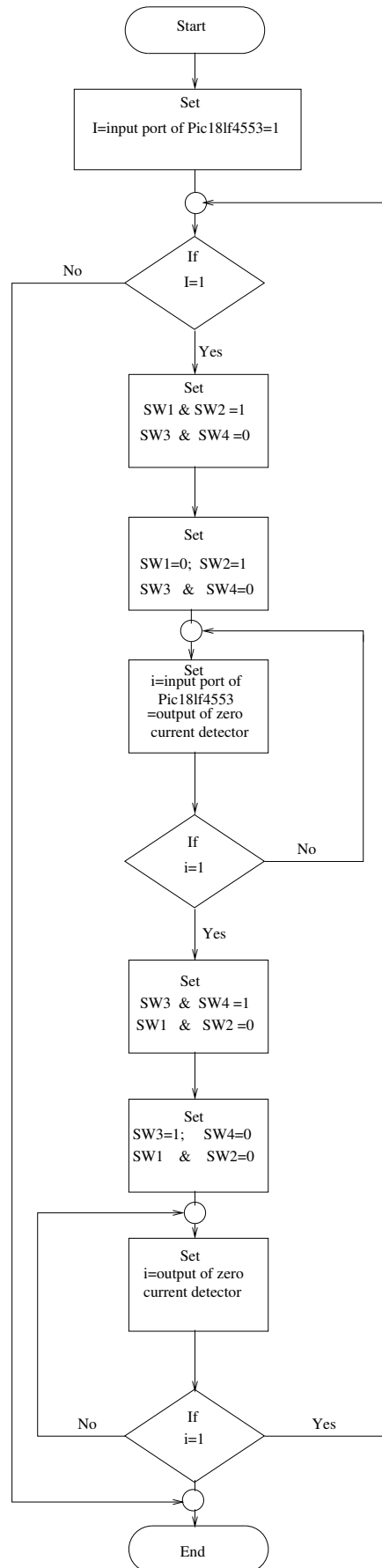
Figure 3.15: Flow Chart of Pic18lf4553 Operation

The main function of the high-performance **Pic18lf4553** processor is to trigger the three MOSFET-driver circuits of Fig. 3.14 with four signals. In order to do that, the processor is programmed with assembly C software which is explained in the flow chart of Fig. 3.15.

As can be seen from this diagram that, the **Pic18lf4553** is programmed in a way so that the zero current detector (ZCD) circuit determines the operation of the four triggering signals of the three MOSFET drivers being used, in a successive manner that achieves all MNPCI operational modes to work in zero current switching (ZCS) condition.

Regarding the last part of control circuit, there are three **MOSFET-drivers** of model **IRS21864pbf**. The reason of choosing this model is because of its suitability to the determination ratings of the switches, which consist of four **MOSFET** semiconductors of model **IRF540Z**. The MOSFET drivers consist from two high side drivers for triggering gates of switches (SW1 and SW2) individually, and from only one high/low side driver for triggering gates of both switches (SW3 and SW4), respectively.

It should be pointed that, although the four MOSFET drivers can be used in this topology, but for better circuit design the three circuit drivers are preferred, in order to decrease the circuit components which decreases the switching losses and hence, increasing the efficiency.

3.8   Experimental Set Up and Results Discussion

Considering the information been introduced so far, Table 3.2 lists the values of circuit parameters for proposed configuration of MNPCI converter prototype which shown in Appendix B, with classical or modified *LLC* topology design of resonant load tank that shown in Fig. 3.8 and Fig. 3.9 respectively. The experimental set up of the prototype design is shown in Fig. 3.16.

It must be notified that, the advantage aspect of adding the current sensor r is to measure the current and to compensate the function of current transformer CT, which should be used in the feedback control circuit of the MNPCI converter design. This step will decrease the financial cost of the IH system, besides the design will avoid the virtual interference between internal inductance of the CT with the inductance of the load-tank.

Therefore, the value of this sensing resistor is chosen carefully with very small magnitude with respect to the equivalent resistance R,therefore; its effect could be neglected, because it has a very little influence on the overall power transmission from MNPCI converter to the resonant load tank side.

Table 3.2: List of Experimental Prototype Values

Circuit parameter	Magnitude and unit	Designed Value Choice
Series inductance, L_1	$105.7\mu H$	
Parallel inductance, L_2	$100\mu H$	
Inductance Ratio, β	1.057	$\left\{\beta = \frac{L_1}{L_2}\right\} \geq 1$
Equivalent resistance, R	$0.3k\Omega$	
Series sensing resistor, r	0.2Ω	$\{r \longrightarrow 0\}$
Parallel resonant compensator, C	$11.8\mu F$	$C = \frac{L_2}{Q_{max}^2 R^2}\frac{\beta+1}{\beta}$
Voltage source capacitors, C_1 and C_2	$470\mu F$, $470\mu F$	
DC rail voltage, V	12v	
Resonant frequency, f_o	$4.639kHz$	$f_o = \frac{1}{2\pi\sqrt{L_{eq}C}}$
Classical impedance, $|Z|$	300Ω	$|Z|_{\omega=\omega_o} = \beta^2 R$
Modified impedance, $|Z_m|$	300.2Ω	$|Z_m|_{\omega=\omega_o} = r + \beta^2 R$
Classical maximum power transfer, $P_{maxclass}$	$0.12W$	$P_{maxclass} = \frac{V_{tank}^2}{\beta^2 R}$
Modified maximum power transfer, P_{maxmod}	$0.11992W$	$P_{maxclass} = \frac{V_{tank}^2}{r + \beta^2 R}$

Considering this, it can be deduced from experimental results given in Table 3.2 that the maximum power transfer from the MNPCI inverter to the resonant load tank of both the classical and modified systems are nearly the same with very small variance
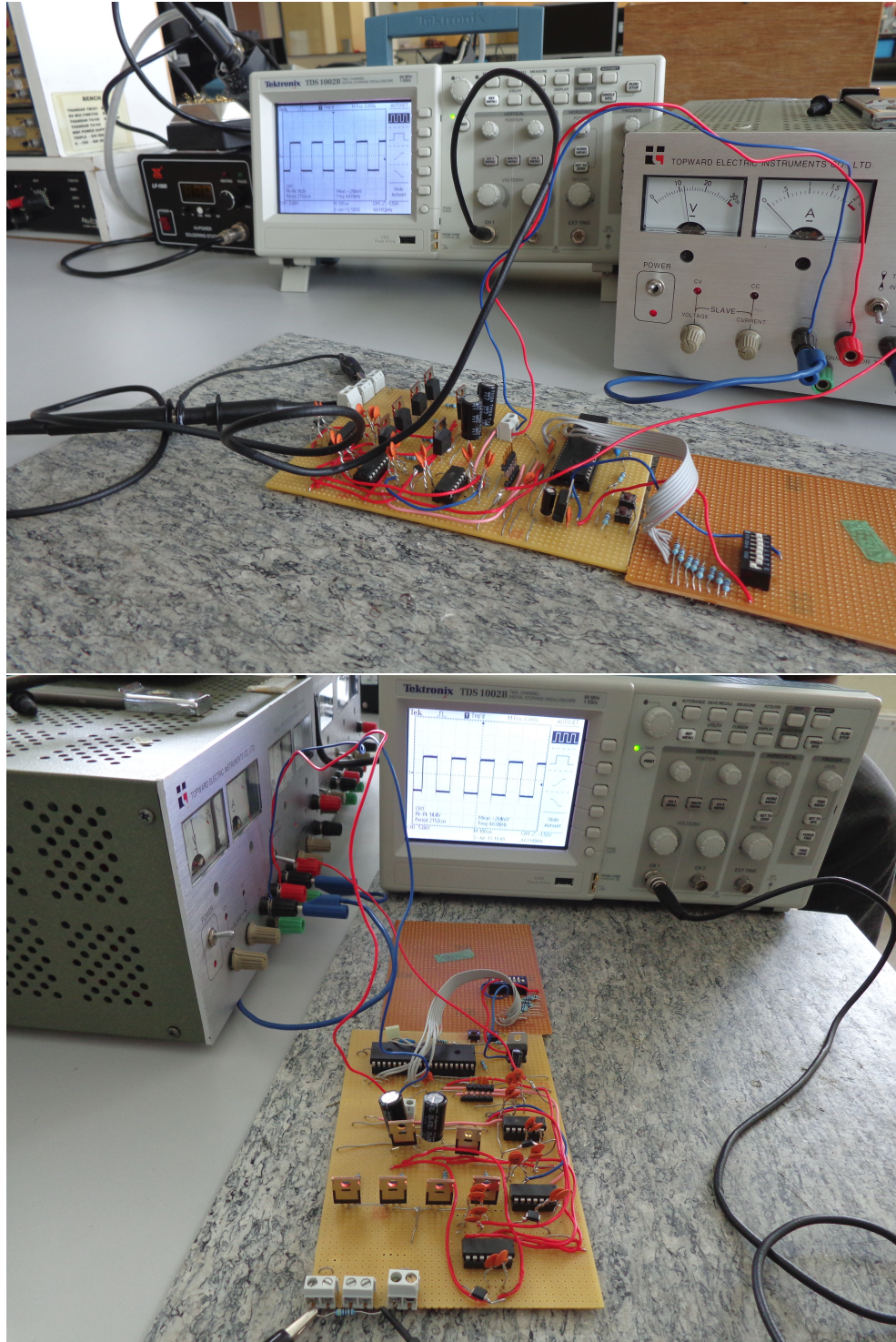
Figure 3.16: Experimental Setup 1

between them. This difference is about 0.06%, which is because of the damping effect of the current sensing resistor r, as can be seen also from Equation (3.20).

But, the resonance state of maximum power delivery from MNPCI converter to the load tank in IH system will be more stable, as the prototype does not use CT in the feedback control circuit which affects the induction load which can be considered with highly inductive properties [39], especially when its inductance variates during the heating cycle, which is extensively discussed later in Chapter 4. Besides, this CT cancellation decreases the size and overall cost of the IH system prototype being designed [40].

This means that with adding r, the maximum power delivery from the MNPCI converter to the resonant load tank is affected by less than 0.1%, i.e., it has a very tiny effect on the system resonant stability, which verifies the prototype model being used.

Besides, the output signals of proposed experimental prototype across the equivalent resistor R and parallel inductor L_2 are of uniform ac waveform, as shown in Fig. 3.17 and Fig. 3.18 respectively. These waveforms matches the ZCS operation of MNPCI converter modes and the modified LLC resonant load tank being explained before.

Finally, it should be notified that the maximum allowed voltage due to Plymouth University system is 20v, and the power has been measured through a current sensing resistor circuit with a tolerance percentage of $\pm 1\%$.
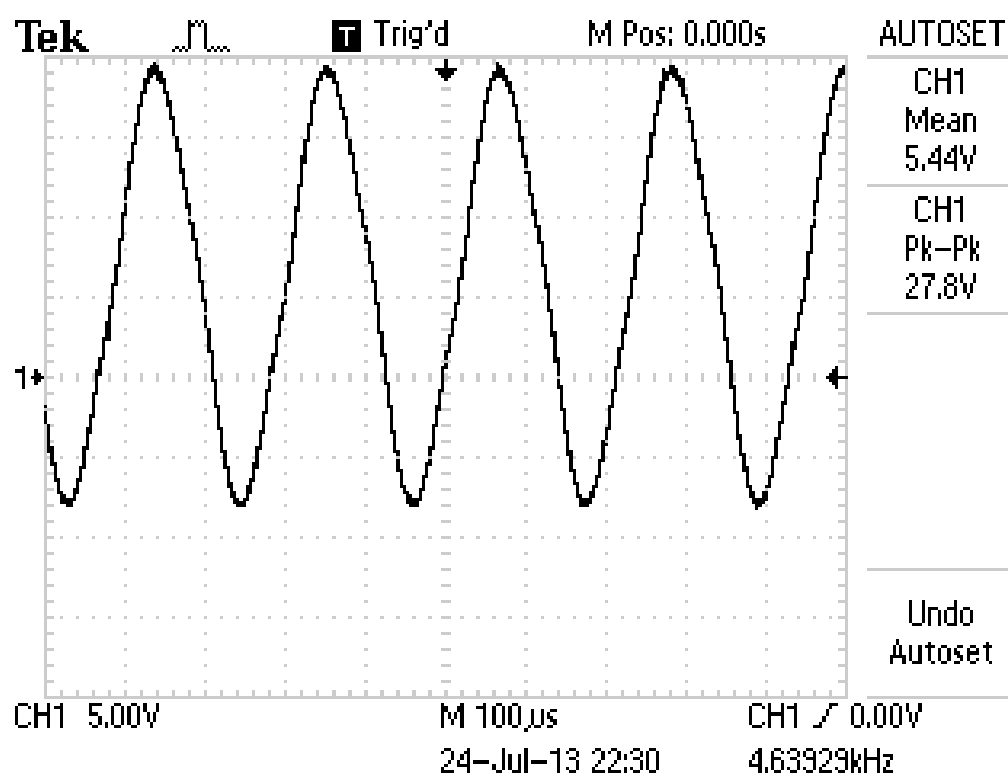
Figure 3.17: Signal of Equivalent Resistor R
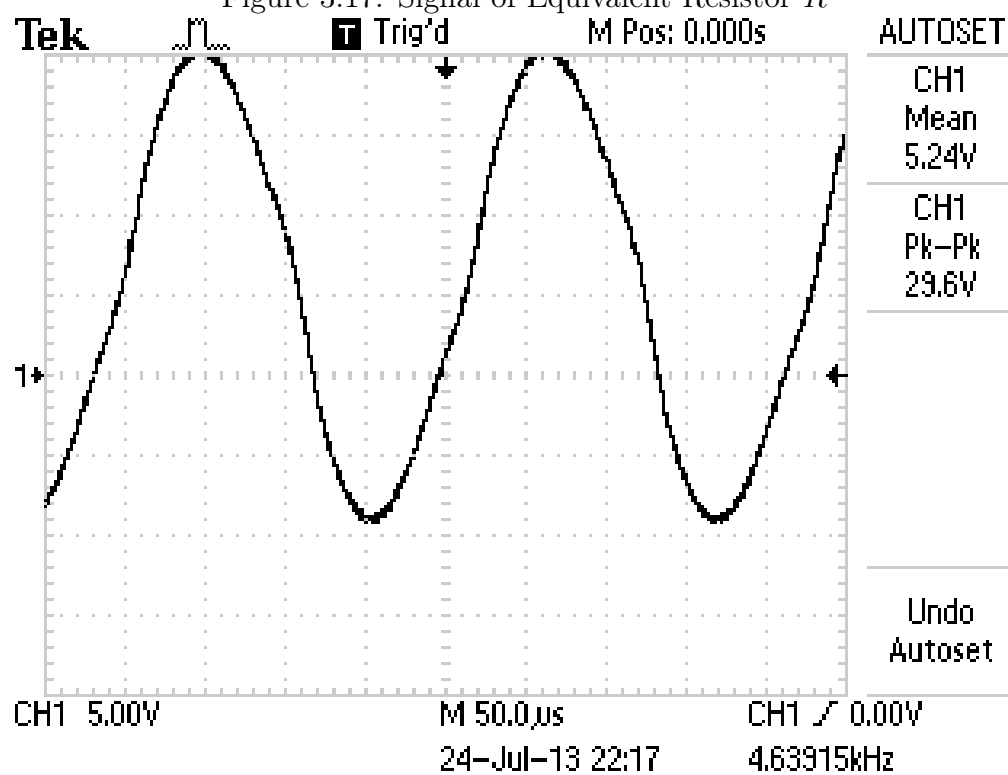
Figure 3.18: Signal of Parallel Inductor L_2

3.9   Conclusion

This Chapter is concerned with the development of three essential components of induction heating system by building, investigating and testing a new IH prototype configuration concerned with these various parts, which consists mainly from IH power supply converter with its control and from resonant load tank.

The first development step is the DC/AC converter of induction heating industrial system. In this portion, a novel experimental prototype of multilevel neutral point clamped inverter (MNPCI) is built and verified successfully, as part of induction heating power supply circuit design.

The next step is the development of IH control circuit. In this portion, the aim is to reduce the switching losses of the design. In order to do that, a zero current detector circuit is designed, it performs a zero current switching operational mode of MNPCI converter. This circuit detects the zero crossing point of the tank current i_{tank} passing through the sensing resistor r being added to the load tank. Its output will send a feedback control signal to the processor **Pic18lf4553**.

The last signal is used to give a signal permission to the Pic to trigger three MOSFET-drivers of two high side with one high/low side types. These MOSFET-drivers are used to drive four MOSFET semiconductors of the MNPCI configuration to be commutated under four operational modes in successive manner.

The third part involves the development of IH resonant load tank. This part includes introducing and analysing a modified LLC topology. The new design involves adding a small current sensing resistor r in series with the resonant load tank, to measure the current of the resonant load tank. The current sensing resistor has a very small damping effect on the maximum power transfer of less than 0.1%, which could be neglected.

Considering these results, an important parameter which has a significant effect on the maximum power transfer from MNPCI converter to the resonant load tank called the inductance ratio β, is introduced.

This parameter, as can be seen from Equations (3.9), (3.10) and (3.20), can control -in a certain limit- the resonance state of induction heating system and hence; controls the power transfer from MNPCI converter to the resonant load tank.

The value of β being chosen in this topology is equal to 1.057, but as the resonant state of IH system changes during the heating cycle, the IR could be changed as well depending mainly on L_1, to keep maximum power transfer from the MNPCI converter to the modified load tank of the topology.

Chapter 4

MNPCI Topology With Optimal Harmonic Noise Control

4.1 Introduction

I n previous chapter, the concept of multilevel neutral point clamped inverter has been introduced, built, and verified as a new power supply element in induction heating system, depending on its advantages of better operational condition of the inverter switches that conduct under half the DC rail voltage tension and inverter current less than output current by Q times, which helps in decreasing the switching losses and facilitating the zero current switching (soft mode) of the induction heating system. Together with using the LLC (or sometimes called LCL) circuit as a load equivalent, due to its benefits such as the ability for short-circuit handling, parasitic mitigation and high current gain [5, 40, 81].

Instead of using fixed values of LLC equivalent circuit parameters - as in the previous model - to represent the MNPCI prototype configuration which may apply for specific case at certain steady state condition, the need rises for more general and reliable model that can apply for a wider range of load variation that may occur during the heating process.

Therefore, and due to the variable nature of induction heating system during the induction heating cycle [40, 53], it is necessary to develop an IH system that operates using resonant MNPCI inverter with switching frequency that can change according to changing load conditions (changing circuit parameters) while IH process taking place, in order to keep tuning to approximately the natural resonant frequency of the configuration at all proposed load values [13].

By describing the induction heating as a process of changeable characteristics, this means exerting a remarkable harmonic distortion on the IH system during the heating cycle, therefore it is be very important to study this harmonic content trying to reduce it to a minimal possible level and hence increasing the power transfer from supply to the proposed load equivalent to maximal point with minimum noise.

For that reason, the MNPCI could be used, as this particular kind of MIF inverters is widely famous with these merits of low harmonic distortion and low switching losses, which can deliver IH system with optimum heating efficiency as it operates at current value nearer to the fundamental value.

Considering the last fact, this chapter will introduce the MNPCI prototype configuration with variable load parameters, in order to match the variable load characteristics during the heating cycle with optimum harmonic control strategy for the proposed IH system and trying to capture the minimum possible harmonic distortion range and hence, knowing the optimum operational point of the proposed system at which the maximum heating power occurs.

Also, this chapter includes a mathematical derivation for the harmonic content representation of output signal produced from the experimental prototype task in details using **Fourier Series** as **'periodic waveform'** rather than **Fourier Transform** as

Fourier Analysis	Signal Waveform

Fourier Transform
Continious and Aperiodic Signals

Fourier Series
Continious and Periodic Signals

Discrete Time Fourier Transform
Discrete and Aperiodic Signals

Discrete Fourier Transform
Discrete and Periodic Signals
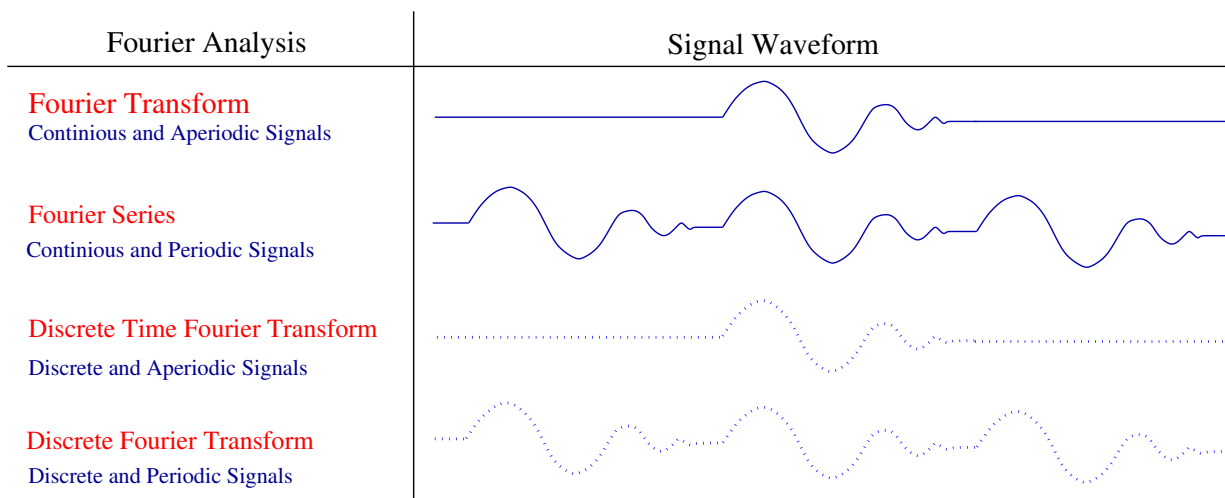
Figure 4.1: Example of Fourier Transform Analysis Types

'Aperiodic Waveform'. Therefore; at the beginning it is very important to have a quick introduction to **Fourier Analysis**, in order to distinguish between each category and utilize the best form for experimental and analytical works.

4.2   Definitions

In this section, there are some key definitions which will be extremely used in the system analysis, as follows:

4.2.1   Fourier Analysis definition

It was introduced first by **Jean Baptiste Joseph Fourier** in (1807) [84], and can be defined as a family of mathematical techniques that decomposes the signals into a set of sinusoids. It consists from four categories depending on the four basic types of signals that can be occurred.

A signal could be either continuous or discrete, and it could be either periodic or aperiodic, these types are demonstrated and summarized clearly in Fig. 4.1.

Aperiodic and Continuous

This Fourier Analysis is simply called **Fourier Transform Waveform**. These signals expand into positive and negative infinity axes without repeating itself.

Periodic and Continuous

This version is known as **Fourier Series Waveform**. The waveform in this kind repeats itself regularly towards positive and negative infinity axes.

Aperiodic and Discrete

Also known as **Discrete Time Fourier Transform Waveform**. The waveform here consists of discrete points, which propagate into positive and negative infinity axes without repeating itself.

Periodic and Discrete

It is so called **Discrete Fourier Transform Waveform**. The discrete point signal waveform in this type repeats itself regularly from negative to positive infinity axes, it is sometimes called **Discrete Fourier Series Waveform**, this category is widely used as a computer waveform representation.

4.2.2   Discrete Fourier Transform DFT

Because it has a finite limited memory, the computer can not deal with input signals $v(t)$ or $i(t)$ in a form of infinite data as in Section 4.2.1 above, therefore; it needs to decompose input signals (for this research the proposed signal is in **Time-Domain**) into a stream of discrete and finite information of **(N - Samples)** integer number.

The DFT computes the real and imaginary array of output signal in **Frequency-Domain** from N - Samples array of input signal in **Time-Domain**.

The output of DFT is denoted by $V(\omega)$ or $I(\omega)$, which contains the amplitudes of Cosine and Sine components respectively [84–86].

Therefore; the formulas of **Discrete Fourier Transform DFT** and **Inverse Discrete Fourier Transform IDFT** in terms of frequency-domain output voltage V_k are expressed as [87–92]:

- **DFT**

$$V_k = \sum_{n=0}^{N-1} v_n . e^{-2i\pi n \frac{k}{N}} \tag{4.1}$$

- **IDFT**

$$v_n = \frac{1}{N} \sum_{n=0}^{N-1} V_k . e^{2i\pi n \frac{k}{N}} \tag{4.2}$$

Where,

V_k is the frequency domain voltage.

v_n is the time domain voltage.

N is integer number equal to the total number of sampling points.

$\frac{k}{N}$ refers to the frequency.

n denotes to the time domain index from $0 \longrightarrow N-1$.

k refers to frequency domain index from $0 \longrightarrow N-1$.

i is a complex operator and it equals to $i = \sqrt{-1}$.

While, the corresponding mathematical representation of real (Re) and imaginary (Im) components of output signal $V[k]$, are going to be as in the following expressions:

$$Re\left\{V[k]\right\} = \sum_{n=0}^{N-1} v[n].Cos\left(\frac{2\pi nk}{N}\right) \tag{4.3}$$

And,

$$Im\left\{V[k]\right\} = -\sum_{n=0}^{N-1} v[n].Sin\left(\frac{2\pi nk}{N}\right) \tag{4.4}$$

Where,

n runs with a domain range from $0 \longrightarrow N-1$.
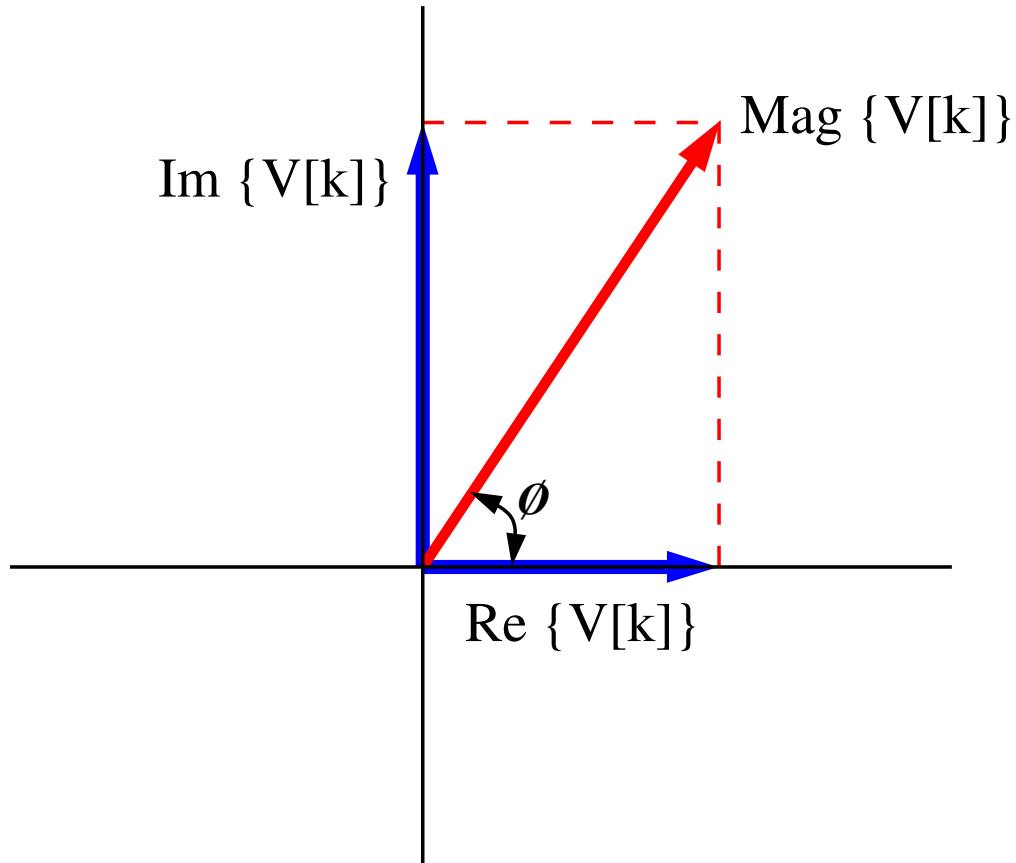
Figure 4.2: Polar Notation of Frequency Domain Output

k runs with a domain range from $0 \longrightarrow N - 1$.

Thus, the total output voltage $V[k]$ in frequency domain is equal to the synthesis of the individual parts Re and Im together, which can be clearly observed from Fig. **??**, as in the following equation:

$$V[k] = Re\left\{V[k]\right\} + Im\left\{V[k]\right\} \tag{4.5}$$

So far, the **Rectangular Notation** is discussed and clarified, in which the frequency domain output is represented by a group of Cosine (Real) and Sine (Imaginary) waves. In the following statement, the **Polar Notation** of frequency domain output is illustrated.

Simply, the polar notation converts the Sine and Cosine rectangular form into equiv-

alent state of frequency domain output in the shape of **magnitude** and **phase shift**, as can be clearly shown in Fig. 4.2.

Therefore, the magnitude and phase shift angle ϕ (or sometimes called θ) are calculated from the following expressions:

$$Mag\left\{V[k]\right\} = \sqrt{Re\left\{V[k]\right\}^2 + Im\left\{V[k]\right\}^2} \tag{4.6}$$

With,

$$Phase\left\{V[k]\right\} = arctan\left(\frac{Im\left\{V[k]\right\}}{Re\left\{V[k]\right\}}\right) \tag{4.7}$$

And the corresponding real and imaginary parts in terms of polar notation is going to be as the following pair of formulas:

$$Re\left\{V[k]\right\} = MagV[k].Cos\left(Phase\left\{V[k]\right\}\right) \tag{4.8}$$

And,

$$Im\left\{V[k]\right\} = MagV[k].Sin\left(Phase\left\{V[k]\right\}\right) \tag{4.9}$$

4.2.3   Average Power

It is defined as the rate of energy flow and normally denoted to the average of real power. For a certain voltage $v(t)$ and current $i(t)$, the average power expression over a time period of T is equal to [93]:

$$P_{av} = \frac{1}{T}\int_0^T v(t)\cdot i(t)\ dt \tag{4.10}$$

Where,

P_{av}, $v(t)$ and $i(t)$: are functions in time-domain.

4.2.4   Total Harmonic Distortion

It is either used to define the harmonic distortion noise in current and/or voltage. It has two definitions; one referred to the **fundamental value**, which is denoted by THD_F. It is defined as the ratio between the summation of rms values of all harmonic components excluding the fundamental to the fundamental value, [93, 94].

Therefore; the THD_F ratio - with respect to current - is expressed by the following formula:

$$THD_F = \frac{\sum\limits_{n=2}^{\infty} In_{rms}Harmonics}{IFundamental} \qquad (4.11)$$

While, the second expression of total harmonic distortion is referred to the **rms value** and it is denoted by THD_R.

It is defined as the ratio between the summation of rms values of all harmonic components except the fundamental to the rms value of all harmonic component including the fundamental value. [94].

Therefore; the THD_R law - with respect to current - is equal to the following expression:

$$THD_R = \frac{\sum\limits_{n=2}^{\infty} In_{rms}Harmonics}{\sum\limits_{n=1}^{\infty} In_{rms}Harmonics} \qquad (4.12)$$

According to Equations 4.11 and 4.12, the relationship between THD_F and THD_R is as follows:

$$THD_R = \frac{THD_F}{\sqrt{1+THD_F^2}} \qquad (4.13)$$

4.2.5   Effective Heating Power

The effective heating power for an AC current with a certain frequency flowing through a resistive load tank can be defined as the square of the current times the amount of resistor, as in the following formula:

$$P_e(f) = I^2(f) * R_e(f) \tag{4.14}$$

Where,

$P_e(f)$ is the effective heating power as a function of f,

$I(f)$ is the resistive current as a function of f,

$R_e(f)$ is the effective resistance of the load as a function of f.

The resistance $R_e(f)$ is inversely proportional to the effective area of heating region, as in the following equation:

$$R_e(f) = \rho.\frac{L}{A_e(f)} (\Omega) \tag{4.15}$$

Where,

R_e is the effective resistance,

ρ is the material resistivity,

L is the material length,

and $A_e(f)$ is the effective cross sectional area of workpiece.

It can be deduced from analysing the skin depth δ expression of Equation 2.12 mentioned before in Chapter 2, that any decrease in effective cross sectional area of material means decrease the heating depth δ and as the square root of frequency is inversely proportional with δ, then the switching frequency is increased as well, as can be seen in Fig. 4.3 and the following relation:

$$\delta \propto \frac{1}{\sqrt{f}} \tag{4.16}$$
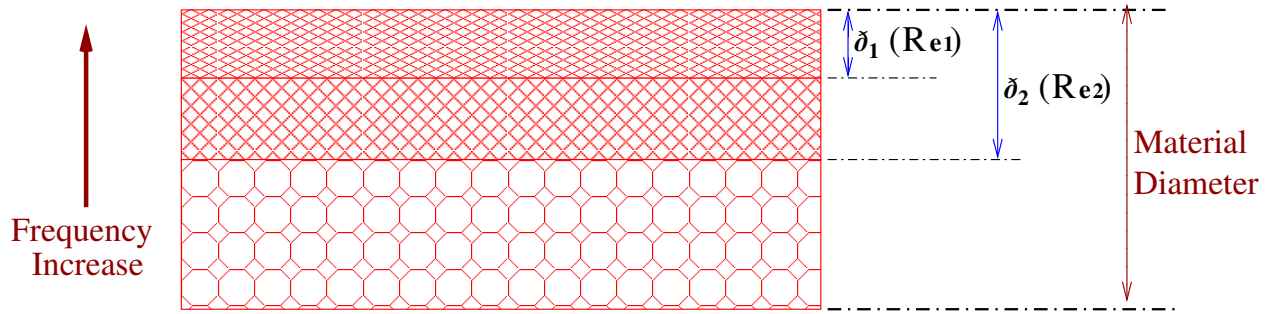
Figure 4.3: Relationship Between Frequency and Skin Depth

As a consequence; the effective resistance $R_e(f)$ is directly proportional to $\sqrt{f}$, as in the following relation:

$$R_e(f) \propto \sqrt{f} \tag{4.17}$$

Therefore, the effective heating power $P_e(f)$ can be expressed in terms of the summation of all components of current harmonics at different frequencies, as in the following formula:

$$P_e(f) \propto \sum_{n=1}^{m} I^2(f_n) \cdot \sqrt{f_n} \tag{4.18}$$

Where,

m is the total number of current harmonics.

f_n is the frequency of harmonic n.
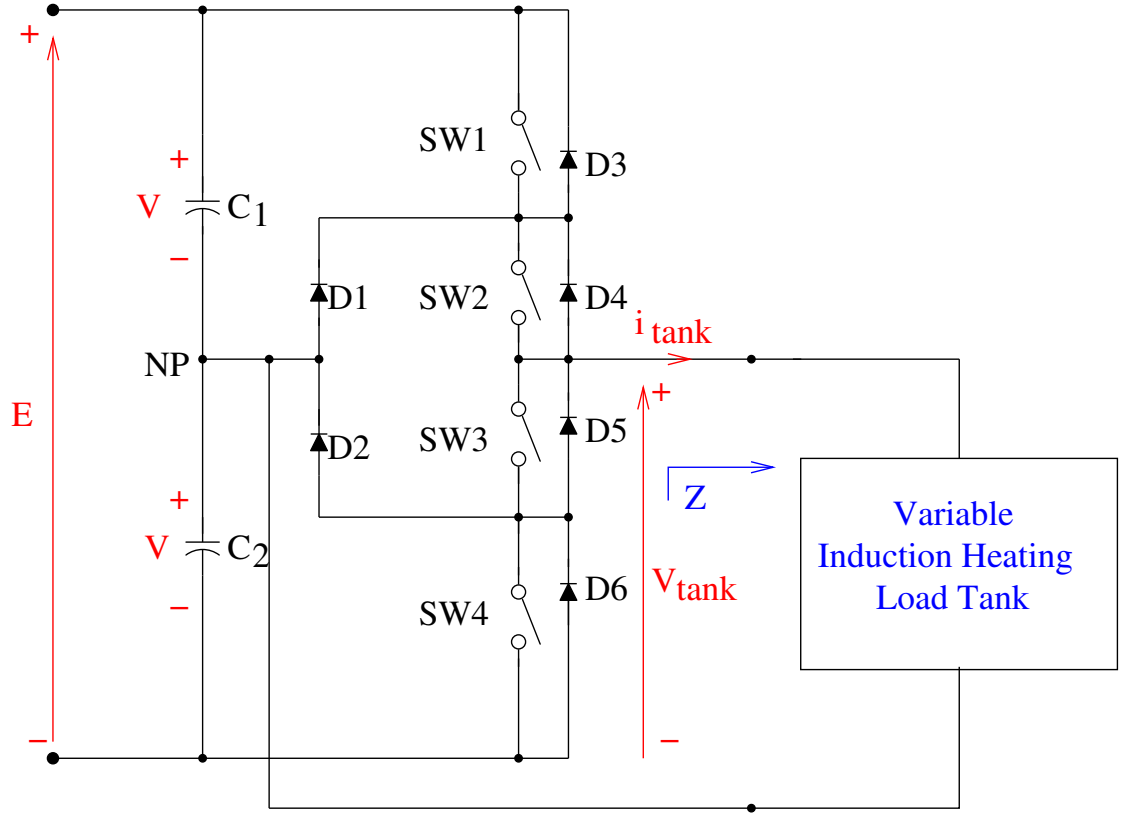
Figure 4.4: MNPCI prototype

4.3 System Description

The main feature difference of the new prototype design from the previous configuration shown in Section 3.4.2 - Fig. 3.7 is being characterized by variable load equivalent instead of fix form, in order to coincide the behaviour of induction heating and for better representation to the heating cycle of IH system, which has changeable behaviour during the process [40, 53].

By considering the new circuit diagram of IH system using hybrid MNPCI converter that is shown in Fig. 4.4, the proposed configuration consists mainly from DC power supply feeding MOSFET-switches of MNPCI converter through two voltage source split capacitors of equal voltage, the output of the converter supplies a variable LLC load equivalent. The whole system is controlled by high performance processor programmed with optimum algorithm which is clarified in details later in this chapter. The various prototype elements will be illustrated in the following sections:

4.3.1   MNPCI Converter

The details of the proposed circuit design of hybrid MNPCI-converter are shown in Fig. 4.4 [49,95,96]. The MOSFET switches of the MNPCI topology operate under maximum of half the DC rail voltage of magnitude $V = |\frac{E}{2}|$, by splitting this voltage tension through two voltage-source bulk capacitors of ($C1$ and $C2$) of equal values, which will maintain constant voltage delivery to the designed configuration just like the voltage fed inverter (VFI) topology [5].

As been mentioned before, the central point between the source capacitors called '**Neutral Point** (**NP**)'. It splits the operational voltages into three successive levels $\left[-\frac{E}{2}, 0 \text{ and } \frac{E}{2} \right]$, which facilitates the soft switching mode of the four operational modes of the MOSFET switches of MNPCI topology explained in Table 3.1 in Section 3.4.1, i.e, this will decrease the switching losses which in turn increase the efficiency [95].

Therefore, the MNPCI topology has **three** operating **modes**: **Positive** (**P**), **Negative** (**N**) and **0**. The clamping diodes ($D1$ and $D2$) are connected to the **NP**. When the switches ($SW1$ and $SW2$) are switched ON, the MNPCI output terminal to the load Z is connected to the **NP** through either of clamping diode $D1$ or $D2$.

During the **P**-mode, the first two upper high MOSFET-switches (SW1 and SW2) are switched ON. Then the **0**-mode is afterwards, the switch SW1 is turned OFF and the storage energy is discharging with the output current flows through the free wheeling diode switch SW2.

While the **N**-mode, the two lower high-low MOSFET-switches (SW3 and SW4) are switched ON. Then, the 0-mode again is afterwards, the SW4 is turned OFF and the storage energy is discharging, with output discharging current flows through the free wheeling diode and switch SW3.
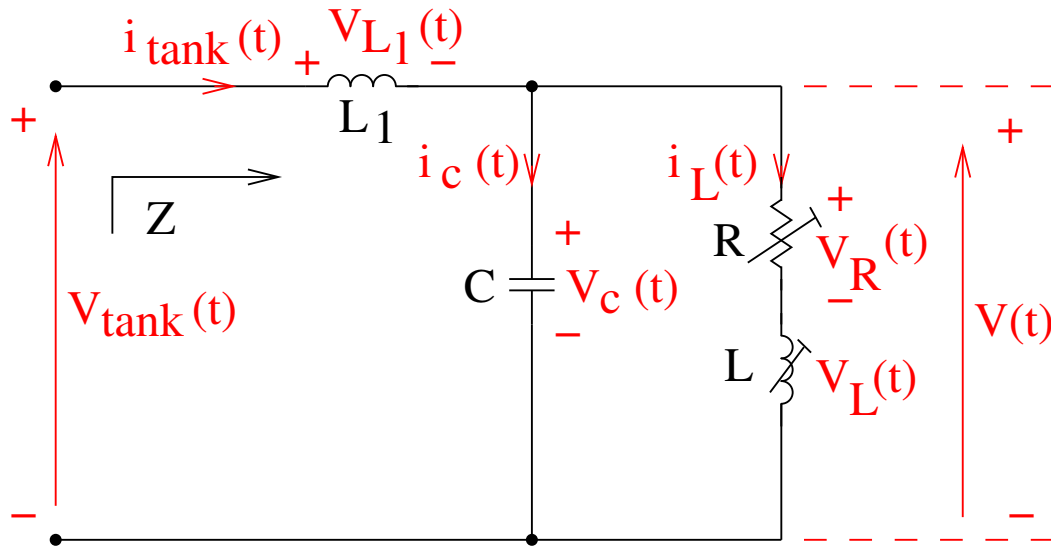
Figure 4.5: Variable LLC Equivalent of IH Load

The MNPCI topology delivers an IH load model of variable LLC equivalent circuit with an output voltage V_{tank}, as in the following Section.

4.3.2   Resonant Load tank Equivalent

As can be pointed from IH load configuration in Fig. 4.5, the inductor - workpiece load set will be modelled using variable inductor - resistor equivalent of R and L, to represent the changeable characteristic of induction heating cycle, both connected in parallel with constant value compensating capacitor C, in order to achieve the resonant mode of IH system at steady state condition.

Besides, It contains series connected inductance L_1, to form the LLC load equivalent circuit which has the following advantages of:

- It maintains constant current delivery to the IH load, with the current flowing through the inductor i_L is greater than the current flowing through the converter semiconductor switches $i_{tank}(t)$ by Q times like the current fed inverter (CFI), therefore Equations (4.19)(4.20) and (4.21) below are applied.

- It has the capability to absorb the undesired inductive parasitic components in IH system.
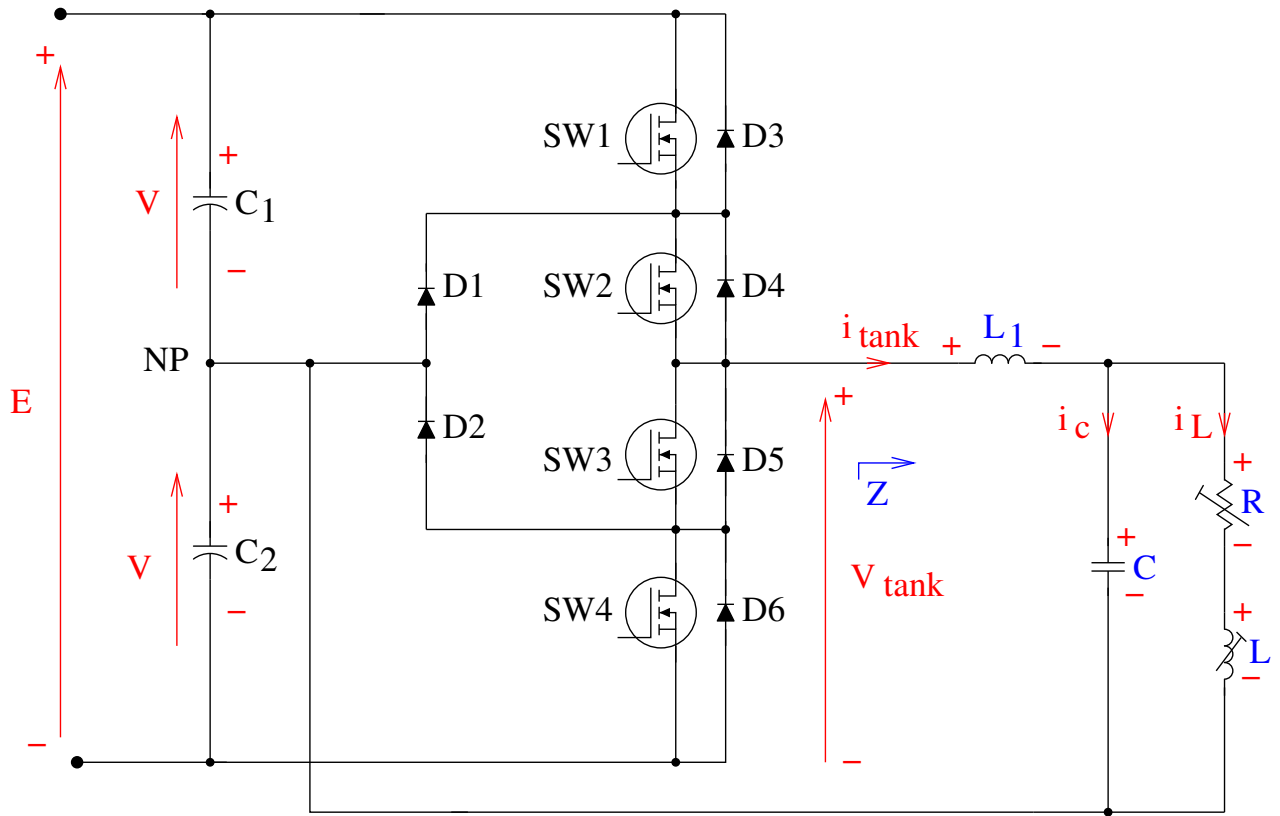
Figure 4.6: Hybrid Configuration With Variable Load

- It compensates the matching transformer absence at load side which decreases the cost and increases the efficiency.

- It offers good short circuit immunity from load short circuit (heating coil and workpiece) and from capacitor inrush current, as it applies a mandatory path of L_1, which keeps MNPCI working under inductance load behaviour even during that problem.

The current gain of IH load configuration can be calculated from tank current $i_{tank}(t)$ which will be divided into inductor-resistance current $i_L(t)$ and capacitor current $i_C(t)$ as follows:

$$i(t)_{tank} = i_C(t) + i_L(t) \tag{4.19}$$

Being, $i_C(t)$ is the compensator current which equal to

$$i_c(t) = (1 + jQ)i_{tank}(t) \tag{4.20}$$

And, the inductor current $i_L(t)$ is equal to

$$i_L(t) = -jQi_{tank}(t) \tag{4.21}$$

Where Q is quality factor.

Therefore, this topology takes the advantage aspect of constant voltage delivery through using the two equal bulk voltage capacitors, like the (VFI), and also gives constant current delivery of gain Q to the load due to modelling with LLC topology, which means it can be considered as a hybrid voltage-current fed inverter (HVCFI) with a high current gain IH system, as can be deduced from the relationship between inverter and load currents given by Equation (4.21), see Fig. 4.6.

4.3.3   Control Circuit

The most important merit of IH system is its variable characteristics during the heating process which means that the control plan of the prototype should be adapted to achieve optimum algorithmic behaviour at all load equivalent conditions, in order to ensure maximum power delivery from MNPCI power supply to IH load.

The control strategy is designed to maintain the phase shift angle between voltage and current approximately zero at all load tested conditions, which facilitates capturing the resonant state and achieves soft switching mode of all MOSFETs of MNPCI configuration.

Considering that, the control circuit consists essentially from high performance board processor **STM32F4DISCOVERY** (**STM32F4**), due to its easy to program besides its high speed execution, better accuracy and more functionality than other pic-processors and suitability to application frequency. The **STM32F4** board used to trigger three MOSFET-drivers of two high-side and one high/low-side MOSFET-drivers. These will
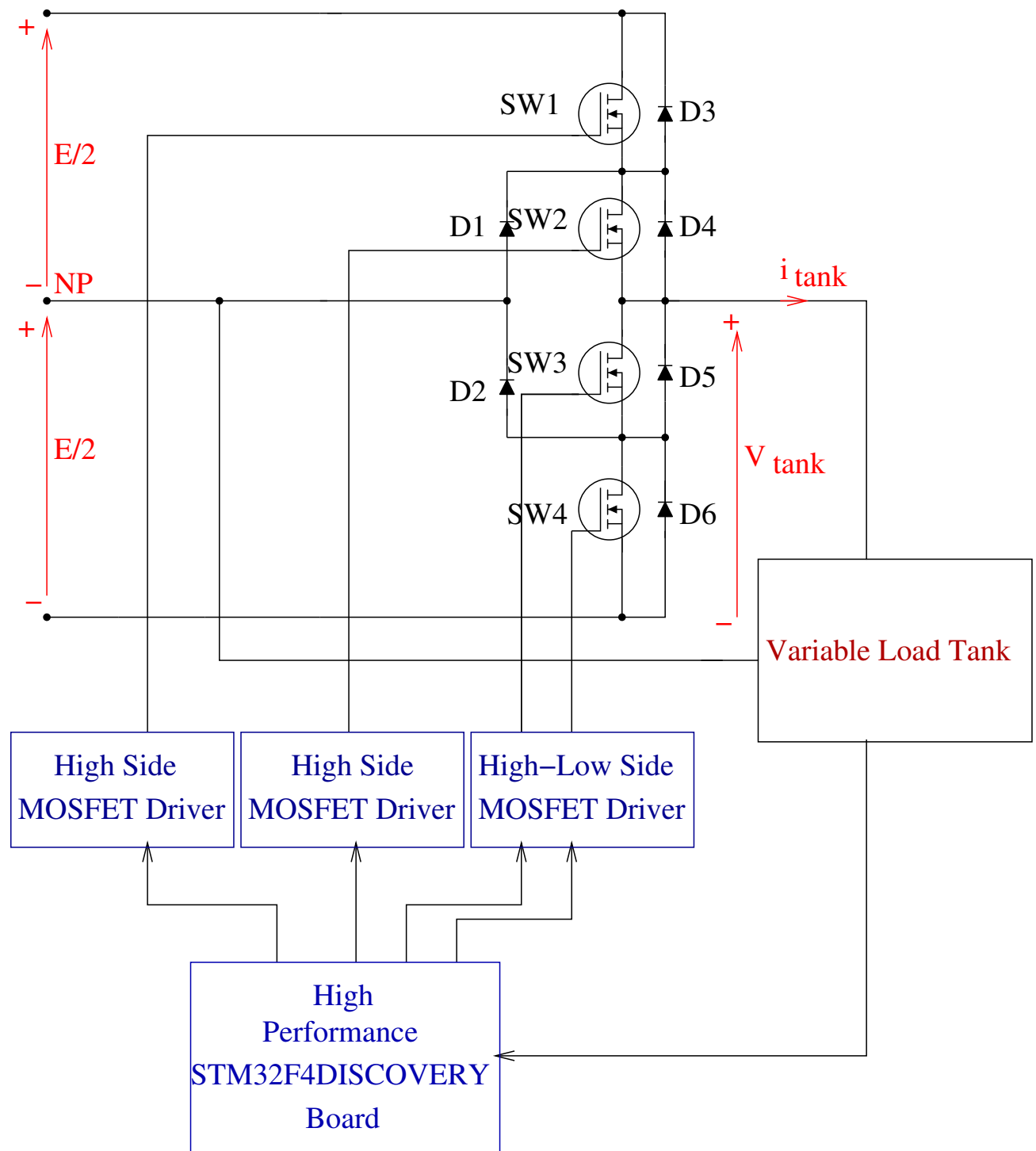
Figure 4.7: Control Circuit
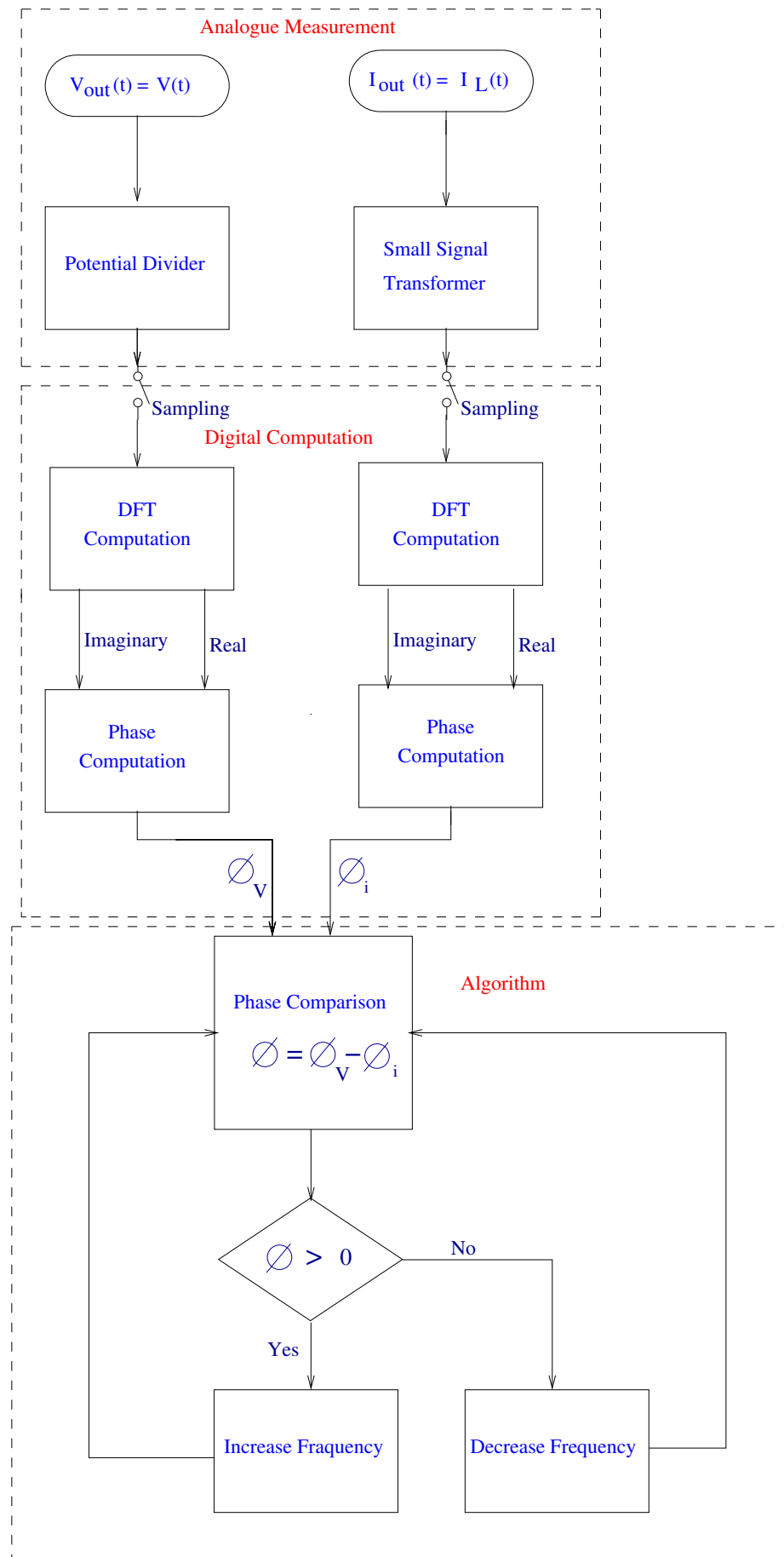
Figure 4.8: Control Algorithm

119

attenuates four MOSFETs of three high side and one low side switches with four modes shown in Table 3.1 before, as shown in Fig. 4.7 above.

The control strategy is designed to maintain the phase shift angle between voltage and current approximately zero at all load tested conditions as can be seen in output voltage and current signals shown in Fig. 4.15 later, which facilitates capturing the resonant state and achieves soft switching mode of the MNPCI prototype MOSFETs.

Considering the optimum algorithm block diagram of control circuit shown in Fig. 4.8, the algorithm decomposes both the voltage and current output signals simultaneously using **Discrete Fourier Transform (DFT)** into their real and imaginary complex components, in order to compute their phase angles and afterwards make a comparison between them to calculate the phase shift angle ϕ. According to ϕ, the frequency will be attenuated to approximately the natural resonant frequency of the circuit while the induction heating load samples being changed during the experimental work.

4.4   Experimental Set Up and Average Power Analysis

Considering the schematic graph results of the experimental prototype values illustrated in Table 4.1, the frequency response behaviour to the variable IH load of proposed prototype during experimental work is drawn in Fig. 4.12, and the experimental set up prototype is shown in Fig. 4.9.

For better understanding the power transfer of the system configuration from the proposed MNPCI converter to the LLC equivalent load, there will be an extensive analysis to the average power transfer in terms of harmonic components of output load voltage and output current, which is delivered from MNPCI topology to the IH load of captured following values: $L1 = 105.7\mu H$, $R = 10.07\Omega$ and $L = 33\mu H$, as can be seen in output voltage and current signals in Fig. 4.15, which clearly clarifies from first sight that, the

phase shift angle ϕ between the two signal is very tiny and can be considered as approximately zero magnitude difference.

But from practical point, and by analysing experimental results of both magnitude responses of harmonic components of output voltage shown in Fig. 4.10, and magnitude responses of output current shown in Fig. 4.11, it is found that there are three harmonic components of output voltage of (ω_1, ω_3 and ω_5), of frequencies f_1(main frequency), $f_3 = 3f_1$ and $f_5 = 5f_1$ respectively, and two harmonics of current of (ω_1 and ω_3) of frequencies f_1(main frequency) and $f_3 = 3f_1$, therefore for simplicity there will be three terms of voltage and current to represent the real and imaginary parts using Fourier Series, and the transfer power will equal to the average power through the resistor R, assuming ideal state and resonant mode, therefore the average power will be expressed as:

Table 4.1: List of Variable Experimental Prototype values

Circuit parameters	Magnitude and unit	Designed Value Choice
Series inductance, L_1	$105.7(\mu H)$	
Parallel inductance, L $\{L_{p1}, L_{p2}, L_{p3}, L_{p4} and L_{p5}\}$	$22, 33, 47, 68, 100(\mu H)$	
Inductance ratio values, β $\{\beta_1, \beta_2, \beta_3, \beta_4 and \beta_5\}$	$4.8, 3.2, 2.25, 1.55, 1.057$	$\{\beta = \frac{L_1}{L}\} \geq 1$
Equivalent resistance, R	$3.37, 10.07, 15.07, 22.07(\Omega)$	
Parallel resonant compensating capacitance, C	$11.8(\mu F)$	$C = \frac{L}{Q_{max}^2 R^2} \frac{\beta+1}{\beta}$
Voltage source capacitors, C_1 and C_2	$470, 470(\mu F)$	

$$P_{av} = P_R = \frac{1}{T} \int_0^T v_R(t) i_R(t) dt$$

$$= \frac{1}{T} \int_0^T \left(v(t) - L\frac{di_L(t)}{dt} \right) i_L(t) dt \qquad (4.22)$$

The $v(t)$ and $i_L(t)$ are the time domain output voltage and current respectively, given
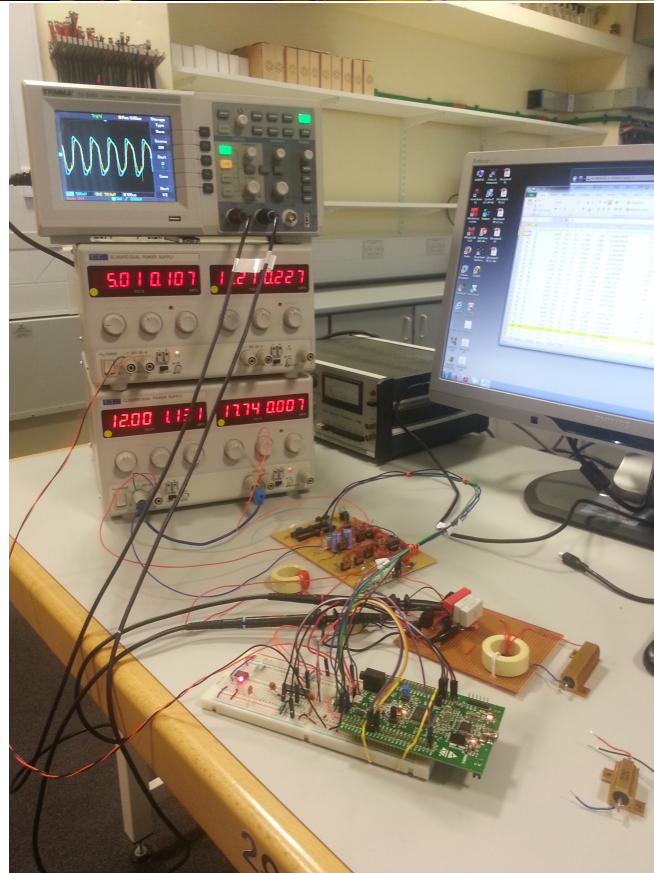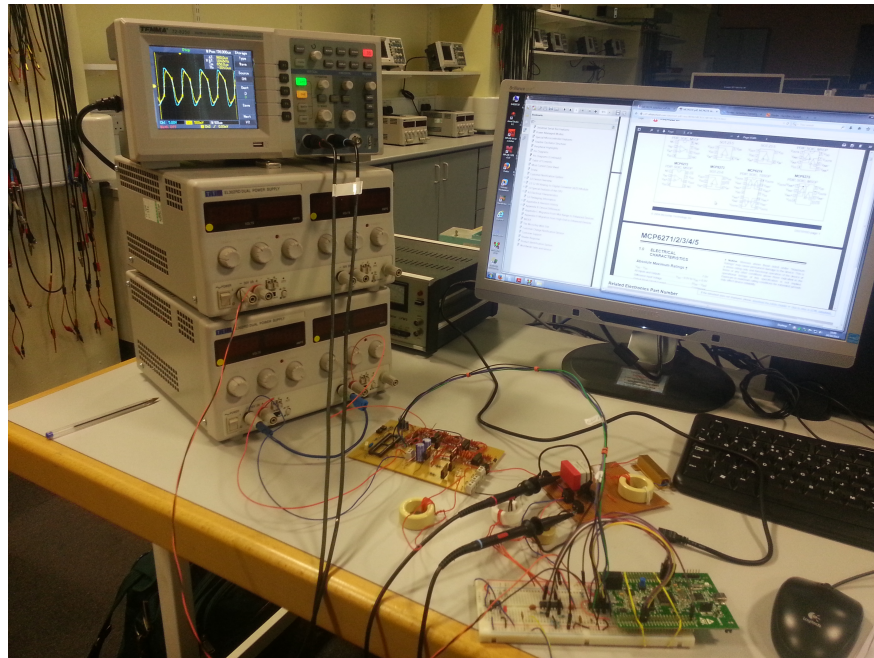
Figure 4.9: Experimental Setup 2

from Fourier Series as follows:

$$v(t) = k_1 Cos\omega_1 t + k_2 Sin\omega_1 t + k_3 Cos\omega_3 t + k_4 Sin\omega_3 t$$
$$+ k_5 Cos\omega_5 t + k_6 Sin\omega_5 t \tag{4.23}$$

With,

$$i_L(t) = k_7 Cos\omega_1 t + k_8 Sin\omega_1 t + k_9 Cos\omega_3 t + k_{10} Sin\omega_3 t$$
$$+ k_{11} Cos\omega_5 t + k_{12} Sin\omega_5 t \tag{4.24}$$

And the derivative of $i_L(t)$ will given by

$$\frac{di_L(t)}{dt} = -k_7 Sin\omega_1 t + k_8 Cos\omega_1 t - k_9 Sin\omega_3 t + k_{10} Cos\omega_3 t$$
$$- k_{11} Sin\omega_5 t + k_{12} Cos\omega_5 t \tag{4.25}$$

By substituting Equations (4.23), (4.24) and (4.25) into Equation (4.22), then the following expression formed:

$$P_{av} = \frac{1}{T} \int_0^T \left[\left[k_1 Cos\omega_1 t + k_2 Sin\omega_1 t \right. \right.$$
$$+ k_3 Cos\omega_3 t + k_4 Sin\omega_3 t$$
$$\left. + k_5 Cos\omega_5 t + k_6 Sin\omega_5 t \right]$$
$$.L \left[k_7 \omega_1 Sin\omega_1 t - k_8 \omega_1 Cos\omega_1 t \right.$$
$$+ k_9 \omega_3 Sin\omega_3 t - k_{10} \omega_3 Cos\omega_3 t$$
$$\left. + k_{11} \omega_5 Sin\omega_5 t - k_{12} \omega_5 Cos\omega_5 t \right] \tag{4.26}$$
$$. \left[k_7 Cos\omega_1 t + k_8 Sin\omega_1 t \right.$$
$$+ k_9 Cos\omega_3 t + k_{10} Sin\omega_3 t$$
$$\left. \left. + k_{11} Cos\omega_5 t + k_{12} Sin\omega_5 t \right] \right] dt$$

123

By simplifying (4.26), then taking the Laplace Transform to it, the equation will be transformed to the following formula:

$$
\begin{aligned}
\mathscr{L}\left\{P_{av}\right\} = \frac{1}{TS}\Bigg[& \frac{k_1k_7 + k_3k_9 + k_4k_{10} + k_5k_{11} + k_6k_{12}}{2S} + \left(\frac{k_1k_7 - k_8k_7\omega_1 L}{2}\right)\frac{S}{S^2 + 4\omega_1^2} \\
& + \left(\frac{k_1k_8 + k_2k_7 + (k_7^2 - k_8^2)\omega_1 L}{2}\right)\frac{2\omega_1}{S^2 + 4\omega_1^2} + \left(\frac{k_3k_9 - k_4k_{10} - 2k_9k_{10}\omega_3 L}{2}\right) \\
& \cdot \frac{S}{S^2 + 4\omega_3^2} + \left(\frac{k_4k_9 + k_3k_{10} + (k_9^2 - k_{10}^2)\omega_3 L}{2}\right)\frac{2\omega_3}{S^2 + 4\omega_3^2} \\
& + \left(\frac{k_5k_{11} - k_6k_{12} - 2k_{11}k_{12}\omega_5 L}{2}\right)\frac{S}{S^2 + 4\omega_5^2} + \left(\frac{k_6k_{11} + k_5k_{12} + (k_{11}^2 - k_{12}^2)\omega_5 L}{2}\right) \\
& \cdot \frac{2\omega_5}{S^2 + 4\omega_5^2} + \left(\frac{k_3k_7 - k_4k_8 + k_1k_9 - k_2k_{10} - k_8k_9(\omega_1 + \omega_3)L - k_7k_{10}(\omega_1 + \omega_3)L}{2}\right) \\
& \cdot \frac{S}{S^2 + (\omega_1 + \omega_3)^2} + \left(\frac{k_3k_7 + k_4k_8 + (k_8k_9 - k_7k_{10})\omega_3 L}{2}\right)\frac{S}{S^2 + (\omega_3 - \omega_1)^2} \\
& + \left(\frac{k_4k_7 + k_1k_{10} + k_3k_8 + k_2k_9 - (k_9 + k_{10})k_8\omega_1 L + k_7k_9\omega_3 L - k_8k_{10}\omega_5 L}{2}\right) \\
& \cdot \frac{(\omega_1 + \omega_3)}{S^2 + (\omega_1 + \omega_3)^2} + \left(\frac{k_4k_7 - k_3k_8 + (k_7 + k_8)k_9\omega_3 L}{2}\right)\frac{(\omega_3 - \omega_1)}{S^2 + (\omega_3 - \omega_1)^2} \\
& + \left(\frac{k_5k_7 + k_6k_8 + (k_8k_{11} - k_7k_{12})\omega_5 L}{2}\right)\frac{S}{S^2 + (\omega_5 - \omega_1)^2} \\
& + \left(\frac{k_5k_7 - k_6k_8 + k_1k_{11} - k_2k_{12} - (k_7k_{12} + k_8k_{11})\omega_1 L - k_7k_{12}\omega_5 L}{2}\right)\frac{S}{S^2 + (\omega_1 + \omega_5)^2} + \\
& \left(\frac{k_6k_7 + k_5k_8 - k_8k_{11} + k_1k_{12} + k_2k_{11} + (k_7k_{11} - k_8k_{12})\omega_5 L + (k_7k_{11} - k_8k_{12})\omega_1 L}{2}\right) \\
& \cdot \frac{(\omega_1 + \omega_5)}{S^2 + (\omega_1 + \omega_5)^2}\Bigg]
\end{aligned}
$$

$$
\begin{aligned}
&+\left(\frac{k_6k_7 - k_5k_8 + (k_8k_{12} + k_7k_{11})\omega_5 L}{2}\right)\frac{(\omega_5 - \omega_1)}{S^2 + (\omega_5 - \omega_1)^2}\\
&+\left(\frac{k_1k_9 + k_2k_{10} + (k_7k_{10} + k_8k_{10} - k_8k_9)\omega_1 L}{2}\right)\frac{S}{S^2 + (\omega_1 - \omega_3)^2}\\
&+\left(\frac{k_2k_9 - k_1k_{10} + k_7k_9\omega_1 L}{2}\right)\frac{\omega_1 - \omega_3}{S^2 + (\omega_1 - \omega_3)^2}\\
&+\left(\frac{k_5k_9 + k_6k_{10} + (k_{10}k_{11} - k_9k_{12})\omega_5 L}{2}\right)\frac{S}{S^2 + (\omega_5 - \omega_3)^2}\\
&+\left(\frac{k_5k_9 - k_6k_{10} - k_4k_{12} - k_{10}k_{11}(\omega_3 + \omega_5)L - k_9k_{12}\omega_3 L}{2}\right)\cdot\frac{S}{S^2 + (\omega_3 + \omega_5)^2}+\\
&\left(\frac{k_6k_9 + k_4k_{11} + k_3k_{12} + k_3k_{11} + k_5k_{10} - k_9k_{12}\omega_5 L + (k_9k_{11} - k_{10}k_{12})(\omega_3 + \omega_5)L}{2}\right)\\
&\cdot\frac{(\omega_3 + \omega_5)}{S^2 + (\omega_3 + \omega_5)^2} + \left(\frac{k_6k_9 - k_5k_{10} + (k_9k_{11} + k_{10}k_{12})\omega_5 L}{2}\right)\frac{(\omega_5 - \omega_3)}{S^2 + (\omega_5 - \omega_3)^2}\\
&+\left(\frac{k_1k_{11} + k_2k_{12} + (k_7k_{12} - k_8k_{11})\omega_1 L}{2}\right)\frac{S}{S^2 + (\omega_1 - \omega_5)^2}\\
&+\left(\frac{k_2k_{11} - k_1k_{12} + (k_7k_{11} + k_8k_{12})\omega_1 L}{2}\right)\frac{(\omega_1 - \omega_5)}{S^2 + (\omega_1 - \omega_5)^2}\\
&+\left(\frac{k_3k_{11} + k_4k_{12} + (k_9k_{12} - k_{10}k_{11})\omega_3 L}{2}\right)\frac{S}{S^2 + (\omega_3 - \omega_5)^2}\\
&+\left(\frac{k_4k_{11} - k_3k_{12} + (k_9k_{11} + k_{10}k_{12})\omega_3 L}{2}\right)\frac{(\omega_3 - \omega_5)}{S^2 + (\omega_3 - \omega_5)^2}\Bigg]\Bigg\}
\end{aligned}
$$
(4.27)

Then, taking the Laplace Inverse of the equation (4.27) gives the following expression:

$$\mathscr{L}^{-1}\left\{\mathscr{L}\left\{P_{av}\right\}\right\} = P_{av} = \frac{1}{T}\left[p_o t + p_1 Sin2\omega_1 t + p_2(1 - Cos2\omega_1 t) + p_3 Sin2\omega_3 t\right.$$

$$+p_4(1 - Cos2\omega_3 t) + p_5 Sin2\omega_5 t + p_6(1 - Cos2\omega_5 t)$$

$$+p_7 Sin(\omega_1 + \omega_3)t + p_8 Sin(\omega_3 - \omega_1)t$$

$$+p_9(1 - Cos(\omega_1 + \omega_3)t + p_{10}(1 - Cos(\omega_3 - \omega_1)t)$$

$$+p_{11} Sin(\omega_5 - \omega_1)t + p_{12} Sin(\omega_1 + \omega_3)t$$

$$+p_{13}(1 - Cos(\omega_1 + \omega_5)t) + p_{14}(1 - Cos(\omega_3 - \omega_1)t)$$

$$+p_{15} Sin(\omega_1 - \omega_3)t + p_{16}(1 - Cos(\omega_1 - \omega_3)t)$$

$$+p_{17} Sin(\omega_5 - \omega_3)t + p_{18} Sin(\omega_3 + \omega_5)t$$

$$+p_{19}(1 - Cos(\omega_3 + \omega_5)t) + p_{20}(1 - Cos(\omega_5 - \omega_3)t)$$

$$+p_{21} Sin(\omega_1 - \omega_5)t + p_{22}(1 - Cos(\omega_1 - \omega_5)t)$$

$$+p_{23} Sin(\omega_3 - \omega_5)t + p_{24}(1 - Cos(\omega_3 - \omega_5)t)$$

$$(4.28)$$

By rearranging equation (4.28) above, the following general formula produced:

$$P_{av} = \frac{1}{T} \left[p_o t + p_T \right.$$

$$+ p_1 Sin 2\omega_1 t - p_2 Cos 2\omega_1 t$$

$$+ p_3 Sin 2\omega_3 t - p_4 Cos 2\omega_3 t$$

$$+ p_5 Sin 2\omega_5 t - p_6 Cos 2\omega_5 t$$

$$+ p_7 Sin(\omega_1 + \omega_3)t - p_9 Cos(\omega_1 + \omega_3)t$$

$$+ p_8 Sin(\omega_3 - \omega_1)t - p_{10} Cos(\omega_3 - \omega_1)t$$

$$+ p_{11} Sin(\omega_5 + \omega_1)t - p_{14} Cos(\omega_5 + \omega_1)t$$

$$+ p_{12} Sin(\omega_1 + \omega_5)t - p_{13} Cos(\omega_1 - \omega_5)t$$

$$+ p_{15} Sin(\omega_1 - \omega_3)t - p_{16} Cos(\omega_1 - \omega_3)t$$

$$+ p_{18} Sin(\omega_3 + \omega_5)t - p_{19} Cos(\omega_3 + \omega_5)t$$

$$+ p_{17} Sin(\omega_5 - \omega_3)t - p_{20} Cos(\omega_5 - \omega_3)t$$

$$+ p_{21} Sin(\omega_1 - \omega_5)t - p_{22} Cos(\omega_1 - \omega_5)t$$

$$\left. + p_{23} Sin(\omega_3 - \omega_5)t - p_{24} Cos(\omega_3 - \omega_5)t \right]$$

$$(4.29)$$

The values of $p_o, p_T, p_1, p_2, p_3, ..., p_{22}, p_{23}$ and p_{24} are power constants, and can be derived from the voltage and current constants after abbreviation and rearranging equation (4.27), therefore; their values will equal to the following general expressions:

$$p_o = \frac{k_1 k_7 + k_3 k_9 + k_4 k_{10} + k_5 k_{11} + k_6 k_{12}}{2} \qquad (4.30)$$

$$p_1 = \frac{k_1 k_7 - k_8 k_7 \omega_1 L}{4\omega_1} \qquad (4.31)$$

$$p_2 = \frac{k_1 k_8 + k_2 k_7 + (k_7^2 - k_8^2)\omega_1 L}{4\omega_1} \tag{4.32}$$

$$p_3 = \frac{k_3 k_9 - k_4 k_{10} - 2k_9 k_{10}\omega_3 L}{4\omega_3} \tag{4.33}$$

$$p_4 = \frac{k_3 k_{10} + k_4 k_9 + (k_9^2 - k_{10}^2)\omega_3 L}{4\omega_3} \tag{4.34}$$

$$p_5 = \frac{k_5 k_{11} - k_6 k_{12} - 2k_{11} k_{12}\omega_5 L}{4\omega_5} \tag{4.35}$$

$$p_6 = \frac{k_5 k_{12} + k_6 k_{11} + (k_{11}^2 - k_{12}^2)\omega_5 L}{4\omega_5} \tag{4.36}$$

$$p_7 = \frac{k_1 k_9 - k_2 k_{10} + k_3 k_7 - k_4 k_8 - (k_7 k_{10} + k_8 k_9)(\omega_1 + \omega_3)L}{2(\omega_1 + \omega_3)} \tag{4.37}$$

$$p_8 = \frac{k_3 k_7 + k_4 k_8 + (k_8 k_9 - k_7 k_{10})\omega_3 L}{2(\omega_3 - \omega_1)} \tag{4.38}$$

$$p_9 = \frac{k_1 k_{10} + k_2 k_9 + k_3 k_8 + k_4 k_7 - (k_9 + k_{10})k_8 \omega_1 L + k_7 k_9 \omega_3 L - k_8 k_{10}\omega_5 L}{2(\omega_1 + \omega_3)} \tag{4.39}$$

$$p_{10} = \frac{-k_3 k_8 + k_4 k_7 + (k_7 + k_8)k_9 \omega_3 L}{2(\omega_3 - \omega_1)} \tag{4.40}$$

$$p_{11} = \frac{k_5 k_7 + k_6 k_8 + (k_8 k_{11} - k_7 k_{12})\omega_5 L}{2(\omega_5 - \omega_1)} \tag{4.41}$$

$$p_{12} = \frac{k_1 k_{11} - k_2 k_{12} + k_5 k_7 - k_6 k_8 - (k_7 k_{12} + k_8 k_{11})\omega_1 L - k_7 k_{12}\omega_5 L}{2(\omega_1 + \omega_5)} \tag{4.42}$$

128

$$p_{13} = \frac{k_1k_{12} + k_2k_{11} + k_5k_8 + k_6k_7 - k_8k_{11} + (k_7k_{11} - k_8k_{12})\omega_1 L + (k_7k_{11} - k_8k_{12})\omega_5 L}{2(\omega_1 + \omega_5)}$$

$$\text{(4.43)}$$

$$p_{14} = \frac{-k_5k_8 + k_6k_7 + (k_8k_{12} + k_7k_{11})\omega_5 L}{2(\omega_5 - \omega_1)} \tag{4.44}$$

$$p_{15} = \frac{k_1k_9 + k_2k_{10} + (k_7k_{10} + k_8k_{10} - k_8k_9)\omega_1 L}{2(\omega_1 - \omega_3)} \tag{4.45}$$

$$p_{16} = \frac{-k_1k_{10} + k_2k_9 + k_7k_9\omega_1 L}{2(\omega_1 - \omega_3)} \tag{4.46}$$

$$p_{17} = \frac{k_5k_9 + k_6k_{10} + (k_{10}k_{11} - k_9k_{12})\omega_5 L}{2(\omega_5 - \omega_3)} \tag{4.47}$$

$$p_{18} = \frac{k_5k_9 - k_6k_{10} - k_4k_{12} - k_9k_{12}\omega_3 L - k_{10}k_{11}(\omega_3 + \omega_5)L}{2(\omega_3 + \omega_5)} \tag{4.48}$$

$$p_{19} = \frac{k_6k_9 + k_4k_{11} + k_3k_{12} + k_3k_{11} + k_5k_{10} - k_9k_{12}\omega_5 L + (k_9k_{11} - k_{10}k_{12})(\omega_3 + \omega_5)L}{2(\omega_3 + \omega_5)}$$

$$\text{(4.49)}$$

$$p_{20} = \frac{-k_5k_{10} + k_6k_9 + (k_9k_{11} + k_{10}k_{12})\omega_5 L}{2(\omega_5 - \omega_3)} \tag{4.50}$$

$$p_{21} = \frac{k_1k_{11} + k_2k_{12} + (k_7k_{12} - k_8k_{11})\omega_1 L}{2(\omega_1 - \omega_5)} \tag{4.51}$$

$$p_{22} = \frac{-k_1k_{12} + k_2k_{11} + (k_7k_{11} + k_8k_{12})\omega_1 L}{2(\omega_1 - \omega_5)} \tag{4.52}$$

$$p_{23} = \frac{k_3k_{11} + k_4k_{12} + (k_9k_{12} - k_{10}k_{11})\omega_3 L}{2(\omega_3 - \omega_5)} \tag{4.53}$$

$$p_{24} = \frac{-k_3 k_{12} + k_4 k_{11} + (k_9 k_{11} + k_{10} k_{12})\omega_3 L}{2(\omega_3 - \omega_5)} \tag{4.54}$$

And the value of p_T is a power constant and its value is equal to the summation of several p-constants as follows:

$$p_T = p_2 + p_4 + p_6 + p_9 + p_{10} + p_{13} + p_{14} + p_{16} + p_{19} + p_{20} + p_{22} + p_{24} \tag{4.55}$$

The values of $k_1, k_2, k_3, ..., k_9, k_{10}$ and k_{12} are constants referred to the amplitudes of all real and imaginary harmonic components of output voltage and current signals.

For simplicity, they can be found directly from **Fast Fourier Transform** (FFT) function using **Matlab software**, after taking the full range signal experimental points for the case under study and multiplying by $\left(\frac{2}{N}\right)$ scaling factor, due to the FFT function formula definition, as shown in the following equation:

$$X[k] = FFT\{x[n]\} = \frac{2}{N} \sum_{n=0}^{N-1} x[n].e^{\frac{-2i\pi nk}{N}} \tag{4.56}$$

Where,

N is the number of sampling points.

$X[k]$ is the frequency domain of any selected variable.

$x[n]$ is the time domain of any selected variable.

n is the time index.

$\frac{k}{N}$ refers to frequency f.

k is the frequency index.

Thus, k_1, k_2, K_3, k_4, k_5 and k_6 are voltage constants and their values equal to,

$$\left.\begin{array}{lll} k_1 = 0.328, & k_2 = -9.0, & k_3 = 0.142 \\[2mm] k_4 = 0.978, & k_5 = -0.1963, & k_6 = -0.498 \end{array}\right\} \qquad (4.57)$$

And $k_7, k_8, k_9, k_{10}, k_{11}$ and k_{12} are current constants and their magnitudes would be as follow,

$$\left.\begin{array}{lll} k_7 = -0.13, & k_8 = -0.75, & k_9 = 0.1 \\[2mm] k_{10} = -3.185 * 10^{-3}, & k_{11} = 0, & k_{12} = 0 \end{array}\right\} \qquad (4.58)$$

Therefore, the values of p constants can be evaluated depending on the values of Equations (4.57) and (4.58) above and found as:

$$p_0 = 15.853 * 10^{-3}, p_T = \frac{0.731 - 0.14\omega_1 L}{\omega_1}$$

$$p_1 = \frac{10.833 * 10^{-3} - 24.604 * 10^{-3}\omega_1 L}{\omega_1}$$

$$p_2 = \frac{0.3583 - 0.1345\omega_1 L}{\omega_1}$$

$$p_3 = \frac{1.488 * 10^{-3} + 0.165 * 10^{-3}\omega_1 L}{\omega_1}$$

$$p_4 = \frac{8.4 * 10^{-3} + 2.679 * 10^{-3}\omega_1 L}{\omega_1}, p_5 = 0$$

$$p_6 = 0, p_7 = \frac{89.4186 * 10^{-3} + 38.386 * 10^{-3}\omega_1 L}{\omega_1}$$

$$p_8 = \frac{-0.187 - 58.21 * 10^{-3}\omega_1 L}{\omega_1}$$

$$p_9 = \frac{0.146 + 2.741 * 10^{-3}\omega_1 L}{\omega_1}$$

$$p_{10} = \frac{-5.754 * 10^{-3} - 8.474 * 10^{-3}\omega_1 L}{\omega_1}$$

$$p_{11} = \frac{49.632 * 10^{-3}}{\omega_1}, p_{12} = \frac{-28.769 * 10^{-3}}{\omega_1}$$

$$p_{13} = \frac{17.671 * 10^{-3}}{\omega_1}, p_{14} = \frac{-10.071 * 10^{-3}}{\omega_1}$$

$$p_{15} = \frac{-15.663 * 10^{-3} - 19.997 * 10^{-3}\omega_1 L}{\omega_1}$$

$$p_{16} = \frac{0.2327 - 3.4183 * 10^{-3}\omega_1 L}{\omega_1}$$

$$P_{17} = \frac{-4.686 * 10^{-3}}{\omega_1}, p_{18} = \frac{-1.3696 * 10^{-3}}{\omega_1}$$

$$p_{19} = \frac{-3.18365 * 10^{-3}}{\omega_1}, p_{20} = \frac{-13.047 * 10^{-3}}{\omega_1}$$

$$p_{21} = p_{22} = p_{23} = p_{24} = 0$$

(4.59)

By considering these values in equation (4.59) above, the general form of average power transfer from MNPCI configuration to IH load after neglecting the zero magnitudes will equal to the following mathematical expression:

$$P_{av} = \frac{1}{T}\left[p_o t + p_T \right.$$

$$+ p_1 \sin 2\omega_1 t - p_2 \cos 2\omega_1 t$$

$$+ p_3 \sin 2\omega_3 t - p_4 \cos 2\omega_3 t$$

$$+ p_7 \sin(\omega_1 + \omega_3)t - p_9 \cos(\omega_1 + \omega_3)t$$

$$+ p_8 \sin(\omega_3 - \omega_1)t - p_{10} \cos(\omega_3 - \omega_1)t$$

$$+ p_{11} \sin(\omega_5 + \omega_1)t - p_{14} \cos(\omega_5 + \omega_1)t$$

$$+ p_{12} \sin(\omega_1 + \omega_5)t - p_{13} \cos(\omega_1 - \omega_5)t$$

$$+ p_{15} \sin(\omega_1 - \omega_3)t - p_{16} \cos(\omega_1 - \omega_3)t$$

$$+ p_{18} \sin(\omega_3 + \omega_5)t - p_{19} \cos(\omega_3 + \omega_5)t$$

$$\left. + p_{17} \sin(\omega_5 - \omega_3)t - p_{20} \cos(\omega_5 - \omega_3)t \right]$$

$$(4.60)$$

As observed experimentally and stated before, the values of $\omega_3 = 3\omega_1$ and $\omega_5 = 5\omega_1$, so ω_3 and ω_5 will be denoted in terms of ω_1. Therefore, by substituting them in equation (4.60) and then simplifying the equation, the transfer power will be as follows in the following formula:
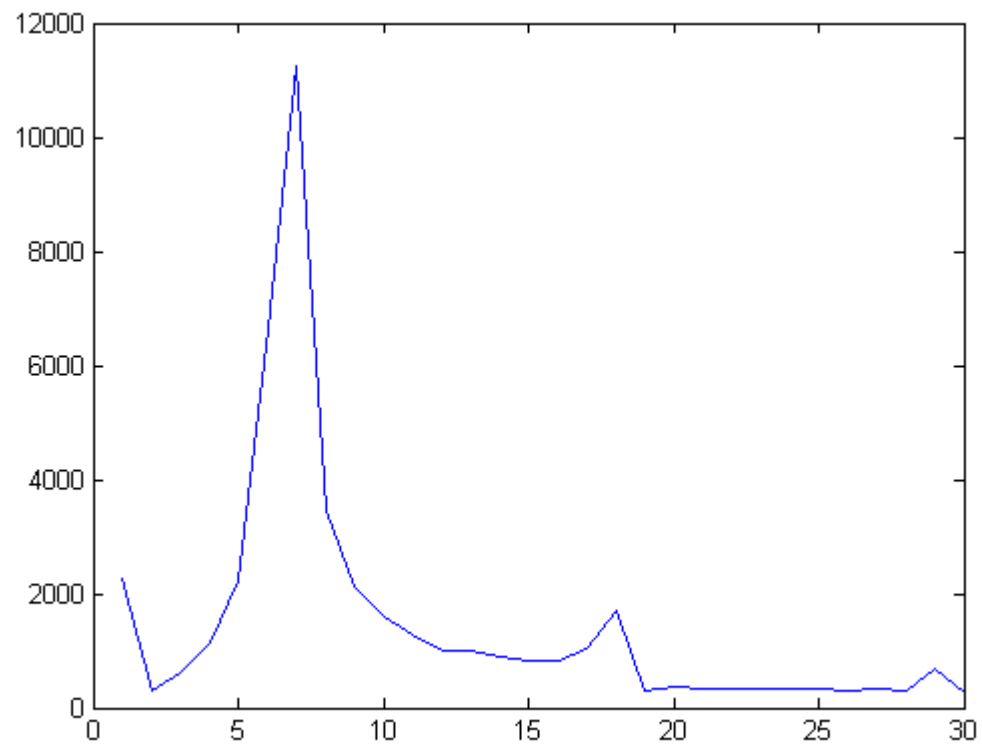
Figure 4.10: Harmonic Components of Output Voltage
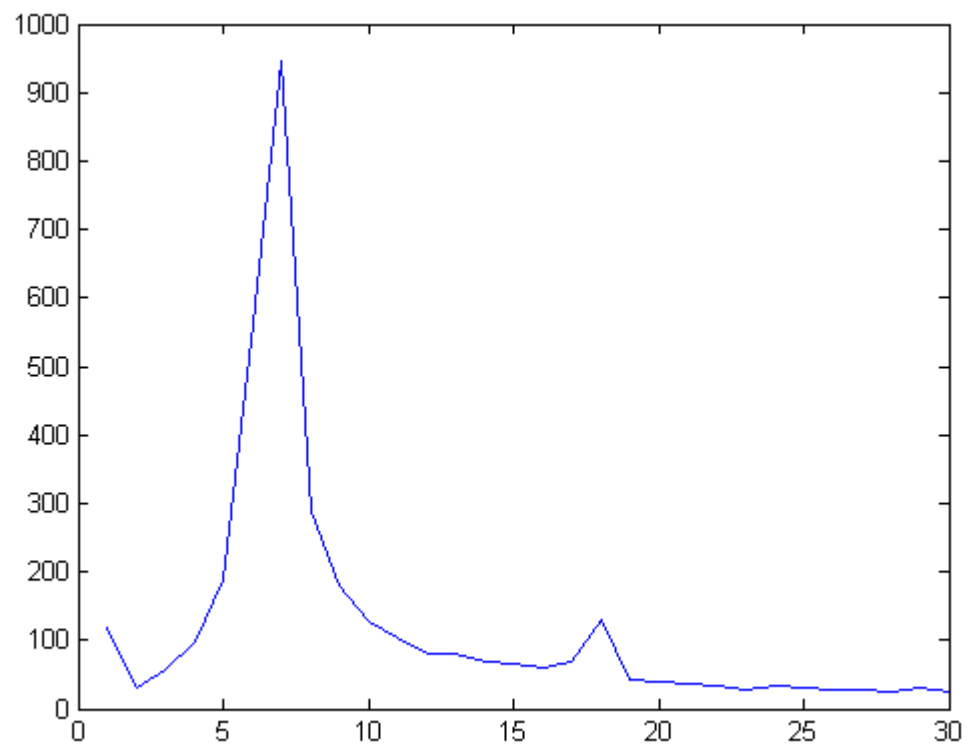
Figure 4.11: Harmonic Components of Output Current

$$P_{av} = \frac{1}{T}\left[p_o t + p_T \right.$$

$$+ p_1 Sin2\omega_1 t - p_2 Cos2\omega_1 t$$

$$+ p_3 Sin6\omega_1 t - p_4 Cos6\omega_1 t$$

$$+ p_7 Sin4\omega_1 t - p_9 Cos4\omega_1 t$$

$$+ p_8 Sin2\omega_1 t - p_{10} Cos2\omega_1 t$$

$$+ p_{11} Sin6\omega_1 t - p_{14} Cos6\omega_1 t$$

$$+ p_{12} Sin6\omega_1 t - p_{13} Cos4\omega_1 t$$

$$- p_{15} Sin2\omega_1 t - p_{16} Cos2\omega_1 t$$

$$+ p_{18} Sin8\omega_1 t - p_{19} Cos8\omega_1 t$$

$$\left. + p_{17} Sin2\omega_1 t - p_{20} Cos2\omega_1 t \right]$$

(4.61)

By simplifying equation (4.61) above, the P_{av} will be transferred to:

$$P_{av} = \frac{1}{T}\left[p_o t + p_T \right.$$

$$+ \left(p_1 + p_8 - p_{15} + p_{17} \right) Sin2\omega_1 t$$

$$- \left(p_2 + p_{10} + p_{16} + p_{20} \right) Cos2\omega_1 t$$

$$+ \left(p_3 + p_{11} + p_{12} \right) Sin6\omega_1 t$$

$$- \left(p_4 + p_{14} \right) Cos6\omega_1 t + p_7 Sin4\omega_1 t$$

$$- \left(p_9 + p_{13} \right) Cos4\omega_1 t$$

$$\left. + p_{18} Sin8\omega_1 t - p_{19} Cos8\omega_1 t \right]$$

(4.62)

135

Therefore, the final form of P_{av} will be denoted as:

$$P_{av} = \frac{1}{T} \left[p_o t + p_T \right.$$

$$+ p_{R1} \sin 2\omega_1 t - p_{R2} \cos 2\omega_1 t$$

$$+ p_7 \sin 4\omega_1 t - p_{R3} \cos 4\omega_1 t$$

$$+ p_{R4} \sin 6\omega_1 t - p_{R5} \cos 6\omega_1 t$$

$$\left. + p_{18} \sin 8\omega_1 t - p_{19} \cos 8\omega_1 t \right]$$

$$(4.63)$$

The value of angular resonant frequency, ω_1 - fundamental is equal to:

$$\omega_1 = 2\pi f_r \qquad (4.64)$$

Where, f_r is the resonant frequency.

And, the p_{R1}, p_{R2}, p_{R3}, p_{R4} and p_{R5} are constants and their values are equal to the following general expressions:

$$p_{R1} = p_1 + p_8 - p_{15} + p_{17} \qquad (4.65)$$

$$p_{R2} = p_2 + p_{10} + p_{16} + p_{20} \qquad (4.66)$$

$$p_{R3} = p_9 + p_{13} \qquad (4.67)$$

$$p_{R4} = p_3 + p_{11} + p_{12} \qquad (4.68)$$

$$p_{R5} = p_4 + p_{14} \qquad (4.69)$$

And according to the equations above, the values of $p_{R1}, ... p_{R5}$ are equal to:

$$\left.\begin{array}{c} p_{R1} = \dfrac{-0.1652 - 62.817 * 10^{-3}\omega_1 L}{\omega_1} \\[2mm] p_{R2} = \dfrac{0.5722 - 0.1464\omega_1 L}{\omega_1} \\[2mm] p_{R3} = \dfrac{0.16367 + 2.741 * 10^{-3}\omega_1 L}{\omega_1} \\[2mm] p_{R4} = \dfrac{22.351 * 10^{-3} + 0.165 * 10^{-3}\omega_1 L}{\omega_1} \\[2mm] p_{R5} = \dfrac{-1.671 * 10^{-3} + 2.679 * 10^{-3}\omega_1 L}{\omega_1} \end{array}\right\} \qquad (4.70)$$

From Equations (4.59) and (4.70) above, it can be clearly deduced that the average power of load, P_{av} depends mainly on the fundamental angular resonant frequency ω_1 and on the parallel inductance L.

While, increasing the equivalent resistance gradually from 3.37Ω to 22.07Ω of IH load tank means in IH changing the material resistance and decreasing the effective cross sectional area of the workpiece, as shown in Fig. 4.3 and according to the law stated in Equation 4.15 before, and the corresponding experimental frequency vs inductance change at different resistances is shown in Fig. 4.12.

The efficiency of proposed MNPCI configuration with respect to switching frequency is clarified in Fig. 4.13, which clearly reveals that the efficiency directly affected by the switching frequency magnitude. The graph also shows that the efficiency curve starts from 64% at switching frequency of $3.06kHz$, then it begins to increase gradually until it reaches 81% at $f = 5.4kHz$, the starts again to increase towards its peak value of about 85% at the operational point that achieves the resonant state of $f = 5.57kHz$, then it begins to decrease gradually step by step until reaches the minimal point of only 9% at $f = 7.59kHz$.

137
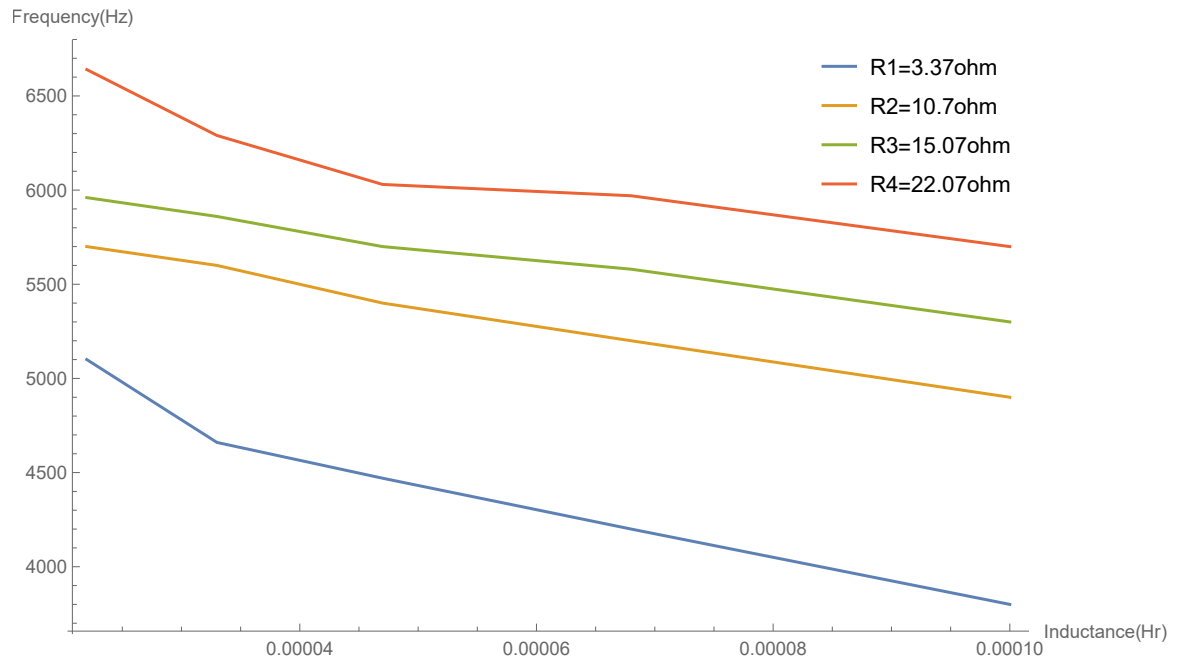
Figure 4.12: Prototype Frequency Response at Different Load Values
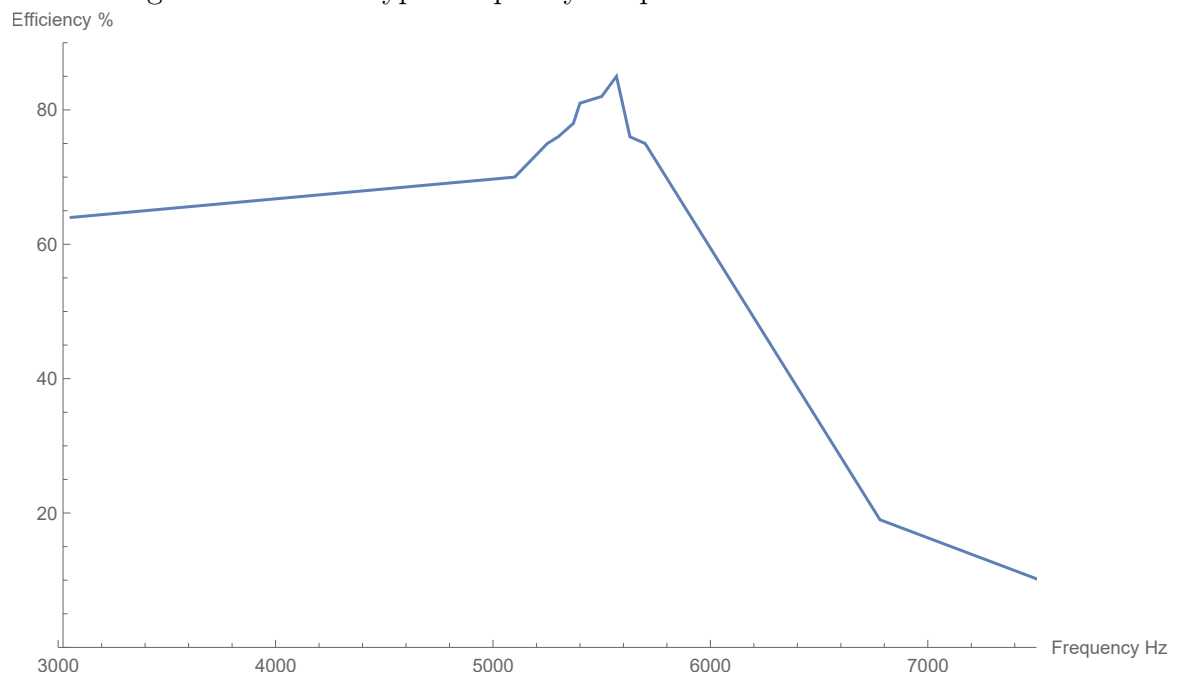
Figure 4.13: Efficiency Versus Frequency

4.5 Power Harmonic Analysis

The ideal output signal $v(t)$ produced from MNPCI prototype under the four opera-
tional modes of Table 3.1 is shown in figure 4.14. To analyse this signal as a periodic
waveform obtained from experimental job in time domain, the Fourier Series is very es-
sential at this point, in order to find the spectrum of the signal especially at any circuit
operating point and to identify the harmonic content of the signal of the proposed system.

Therefore, in the following section, there will be an intensive analysis to the harmonic
distortion content of the signal, so that it will be very easy to understand the control
strategy well:

4.6 The Calculation of Fourier Series of $v(t)$ as a 'Pe-

riodic Signal'

To analyse the output waveform of voltage $v(t)$ as a periodic waveform, the Fourier Series
is the main key for two main reasons, first: to obtain the signal spectra especially at
the circuit operational point in order to identify the harmonic content of the signal and
second, as a consequence, will attain the optimum operating point of proposed MNPCI
system, which ensures minimum harmonic distortion and hence optimum harmonic con-
trol for power transfer from MNPCI supply to IH load.

Therefore, starting from the law of Fourier Series in time domain as a periodic func-
tion, as in the following general formula [97]:

$$g(t) = a_o + \sum_{n=0}^{m}(a_n Cos(n\omega t) + b_n Sin(n\omega t)) \tag{4.71}$$

Where, $g(t)$ is the Fourier Series equivalent function of $v(t)$ and,

$$\omega = 2\pi f \tag{4.72}$$
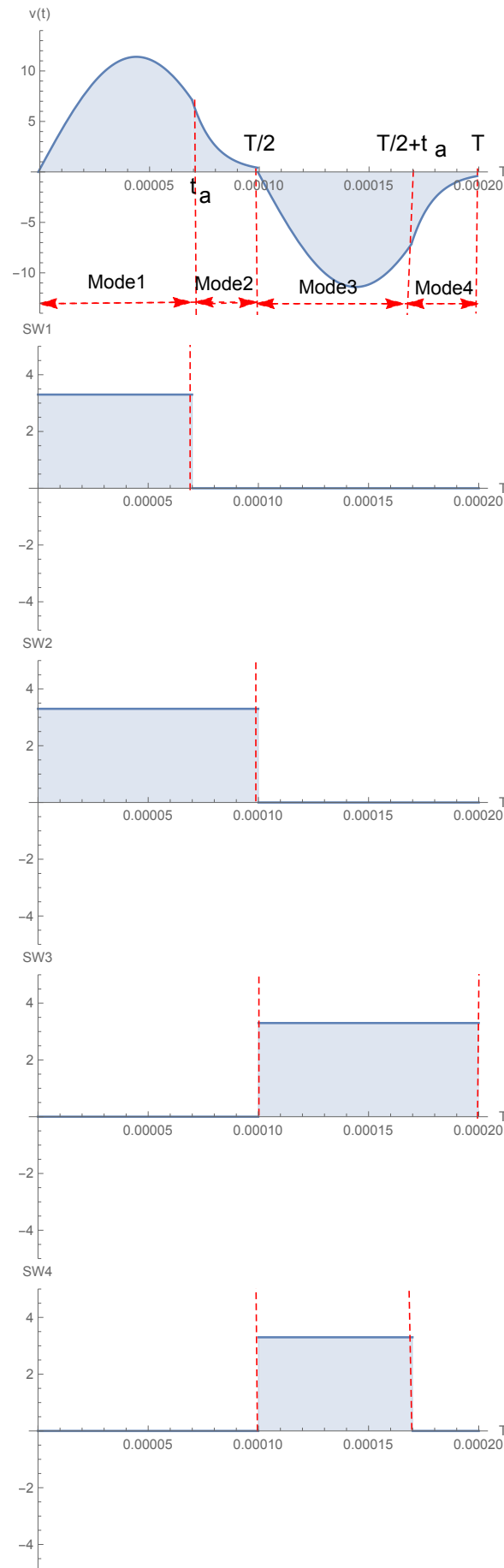
Figure 4.14: Output Signal $v(t)$

With a_o a_n and b_n are Fourier Series amplitude coefficients and they are given by the following equations:

$$a_o = \frac{1}{T} \int_0^T v(t)dt \qquad (4.73)$$

$$a_n = \frac{2}{T} \int_0^T v(t)Cos(n\omega t)dt \qquad (4.74)$$

$$b_n = \frac{2}{T} \int_0^T v(t)Sin(n\omega t)dt \qquad (4.75)$$

While, the output voltage $v(t)$ will equal to the following succession segments over the overall period from $0 \longrightarrow T$ interval,

$$v(t) = \begin{cases} V_p.Sin\left(2\pi f_n t\right) & \text{for } (0 < t \leq t_\alpha), \\ V_s.e^{-\frac{t-t_\alpha}{\tau}} & \text{for } \left(t_\alpha < t \leq \frac{T}{2}\right), \\ V_p. - Sin\left(2\pi f_n\left(t - \frac{T}{2}\right)\right) & \text{for } \left(\frac{T}{2} < t \leq \frac{T}{2} + t_\alpha\right), \\ V_s. - e^{-\frac{t-(\frac{T}{2}+t_\alpha)}{\tau}} & \text{for } \left(\frac{T}{2} + t_\alpha < t \leq T\right). \end{cases} \qquad (4.76)$$

By applying the equation (4.76) in the equation (4.73), then yield

$$a_o = \frac{1}{T}\int_0^T v(t)dt = \frac{1}{T}\left[\int_0^{t_\alpha} v(t)dt + \int_{t_\alpha}^{\frac{T}{2}} v(t)dt + \int_{\frac{T}{2}}^{\frac{T}{2}+t_\alpha} v(t)dt + \int_{\frac{T}{2}+t_\alpha}^{T} v(t)dt\right]$$

$$= \frac{1}{T}\left[\int_0^{t_\alpha} V_p.Sin\left(2\pi f_n t\right)dt + \int_{t_\alpha}^{\frac{T}{2}} V_s.e^{-\frac{t-t_\alpha}{\tau}}dt\right.$$

$$- \int_{\frac{T}{2}}^{\frac{T}{2}-t_\alpha} V_p.Sin\left(2\pi f_n\left(t-\frac{T}{2}\right)\right)dt$$

$$\left. - \int_{\frac{T}{2}+t_\alpha}^{T} V_s.e^{-\frac{t-\left(\frac{T}{2}+t_\alpha\right)}{\tau}}dt\right] = 0$$

$$(4.77)$$

The a_o coefficient stands for the mean value of Fourier Series function (or as electrical

definition it is the DC component) of the output signal function and mathematically it

equals the average value of the area under the curve of the $v(t)$ function, and as the two

periods of operational modes are symmetrical above (for +ve cycle) and below (for -ve

cycle) the horizontal axis of time domain over the periodic interval of T, then the value

of a_o equals zero.

4.6.1   The calculation of a_n amplitude coefficient:

Starting from equation(4.74) above, then the value of a_n coefficient will be given by:

$$a_n = \frac{2}{T} \int_0^T v(t) Cos(n\omega t) dt$$

$$= \frac{2}{T} \left[\int_0^{t_\alpha} V_p.Sin(2\pi f_n t).Cos(2\pi n f t) dt \right.$$

$$+ \int_{t_\alpha}^{\frac{T}{2}} V_s.e^{-\left(\frac{t-t_\alpha}{\tau}\right)}.Cos(2\pi n f t) dt$$

$$- \int_{\frac{T}{2}}^{\frac{T}{2}+t_\alpha} V_p.Sin\left(2\pi f_n \left(t - \frac{T}{2}\right)\right).Cos(2\pi n f t) dt$$

$$\left. - \int_{\frac{T}{2}+t_\alpha}^{T} V_s.e^{-\frac{t-\left(\frac{T}{2}+t_\alpha\right)}{\tau}}.Cos(2\pi n f t) dt \right]$$

$$(4.78)$$

By referring each Sine and Cosine functions in equation (4.78) into their relation with the complex exponential function, then the following exponential expression formula is formed:

$$a_n = \frac{2}{T} \left[V_p \int_0^{t_\alpha} \left(\frac{e^{2i\pi f_n t} - e^{-2i\pi f_n t}}{2i} \right) \cdot \left(\frac{e^{2i\pi n f t} + e^{-2i\pi n f t}}{2} \right) dt \right.$$

$$-V_p \int_{\frac{T}{2}}^{\frac{T}{2}+t_\alpha} \left(\frac{e^{2i\pi f_n \left(t-\frac{T}{2}\right)} - e^{-2i\pi f_n \left(t-\frac{T}{2}\right)}}{2i} \right) \cdot \left(\frac{e^{2i\pi n f t} + e^{-2i\pi n f t}}{2} \right) dt$$

$$+V_s \int_{t_\alpha}^{\frac{T}{2}} e^{-\left(\frac{t-t_\alpha}{\tau}\right)} \cdot \left(\frac{e^{2i\pi n f t} + e^{-2i\pi n f t}}{2} \right) dt$$

$$\left. -V_s \int_{\frac{T}{2}+t_\alpha}^{T} e^{-\frac{t-\left(\frac{T}{2}+t_\alpha\right)}{\tau}} \cdot \left(\frac{e^{2i\pi n f t} + e^{-2i\pi n f t}}{2} \right) dt \right]$$

$$(4.79)$$

Then, with distributing the exponential functions in equation (4.79) with each other, the following integration formulas are produced:

$$a_n = \frac{1}{T} \left[\frac{V_p}{2i} \cdot \left[\int_0^{t_\alpha} e^{2i\pi(nf+f_n)t} dt + \int_0^{t_\alpha} e^{-2i\pi(nf-f_n)t} dt \right. \right.$$

$$- \int_0^{t_\alpha} e^{2i\pi(nf-f_n)t} dt - \int_0^{t_\alpha} e^{-2i\pi(nf+f_n)t} dt$$

$$- \int_{\frac{T}{2}}^{\frac{T}{2}+t_\alpha} e^{i(2\pi(nf+f_n)t-\pi f_n T)} dt - \int_{\frac{T}{2}}^{\frac{T}{2}+t_\alpha} e^{i(2\pi(nf-f_n)t+\pi f_n T)} dt$$

$$\left. + \int_{\frac{T}{2}}^{\frac{T}{2}+t_\alpha} e^{i(2\pi(nf-f_n)+\pi f_n T)} dt + \int_{\frac{T}{2}}^{\frac{T}{2}+t_\alpha} e^{-i(2\pi(nf+f_n)-\pi f_n T)} dt \right]$$

$$+ Vs \left[\int_{t_\alpha}^{\frac{T}{2}} e^{\frac{t_\alpha+(2i\pi\tau nf-1)t}{\tau}} dt + \int_{t_\alpha}^{\frac{T}{2}} e^{\frac{t_\alpha-(2i\pi\tau nf+1)t}{\tau}} dt \right.$$

$$\left. \left. - \int_{t_\alpha}^{\frac{T}{2}} e^{\frac{\left(\frac{T}{2}+t_\alpha\right)+(2i\pi\tau nf-1)t}{\tau}} dt - \int_{t_\alpha}^{\frac{T}{2}} e^{\frac{\left(\frac{T}{2}+t_\alpha\right)-(2i\pi\tau nf+1)t}{\tau}} dt \right] \right]$$

$$(4.80)$$

And, then by taking the integration of each term under the time interval being indicated

in equation (4.80), then the expression will be as:

$$a_n = \frac{1}{T}\left[\frac{-V_p}{4\pi}\cdot\left[\frac{1}{(nf+f_n)}\cdot\left(e^{2i\pi(nf+f_n)t_\alpha} - e^0\right)\right.\right.$$

$$-\frac{1}{(nf-f_n)}\left(e^{-2i\pi(nf-f_n)t_\alpha} - e^0\right) - \frac{1}{(nf-f_n)}\cdot\left(e^{2i\pi(nf-f_n)t_\alpha} - e^0\right)$$

$$+\frac{1}{(nf+f_n)}\left(e^{-2i\pi(nf+f_n)t_\alpha} - e^0\right)$$

$$-\frac{1}{(nf+f_n)}\left(e^{i\pi\left(2(nf+f_n)\left(\frac{T}{2}+t_\alpha\right)-f_nT\right)} - e^{i\pi\left(2(nf+f_n)\left(\frac{T}{2}\right)-f_nT\right)}\right)$$

$$+\frac{1}{(nf-f_n)}\left(e^{-i\pi\left(2(nf-f_n)\left(\frac{T}{2}+t_\alpha\right)+f_nT\right)} - e^{-i\pi\left(2(nf-f_n)\left(\frac{T}{2}\right)+f_nT\right)}\right)$$

$$+\frac{1}{(nf-f_n)}\left(e^{i\pi\left(2(nf-f_n)\left(\frac{T}{2}+t_\alpha\right)+f_nT\right)} - e^{i\pi\left(2(nf-f_n)\left(\frac{T}{2}\right)+f_nT\right)}\right)$$

$$\left.-\frac{1}{(nf+f_n)}\left(e^{-i\pi\left(2(nf+f_n)\left(\frac{T}{2}+t_\alpha\right)-f_nT\right)} - e^{-i\pi\left(2(nf+f_n)\left(\frac{T}{2}\right)-f_nT\right)}\right)\right]$$

$$+V_s\tau.\left[\frac{1}{(2i\pi\tau nf-1)}\cdot\left(e^{\frac{t_\alpha+(2i\pi\tau nf-1)\left(\frac{T}{2}\right)}{\tau}} - e^{\frac{t_\alpha+(2i\pi\tau nf-1)t_\alpha}{\tau}}\right)\right.$$

$$-\frac{1}{(2i\pi\tau nf+1)}\left(e^{\frac{t_\alpha-(2i\pi\tau nf+1)\left(\frac{T}{2}\right)}{\tau}} - e^{\frac{t_\alpha-(2i\pi\tau nf+1)t_\alpha}{\tau}}\right)$$

$$-\frac{1}{(2i\pi\tau nf-1)}\left(e^{\frac{\left(\frac{T}{2}+t_\alpha\right)+(2i\pi\tau nf-1)T}{\tau}} - e^{\frac{\left(\frac{T}{2}+t_\alpha\right)+(2i\pi\tau nf-1)\left(\frac{T}{2}+t_\alpha\right)}{\tau}}\right)$$

$$\left.\left.\left.-\frac{1}{(2i\pi\tau nf+1)}\left(e^{\frac{\left(\frac{T}{2}+t_\alpha\right)-(2i\pi\tau nf+1)T}{\tau}} - e^{\frac{\left(\frac{T}{2}+t_\alpha\right)-(2i\pi\tau nf+1)\left(\frac{T}{2}+t_\alpha\right)}{\tau}}\right)\right]\right]\right]$$

$$(4.81)$$

From equation (4.81) above, by taking the terms '$(nf+f_n)(nf-f_n)$' for upper Sine representation functions as a common, and the terms '$(2i\pi\tau nf-1)(2i\pi\tau nf+1)$' for the lower exponential representation functions as a common also, then the equation will be transformed to the following expression

$$a_n = \frac{1}{T}\left[\frac{-V_p}{4\pi(nf+f_n)(nf-f_n)}\cdot\left[(nf-f_n)\left(e^{2i\pi(nf+f_n)t_\alpha}-1\right)\right.\right.$$

$$-(nf+f_n)\left(e^{-2i\pi(nf-f_n)t_\alpha}-1\right)-(nf+f_n)\left(e^{2i\pi(nf-f_n)t_\alpha}-1\right)$$

$$+(nf-f_n)\left(e^{-2i\pi(nf+f_n)t_\alpha}-1\right)-(nf-f_n)e^{i\pi\left(2(nf+f_n)\left(\frac{T}{2}+t_\alpha\right)-f_nT\right)}$$

$$+(nf-f_n)e^{i\pi\left(2(nf+f_n)\left(\frac{T}{2}\right)-f_nT\right)}+(nf+f_n)e^{-i\pi\left(2(nf-f_n)\left(\frac{T}{2}+t_\alpha\right)+f_nT\right)}$$

$$-(nf+f_n)e^{-i\pi\left(2(nf-f_n)\left(\frac{T}{2}\right)+f_nT\right)}+(nf+f_n)e^{i\pi\left(2(nf-f_n)\left(\frac{T}{2}+t_\alpha\right)+f_nT\right)}$$

$$-(nf+f_n)e^{i\pi\left(2(nf-f_n)\left(\frac{T}{2}\right)+f_nT\right)}-(nf-f_n)e^{-i\pi\left(2(nf+f_n)\left(\frac{T}{2}+t_\alpha\right)-f_nT\right)}$$

$$\left.+(nf-f_n)e^{i\pi\left(2(nf+f_n)\left(\frac{T}{2}\right)-f_nT\right)}\right]$$

$$+\frac{V_s\tau}{(2i\pi\tau nf-1)(2i\pi\tau nf+1)}\cdot\left[(2i\pi\tau nf+1)e^{-\left(\frac{\frac{T}{2}-t_\alpha}{\tau}\right)}e^{i\pi nfT}\right.$$

$$-(2i\pi\tau nf+1)e^{2i\pi nft_\alpha}-(2i\pi\tau nf-1)e^{-\left(\frac{\frac{T}{2}-t_\alpha}{\tau}\right)}e^{-i\pi nfT}$$

$$+(2i\pi\tau nf-1)e^{-2i\pi nft_\alpha}-(2i\pi\tau nf+1)e^{-\left(\frac{\frac{T}{2}-t_\alpha}{\tau}\right)}e^{2i\pi nfT}$$

$$+(2i\pi\tau nf+1)e^{2i\pi nf\left(\frac{T}{2}+t_\alpha\right)}+(2i\pi\tau nf-1)e^{-\left(\frac{\frac{T}{2}-t_\alpha}{\tau}\right)}e^{-2i\pi nfT}$$

$$\left.\left.-(2i\pi\tau nf-1)e^{-2i\pi nf\left(\frac{T}{2}+t_\alpha\right)}\right]\right]$$

$$\tag{4.82}$$

Then, rearranging equation (4.82) by assembling each two similar exponential terms altogether, as in the following mathematical steps:

$$
\begin{aligned}
a_n = \frac{1}{T}\Bigg[& \frac{-V_p}{4\pi\left(n^2 f^2 - f_n^2\right)} \cdot \Bigg[2(nf - f_n)\left(\frac{e^{2i\pi(nf+f_n)t_\alpha} + e^{-2i\pi(nf+f_n)t_\alpha}}{2} \right) \\
& -2(nf + f_n)\left(\frac{e^{2i\pi(nf-f_n)t_\alpha} + e^{-2i\pi(nf-f_n)t_\alpha}}{2} \right) \\
& -(nf - f_n) + (nf + f_n) + (nf + f_n) - (nf - f_n) \\
-2(nf - f_n)&\left(\frac{e^{i\pi\left(2(nf+f_n)\left(\frac{T}{2}+t_\alpha\right)-f_n T\right)} + e^{-i\pi\left(2(nf+f_n)\left(\frac{T}{2}+t_\alpha\right)-f_n T\right)}}{2} \right) \\
+2(nf + f_n)&\left(\frac{e^{i\pi\left(2(nf-f_n)\left(\frac{T}{2}+t_\alpha\right)+f_n T\right)} + e^{-i\pi\left(2(nf-f_n)\left(\frac{T}{2}+t_\alpha\right)+f_n T\right)}}{2} \right) \\
+2(nf - f_n)&\left(\frac{e^{i\pi\left(2(nf+f_n)\left(\frac{T}{2}\right)-f_n T\right)} + e^{-i\pi\left(2(nf+f_n)\left(\frac{T}{2}\right)-f_n T\right)}}{2} \right) \\
-2(nf + f_n)&\left(\frac{e^{i\pi\left(2(nf-f_n)\left(\frac{T}{2}\right)+f_n T\right)} + e^{-i\pi\left(2(nf-f_n)\left(\frac{T}{2}\right)+f_n T\right)}}{2} \right) \Bigg] \\[2ex]
+ \frac{V_s \tau}{\left(-4\pi^2\tau^2 n^2 f^2 - 1\right)}&\Bigg[-(2i\pi\tau nf + 1)e^{-\left(\frac{\frac{T}{2}-t_\alpha}{\tau}\right)}\left(e^{2i\pi nfT} - e^{i\pi nfT} \right) \\
& -(2i\pi\tau nf - 1)e^{-\left(\frac{\frac{T}{2}-t_\alpha}{\tau}\right)}\left(e^{-2i\pi nfT} - e^{-i\pi nfT} \right) \\
& +(2i\pi\tau nf + 1)e^{2i\pi nf t_\alpha}\left(e^{i\pi nfT} - 1 \right) \\
& -(2i\pi\tau nf - 1)e^{-2i\pi nf t_\alpha}\left(e^{-i\pi nfT} - 1 \right) \Bigg]\Bigg]
\end{aligned}
$$

$$(4.83)$$

By using the exponential definition of the Cosine function in equation(4.83), the final

a_n picture will equal to the following formula:

$$
\begin{aligned}
a_n = \frac{1}{T}\Bigg[& \frac{V_p}{2\pi\left(n^2 f^2 - f_n^2\right)} \cdot \Bigg[-(nf - f_n)Cos(2\pi(nf + f_n)t_\alpha) \\
& +(nf + f_n)Cos(2\pi(nf - f_n)t_\alpha) - 2f_n \\
& +(nf - f_n)Cos\left(\pi\left(2(nf + f_n)\left(\frac{T}{2} + t_\alpha\right) - f_n T\right)\right) \\
& -(nf + f_n)Cos\left(\pi\left(2(nf - f_n)\left(\frac{T}{2} + t_\alpha\right) + f_n T\right)\right) \\
& +2f_n Cos\left(\pi n f T\right) \Bigg] \\
& +\frac{V_s \tau}{(4\pi^2\tau^2 n^2 f^2 + 1)}\cdot\Bigg[(2i\pi\tau nf + 1)e^{-\left(\frac{\frac{T}{2}-t_\alpha}{\tau}\right)}\left(e^{2i\pi nfT} - e^{i\pi nfT}\right) \\
& -(2i\pi\tau nf - 1)e^{-\left(\frac{\frac{T}{2}-t_\alpha}{\tau}\right)}\left(e^{-2i\pi nfT} - e^{-i\pi nfT}\right) \\
& +(2i\pi\tau nf + 1)e^{2i\pi nft_\alpha}\left(1 - e^{i\pi nfT}\right) \\
& -(2i\pi\tau nf - 1)e^{2i\pi nft_\alpha}\left(1 - e^{-i\pi nfT}\right) \Bigg] \Bigg]
\end{aligned}
$$

$$(4.84)$$

4.6.2   The calculation of b_n amplitude coefficient:

Returning to the general representation of b_n in equation (4.75) stated before, the b_n will equal to the integration of the four-segment parts of output voltage waveform, $v(t)$ over the time shown in each period, as in the following expression

$$b_n = \frac{2}{T} \int_0^T v(t) Sin(n\omega t) dt$$

$$= \frac{2}{T} \left[\int_0^{t_\alpha} V_p . Sin(2\pi f_n t) . Sin(2\pi n f t dt) \right.$$

$$+ \int_{t_\alpha}^{\frac{T}{2}} V_s . e^{-\left(\frac{t-t_\alpha}{\tau}\right)} . Sin(2\pi n f t) dt$$

$$- \int_{\frac{T}{2}}^{\frac{T}{2}+t_\alpha} V_p . Sin\left(2\pi f \left(t - \frac{T}{2}\right)\right) . Sin(2\pi n f t) dt$$

$$\left. - \int_{\frac{T}{2}+t_\alpha}^{T} V_s . e^{-\left(\frac{t-\left(\frac{T}{2}+t_\alpha\right)}{\tau}\right)} . Sin(2\pi n f t) dt \right] \qquad (4.85)$$

With the retrieval of Sine function representation as a complex exponential function into equation (4.85), then the following exponential expression formula of b_n is formed:

$$b_n = \frac{2}{T} \left[V_p \int_0^{t_\alpha} \left(\frac{e^{2i\pi f_n t} - e^{-2i\pi f_n t}}{2i}\right) \left(\frac{e^{2i\pi n f t} - e^{-2i\pi n f t}}{2i}\right) dt \right.$$

$$+ V_s \int_{t_\alpha}^{\frac{T}{2}} e^{-\left(\frac{t-t_\alpha}{\tau}\right)} \left(\frac{e^{2i\pi n f t} - e^{-2i\pi n f t}}{2i}\right) dt$$

$$- V_p \int_{\frac{T}{2}}^{\frac{T}{2}+t_\alpha} \left(\frac{e^{2i\pi f_n \left(t - \frac{T}{2}\right)} - e^{-2i\pi f_n \left(t - \frac{T}{2}\right)}}{2i}\right) \left(\frac{e^{2i\pi n f t} - e^{-2i\pi n f t}}{2i}\right) dt$$

$$\left. - V_s \int_{\frac{T}{2}+t_\alpha}^{T} e^{-\left(\frac{t-\left(\frac{T}{2}+t_\alpha\right)}{\tau}\right)} \left(\frac{e^{2i\pi n f t} - e^{-2i\pi n f t}}{2i}\right) dt \right]$$

$$(4.86)$$

Then, with distributing the exponential functions in equation (4.86) by each other,

the following b_n-integration formulas are produced:

$$b_n = \frac{2}{T}\left[\frac{-V_p}{4}\cdot\left[\int_0^{t_\alpha} e^{2i\pi f_n t}.e^{2i\pi n f t}dt - \int_0^{t_\alpha} e^{2i\pi f_n t}.e^{-2i\pi n f t}dt\right.\right.$$

$$\left.-\int_0^{t_\alpha} e^{-2i\pi f_n t}.e^{2i\pi n f t}dt + \int_0^{t_\alpha} e^{-2i\pi f_n t}.e^{-2i\pi n f t}dt\right]$$

$$+\frac{V_p}{4}\cdot\left[\int_{\frac{T}{2}}^{\frac{T}{2}+t_\alpha} e^{2i\pi f_n\left(t-\frac{T}{2}\right)}.e^{2i\pi n f t}dt - \int_{\frac{T}{2}}^{\frac{T}{2}+t_\alpha} e^{2i\pi f_n\left(t-\frac{T}{2}\right)}.e^{-2i\pi n f t}dt\right.$$

$$\left.-\int_{\frac{T}{2}}^{\frac{T}{2}+t_\alpha} e^{-2i\pi f_n\left(t-\frac{T}{2}\right)}.e^{2i\pi n f t}dt + \int_{\frac{T}{2}}^{\frac{T}{2}+t_\alpha} e^{-2i\pi f_n\left(t-\frac{T}{2}\right)}.e^{-2i\pi n f t}dt\right]$$

$$+\frac{V_s}{2i}\left[\int_{t_\alpha}^{\frac{T}{2}} e^{-\left(\frac{t-t_\alpha}{\tau}\right)}.e^{2i\pi n f t}dt - \int_{t_\alpha}^{\frac{T}{2}} e^{-\left(\frac{t-t_\alpha}{\tau}\right)}.e^{-2i\pi n f t}dt\right]$$

$$-\frac{V_s}{2i}\left[\int_{\frac{T}{2}+t_\alpha}^{T} e^{-\left(\frac{t-\left(\frac{T}{2}+t_\alpha\right)}{\tau}\right)}.e^{2i\pi n f t}dt - \int_{\frac{T}{2}+t_\alpha}^{T} e^{-\left(\frac{t-\left(\frac{T}{2}+t_\alpha\right)}{\tau}\right)}.e^{-2i\pi n f t}dt\right]\right]$$

$$(4.87)$$

Then, by combining the power root of the exponentials of (4.87) altogether, then the

following equation formed:

$$b_n = \frac{2}{T} \left[\frac{-V_p}{4} \cdot \left[\int_0^{t_\alpha} e^{2i\pi(nf+f_n)t} dt - \int_0^{t_\alpha} e^{-2i\pi(nf-f_n)t} dt \right. \right.$$

$$\left. - \int_0^{t_\alpha} e^{2i\pi(nf-f_n)t} dt + \int_0^{t_\alpha} e^{-2i\pi(nf+f_n)t} dt \right]$$

$$+ \frac{V_p}{4} \cdot \left[\int_{\frac{T}{2}}^{\frac{T}{2}+t_\alpha} e^{2i\pi(nf+f_n)t - i\pi f_n T} dt - \int_{\frac{T}{2}}^{\frac{T}{2}+t_\alpha} e^{-2i\pi(nf-f_n)t - i\pi f_n T} dt \right.$$

$$\left. - \int_{\frac{T}{2}}^{\frac{T}{2}+t_\alpha} e^{2i\pi(nf-f_n)t + i\pi f_n T} dt + \int_{\frac{T}{2}}^{\frac{T}{2}+t_\alpha} e^{-2i\pi(f+f_n)t + i\pi f_n T} dt \right]$$

$$+ \frac{V_s}{2i} \cdot \left[\int_{t_\alpha}^{\frac{T}{2}} e^{\frac{t_\alpha + (2i\pi\tau nf - 1)t}{\tau}} dt - \int_{t_\alpha}^{\frac{T}{2}} e^{\frac{t_\alpha - (2i\pi\tau nf + 1)t}{\tau}} dt \right]$$

$$\left. - \frac{V_s}{2i} \cdot \left[\int_{\frac{T}{2}+t_\alpha}^{T} e^{\frac{\left(\frac{T}{2}+t_\alpha\right)+(2i\pi\tau nf-1)t}{\tau}} dt - \int_{\frac{T}{2}+t_\alpha}^{T} e^{\frac{\left(\frac{T}{2}+t_\alpha\right)-(2i\pi\tau nf+1)t}{\tau}} dt \right] \right]$$

$$(4.88)$$

Then, with taking the integration of each individual term under the time interval

being indicated in equation (4.88), then the b_n expression will be as:

$$
\begin{aligned}
b_n = \frac{1}{T} &\Bigg[\frac{-V_p}{2} \cdot \Bigg[\frac{1}{2i\pi(nf+f_n)} \left(e^{2i\pi(nf+f_n)t_\alpha} - e^0 \right) \\
& - \frac{1}{-2i\pi(nf-f_n)} \left(e^{-2i\pi(nf-f_n)t_\alpha} - e^0 \right) \\
& - \frac{1}{2i\pi(nf-f_n)} \left(e^{2i\pi(nf-f_n)t_\alpha} - e^0 \right) \\
& + \frac{1}{-2i\pi(nf+f_n)} \left(e^{-2i\pi(nf+f_n)t_\alpha} - e^0 \right) \Bigg] \\
& + \frac{V_p}{2} \cdot \Bigg[\frac{1}{2i\pi(nf+f_n)} \left(e^{2i\pi(nf+f_n)\left(\frac{T}{2}+t_\alpha\right)-i\pi f_n T} - e^{2i\pi(nf+f_n)\left(\frac{T}{2}\right)-i\pi f_n T} \right) \\
& - \frac{1}{-2i\pi(nf-f_n)} \left(e^{-2i\pi(nf-f_n)\left(\frac{T}{2}+t_\alpha\right)-i\pi f_n T} - e^{-2i\pi(nf-voltage f_n)\left(\frac{T}{2}\right)-i\pi f_n T} \right) \\
& - \frac{1}{2i\pi(nf-f_n)} \left(e^{2i\pi(nf-f_n)\left(\frac{T}{2}+t_\alpha\right)+i\pi f_n T} - e^{2i\pi(nf-f_n)\left(\frac{T}{2}\right)+i\pi f_n T} \right) \\
& + \frac{1}{-2i\pi(nf+f_n)} \left(e^{-2i\pi(nf+f_n)\left(\frac{T}{2}+t_\alpha\right)+i\pi f_n T} - e^{-2i\pi(nf+f_n)\left(\frac{T}{2}\right)+i\pi f_n T} \right) \Bigg] \\
& + V_s \cdot \Bigg[\frac{\tau}{-(2\pi\tau nf+i)} \left(e^{\frac{t_\alpha+(2i\pi\tau nf-1)\left(\frac{T}{2}\right)}{\tau}} - e^{\frac{t_\alpha+(2i\pi\tau nf-1)t_\alpha}{\tau}} \right) \\
& - \frac{\tau}{(2\pi\tau nf-i)} \left(e^{\frac{t_\alpha-(2i\pi\tau nf+1)\left(\frac{T}{2}\right)}{\tau}} - e^{\frac{t_\alpha-(2i\pi\tau nf+1)t_\alpha}{\tau}} \right) \Bigg] \\
& - V_s \cdot \Bigg[\frac{\tau}{-(2\pi\tau nf+i)} \left(e^{\frac{\left(\frac{T}{2}+t_\alpha\right)+(2i\pi\tau nf-1)T}{\tau}} - e^{\frac{\left(\frac{T}{2}+t_\alpha\right)+(2i\pi\tau nf-1)\left(\frac{T}{2}+t_\alpha\right)}{\tau}} \right) \\
& - \frac{\tau}{(2\pi\tau nf-i)} \left(e^{\frac{\left(\frac{T}{2}+t_\alpha\right)-(2i\pi\tau nf+1)T}{\tau}} - e^{\frac{\left(\frac{T}{2}+t_\alpha\right)-(2i\pi\tau nf+1)\left(\frac{T}{2}+t_\alpha\right)}{\tau}} \right) \Bigg] \Bigg]
\end{aligned}
$$

$$(4.89)$$

Considering equation (4.89) above, by taking the terms '$(nf - f_n)(nf + f_n)$' for Sine representation functions as a common, and the terms '$(2\pi\tau nf - i)(2\pi\tau nf + i)$' for the lower exponential representation functions as a common, then the equation will be transformed to the following expression

$$b_n = \frac{1}{T}\left[\frac{V_p}{4i\pi(nf - f_n)(nf - f_n)}\cdot\left[-(nf - f_n)e^{2i\pi(nf+f_n)t_\alpha} + (nf - f_n)\right.\right.$$

$$-(nf + f_n)e^{-2i\pi(nf-f_n)t_\alpha} + (nf + f_n)$$

$$+(nf + f_n)e^{2i\pi(nf-f_n)t_\alpha} - (nf + f_n)$$

$$+(nf - f_n)e^{-2i\pi(nf+f_n)t_\alpha} - (nf - f_n)$$

$$+(nf - f_n)e^{i\pi\left(2(nf+f_n)\left(\frac{T}{2}+t_\alpha\right)-f_nT\right)}$$

$$-(nf - f_n)e^{i\pi\left(2(nf+f_n)\left(\frac{T}{2}\right)-f_nT\right)}$$

$$+(nf + f_n)e^{-i\pi\left(2(nf-f_n)\left(\frac{T}{2}+t_\alpha\right)+f_nT\right)}$$

$$-(nf + f_n)e^{-i\pi\left(2(nf-f_n)\left(\frac{T}{2}\right)+f_nT\right)}$$

$$-(nf + f_n)e^{i\pi\left(2(nf-f_n)\left(\frac{T}{2}+t_\alpha\right)+f_nT\right)}$$

$$+(nf + f_n)e^{i\pi\left(2(nf-f_n)\left(\frac{T}{2}\right)+f_nT\right)}$$

$$-(nf - f_n)e^{-i\pi\left(2(nf-f_n)\left(\frac{T}{2}+t_\alpha\right)-f_nT\right)}$$

$$\left.+(nf - f_n)e^{-i\pi\left(2(nf-f_n)\left(\frac{T}{2}\right)-f_nT\right)}\right]$$

$$+\frac{V_s\tau}{(2\pi\tau nf - i)(2\pi\tau nf + i)}\cdot\left[-(2\pi\tau nf - i)e^{-\left(\frac{\frac{T}{2}-t_\alpha}{\tau}\right)+i\pi nfT}\right.$$

$$+(2\pi\tau nf - i)e^{2i\pi nft_\alpha}$$

$$-(2\pi\tau nf + i)e^{-\left(\frac{\frac{T}{2}-t_\alpha}{\tau}\right)-i\pi nfT}$$

$$+(2\pi\tau nf + i)e^{-2i\pi nft_\alpha}$$

$$+(2\pi\tau nf - i)e^{-\left(\frac{\frac{T}{2}-t_\alpha}{\tau}\right)+2i\pi nfT}$$

$$-(2\pi\tau nf - i)e^{2i\pi nf\left(\frac{T}{2}+t_\alpha\right)}$$

$$+(2\pi\tau nf + i)e^{-\left(\frac{\frac{T}{2}-t_\alpha}{\tau}\right)-2i\pi nfT}$$

$$\left.\left.-(2\pi\tau nf + i)e^{-2i\pi nf\left(\frac{T}{2}+t_\alpha\right)}\right]\right]$$

$$(4.90)$$

Then, with rearranging equation (4.90) again by assembling each two similar expo-

nential terms but with different sign altogether, as in the following mathematical steps:

$$b_n = \frac{1}{T}\left[\frac{V_p}{2\pi(n^2f^2 - f_n^2)}\cdot\left[-(nf - f_n)\left(\frac{e^{2i\pi(nf+f_n)t_\alpha} - e^{-2i\pi(nf+f_n)t_\alpha}}{2i}\right)\right.\right.$$

$$-(nf + f_n)\left(\frac{e^{2i\pi(nf-f_n)t_\alpha} - e^{-2i\pi(nf-f_n)t_\alpha}}{2i}\right)$$

$$+(nf - f_n)\left(\frac{e^{i\pi\left(2(nf+f_n)\left(\frac{T}{2}+t_\alpha\right)-f_nT\right)} - e^{-i\pi\left(2(nf+f_n)\left(\frac{T}{2}+t_\alpha\right)-f_nT\right)}}{2i}\right)$$

$$-(nf - f_n)\left(\frac{e^{i\pi\left(2(nf+f_n)\left(\frac{T}{2}\right)-f_nT\right)} - e^{-i\pi\left(2(nf+f_n)\left(\frac{T}{2}\right)-f_nT\right)}}{2i}\right)$$

$$-(nf + f_n)\left(\frac{e^{i\pi\left(2(nf-f_n)\left(\frac{T}{2}+t_\alpha\right)+f_nT\right)} - e^{-i\pi\left(2(nf-f_n)\left(\frac{T}{2}+t_\alpha\right)+f_nT\right)}}{2i}\right)$$

$$+(nf + f_n)\left.\left(\frac{e^{i\pi\left(2(nf-f_n)\left(\frac{T}{2}\right)+f_nT\right)} - e^{-i\pi\left(2(nf-f_n)\left(\frac{T}{2}\right)+f_nT\right)}}{2i}\right)\right]$$

$$+\frac{V_s\tau}{(4\pi^2\tau^2n^2f^2 - i^2)}\cdot\left[(2\pi\tau nf - i)e^{-\left(\frac{\frac{T}{2}-t_\alpha}{\tau}\right)}\left(e^{2i\pi nfT} - e^{i\pi nfT}\right)\right.$$

$$+(2\pi\tau nf + i)e^{-\left(\frac{\frac{T}{2}-t_\alpha}{\tau}\right)}\left(e^{-2i\pi nfT} - e^{-i\pi nfT}\right)$$

$$+(2\pi\tau nf - i)e^{2i\pi nft_\alpha}\left(1 - e^{i\pi nfT}\right)$$

$$\left.\left.+(2\pi\tau nf + i)e^{-2i\pi nft_\alpha}\left(1 - e^{i\pi nfT}\right)\right]\right]$$

$$(4.91)$$

Depending on the exponential definition of the Sine function, by substituting this in equation(4.91), the final picture of a_n will equal to the following formula:

$$b_n = \frac{1}{T}\left[\frac{V_p}{2\pi\left(n^2f^2 - f_n^2\right)} \cdot \left[-(nf - f_n)Sin(2\pi(nf + f_n)t_\alpha)\right.\right.$$

$$+(nf + f_n)Sin(2\pi(nf - f_n)t_\alpha)$$

$$+(nf - f_n)Sin\left(\pi\left(2(nf - f_n)\left(\frac{T}{2} + t_\alpha\right) - f_nT\right)\right)$$

$$-(nf - f_n)Sin\left(\pi\left(2(nf + f_n)\left(\frac{T}{2}\right) - f_nT\right)\right)$$

$$-(nf + f_n)Sin\left(\pi\left(2(nf - f_n)\left(\frac{T}{2} + t_\alpha\right) + f_nT\right)\right)$$

$$\left.+(nf + f_n)Sin\left(\pi\left(2(nf - f_n)\left(\frac{T}{2}\right) + f_nT\right)\right)\right]$$

$$+\frac{V_s\tau}{\left(4\pi^2\tau^2n^2f^2 + 1\right)} \cdot \left[(2\pi\tau nf - i)e^{-\left(\frac{\frac{T}{2} - t_\alpha}{\tau}\right)}\left(e^{2i\pi nfT} - e^{i\pi nfT}\right)\right.$$

$$+(2\pi\tau nf + i)e^{-\left(\frac{\frac{T}{2} - t_\alpha}{\tau}\right)}\left(e^{-2i\pi nfT} - e^{-i\pi nfT}\right)$$

$$+(2\pi\tau nf - i)e^{2i\pi nft_\alpha}\left(1 - e^{i\pi nfT}\right)$$

$$\left.\left.+(2\pi\tau nf + i)e^{-2i\pi nft_\alpha}\left(1 - e^{-i\pi nfT}\right)\right]\right]$$

$$(4.92)$$

Thus; the spectrum magnitude of $v(t)$ output signal is given by:

$$S_n = \sqrt{a_n^2 + b_n^2} \tag{4.93}$$

156

4.7   The Optimum Harmonic Control of System Configuration

For better understanding the control strategy of the configuration, there will be an extensive analysis to the efficient heating power in terms of harmonic components of output load voltage and current waveforms delivered from MNPCI topology to the IH load tank of captured values: $L1 = 105.7\mu H$, $R = 10.07\Omega$ and $L = 33\mu H$, as in experimental output voltage and current signals shown in 4.15, which clearly clarifies that the phase shift angle between $v(t)$ and $i(t)$ is approximately zero magnitude difference with performing soft switching mode condition.

The corresponding experimental result of **Frequency Spectrum FS** analysis for MNPCI prototype is shown in Fig. 4.16, it can be deduced from first sight that the harmonic content are the fundamental 1st, 3rd, 5th and finally the 7th harmonic. Therefore, the following analysis concentrates mainly on those particular harmonics with comparing their amplitude values at different operational points.

By comparing the **FS** of three operational points at different ON switching time values of $t_\alpha = 51.2\mu sec$ (shown in Fig. 4.17) with **FS** of $t_\alpha = 72.6\mu sec$ (shown in Fig. 4.20) and with **FS** of $t_\alpha = 89.3\mu sec$ (shown in Fig. 4.23), illustrates that the MNPCI configuration expresses harmonic content of approximately 1st, 3rd and 5th basic harmonics, with relatively low 7th harmonic oscillation (it can be neglected depending on the selected time t_α), which coincide with the **FS** shown in Fig. 4.16.

The configuration posses better characteristic of lower signal harmonic distortion content at $t_\alpha = 72.6\mu sec$ and at $t_\alpha = 89.3\mu sec$ than $t_\alpha = 51.2\mu sec$, which is the main goal of the configuration, therefore; the prototype can be controlled through convenient choice of t_α optimum operational point. This indicates that this selection controls the content of harmonic distortion noise of output voltage $v(t)$ and current $i(t)$ and hence, controls

the maximum heating power.

Therefore, a 21 operational points with equal step interval of t_α are selected for comparison starting from $\left(\frac{1}{4f_n}\right) \longrightarrow \left(\frac{T}{2}\right)$ limit, which represents the estimated effective ON time range starting from minimum time of t_α with maximum harmonic distortion, then t_α rises up step by step until reaches its maximum ON switching time of t_α, meanwhile the amplitude of harmonic distortion decreases until it reaches the minimum possible value, as can be seen in Fig. 4.26 and Fig. 4.27, although this graph seems to be nested that one can not recognize the interlinked lines, but this curve illustrates the operational band borders of harmonic amplitude change of the proposed MNPCI configuration. To show the curve of harmonic change more clearly, less points must be chosen for comparison as shown in Fig. 4.28 and Fig. 4.29.

To identify the optimum operational point, it is important to determine the $\left(\frac{V_{rms}}{V_{rmsmax}}\right)$ for the selected t_α points, as in Fig. 4.30, which demonstrates that the voltage ratio between output voltage to maximum rms voltage starts from operational point of $t_\alpha = \frac{1}{4f_n}$, then rises gradually from minimum value of 76.4% with a distortion percent of 24% at $t_\alpha = 41.7\mu sec$, until it reaches an average value of about 95% with distortion noise of 5% at $t_\alpha = 63.1\mu sec$ and then it keeps increasing to the maximum peak of 96.8% at $t_\alpha = 72.6\mu sec$, that means the harmonic noise at this specific operational point is only 3% which is the minimal possible noise at all. Afterwards, it slightly decreases to settle at the average value again until half of signal cycle time limit $t_\alpha = \frac{T}{2}$.

This notice can be also observed clearly from the frequency response of 3rd harmonic located in Fig. 4.26, for which the value of relative harmonic amplitude starts from 34% at $t_\alpha = \frac{1}{4f_n}$ and ends at only 5.6% at $t_\alpha = \frac{T}{2}$.

While Fig. 4.31 shows the behaviour of different current harmonics for $1^{st}, 3^{rd}, 5^{th}$ and 7th at different t_α values, in which the 1st Harmonic starts from 69% at $t_\alpha = 41.7\mu sec$,
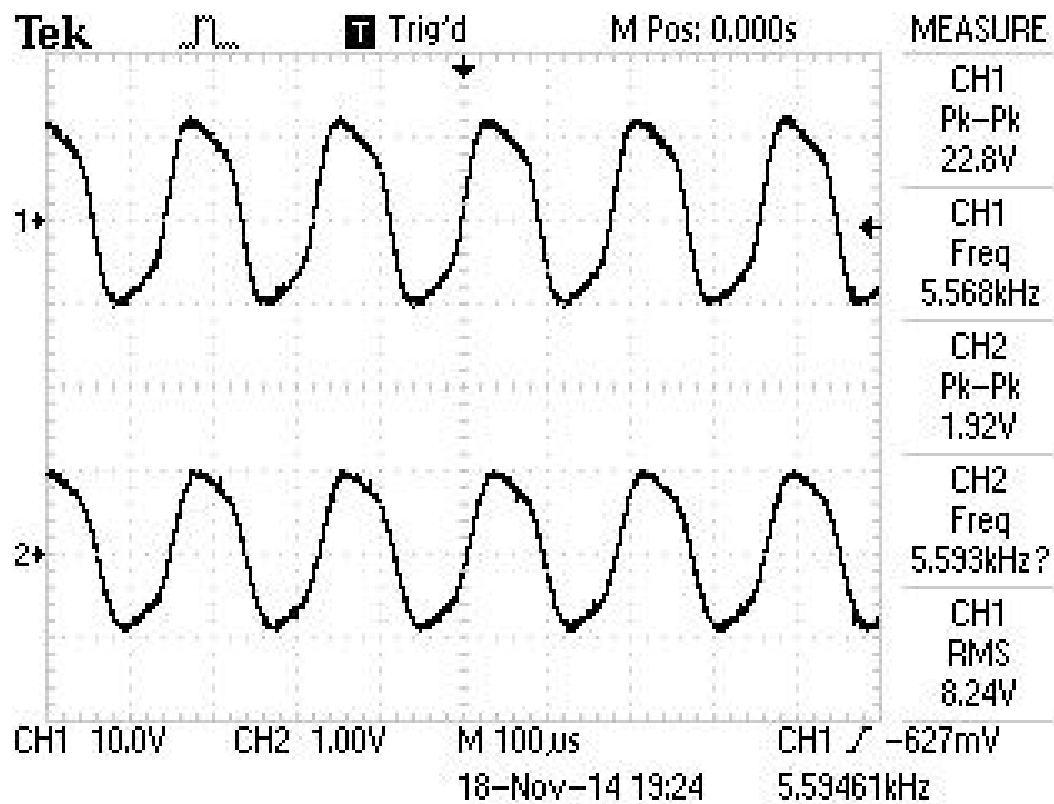
Figure 4.15: Ch1 - Output Voltage (10v/div), and Ch2 - Current (1v/div) Signals of prototype values: $L1 = 105.7\mu H$, $R = 10.07\Omega$ and $L = 33\mu H$
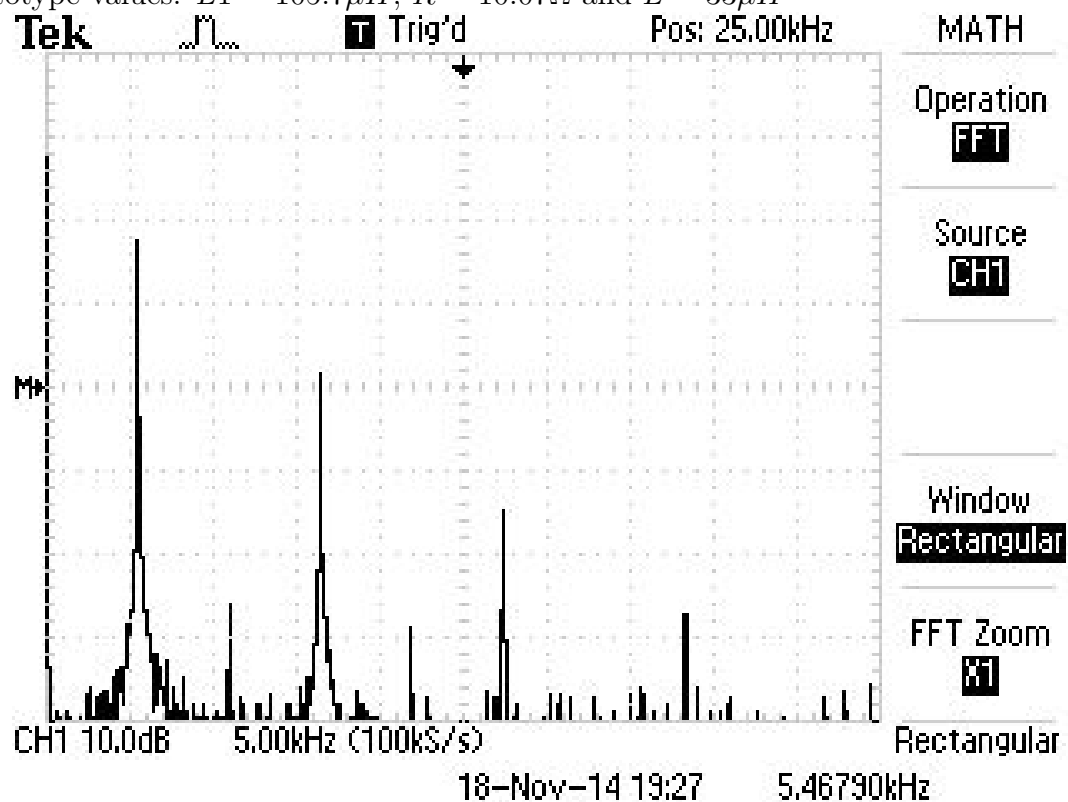
Figure 4.16: Experimental Frequency Spectrum Analysis of Output Voltage, $v(t)$ of prototype values:$L1 = 105.7\mu H$, $R = 10.07\Omega$ and $L = 33\mu H$ and $t_\alpha = 72\mu sec$ (10db/div)
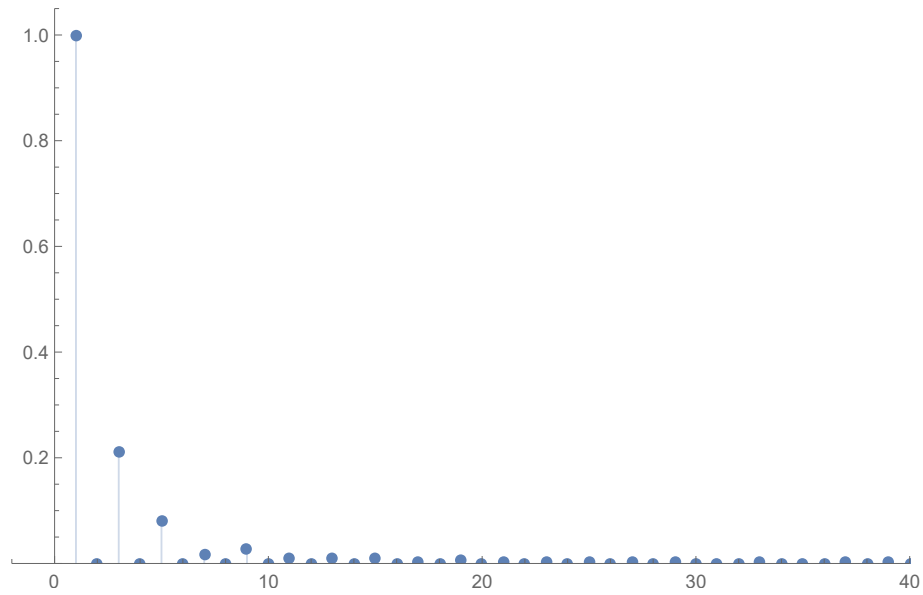
Figure 4.17: Frequency Spectrum at $t_\alpha = 51.2\mu sec$
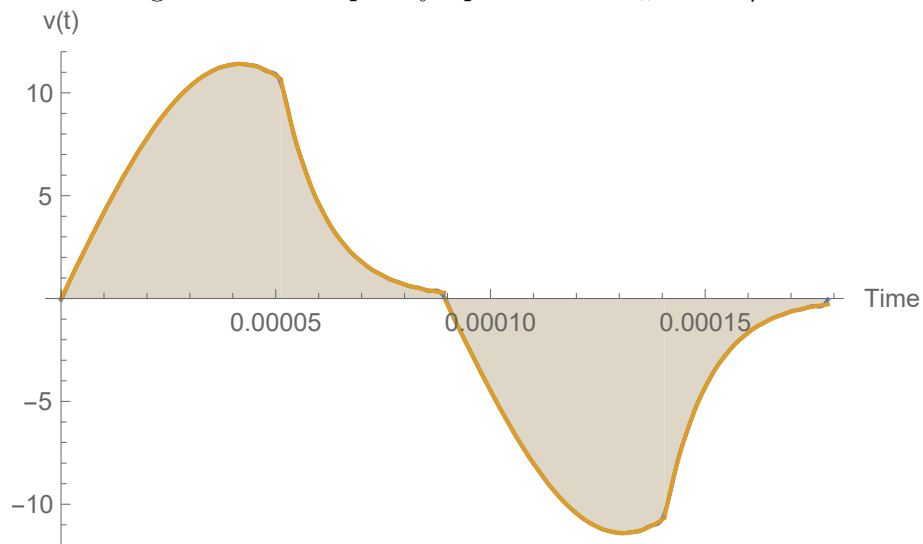
Figure 4.18: Typical $v(t)$ at $t_\alpha = 51.2\mu sec$
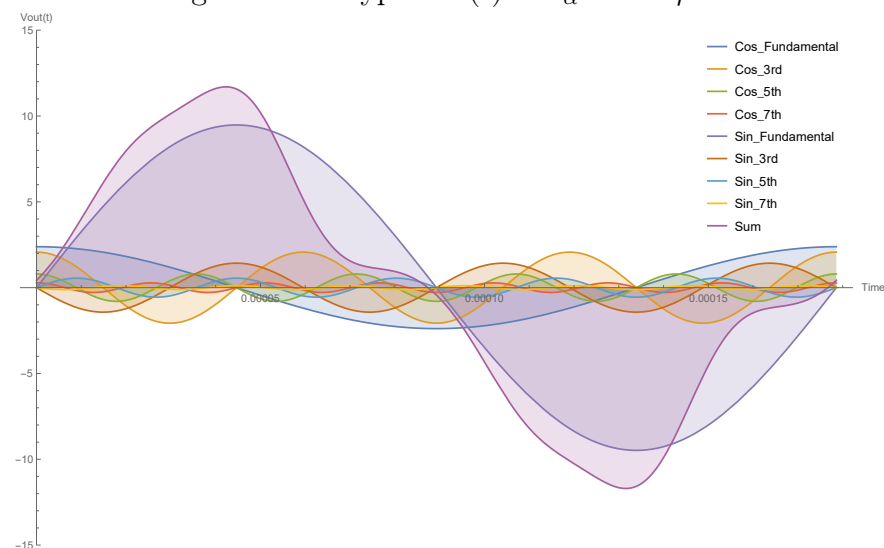
Figure 4.19: $v(t)$ with $1^{st}, 3^{rd}, 5^{th}$ and 7th Harmonics at $t_\alpha = 51.2\mu sec$
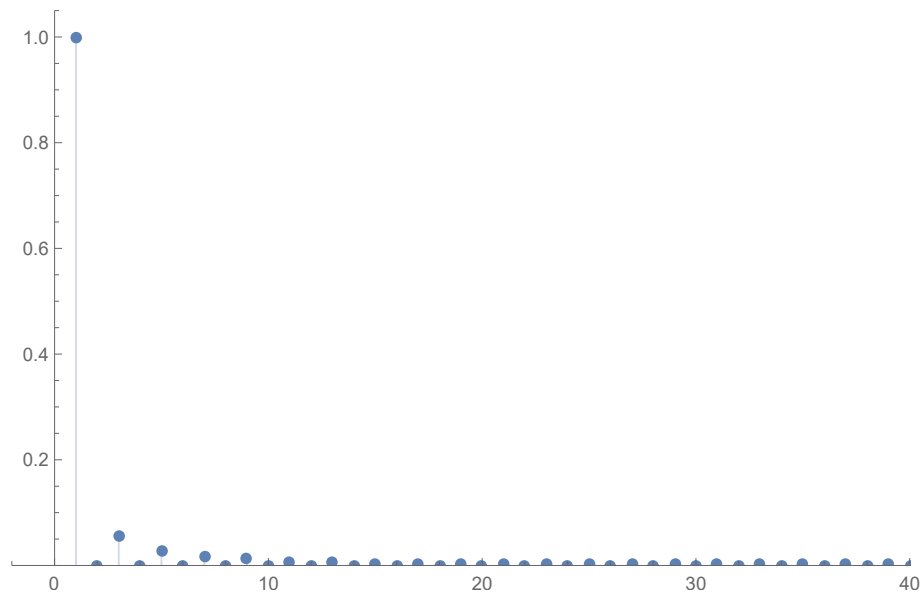
Figure 4.20: Frequency Spectrum at $t_\alpha = 72.6\mu sec$
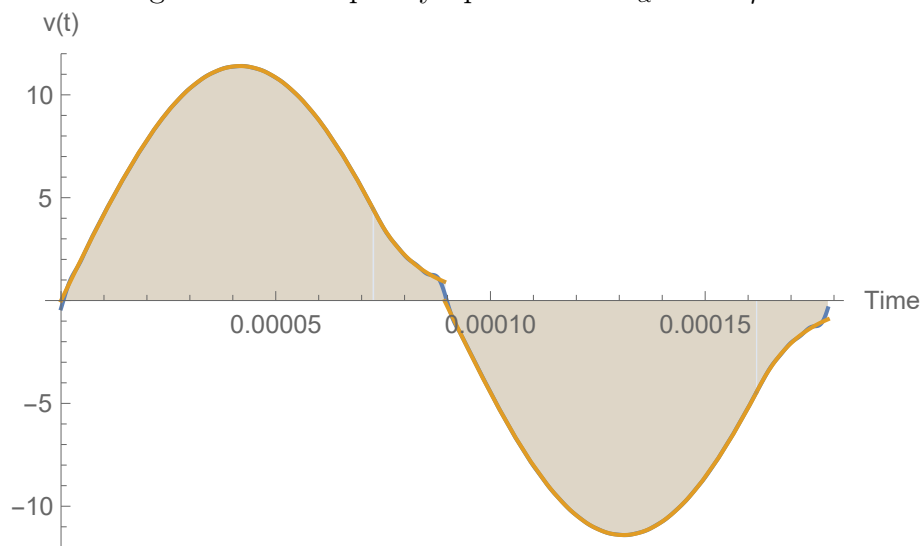
Figure 4.21: Typical $v(t)$ at $t_\alpha = 72.6\mu sec$
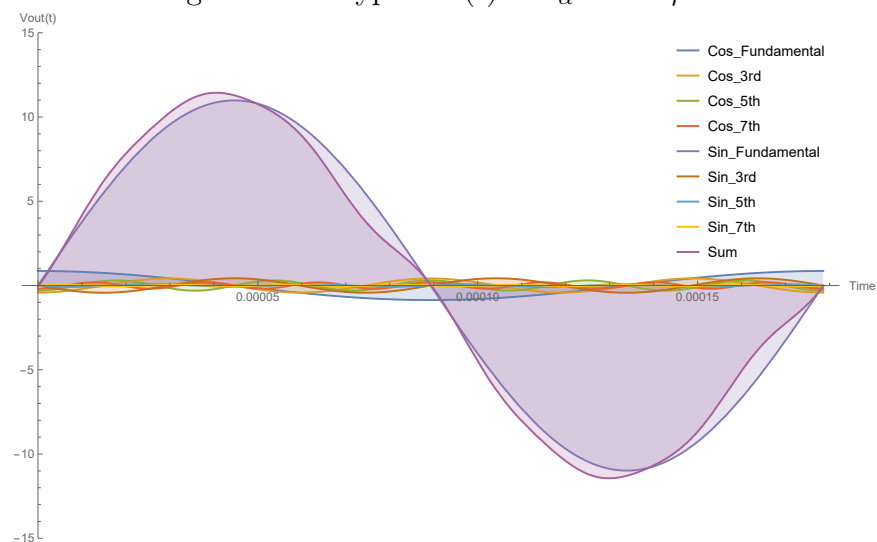
Figure 4.22: $v(t)$ with $1^{st}, 3^{rd}, 5^{th}$ and 7th Harmonics at $t_\alpha = 72.6\mu sec$
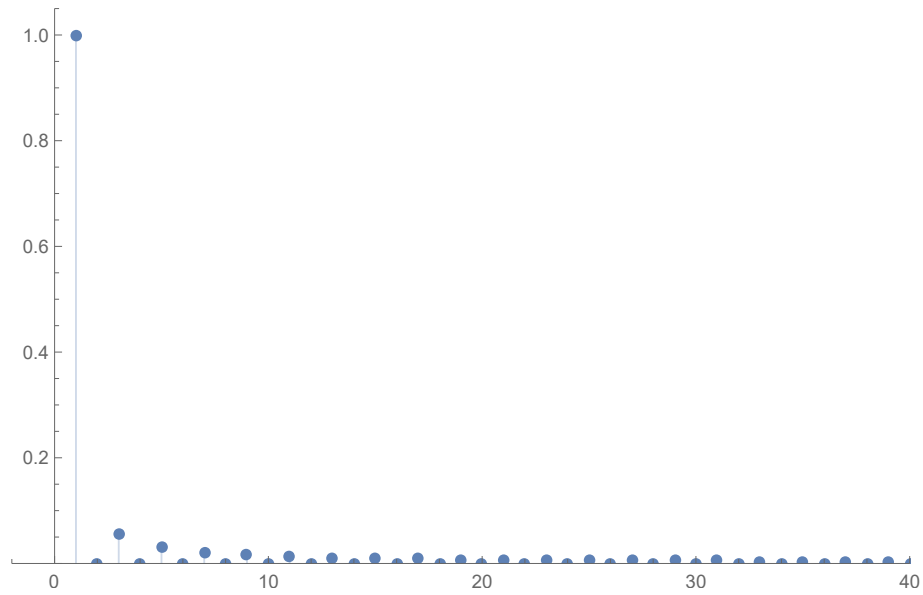
Figure 4.23: Frequency Spectrum at $t_\alpha = 89.3\mu sec$
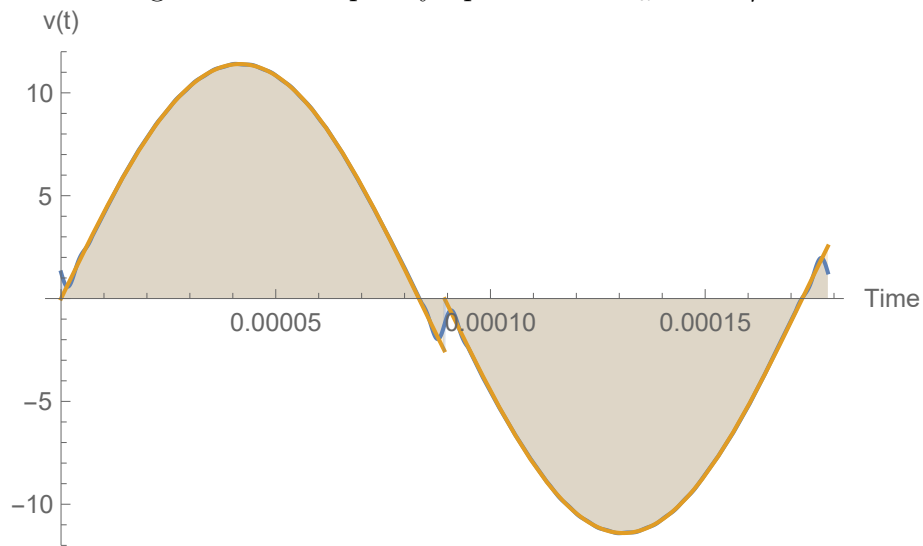
Figure 4.24: Typical $v(t)$ at $t_\alpha = 89.3\mu sec$
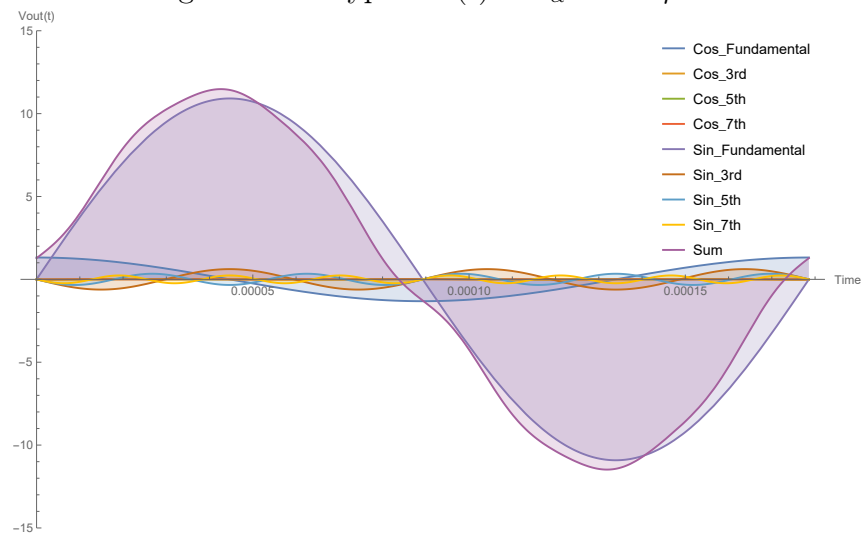
Figure 4.25: $v(t)$ with 1st,3rd,5th and 7th Harmonics at $t_\alpha = 89.3\mu sec$
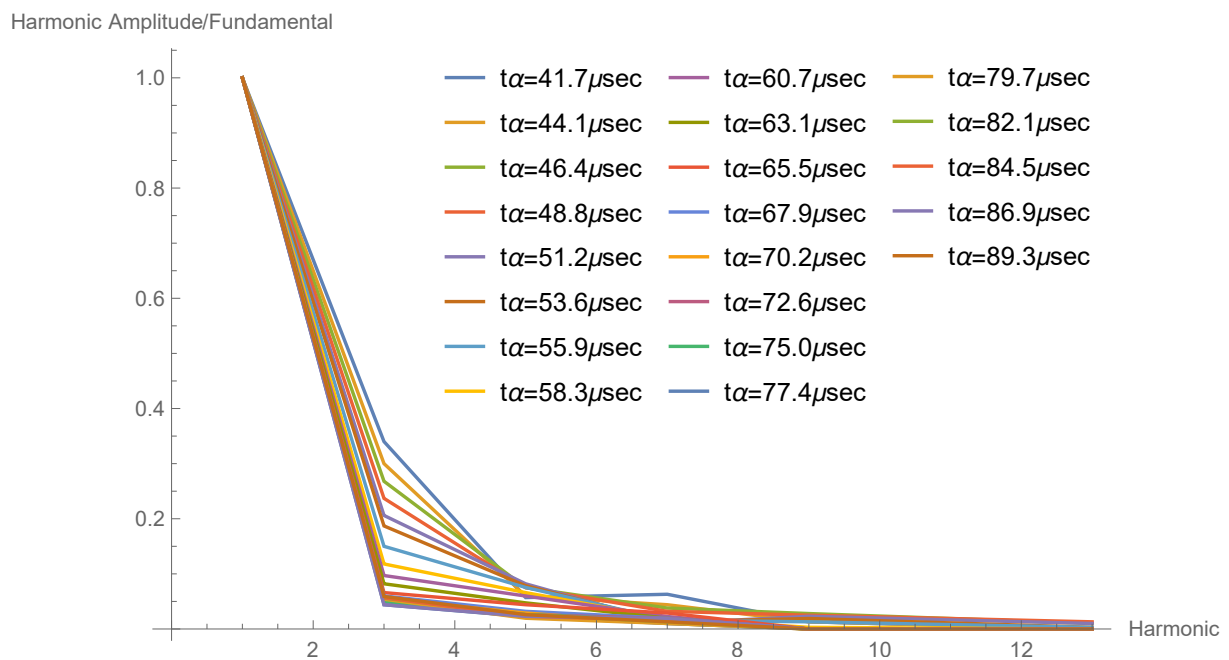
Figure 4.26: Frequency Spectrum of 21-Operational Points of ON-Switching Time t_α
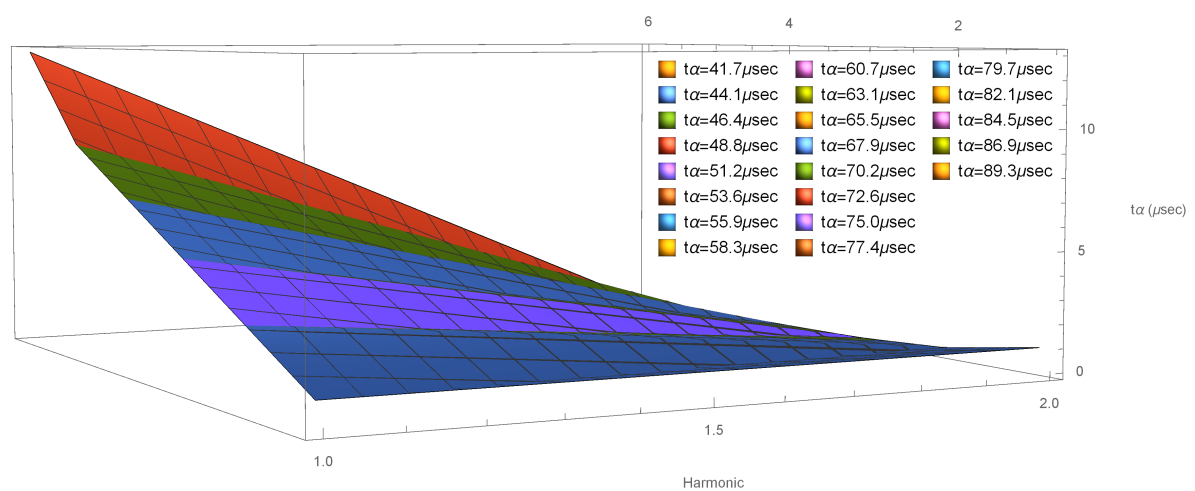
Figure 4.27: 3-Dimension Frequency Spectrum Surface of 21-Operational Points of ON-Switching Time t_α

Harmonic Amplitude/Fundamental
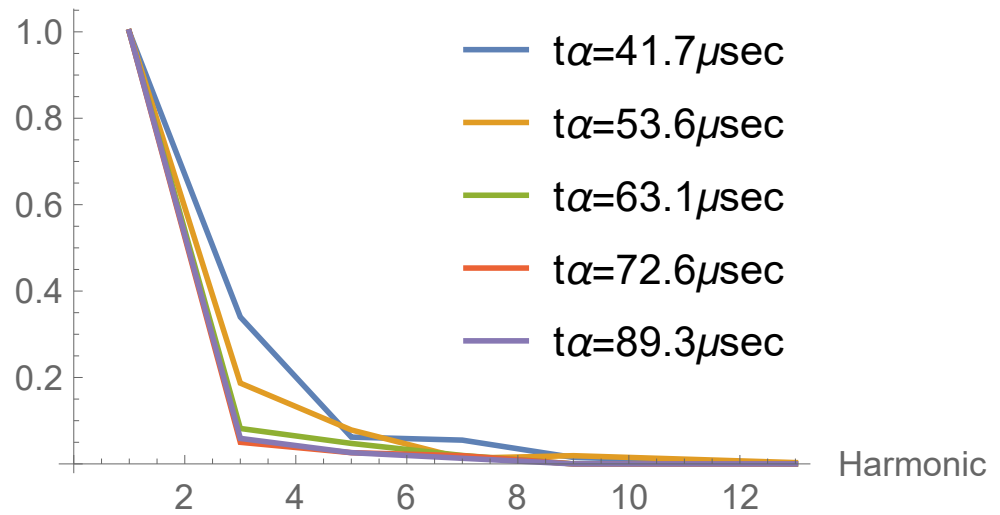
Figure 4.28: Frequency Spectrum of 5-Operational Points of ON-Switching Time t_α
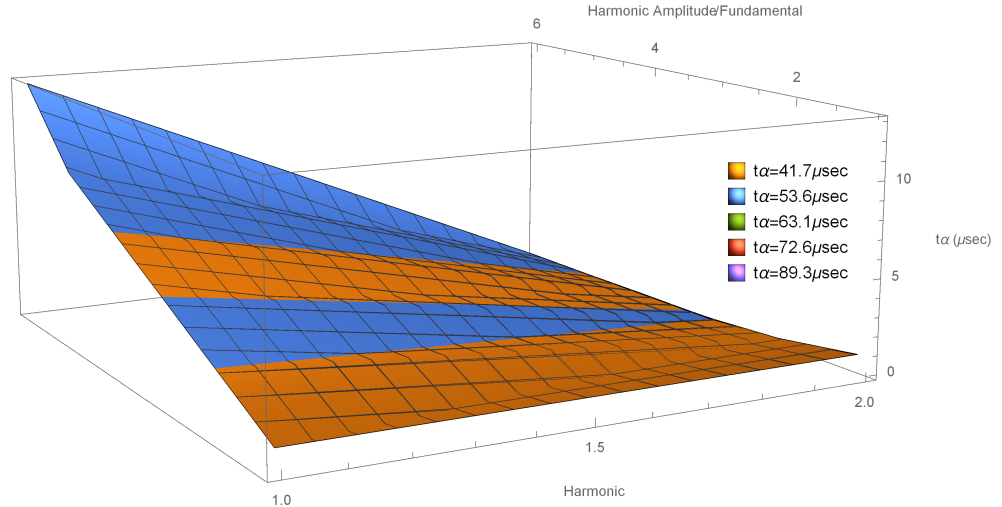
Figure 4.29: 3-Dimension Frequency Spectrum Surface of 5-Operational Points of ON-Switching Time t_α

164

then rises gradually until it reaches the average value of 92% at $t_\alpha = 65.5\mu sec$ and then reaches the maximum value 93% at $t_\alpha = 72.6\mu sec$, meanwhile the 3^{ed} harmonic starts from maximum value of 23.6% at $t_\alpha = 41.7\mu sec$, but then it decreases until it reaches the minimum average value of 5% at $t_\alpha = 72.6\mu sec$. While, the 5th harmonic oscillates from minimum of 4% at $t_\alpha = 41.7\mu sec$ and then rises up to 7% at $t_\alpha = 53.5\mu sec$, but then it falls down to 2.8% at $t_\alpha = 72.6\mu sec$.

But, there is a balance relationship between the ON time operational point t_α and the magnitudes of current harmonic of $3^{ed}, 5^{th}$ and 7th components. It can be easily observed from Fig. 4.31, that the 3rd harmonic has the highest effect on the proposed system, due to have higher amplitude with respect to other harmonics, while the 7th has the least effect on the system. By comparing the frequency spectrum of the three essential harmonics, the 3^{ed} may reach peak of 34%, and the 7th harmonic can reach only 6.3% as a maximum value, while the 5th lays at the middle value position in between them with maximum of 8%.

Therefore; the 3^{ed} harmonic together with the fundamental exert the maximum influence on the optimal efficiency of the proposed system. They need to be chosen with a best (minimum) value in the first place, then looking at the other harmonics behaviour but without neglecting their effect, because from noticing the harmonics amplitude curve of 5th harmonic in Fig. 4.31, it might be increased at the same time of decreasing the amplitude of 3^{ed} harmonic. Therefore; the selection of t_α operational point has a critical value during the control process.

The resultant **Effective Heating Power** $P_e(f)$ of the proposed system is shown in fig.4.32. It begins from minimum value of 43.6 at $t_\alpha = 41.7\mu sec$ and rises until reach the optimum of 65.24 at $t_\alpha = 72.6\mu sec$ and then drops a little to settle at average of 64.5. This curve gives a clear picture of the changing characteristic of heating efficiency, which can be controlled to the maximum value through setting the t_α to an optimum possible

point of $t_\alpha = 72.6\mu sec$.

This fact implies that, by **setting** the **ON switching time** t_α to a suitable value, the **Total Harmonic Distortion THD** of the system can be reduced to a minimum level, as a consequence; controlling the t_α performs maximum power transfer.

And according to **IEEE STD 519 Standards** [98], the maximum accepted THD percentage of the inverter is 20%, therefore; through observing the THD curves for the configuration of both THD_F and THD_R shown in Fig. 4.33, reveals that the accepted corresponding operational region (where both curves meet together) begins from threshold ON time of $t_\alpha = 53.6\mu sec$, at which the THD is 20%.

Therefore; the ON time $t_\alpha = 53.6\mu sec$ is considered as the maximum threshold acceptable operational time of the proposed configuration, which represents about $\left(\frac{T}{3.3}\right)$ of the output signal total time, therefore; the limits of acceptable operational region lies between $\left(\frac{T}{3.3} < t_\alpha < \frac{T}{2}\right)$ period.

Then after; the harmonic distortion noise begins to decrease gradually until it reaches the minimum value of $THD = 6.5\%$ at $t_\alpha = 72.6\mu sec$, and then it settles on the average of $THD = 6.75\%$, which verifies the reliability of the proposed control strategy of the configuration, as it operates at $t_\alpha = 72\mu sec$ operational point, i.e, with $THD = 6.5\%$, which is much lower than the maximum threshold limit of **IEEE STD 519 Standards**.

Vrms/Vrmsmax
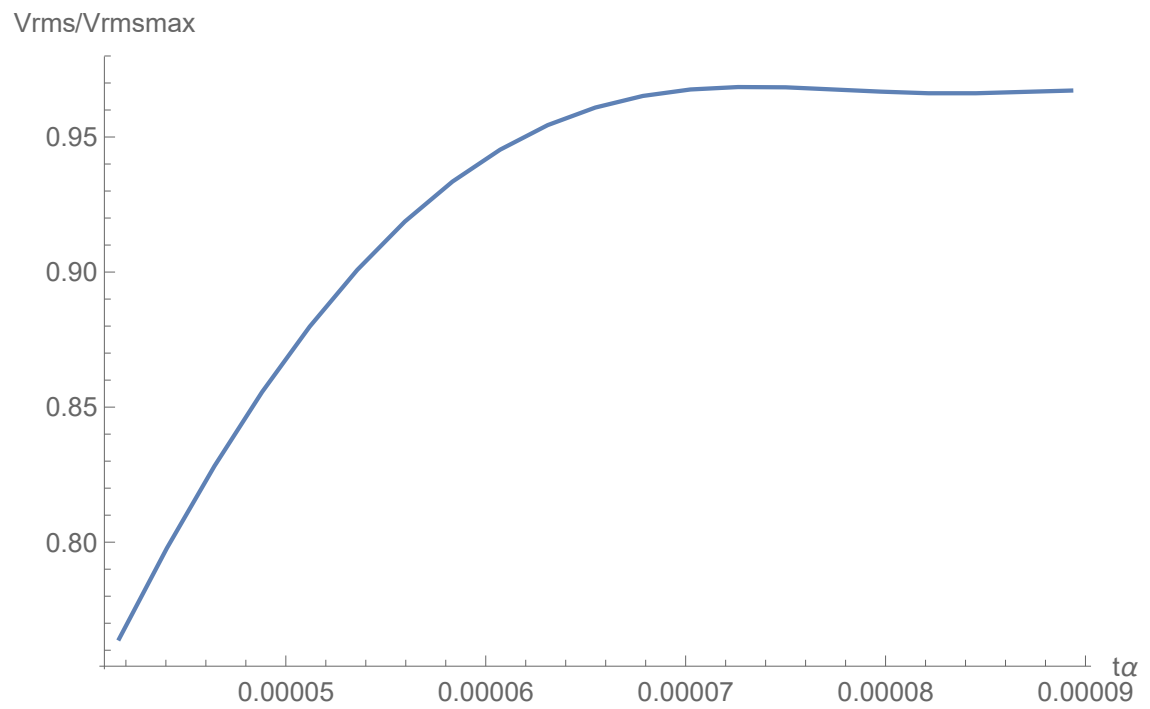
Figure 4.30: Output Voltage Ratio

Amplitude
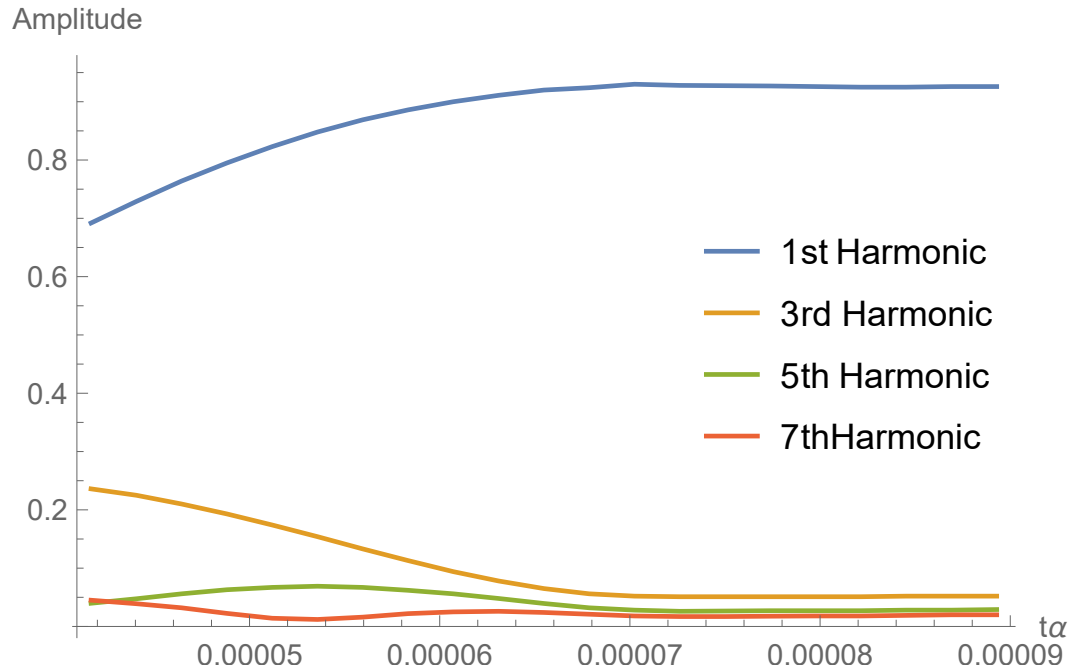
Figure 4.31: Current Harmonics

167

Effective Heating Power
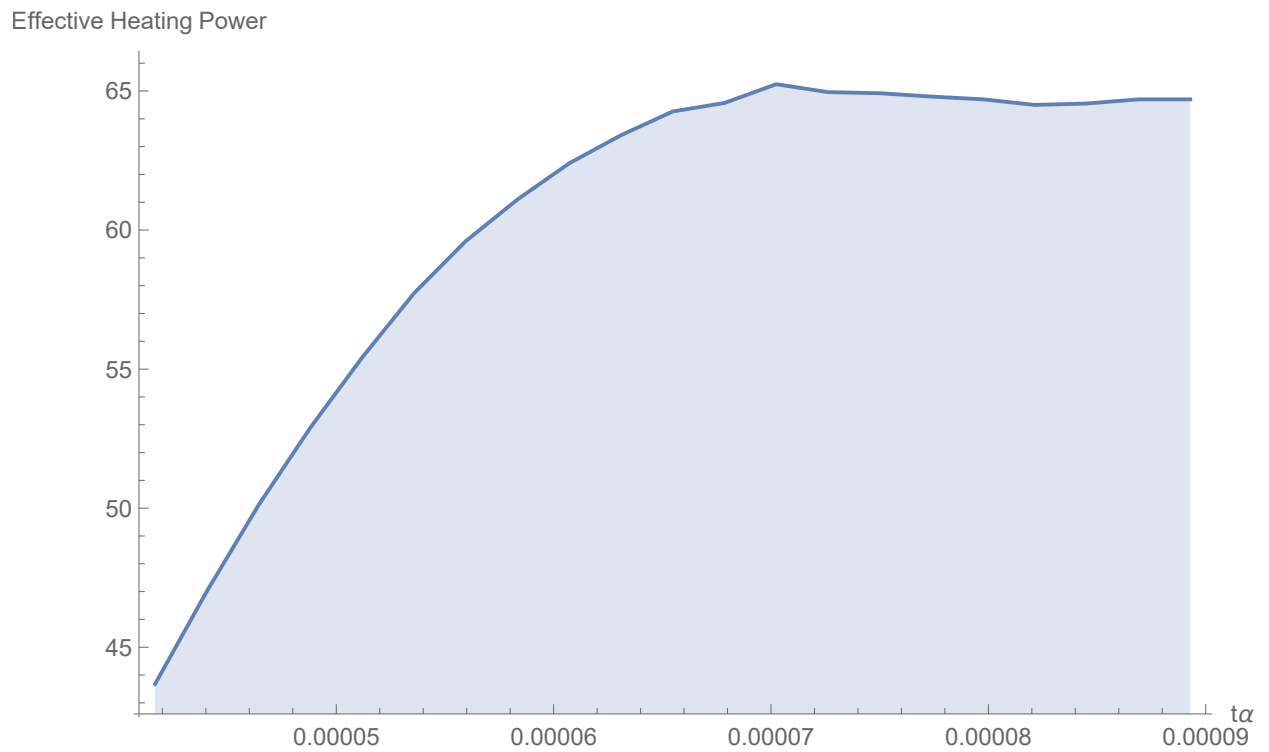
Figure 4.32: Effective Heating Power

THD(%)
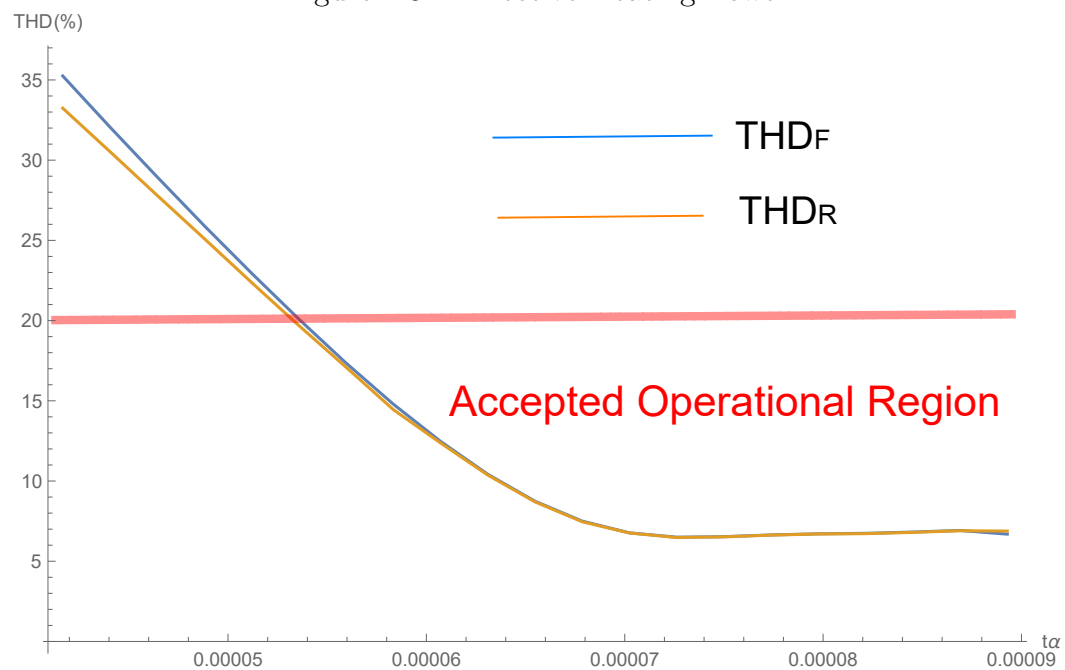
Figure 4.33: Total Harmonic Distortion THD Versus ON Switching Time t_α

4.8   Comparison between MNPCI and H-Bridge Topologies

In order to verify the MNPCI prototype reliability, a comparison with H-bridge is very important to prove the configuration advantages. Therefore; the following section is introducing some differences between the two topologies for: **output waveform**, **harmonic content**, **dead time** and finally the **power losses**.

4.8.1   Output Waveform, Harmonic Content and Dead Time Comparisons

The harmonic content of output current obtained from MNPCI topology differs from that in the H-bridge, because the output waveform of MNPCI consists from harmonic components, which entails that the heating power is equal to the summation of all components at different frequencies, as declared in Sections 4.2.5 and 4.7 before, which means that the total heating power is equal to the summation of all heating powers at different frequencies of harmonic orders.

While in the H-bridge (which its main topologies was explained in Chapter 2-Section 2.6), the ideal output waveform is approximately regular sine wave, as shown in Fig. 4.34, which means that there is only fundamental Harmonic included in the spectrum, as can be seen in the **Frequency Spectrum** shown in Fig. 4.35.

From heating power aspect with the same IH load, there is no big difference between the MNPCI and H-bridge topologies at this point, because all harmonics contained in MNPCI current waveform will produce dissipated heat in the material to be heated but with different frequencies, while at the H-bridge, the current produces heating power with only one fundamental frequency, i.e., both configurations induce approximately same eddy currents and hence, produce same heating power inside the workpiece and that is the main issue, and that can be proved by observing the squared curves of output voltages, which have nearly the same shape and area under the curve for both topologies,
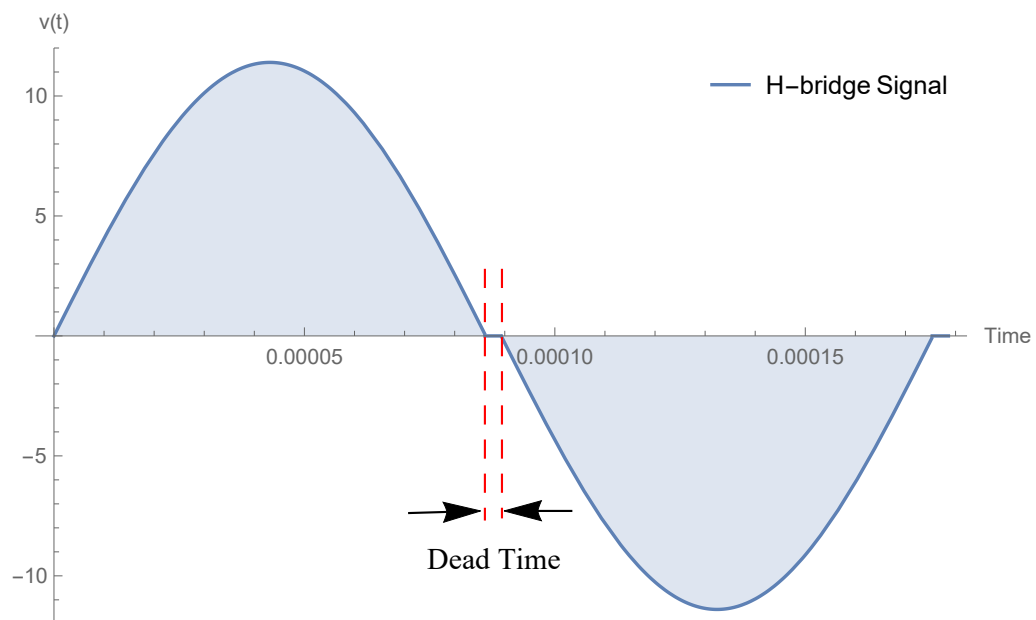
Figure 4.34: H-Bridge Output Waveform
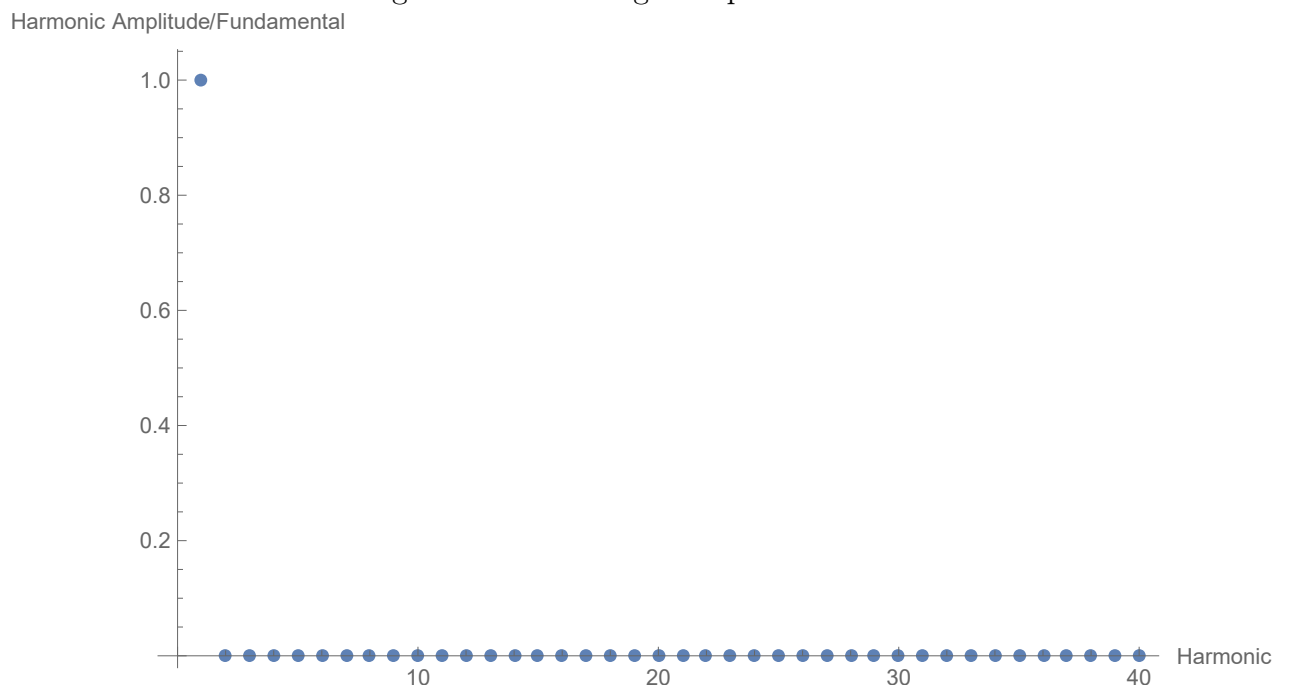
Figure 4.35: H-Bridge Frequency Spectrum

but with shifted voltage peak, as in Fig. 4.37.

And, from observing both output waveforms of MNPCI and H-bridge in Fig. 4.36, it can be deduced that both waveforms initiates from same starting point for both positive and negative cycles, whereas; they ends with different points. This is because of the **presence** of **Dead-Time** (**DT**) condition in the **H-bridge** topology between the waveform segments and the **absence** of **DT** in the **MNPCI** configuration. The reason of that; in the H-bridge, the **Dead-time** is very essential, to prevent the interaction between positive and negative modes happens and to ensure that the zero voltage switching (ZVS) occurs safely.

While in the MNPCI topology, the **Dead-Time** is **included in** the **Constant-Time** τ, therefore; τ should be chosen with appropriate value to guarantee doing the same above job, as shown in Fig. 4.38.

4.8.2   Power Losses Comparison

The power MOSFET switch as part of the AC/DC inverter in IH system has mainly two kinds of **power dissipations** that affects the efficiency of the proposed IH configuration: the first is the **switching losses**, and the second is the **conduction losses**, therefore; this section compares the power losses between the **MNPCI** and the **H-bridge** topologies, assuming both of them have the **same MOSFET switches** category, in order to deduce which one has better power losses characteristics than the other, as follows:

Switching Losses:

This kind of losses depends on the MOSFET parameters taken from the data sheet of the switch, which is very important in determining the maximum junction temperature and hence, predicting whether the topology needs heat sink protection or not.

It is divided into two main categories, as follows:

- **Transient Time Losses**: Which is produced during turning-ON and OFF the
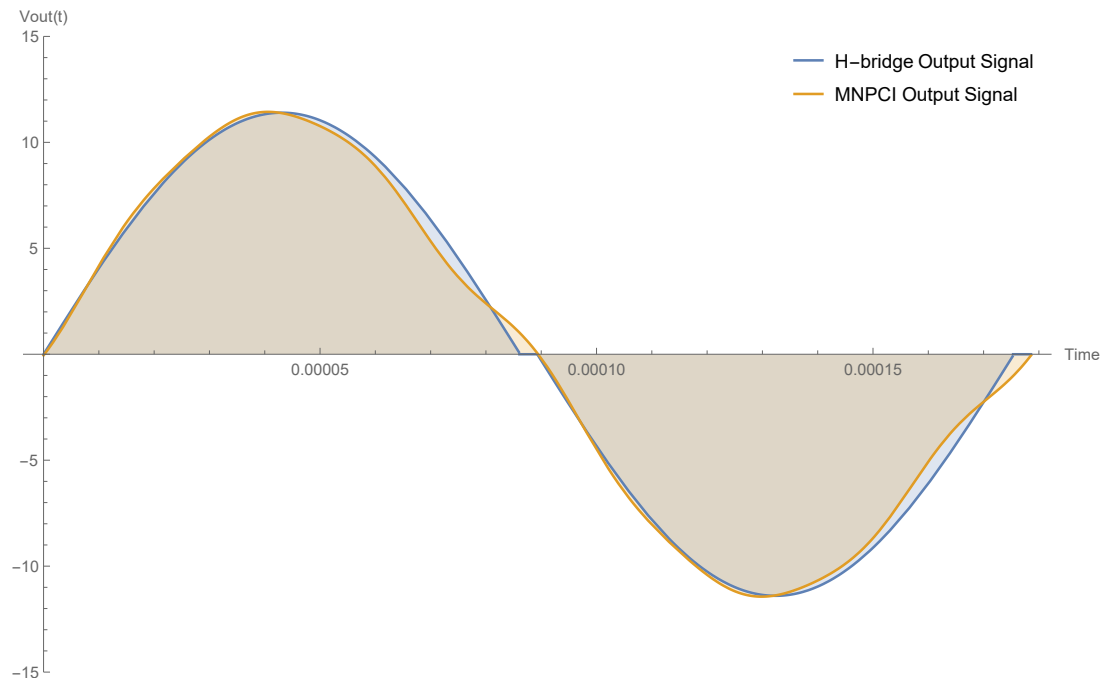
Figure 4.36: MNPCI and H-Bridge Output Waveforms
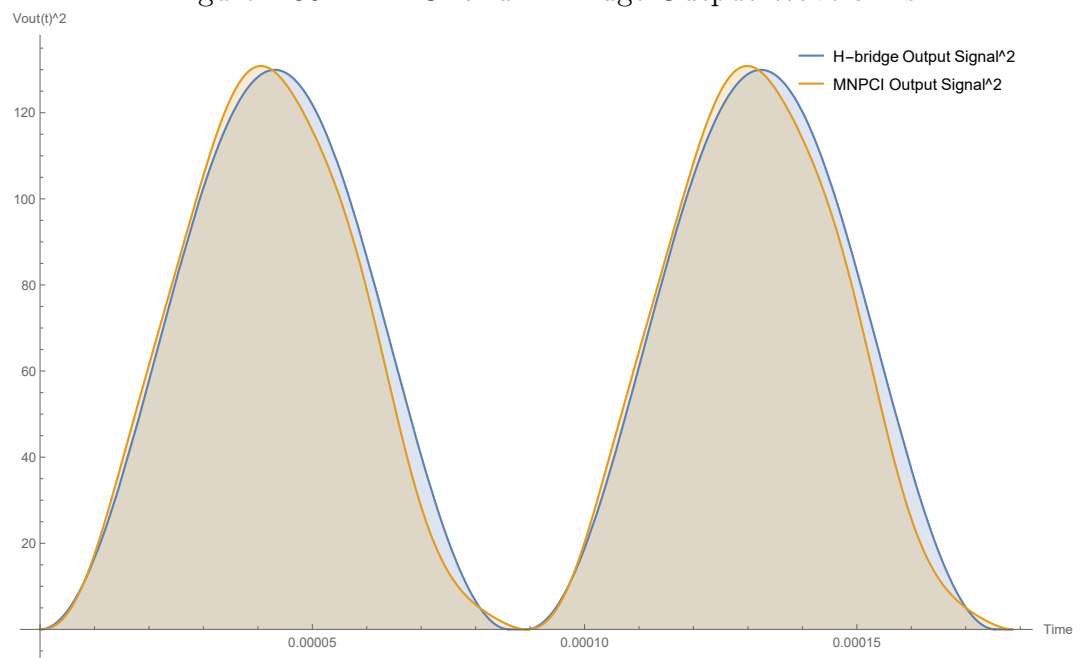
Figure 4.37: MNPCI and H-Bridge Squared Output Waveforms
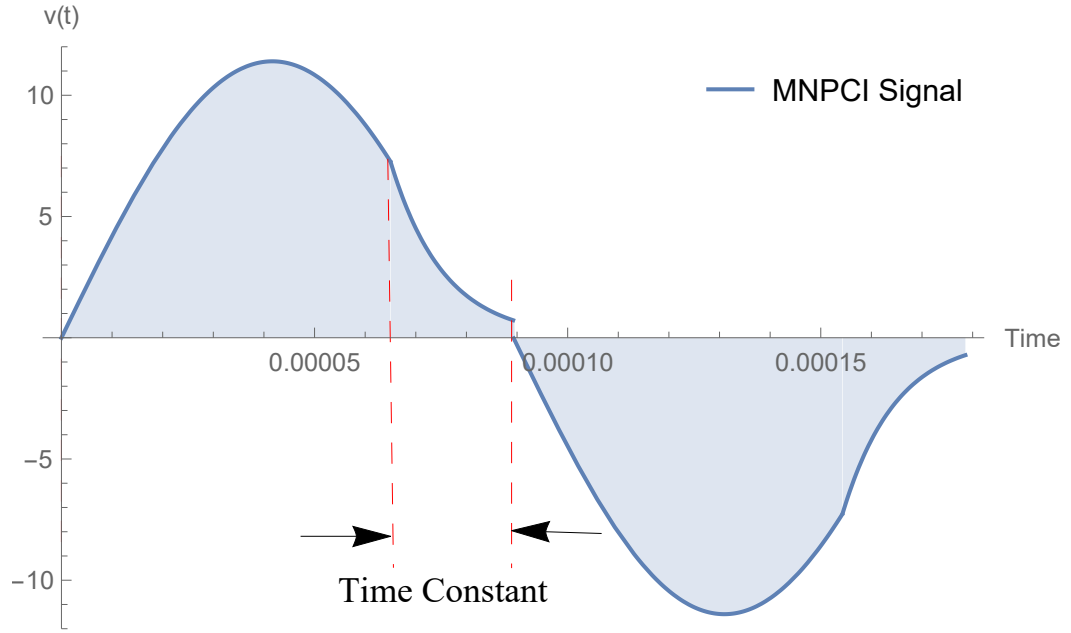
Figure 4.38: Typical MNPCI Waveform with Time Constant (τ)

MOSFET semiconductor.

This type of losses can be calculated from the following equation [99]:

$$P_{SW1} = \frac{1}{2} I_D . V_D \left(t_{ON} + t_{OFF} \right) . f \tag{4.94}$$

Where,

P_{SW1}: is the switching losses due to transient time.

I_D and V_D: are the drain-source current and drain-source voltage respectively, assuming that i_{DS} and v_{DS} are both with linear transition characteristics.

f: is the switching frequency of the load current, and

t_{ON} and t_{OFF}: are the turn-ON and turn-OFF transient switching times respectively.

- **Output Capacitance Losses**: It is produced when stored energy in output capacitance of the MOSFET during turn-OFF period is dissipated internally through the MOSFET in the form of Joule heating energy during the turn-ON operating state.

This type of power dissipation is expressed as in the following equation [99]:

$$P_{SW2} = \frac{1}{2} C_{OSS} . V_D^2 . f \tag{4.95}$$

Where,

C_{OSS} is the MOSFET output capacitance, which is given from the following expression:

$$C_{OSS} = C_{GD} + C_{DS} \tag{4.96}$$

Being,

C_{GD}: is the gate-drain capacitance, and

C_{DS}: is the drain-source capacitance.

Therefore; the total switching losses equals to the summation of both transient and capacitance losses, as follows:

$$P_{SW} = P_{SW1} + P_{SW2} \tag{4.97}$$

Due to using the same MOSFET category for both **MNPCI** and **H-bridge** topologies, and assuming ideal state of switches and both are working under resonance operational mode, then the **switching losses** are approximately **the same**, and it can be calculated directly from the specifications of the **data sheet** parameters.
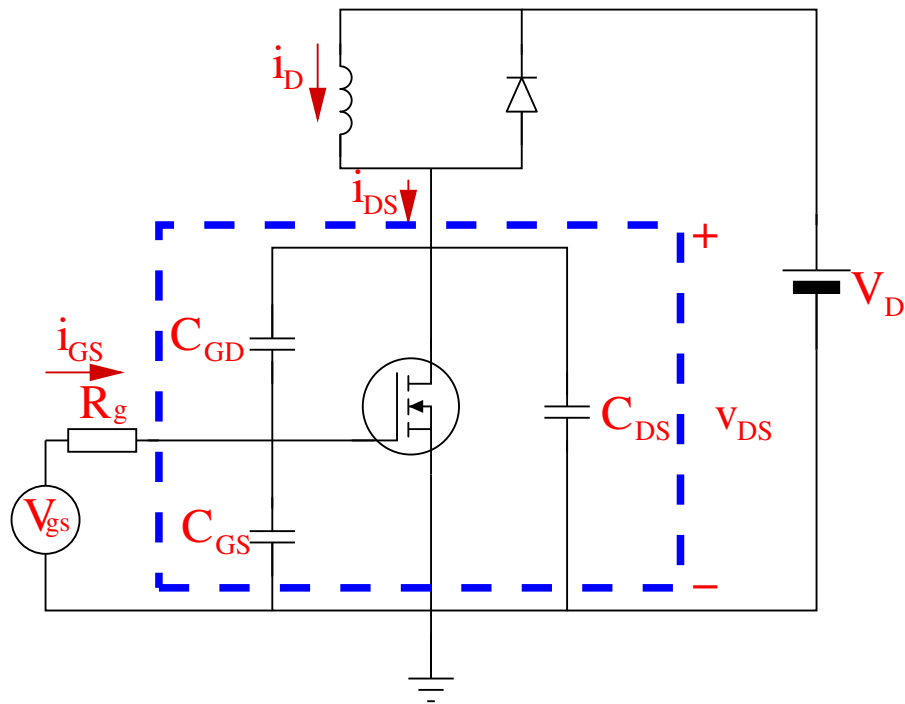
Figure 4.39: MOSFET Switching and Equivalent Circuit
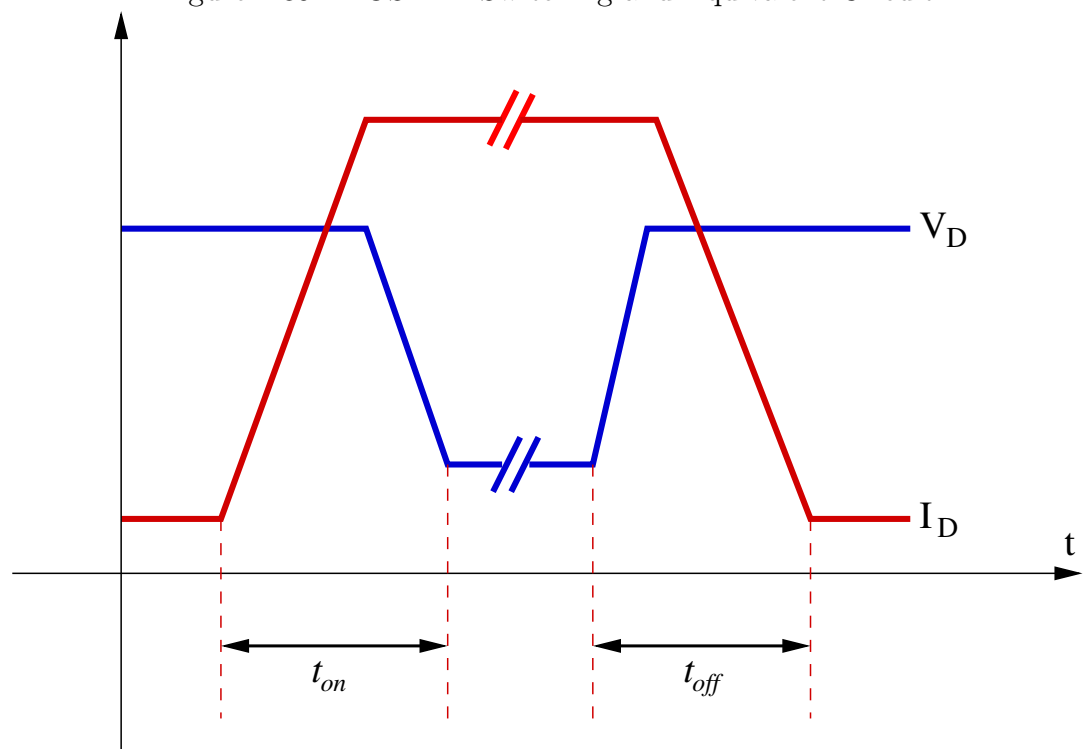
Figure 4.40: MOSFET Waveforms for Inductive Mode

Conduction Losses

It is formed when the MOSFET operates under ON-switching state, thus; the MOSFET acts like a constant resistance $R_{DS(ON)}$. This resistor is linearly proportional to the ratio of v_{DS} over i_D change, as follows [100]:

$$R_{DS(ON)} = \left.\frac{\partial v_{DS}}{\partial i_D}\right|_{v_{GS}=constant} \tag{4.98}$$

Where,

$R_{DS(ON)}$ is the ON state resistance and its value is constant and taken from the MOSFET data sheet.

Therefore; the conduction losses for a specified MOSFET is equal to the following expression:

$$P_{cond.} = I_D^2 . R_{DS(ON)} \tag{4.99}$$

Where, $P_{cond.}$: is the conduction power losses of the MOSFET.

The **ON-state** operational modes of the **MNPCI** configuration is completely **different** from that in the **H-bridge** topology, because at the **MNPCI**, both switches specified for positive or negative modes work together for a certain switching time t_α, then one of them is turned-OFF and the other keeps working for the rest of the cycle, while at the **H-bridge** both MOSFETs of different inverter legs operate together for all cycle of both the positive and the negative modes. Which means there is a new factor of **Duty Cycle** (D) should be introduced in Equation (4.99) to agree with this difference of operation.

Therefore; the conduction losses that satisfies the above condition is equal to the following equation:

$$P_{cond.} = D.I_D^2.R_{DS(ON)} \qquad (4.100)$$

Where,

D: is the Duty Cycle, and for one of the MNPCI switches, it can be found from the following expression:

$$D_1 = \frac{T_{ON1}}{T} = \frac{t_\alpha|_{HalfofSignalTime}}{T} = \frac{89.3\mu sec}{178.6\mu sec} = 0.5 \qquad (4.101)$$

Being, T: is the total signal time period in second.

And the Duty Cycle for the other MNPCI-switch is given by the following formula:

$$D_2 = \frac{T_{ON2}}{T} = \frac{t_\alpha|_{PointofOperation}}{T} = \frac{72.6\mu sec}{178.6\mu sec} = 0.406 \qquad (4.102)$$

Thus; the **conduction losses** of the **MNPCI** prototype $(P_{MNPCIcond.})$ is equal to the following expression:

$$P_{MNPCIcond.} = 2\left(D_1.I_D^2.R_{DS(ON)} + D_2.I_D^2.R_{DS(ON)}\right)$$
$$= 2\left(0.5.I_D^2.R_{DS(ON)} + 0.406.I_D^2.R_{DS(ON)}\right)$$
$$P_{MNPCIcond.} = 1.812.I_D^2.R_{DS(ON)}$$

$$(4.103)$$

The Duty Cycle of the **H-bridge** switches is similar to D_1, due to operating the successive switches for half period of signal at each positive and negative cycles, therefore; the **conduction losses** of the H-bridge inverter $(P_{H-bridgecond.})$ is equal to the following formula:

$$P_{H-bridgecond.} = 4\left(D_1.I_D^2.R_{DS(ON)}\right) = 4\left(0.5.I_D^2.R_{DS(ON)}\right)$$

$$P_{H-bridgecond.} = 2.I_D^2.R_{DS(ON)} \tag{4.104}$$

Therefore; the percentage of the **conduction losses difference** between the **MN-PCI** at point of operation and the **H-bridge** topology $(P_{Diff.})$ is equal to the following expression:

$$P_{Diff.} = \frac{P_{H-bridgecond.} - P_{MNPCIcond.}}{P_{H-bridgecond.}}.100\%$$
$$= \frac{2.I_D^2.R_{DS(ON)} - 1.812.I_D^2.R_{DS(ON)}}{2.I_D^2.R_{DS(ON)}}.100\%$$

$$P_{Diff.} = 9.4\% \tag{4.105}$$

By considering the last percentage; this fact means that the **MNPCI configuration** at selected point of operation of $t_\alpha = 72.6\mu sec$ has **better dissipated power** than the **losses** in **H-bridge** by (9.4%), i.e. gaining **higher efficiency** and **less cost**, which **verifies** the **MNPCI** topology choice.

4.9   Operational Region and Proposed Applications

According to Fig. 1.9 introduced earlier in Chapter 1 for optimum operation of LLC topology, the experimental values of the load inductance in Table 4.1 are chosen carefully so that the inductance ratio (β), which is defined as the ratio between the series to parallel inductance in the topology, is varied in the range between $(1.057 \longrightarrow 4.8)$, and the phase shift angle (ϕ) between voltage and current is less than (6°) being measured experimentally, which ensures that the IH system operates within the best performance region specified by the blue lines, as clearly shown in the red region in Fig. 4.41.

The quality factor achieved by the configuration is $(Q \geq 20)$, which implies that the current gain of the IH load is at least twenty times the MNPCI configuration current, i.e. if the inverter current is 10 Amp., then the load current is at least 200 Amp.. This current gain depends on the point of operation, which in turn depends on β and ϕ values. For the selected point of operation of ON switching time $(t_\alpha = 72.6\mu sec)$ with IH load tank values of $L1 = 105.7\mu H$, $R = 10.07$ and $L = 33\mu H$, the inductance ratio equals to 3.2, thus; the current gain is greater than 30, as can be seen in Fig. 4.41, which means that the prototype load current is more than thirty times the MNPCI current, i.e. achieving very high current gain with less switching and conduction losses and hence decreasing the dissipated power and cost with higher efficiency.

Therefore, the MNPCI configuration is very suitable for industrial applications, like heating materials, surface hardening, tube welding and coreless furnaces used for melting metals [10], also it is convenient for domestic applications like cooking pans and water-heaters, but because of the presence of harmonics in the output current signal, the usage of MNPCI in some of the medical applications that requires precise and local heating will be limited, as there is more than one penetration depth rather than one shot, which requires more developments to be done on the prototype like using more fitted design with powerful capacitors to reduce the harmonics to the minimum possible level.
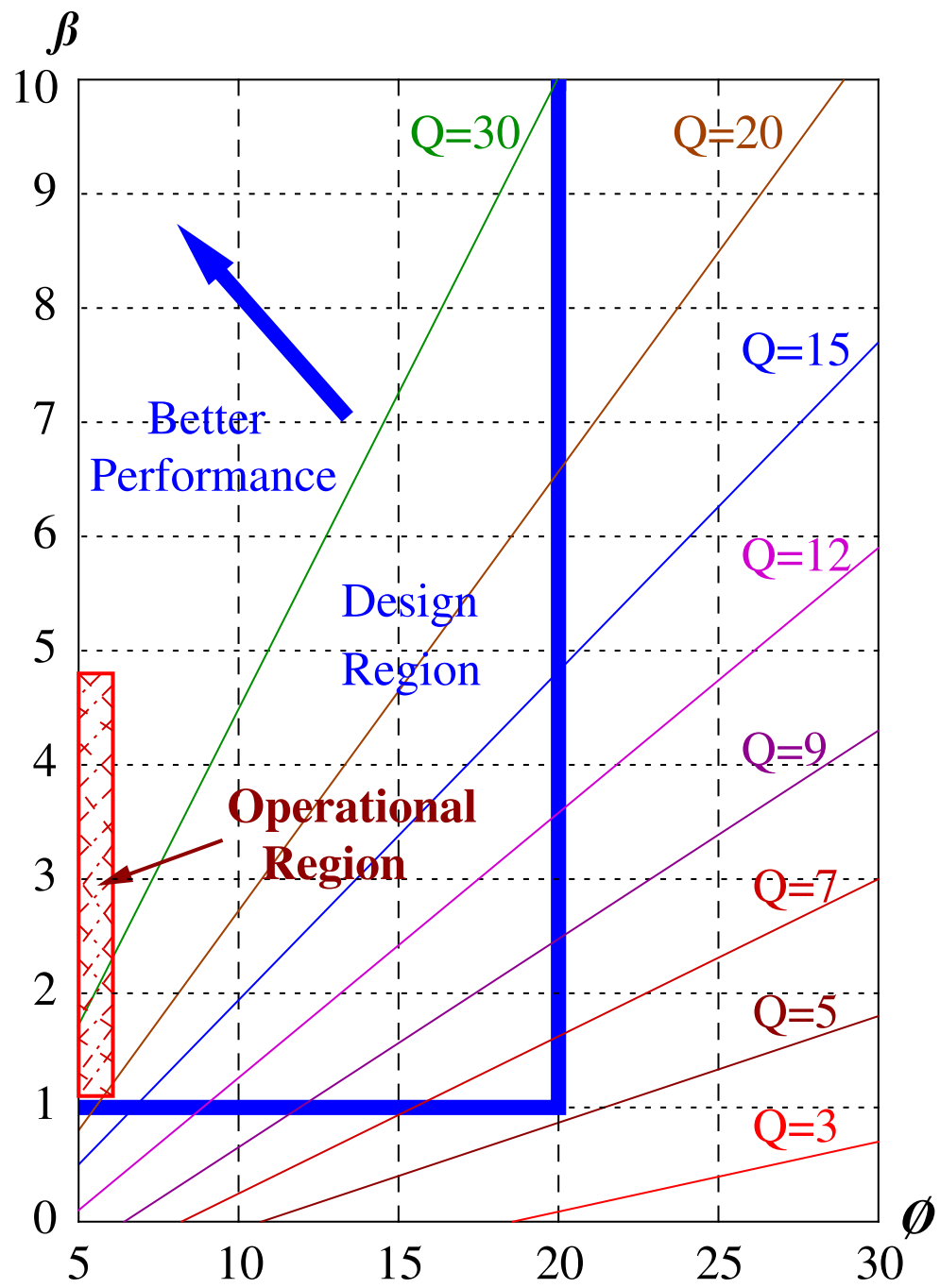
Figure 4.41: Experimental Operational Region

4.10   Conclusion

This chapter introduces a new IH system using MNPCI topology connected to a variable resonant load tank. The design involves utilizing the LLC topology to model the variable load tank to match the changeable load behaviour characteristics during the heating cycle. The new configuration operates under half the DC rail voltage and performs the soft switching modes of both the ZCS and the ZVS, which reduces the switching losses and increases the efficiency to more than 85 %.

The control algorithm is chosen to maintain approximately zero to 6° phase shift angle between output voltage and current at all load conditions. The experimental IH load tank values are chosen carefully to operate under optimum condition within inductance ration β between $(1.057 \longrightarrow 4.8)$ range, with current of gain exceeded thirty at selected point of operation.

The analysis of the system showed that the average power derivation depends primarily on the fundamental angular frequency and on the inductor magnitude and it is consisted from harmonics. Also, the analysis showed that increasing the equivalent resistance means decreasing the effective cross sectional area and decreasing the skin depth, as a consequence; the switching frequency of the proposed prototype is increased. The experimental results showed that the harmonic content of proposed system consists mainly from 1st, 3rd, 5th harmonic components and with 7th component but with less effect on harmonic map that can be neglected depending mainly on the operational point selection. The 1st, 3rd components are the most efficient harmonics, because of their amplitude values as compared with the amplitudes of the rest harmonics of 5th and 7th components.

The proposed configuration is verified as a design with the property of low harmonic distortion noise, due to the utilizing of MNPCI topology.

The optimal control strategy includes the selection of best operational point of ON switching time t_α, which ensures minimum harmonic distortion noise and as a consequence maximum heating power percentage is achieved. The estimated effective ON time range lies between time interval of $\left(\frac{1}{4f_n} < t_\alpha < \frac{T}{2}\right)$, at these limits the configuration may operate under the peak point condition within the acceptable operational region at which optimal power delivered to the IH load tank.

The acceptable operational region of configuration ON time range lies between time period of $\left(\frac{T}{3.3} < t_\alpha < \frac{T}{2}\right)$, within those limits the configuration operates under the optimal power condition.

The analytical analysis shows precise coincide with the experimental results, through the optimum operational point of both has exactly the same value, which proves the reliability of the proposed configuration, with efficiency achieved of the proposed topology exceeded the 85%, however; this percentage can be increased through using more powerful voltage source capacitors rather than electrolytic capacitors used in the design to achieve more efficient IH prototype, but with the drawback of increasing the cost.

Therefore; MNPCI prototype is verified as a reliable IH inverter design through operating under minimum THD value condition of about 6.5%, which is below the maximum acceptable threshold limits according to **IEEE STD 519 Standards**. The corresponding proposed applications of the MNPCI prototype are the industrial and domestic, due to high output current gain value of more than 30 and lower cost and dissipated power.

Chapter 5

Conclusions and Suggested Future Work

5.1 Conclusion

T he selection of inverter has a great effect on the efficiency of IH system design, because IH configuration has the feature of high inductance characteristic and variable load behaviour of specifically workpiece material inductance and resistance during the heating cycle, which entails high injection of harmful harmonic content to the system, especially when talk about high current/voltage and power, as in industrial plant systems. This is certainly a drawback that causes increasing in the losses and hence, decreasing the efficiency of the configuration. For that reason, choosing an appropriate inverter plays a primary role in mitigating and reducing the undesired harmonic noise particularly when accompanied by optimal control algorithm and suitable resonant load tank topology, they are together perform maximum effective power transfer from IH supply to the IH load circuit.

According to that and due to its popular merit of low harmonic distortion inverter, especially when used in medium power application as AC motor drive and in high power applications with medium voltage such as laminators, mills, conveyors, pumps, fans,

compressors...etc or even in other power application like solar cell circuits, the idea arose of using MNPCI topology to develop a novel DC/AC inverter in IH configuration with better harmonic noise properties.

Therefore, the first phase of this research focuses on the investigation and construction of a new resonant converter using MNPCI configuration. The proposed design has shared the advantage aspects of both VFI and CFI converter topologies, thus; it can be considered as a Hybrid Voltage-Current Fed Inverter (HVCFI) topology.

Through using two bulk voltage source capacitors of equal values, the design supplies constant voltage delivery of half the DC rail voltage that maintains exerting half the DC main source tension on the inverter MOSFET-switches, which facilitates the soft switching mode achievement and decreases a lot the switching losses and thus increases the efficiency.

The LLC equivalent is utilized to model the resonant load tank topology, due to; First: its high load current gain ratio of Q times the inverter current, Second: the ability to absorb the parasitic inductance components by connecting an extra series inductor with the parallel resonant load, Third: the ability to compensate the matching transformer which reduces the capital cost and Fourth: the capability for short circuit immunity especially from capacitor rush current which occurs at time of start charging and that may cause damage to the sensitive components like MOSFETs.

So, the MNPCI current is smaller by Q times than the load current which means less switching losses and less dissipated heat inside the inverter switches, therefore no heat sinc protection is needed during the experimental work, which means less cost. Besides, a Zero Current Detector (ZCD) circuit is built to achieve zero current switching mode and to compensate the existence of Current Transformer (CT) required for load feedback, which gives again the benefit of less cost, size and better efficiency.

Therefore, a modified design of *LLC* topology is introduced and verified, by adding an extra current sensing resistor of very small value in series with the conventional *LLC* model. This resistor has a tiny damping effect on the maximum power transfer from MNPCI supply to the optimized *LLC* load of less than 0.1% only, which can be neglected.

This research work has been presented and published in [95].

In order to match the changeable characteristics of IH load during the heating cycle, a variable *LLC* resonant load tank topology is built and verified to form the second phase of the research. The corresponding control strategy requires the MNPCI design to operate under variable switching frequency and according to changing load conditions, in order to keep tuning to the natural resonant frequency and achieves approximately zero phase shift angle ϕ between output voltage and current and conducting under ZCS and ZVS modes at all load cases, which decreases the switching losses and increases the efficiency to more than 85%.

The configuration design, output signal and basis of operation has been discussed intensively, depending on its four operational modes and on operation under half the DC rail voltage, which reduces the MOSFETs losses of MNPCI topology at all proposed load conditions. The power analysis is then derived in details taking into account the harmonic components appeared in the output experimental signal.

This work has been presented and published in [96].

To prove the harmonic reduction theory of the proposed system, an intensive analysis to the harmonic amplitude content of different harmonic orders existed in the output signal of both current and voltage, is done for a specific load case. The analysis of experimental work revealed that the t_α range condition for maximum power transfer condition lays between ON switching time period of $\left\{ \frac{1}{4f_n} < t_\alpha < \frac{T}{2} \right\}$ limits.

The value of switching frequency f_n that achieves resonant state is hardly to be manipulated, because it depends mainly on the hardware aspect specifications of the inverter and the LLC resonant load tank parameters, and as the change of total output signal time T is also difficult (but not impossible), due to be depending on the value of time constant τ, which in turn depends again on the hardware of both series inductance and equivalent resistance (L_1 and R), therefore; the best and easiest way to achieve the optimum harmonic control is changing the ON switching time t_α, in order to perform best operational point within the two restricted time limits that have in between the lowest harmonic noise level and optimal heating power.

Therefore, a 21 point of different t_α are selected starting from $\left\{t_\alpha = \frac{1}{4f_n}\right\} \longrightarrow$ $\left\{t_\alpha = \frac{T}{2}\right\}$, in order to draw a map for harmonic amplitude band change limit, also a curve of 5 operational points of t_α are drawn, and a comparison is made between the corresponding harmonic distortion content of three selected values of t_α, to find the optimal operational point from them.

Thus, through comparing the **Frequency Spectrum FS** analysis between three different operational points at ON switching time of $t_\alpha = 51.2\mu sec$ with $t_\alpha = 72.6\mu sec$ and $t_\alpha = 89.3\mu sec$, shows that the configuration spectrum expresses harmonic content of only 1st, 3^{ed} and 5th basic harmonics, with generally very low 7th harmonic oscillation that can be neglected at some point depending on the selected time t_α. In spite of having best harmonic content at $t_\alpha = 72.6\mu sec$, but generally the configuration still have low harmonic distortion levels, which is the main prospective goal of the proposed prototype design.

To identify the optimum operational point of the MNPCI configuration, it is very important to find the available power for the selected t_α points. This determination demonstrates that the available power begins from initial operational point of $\left\{t_\alpha = \frac{1}{4f_n}\right\}$, starting from minimum value of 76.4% with a distortion percent of 24% at $t_\alpha = 41.7\mu sec$,

then it rises up until reaches an average value of about 95% with distortion noise of 5% at $t_\alpha = 63.1\mu sec$ and then it keeps increasing to the maximum peak of 96.8% at $t_\alpha = 72.6\mu sec$, which means the harmonic noise at this specific operational point is only 3%, which is the minimal possible noise at all and hence, it represents the optimal eligible operational point. Afterwards, it slightly decreases to settle at the average value again until half of signal cycle time limit $\left\{t_\alpha = \frac{T}{2}\right\}$.

Therefore, from the above it can be deduced that the harmonic noise can be controlled and mitigated through the appropriate choice of optimum operational point at specific ON switching time t_α being calculated and observed. In other words, this indicates that the t_α selection controls the **Total Harmonic Distortion THD** content of output voltage $v(t)$ and current $i(t)$ and hence, controls the maximum heating power by increasing the fundamental harmonic amplitude on account of minimizing the rest 3^{ed}, 5th and 7th harmonics.

The reliability of the MNPCI configuration is verified through comparing the THD content at the selected operational point of ON switching time t_α of the proposed prototype with the **IEEE STD 519 Standards**, which shows that it is conducting within the acceptable operational region limit of $\left\{\frac{T}{3.3} < t_\alpha < \frac{T}{2}\right\}$ and under minimum Total Harmonic Distortion condition of $\{THD = 6.5\%\}$, which is much lower than the IEEE standard permissible threshold level that equals upto $\{THD = 20\%\}$.

This research work has been presented and published in [101].

Finally, it should be pointed that the main disadvantage aspect of the configuration is increasing its compensating capacitor C value by a factor of $\left\{\frac{\beta+1}{\beta}\right\}$ more than the series resonant compensator, which means definitely more cost, but this increase still can be controlled by inductance ratio β choice, besides it can be mitigated through increasing the capacitance voltage, for which applying maximum voltage of V_c gives minimum capacitance, because $\left\{C \propto \frac{1}{V_c}\right\}$.

5.2   Suggested Future Work

I n order to develop this research, the following modification improvements could be included as a future work:

- To complete the full picture of IH circuit configuration, it is very important to add the AC/DC rectifier phase to the MNPCI prototype instead of normal DC supply, either as a non-controlled stage of a simple diode-bridge rectifier, or even as a controlled thyristor bridge rectifier with complicated control algorithm and more switching losses, but with the advantage aspect of being capable to control the input power.

- Further investigation should be done accompanied with connecting the AC/DC rectifier stage regarding the harmonic distortion content injected to the AC grid side, to find its effect on the balance of the system.

- Another investigation can be done by adding a DC/DC Buck converter as a power control stage after the non controlled AC/DC diode rectifier side, to improve the power factor by reducing the switching losses of rectifier side. The output voltage of this intermediate Buck stage should be chosen carefully in order not to exert over voltage tension on the MNPCI switches.

- Investigations can be done also by changing the inductance ratio β, by connecting variable series inductance instead of fixed value in the LLC topology, through which maximum power transfer can be controlled and the total signal time-limit can be varied through changing the time constant τ of resonant load tank circuit.

- Investigation can be included through inserting a matching transformer for load matching purposes, accompanied with analysis must be done to its effect on harmonic noise in proposed IH system.

- Another modification can be done by using another topology of resonant load tank like CCL or CLL and make a comparison between the output power and efficiency of different topologies.

- Another improvement can be done to the proposed prototype by using more powerful voltage source capacitors at the DC side, to improve power delivery to the MNPCI inverter.

- Another modification can be included through experimenting the proposed MN-PCI supply on a domestic IH load application.

- Another modification to the control strategy of the prototype design can be done, through inserting the t_α feedback automatic tracking control to the optimum algorithm, depending on the THD curve being introduced before.

Bibliography

[1] E. Laithwaite, "The influence of michael faraday on power engineering," *Power Engineering Journal*, vol. 5, no. 5, pp. 209–219, 1991.

[2] J. Davies and P. Simpson, *Induction heating handbook.* McGraw-Hill, 1979.

[3] W. Moreland, "The induction range: Its performance and its development problems," *Industry Applications, IEEE Transactions on*, vol. IA-9, no. 1, pp. 81–85, Jan 1973.

[4] P. Stauffer, T. C. Cetas, and R. C. Jones, "Magnetic induction heating of ferromagnetic implants for inducing localized hyperthermia in deep-seated tumors," *Biomedical Engineering, IEEE Transactions on*, vol. BME-31, no. 2, pp. 235–251, Feb 1984.

[5] G. Martin Segura *et al.*, "Induction heating converter's design, control and modeling applied to continuous wire heating," 2012.

[6] F. Forest, S. Faucher, J. Y. Gaspard, D. Montloup, J. J. Huselstein, and C. Joubert, "Frequency-synchronized resonant converters for the supply of multiwinding coils in induction cooking appliances," *IEEE Transactions on Industrial Electronics*, vol. 54, no. 1, pp. 441–452, Feb 2007.

[7] F. Forest, E. Laboure, F. Costa, and J. Y. Gaspard, "Principle of a multiload/single converter system for low power induction heating," *IEEE Transactions on Power Electronics*, vol. 15, no. 2, pp. 223–230, 2000.

[8] O. Lucia, L. A. Barragan, J. M. Burdio, Ó. Jiménez, D. Navarro, and I. Urriza, "A versatile power electronics test-bench architecture applied to domestic induction heating," *IEEE Transactions on Industrial Electronics*, vol. 58, no. 3, pp. 998–1007, 2011.

[9] J. M. Burdio, F. Monterde, J. R. Garcia, L. A. Barragan, and A. Martinez, "A two-output series-resonant inverter for induction-heating cooking appliances," *IEEE Transactions on Power Electronics*, vol. 20, no. 4, pp. 815–822, 2005.

[10] J. Espi Huerta, E. Dede Garcia Santamaria, R. Garcia Gil, and J. Castello Moreno, "Design of the l-lc resonant inverter for induction heating based on its equivalent sri," *Industrial Electronics, IEEE Transactions on*, vol. 54, no. 6, pp. 3178–3187, 2007.

[11] V. Esteve, E. Sanchis-Kilders, J. Jordan, E. J. Dede, C. Cases, E. Maset, J. B. Ejea, and A. Ferreres, "Improving the efficiency of igbt series-resonant inverters using pulse density modulation," *Industrial Electronics, IEEE Transactions on*, vol. 58, no. 3, pp. 979–987, 2011.

[12] H. Fujita, N. Uchida, and K. Ozaki, "A new zone-control induction heating system using multiple inverter units applicable under mutual magnetic coupling conditions," *IEEE Transactions on Power Electronics*, vol. 26, no. 7, pp. 2009–2017, July 2011.

[13] I. Yilmaz, M. Ermis, and I. Cadirci, "Medium-frequency induction melting furnace as a load on the power system," *Industry Applications, IEEE Transactions on*, vol. 48, no. 4, pp. 1203–1214, 2012.

[14] S. Chudjuarjeen, A. Sangswang, and C. Koompai, "An improved llc resonant inverter for induction-heating applications with asymmetrical control," *IEEE Transactions on Industrial Electronics*, vol. 58, no. 7, pp. 2915–2925, 2011.

191

[15] C.-C. Tai and M.-K. Chen, "A compact half-bridge induction heating system for magnetic nanoparticle thermotherapy applications," *Biomedical Engineering: Applications, Basis and Communications*, vol. 19, no. 01, pp. 27–35, 2007.

[16] C.-C. Tai and C.-C. Chen, "The design of a half-bridge series-resonant type heating system for magnetic nanoparticle thermotherapy."

[17] A. Mühlbauer, *History of Induction Heating and Melting*, ser. Edition heat processing.   Vulkan, 2008. [Online]. Available: https://books.google.co.uk/books?id=vHn1ge59cZsC

[18] G. Landi and A. Bakuzis, "On the energy conversion efficiency in magnetic hyperthermia applications: A new perspective to analyze the departure from the linear regime," *Journal of Applied Physics*, vol. 111, no. 8, p. 083915, 2012.

[19] H. P. Ngoc, H. Fujita, K. Ozaki, and N. Uchida, "Phase angle control of high-frequency resonant currents in a multiple inverter system for zone-control induction heating," *IEEE Transactions on power electronics*, vol. 26, no. 11, pp. 3357–3366, 2011.

[20] Y. Kawaguchi, E. Hiraki, T. Tanaka, H. Sadakata, A. Fujita, H. Omori, and M. Nakaoka, "A comparative evaluation of dcm control and ccm control for soft-switching pfc converter," in *IECON 2010 - 36th Annual Conference on IEEE Industrial Electronics Society*, Nov 2010, pp. 250–255.

[21] F. P. Dawson and P. Jain, "A comparison of load commutated inverter systems for induction heating and melting applications," *Power Electronics, IEEE Transactions on*, vol. 6, no. 3, pp. 430–441, 1991.

[22] M. K. Kazimierczuk and D. Czarkowski, *Resonant power converters*.   John Wiley & Sons, 2012.

[23] O. LucÃŋa, J. M. BurdÃŋo, I. MillÃąn, J. Acero, and L. A. BarragÃąn, "Efficiency-oriented design of zvs half-bridge series resonant inverter with variable frequency

duty cycle control," *IEEE Transactions on Power Electronics*, vol. 25, no. 7, pp. 1671–1674, July 2010.

[24] R. L. Steigerwald, "A comparison of half-bridge resonant converter topologies," *IEEE Transactions on Power Electronics*, vol. 3, no. 2, pp. 174–182, Apr 1988.

[25] E. J. Dede, J. V. Gonzalez, J. A. Linares, J. Jordan, D. Ramirez, and P. Rueda, "25-kw/50-khz generator for induction heating," *IEEE transactions on industrial electronics*, vol. 38, no. 3, pp. 203–209, 1991.

[26] H. W. Koertzen, J. D. van Wyk, and J. A. Ferreira, "Design of the half-bridge, series resonant converter for induction cooking," in *Power Electronics Specialists Conference, 1995. PESC '95 Record., 26th Annual IEEE*, vol. 2, Jun 1995, pp. 729–735 vol.2.

[27] M. Kamli, S. Yamamoto, and M. Abe, "A 50-150 khz half-bridge inverter for induction heating applications," *Industrial Electronics, IEEE Transactions on*, vol. 43, no. 1, pp. 163–172, 1996.

[28] H. Koertzen, J. Ferreria, and J. Van Wyk, "A comparative study of single switch induction heating converters using novel component effectivity concepts," in *Power Electronics Specialists Conference, 1992. PESC'92 Record., 23rd Annual IEEE*. IEEE, pp. 298–305.

[29] C. Edgerley, L. Smith, and C. F. Wilford, "Electric metal melting-a review," *Power Engineering Journal*, vol. 2, no. 2, pp. 83–92, 1988.

[30] E. Dede, J. Jordan, J. Linares, J. Gonzalez, V. Esteve, D. Ramirez, and E. Maset, "On the design of medium and high power current fed inverters for induction heating," in *Industry Applications Society Annual Meeting, 1991., Conference Record of the 1991 IEEE*, 1991, pp. 1047–1053 vol.1.

[31] L. Grajales, J. Sabate, K. Wang, W. Tabisz, and F. Lee, "Design of a 10 kw, 500 khz phase-shift controlled series-resonant inverter for induction heating," in *Industry*

Applications Society Annual Meeting, 1993., Conference Record of the 1993 IEEE. IEEE, 1993, pp. 843–849.

[32] H. Fujita and H. Akagi, "Pulse-density-modulated power control of a 4 kw, 450 khz voltage-source inverter for induction melting applications," *Industry Applications, IEEE Transactions on*, vol. 32, no. 2, pp. 279–286, 1996.

[33] J. Ho and M. Lee, "A novel pwm inverter control circuitry for induction heating," in *Power Electronics Congress, 1996. Technical Proceedings. CIEP'96., V IEEE International*. IEEE, 1996, pp. 113–119.

[34] P. Dorland, J. Van Wyk, and O. Stielau, "On the influence of coil design and electromagnetic configuration on the efficiency of an induction melting furnace," *Industry Applications, IEEE Transactions on*, vol. 36, no. 4, pp. 946–957, 2000.

[35] I. Khan, J. Tapson, and I. De Vries, "Frequency control of a current-fed inverter for induction heating," in *Industrial Electronics, 2000. ISIE 2000. Proceedings of the 2000 IEEE International Symposium on*, vol. 1, 2000, pp. 343–346 vol.1.

[36] M.-P. Chen, J.-K. Chen, K. Murata, M. Nakahara, and K. Harada, "Surge analysis of induction heating power supply with pll," *Power Electronics, IEEE Transactions on*, vol. 16, no. 5, pp. 702–709, 2001.

[37] S. Chudjuarjeen, C. Koompai, and V. Monyakul, "Full-bridge current-fed inverter with automatic frequency control for forging application," in *TENCON 2004. 2004 IEEE Region 10 Conference*, vol. 500. IEEE, 2004, pp. 128–131.

[38] H. Tanimatsu, T. Ahmed, E. Hiraki, I. Hirota, H. Omori, N. A. Ahmed, H. W. Lee, and M. Nakaoka, "Utility frequency ac connected high frequency ac one stage power processing conversion circuits with boosted dc voltage rail," in *2005 International Conference on Electrical Machines and Systems*, vol. 2, Sept 2005, pp. 1101–1106 Vol. 2.

[39] L. Jingang, Z. Yanru, and M. Xin, "Study on a new way of load-matched for voltage-source induction heating inverters," in *Industrial Electronics and Applications, 2006 1ST IEEE Conference on*, 2006, pp. 1–5.

[40] Z. Wang, Z. Lou, and H. Chen, "A novel dual-llc resonant soft switching converter for super high frequency induction heating power supplies," in *Power Electronics Specialists Conference, 2007. PESC 2007. IEEE*, 2007, pp. 2561–2566.

[41] S. Kubota, M. Sato, F. Ito, Y. Shimaoka, and K. Nishioka, "Soft switching pwm inverter for induction heating applied to heating of ferromagnetic metal," in *Power Electronics and Motion Control Conference, 2008. EPE-PEMC 2008. 13th*. IEEE, 2008, pp. 1309–1315.

[42] H. Sugimura, S.-P. Mun, S.-K. Kwon, E. Hiraki, and M. Nakaoka, "Active voltage clamped edge-resonant soft switching pwm high frequency cyclo-converter using bidirectional switches," in *Power Electronics Specialists Conference, 2008. PESC 2008. IEEE*. IEEE, 2008, pp. 3917–3923.

[43] O. Lucia, J. Burdio, I. Millan, J. Acero, and S. Llorente, "Efficiency optimization of half-bridge series resonant inverter with asymmetrical duty cycle control for domestic induction heating," in *Power Electronics and Applications, 2009. EPE'09. 13th European Conference on*. IEEE, 2009, pp. 1–6.

[44] S. M. W. Ahmed, M. Eissa, M. Edress, and T. S. Abdel-Hameed, "A multi-output high frequency cycloinverter operation for induction-heating cooking appliances-harmonic study," in *Industrial Electronics and Applications, 2009. ICIEA 2009. 4th IEEE Conference on*. IEEE, 2009, pp. 2267–2272.

[45] R. Fuentes, J. Juliet, J. Estrada, F. Ahumada, and F. Campaña, "Design aspects and experimental results of a high power factor induction heating system," in *Industrial Electronics, 2009. IECON'09. 35th Annual Conference of IEEE*. IEEE, 2009, pp. 373–377.

[46] Q. Xiao, J. Zhao, and M. Wang, "Research on frequency tracking capacitive pwm of induction heating power supply," in *Challenges in Environmental Science and Computer Engineering (CESCE), 2010 International Conference on*, vol. 2. IEEE, 2010, pp. 377–380.

[47] J. Jittakort, A. Sangswang, S. Naetiladdanon, C. Koompai, and S. Chudjuarjeen, "A soft switching class d current source inverter for induction heating with non-ferromagnetic load," in *Power Electronics and Applications (EPE 2011), Proceedings of the 2011-14th European Conference on.* IEEE, 2011, pp. 1–10.

[48] H. Sarnago, O. LucÃŋa, A. Mediano, and J. M. BurdÃŋo, "High-efficiency power converters for domestic induction heating applications," in *IECON 2012 - 38th Annual Conference on IEEE Industrial Electronics Society*, Oct 2012, pp. 3268–3273.

[49] D. Boian, C. Biris, R. Teodorescu, and M. Sztykiel, "Development of modulation strategies for npc converter addressing dc link voltage balancing and cmv reduction," in *Power Electronics for Distributed Generation Systems (PEDG), 2012 3rd IEEE International Symposium on.* IEEE, 2012, pp. 828–835.

[50] J. Rodriguez, J.-S. Lai, and F. Z. Peng, "Multilevel inverters: a survey of topologies, controls, and applications," *Industrial Electronics, IEEE Transactions on*, vol. 49, no. 4, pp. 724–738, 2002.

[51] B. Wu, *High-power converters and AC drives.* Wiley, 2006.

[52] E. Cengelci, S. U. Sulistijo, B. Woo, P. Enjeti, R. Teodorescu, and F. Blaabjerg, "A new medium voltage pwm inverter topology for adjustable speed drives," in *Industry Applications Conference, 1998. Thirty-Third IAS Annual Meeting. The 1998 IEEE*, vol. 2, 1998, pp. 1416–1423 vol.2.

[53] Y. Ge, R. Hu, Z. Zhang, and Q. Shen, "Optimization control of induction hardening process," in *Mechatronics and Automation, Proceedings of the 2006 IEEE International Conference on*, June 2006, pp. 1126–1130.

[54] C. Koughia, S. Kasap, and P. Capper, "Springer handbook of electronic and photonic materials," 2007.

[55] S. Yamada, E. Otsuki, and T. Otsuka, "Ac resistivity of mn-zn ferrites," in *Telecommunications Energy Conference, 1991. INTELEC'91., 13th International.* IEEE, 1991, pp. 703–708.

[56] M. J. Tung, W. C. Chang, C. S. Liu, T. Y. Liu, C. J. Chen, and T. Y. Tseng, "Study of loss mechanisms of mn-zn ferrites in the frequency from 1 mhz to 10 mhz," *IEEE Transactions on Magnetics*, vol. 29, no. 6, pp. 3526–3528, Nov 1993.

[57] A. H. Al-Omari, S. MacVeigh, M. Z. Ahmed, P. Davey, M. Blackler, and J. Welsh, "A new method to analyse eddy current loss in an integrated magnetic structure for boost converter," in *2016 IEEE Transportation Electrification Conference and Expo, Asia-Pacific (ITEC Asia-Pacific)*, June 2016, pp. 537–542.

[58] "Ieee recommended practice for electrical impedance, induction, and skin effect heating of pipelines and vessels," *IEEE Std 844-2000*, pp. i–104, 2000.

[59] S. Kubota, M. Sato, F. Ito, N. Ogawa, and Y. Shimaoka, "The design method of the inverter for heating both a ferromagnetic metal and a paramagnetic metal," in *Power Electronics and Applications, 2007 European Conference on*, Sept 2007, pp. 1–10.

[60] V. Rudnev, D. Loveless, R. Cook, and M. Black, *Handbook of Induction Heating*, ser. Manufacturing Engineering and Materials Processing. Taylor & Francis, 2002.

[61] I. Khan, J. Tapson, and I. de Vries, "An induction furnace employing a 100 khz mosfet full-bridge current-source load-resonant inverter," in *Industrial Electronics, 1998. Proceedings. ISIE'98. IEEE International Symposium on*, vol. 2. IEEE, 1998, pp. 530–534.

[62] S. S. Zinn, S. L. Semiatin, B. M. I. C. Laboratories, and E. P. R. Institute, *Elements of induction heating : design, control, and applications / S. Zinn and S.L. Semiatin*

; *EPRI program managers, I.L. Harry and R.D. Jeffress.* Metals Park, Ohio : ASM International, 1988, "Bulk of the work was sponsored by the Electric Power Research Institute (EPRI) through its contract with Battelle Columbus Division"– Pref.

[63] J. Davies, *Conduction and Induction Heating*, ser. IEE power engineering series. P. Peregrinus Limited, 1990.

[64] R. Baker, "Heating of nonmagnetic electric conductors by magnetic induction - longitudinal flux," *American Institute of Electrical Engineers, Transactions of the*, vol. 63, no. 6, pp. 273–278, 1944.

[65] C. Tudbury, *Basics of induction heating*, ser. Basics of Induction Heating. J. F. Rider, 1960, no. v. 1.

[66] J. Tremayne, "Impedance and phase balancing of mains-frequency induction furnaces," *Electric Power Applications, IEE Proceedings B*, vol. 130, no. 3, pp. 161–170, 1983.

[67] K. Reichert, "The calculation of coreless furnace with electricity conducting crucible," *Archiv fÃijr Elektrotechnik*, vol. 49, no. 6, pp. 376–397, 1965.

[68] A. LundbÃďck, "Finite element modelling and simulation of welding of aerospace components," 2003.

[69] J. Donea, S. Giuliani, and A. Philippe, "Finite elements in the solution of electromagnetic induction problems," *International Journal for Numerical Methods in Engineering*, vol. 8, no. 2, pp. 359–367, 1974.

[70] S. Salon and J. DAngelo, "Applications of the hybrid finite element-boundary element method in electromagnetics," *Magnetics, IEEE Transactions on*, vol. 24, no. 1, pp. 80–85, 1988.

[71] C. H. GuĭĹr and J. Pan, *Handbook of thermal process modeling of steels*, ser. International Federation of Heat Treatment and Surface Engineering. CRC Press, 2009.

[72] N. Mohan, T. Undeland, and W. Robbins, *Power electronics: converters, applications, and design*, 2nd ed. Wiley, 1995.

[73] R. Baker and L. Bannister, "Electric power converter," *U.S.Patent*, no. 3867643, February,1975.

[74] F. Gao, P. Loh, F. Blaabjerg, R. Teodorescu, and D. Vilathgamuwa, "Five-level z-source neutral-point-clamped inverter," in *Power Electronics and Drive Systems, 2007. PEDS '07. 7th International Conference on*, Nov 2007, pp. 1054–1061.

[75] R. Baker, "Switching circuit," *U.S.Patent*, no. 4210826, July,1980.

[76] A. Nabae, I. Takahashi, and H. Akagi, "A new neutral-point-clamped pwm inverter," *Industry Applications, IEEE Transactions on*, vol. IA-17, no. 5, pp. 518–523, 1981.

[77] J.-S. Lai and F. Z. Peng, "Multilevel converters-a new breed of power converters," in *Industry Applications Conference, 1995. Thirtieth IAS Annual Meeting, IAS '95., Conference Record of the 1995 IEEE*, vol. 3, 1995, pp. 2348–2356 vol.3.

[78] J.-C. Wu and C.-W. Chou, "A solar power generation system with a seven-level inverter," *Power Electronics, IEEE Transactions on*, vol. 29, no. 7, pp. 3454–3462, 2014.

[79] D. H. Lee, S. Lee, and F. Lee, "An analysis of midpoint balance for the neutral-point-clamped three-level vsi," in *Power Electronics Specialists Conference, 1998. PESC 98 Record. 29th Annual IEEE*, vol. 1, 1998, pp. 193–199 vol.1.

[80] K. H. Bhalodi and P. Agrawal, "Space vector modulation with dc-link voltage balancing control for three-level inverters," in *Power Electronics, Drives and Energy Systems, 2006. PEDES'06. International Conference on*. IEEE, 2006, pp. 1–6.

[81] Z. Gao and Y. Zhou, "Research on switching losses for induction heating power supply with llc resonant load," in *Electronic and Mechanical Engineering and Information Technology (EMEIT), 2011 International Conference on*, vol. 5. IEEE, 2011, pp. 2474–2477.

[82] D. Douglass, "Current transformer accuracy with asymmetric and high frequency fault currents," *Power Apparatus and Systems, IEEE Transactions on*, vol. PAS-100, no. 3, pp. 1006–1012, 1981.

[83] A. Elhaffar and M. Lehtonen, "High frequency current transformer modeling for traveling waves detection," in *Power Engineering Society General Meeting, 2007. IEEE*, 2007, pp. 1–6.

[84] S. Smith, *The Scientist and Engineer's Guide to Digital Signal Processing*. California Technical Pub.

[85] A. Al-Omari, M. Ahmed, and D. Bearne, "A new method for grid-tie inverters synchronization based on rdft with linear approximation," in *Power Electronics and Drive Systems (PEDS), 2015 IEEE 11th International Conference on*, June 2015, pp. 626–629.

[86] R. Teodorescu, M. Liserre, and P. Rodr̃iguez, *Grid Converters for Photovoltaic and Wind Power Systems*, ser. Wiley - IEEE. Wiley, 2011.

[87] J. G. Proakis and D. K. Manolakis, *Digital Signal Processing (4th Edition)*. Upper Saddle River, NJ, USA: Prentice-Hall, Inc., 2006.

[88] B. Mulgrew, P. Grant, and J. Thompson, *Digital Signal Processing: Concepts and Applications*. Palgrave Macmillan, 2003.

[89] S. Mitra, *Digital Signal Processing: A Computer-based Approach*, ser. McGraw-Hill international edition electrical engineering series. McGraw-Hill/Irwin, 2001.

[90] T. Funaki and S. Tanaka, "Error estimation and correction of dft in synchronized phasor measurement," in *Transmission and Distribution Conference and Exhibition 2002: Asia Pacific. IEEE/PES*, vol. 1, Oct 2002, pp. 448–453 vol.1.

[91] W. Zhuo and E. Micheli-Tzanakou, "A high performance continuous data flow filter using sliding discrete fourier transform (dft) and one point inverse dft," in *Information Technology Applications in Biomedicine, 1998. ITAB 98. Proceedings. 1998 IEEE International Conference on*, May 1998, pp. 51–56.

[92] D. Young and N. Beaulieu, "On the generation of correlated rayleigh random variates by inverse discrete fourier transform," in *Universal Personal Communications, 1996. Record., 1996 5th IEEE International Conference on*, vol. 1, Sep 1996, pp. 231–235 vol.1.

[93] M. Z. Ahmed, *ELEC 214, Electromagnetic Compatability and Power Electronics Notes.* UK: Plymouth University, 2004.

[94] D. Shmilovitz, "On the definition of total harmonic distortion and its effect on measurement interpretation," *IEEE Transactions on Power delivery*, vol. 20, no. 1, pp. 526–528, 2005.

[95] B. Flayyih, M. Ahmed, and M. Ambroze, "A novel hybrid voltage-current fed induction heating power supply system using multilevel neutral point clamped inverter," in *Energy Conference (ENERGYCON), 2014 IEEE International*, May 2014, pp. 189–194.

[96] B. Flayyih, M. Ahmed, and S. MacVeigh, "A comprehensive power analysis of induction heating power supply system using multilevel neutral point clamped inverter with optimum control algorithm," in *Power Electronics and Drive Systems (PEDS), 2015 IEEE 11th International Conference on*, June 2015, pp. 727–731.

[97] J.-H. Ko, S.-J. Park, and S.-M. Park, "The only cc mode charger using estimation of battery internal voltage," in *Industrial Technology (ICIT), 2014 IEEE International Conference on*, Feb 2014, pp. 957–962.

[98] T. Hoevenaars, K. LeDoux, and M. Colosino, "Interpreting ieee std 519 and meeting its harmonic limits in vfd applications," in *Petroleum and Chemical Industry Conference, 2003. Record of Conference Papers. IEEE Industry Applications Society 50th Annual*, Sept 2003, pp. 145–150.

[99] Z. J. Shen, Y. Xiong, X. Cheng, Y. Fu, and P. Kumar, "Power mosfet switching loss analysis: A new insight," in *Conference Record of the 2006 IEEE Industry Applications Conference Forty-First IAS Annual Meeting*, vol. 3, Oct 2006, pp. 1438–1442.

[100] M. H. Rashid, *Power electronics handbook: devices, circuits and applications*. Academic press, 2010.

[101] B. M. Flayyih, M. Z. Ahmed, and M. Ambroze, "An optimum harmonic control of induction heating power supply system using multilevel neutral point clamped inverter," in *2016 IEEE Transportation Electrification Conference and Expo, Asia-Pacific (ITEC Asia-Pacific)*, June 2016, pp. 531–536.

Appendix A

Published Papers

A.1 Energycon 2014 IEEE International Energy Conference, Dubrovnik-Croatia, from 13th - 16th May 2014

"A Novel Hybrid Voltage-Current Fed Induction Heating Power Supply System Using Multilevel Neutral Point Clamped Inverter"

This paper was presented by the author in IEEE Energycon 2014.

A Novel Votage-Current Fed Induction Heating Power Supply System Using Multilevel Neutral Point Clamped Inverter

Bashar Mohammed Flayyih [#1], Mohammed Zaki Ahmed [#2], Marcel Ambroze [#3]

 # Mathematical and Computer Science, Plymouth University
Plymouth, UK
[1] bashar.flayyih@plymouth.ac.uk
[2] M.Ahmed@plymouth.ac.uk
[3] M.Ambroze@plymouth.ac.uk

Abstract—**A novel induction heating power supply topology using multilevel neutral point clamped inverter (MNPCI) is introduced and investigated in this paper. The proposed converter topology decreases the switching losses by lowering the DC link voltage to half its value with the operation under soft switching mode condition. Depending on the modified LLC optimum design being introduced, it shares the advantage features of both voltage fed and current fed inverters with the capability to asborb the undesired parasitic components in the design. The new design involves adding new circuit parameter that helps in controlling the power transfer from the MNPCI to the resonant load tank.**

Index Terms—**Induction heating, MNPCI topology, Optimum LLC design**

I. INTRODUCTION

The electromagnetic effect was first introduced by Michel Faraday(1831) [1]; he showed that currents could be induced in a closed or secondary circuit as a result of varying current in a neighboring primary circuit. His idea was widely used in induction heating (IH) field but with little difference of considering the primary circuit is the heating inductor and the secondary is the workpiece load to be heated. Induction heating is used then in many industrial applications like hardening, forming, annealing, brazing and metal melting or alloying. The mostly used power supply topologies in these applications, are the voltage fed inverters (VFI) and the current fed inverters (CFI) [2] They belong to the so called load resonat power converters (LRPC) family [3]. Each has its own properties which favourates using it according to the characteristics of the application and the type of oscillatory circuit category being used. The load tank circuit equivalent consists of resistor and inductor set to be connected with the compensating capacitor either in series (in VFI) or in parallel (in CFI). Although each one of these two topologies has advantages, but it still suffers from some drawbacks. In the VFI topology, the current flowing in the converter semiconductor switches is the same as that flowing in the load tank. This means the need of using matching transformer in between, which increases the cost of IH system and decreases the efficiency [4] [5]. While in the CFI, the current flowing through the converter switches is Q (quality factor) times lower than that flowing through the heating inductor, therefore it will be so difficult to use commercial equipments because of the requirement of overvoltage protection systems. [6]. To avoid these restrictions, an IH load configuration is designed, with adding a new parameter to classic LLC topology [7] [8].

A novel IH power supply using multilevel neutral point clamped inverter (MNPCI) topology is introduced in this paper. The new configuration takes the advantages of both VFI and CFI topologies, as this design uses VFI configuration, benefiting from commercial devices and protection system and the current flowing in the MNPCI semiconductors is lower than that flowing in the inductor by Q times, just like CFI. Besides, it operates under half the DC link tension which facilitate commutating under soft switching mode and thus, decreases the switching losses. Therefore, this new topology can be considered as a hybrid voltage-current fed inverter (HVCFI).

II. INDUCTION HEATING PRINCIPLES

In its simplest form, the output of induction device consists of water cooled copper coil fed with AC current from an IH power supply and surrounds the workpiece to be heated. The basic concept of induction heating is similar to the well known transformer theory with the inductor as a primary , but modified and based on a single turn-short circuited secondary winding as the workpiece representation. Therefore, its current will be high and considerable losses will be developed. When the coil is excited by an AC current, it produces an alternating magnetic field. The variation in the field induces eddy currents along paths concentric with the axis. The magnetic field of eddy currents opposes the main field according to Lenz law. This energy dissipation mechanism is called Joule effect. The current density varies exponentially inside the workpiece, and when it falls to about one third of its surface value, it is called skin (or penetration) depth, which can be given from equation
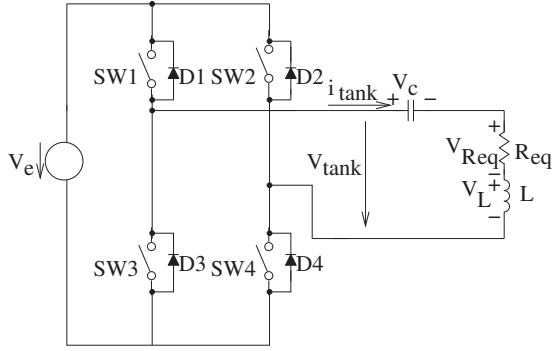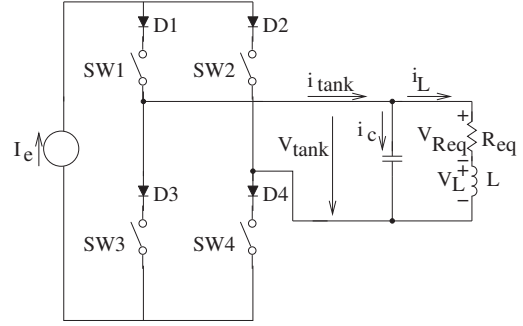
Fig. 1: Voltage-fed inverter

Fig. 2: Current fed inverter

[9]

$$\delta = \sqrt{\frac{\rho}{\mu f \pi}} \tag{1}$$

Where δ is the skin depth, ρ is workpiece electrical resistivity, μ is workpiece magnetic permeability, being $(\mu = \mu_o \mu_r)$ where μ_o is vacuum permeability equals $4\pi.10^{-7} H/m$ and μ_r is relative permeability.

A. Induction heating converters

Usually, the IH converters operate at resonant frequency mode , which permits them from having higher efficiency. They can be classified mainly into two categories: voltage-fed inverters (VFI) and current-fed inverters (CFI).

1) Voltage-fed inverter: It is based on series resonant load tank which acts as a current source, with VFI supplied from constant voltage source. This implies that the VFI is fed from high capacitor that maintains constant voltage, see Fig. 1. The voltage of the load tank is equal to the voltages across V_C, V_L and V_{Req} as follows

$$V_{tank} = V_C + V_L + V_{Req} \tag{2}$$

Being, the voltage across the capacitor V_C is equal to

$$V_C = \frac{1}{j\omega C}\frac{V_{tank}}{R_{eq}} = -jQV_{tank} \tag{3}$$

While, the voltage across the inductor V_L is equal to

$$V_L = j\omega L \frac{V_{tank}}{R_{eq}} = jQV_{tank} \tag{4}$$

And the voltage across the resistance V_{Req} is as

$$V_{Req} = R_{eq}\frac{V_{tank}}{R_{eq}} = V_{tank} \tag{5}$$

Where Q is quality factor.

2) Current-fed Inverter: It is refered to the parallel resonant load tank which bahaves like a voltage source with the CFI need to be supplied from high inductance that maintains constant current, as shown in Fig. 2. The load tank current i_{tank} is divided into inductor-resistence current i_L and capacitor current i_C as follows

$$i_{tank} = i_C + i_L \tag{6}$$
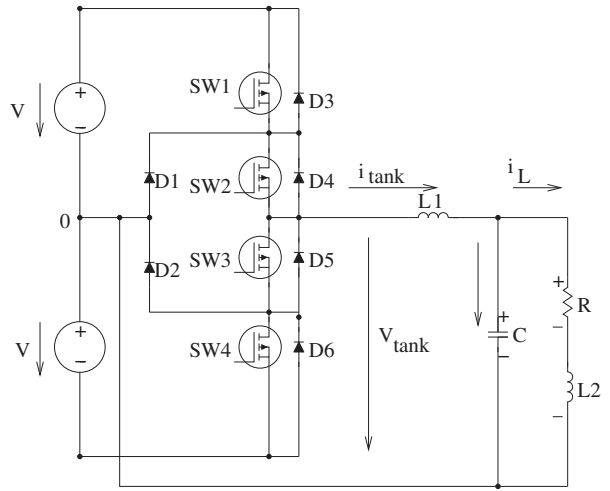
Being, i_C is the compensator current which equal to

$$i_c = (1 + jQ)i_{tank} \tag{7}$$

And, the inductor current i_L is equal to

$$i_L = -jQi_{tank} \tag{8}$$

B. Multi level Neutral point clamped inverter

The prototype design of MNPCI is shown in Fig. 3 [10]. This topology uses the VFI configuration by using two voltage source capacitors of voltage V, which maintain constant voltage delivery of half the DC link voltage. Therefore, it benefits from commercial devices and protection system. Besides, this design contains series connected inductance L_1 which has three advantages of:

- It maintains constant current delivery to the parallel load tank, thus the current flowing through the converter semiconductor switches i_{tank} is lower than that flowing in the inductor i_L by Q times, just like CFI topology and the Equations of 6,7 and 8 can be applied.

Fig. 3: Multilevel neutral point clamped inverter

206
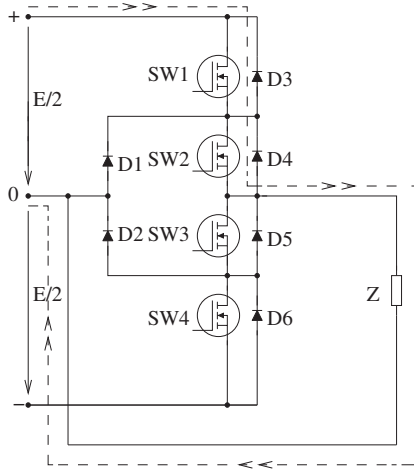
Fig. 4: P-mode of MNPCI topology
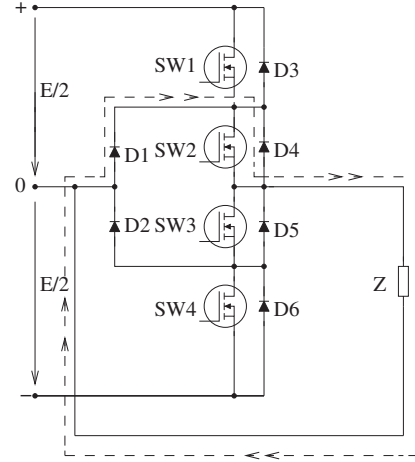
Fig. 5: 0-mode of MNPCI topology

- It has the ability to absorbe the undesired inductive parasitic components generated from the IH system.
- It can compensate the presence of matching transformer that normally connected at the resonant load side, which decreases the cost and increases the efficiency.

In this design, the intermediate point between the source capacitors is called neutral point. The DC bus voltage is splitted into three levels by the two series connected bulk voltage source capacitors. Therefore, the tension applied to the MNPCI is half the main rail DC voltage, which facilitates the soft switching mode and thus, decreases the switching losses of the inverter MOSFET semiconductors.

1) Circuit commutation: The output values of the MNPCI voltage is $\frac{+E}{2}$, 0 and $\frac{-E}{2}$, see Table I . Generally, to achieve these levels, there are three commutation states positive (P) , negative (N) and 0. Where, E is the main rail DC voltage.

TABLE I: Neutral point clamped operational states

	SW1	SW2	SW3	SW4	Output voltage
Mode P	1	1	0	0	$\frac{+E}{2}$
Mode 0	0	1	0	0	0
Mode N	0	0	1	1	$\frac{-E}{2}$
Mode 0	0	0	1	0	0

In P-mode, the two upper high/side switches $SW1$ and $SW2$ are both switched on, with output voltage level as $\frac{+E}{2}$. In N-mode, the two lower high-low/side switches $SW3$ and $SW4$ are both switched on with output voltage level of $\frac{-E}{2}$. While in 0-mode, either of the two inner high/side switches $SW2$ or $SW3$ is switched on, see Fig. 4,Fig. 5, Fig. 6 and Fig. 7 , respectively.

2) Power transfer of LLC topology: From analyzing the load tank circuit representation of Fig. 8, the equivalent impedance Z, is equal to

$$Z = j\omega L_1 + \frac{1}{j\omega C + \frac{1}{R+j\omega L_2}} \qquad (9)$$

Fig. 6: N-mode of MNPCI topology

Fig. 7: 0-mode of MNPCI topology

207

Fig. 8: LLC load tank

By rearranging Equation 9, gives the following formula

$$Z = \frac{R - \omega^2 R L_1 C + j(\omega L_2 + \omega L_1 - \omega^3 L_1 L_2 C)}{1 - \omega^2 L_2 C + jRC\omega} \quad (10)$$

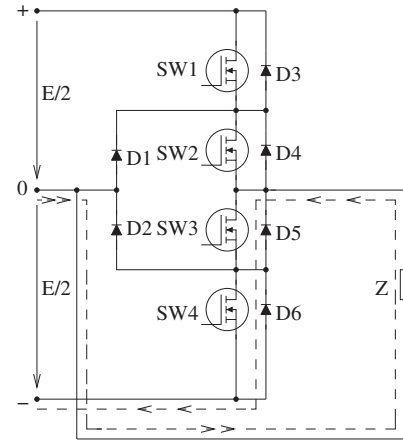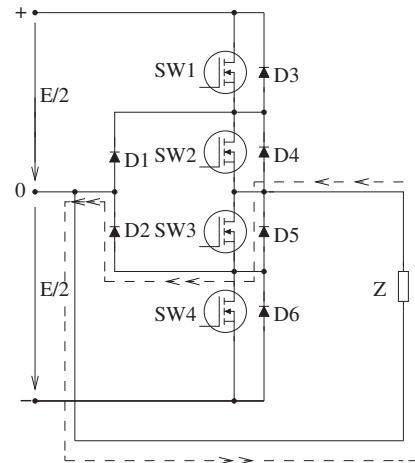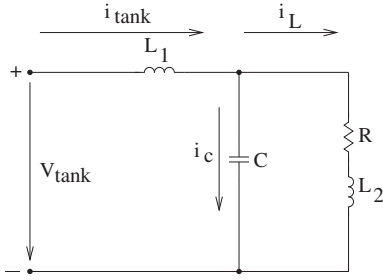The magnitude of the total impedance Z will be as follows

$$|Z| = \frac{\sqrt{(R - RL_1 C\omega^2)^2 + (L_1\omega + L_2\omega - L_1 L_2 C\omega^3)^2}}{\sqrt{(1 - L_2 C\omega^2)^2 + (RC\omega)^2}} \quad (11)$$

And, the phase shift angle will be as

$$\varphi = \arctan\frac{L_1\omega + L_2\omega - L_1 L_2 C\omega^3}{R - RL_1 C\omega^2} - \arctan\frac{RC\omega}{1 - L_2 C\omega^2} \quad (12)$$

From transfer function of Equation 10, two poles can be derived. The first is the parallel pole ω_p, due to parallel inductance L_2 and the second is the series pole ω_o, due to the effect of both series/parallel inductances L_1 and L_2, as in the following expressions

-
$$\omega_p = \frac{1}{\sqrt{L_2 C}} \quad (13)$$

-
$$\omega_o = \frac{1}{\sqrt{L_{eq} C}} \quad (14)$$

Where

$$L_{eq} = \frac{L_1 L_2}{L_1 + L_2} \quad (15)$$

Considering that, the series resonant frequency takes into cosideration the influence of both paralleled inductances, therefore; it expresses better representation to the circuit design at this operational point of the heating cycle [5]. Therefore, by substituting ω_o into Z and assuming that reactive power is minimum with respect to the maximum transferred power (P_{max}), due to resonant case, the following formula approximation is formed

$$P_{max} = \frac{V_{tank}^2}{Z} = \frac{V_{tank}^2}{R}\left(\frac{L_2}{L_1}\right)^2 = \frac{V_{tank}^2}{\beta^2 R} \quad (16)$$

being

$$\beta = \frac{L_1}{L_2} \quad (17)$$

Where V_{tank} is the root mean square value (r.m.s) of the fundemental voltage of the load-tank.
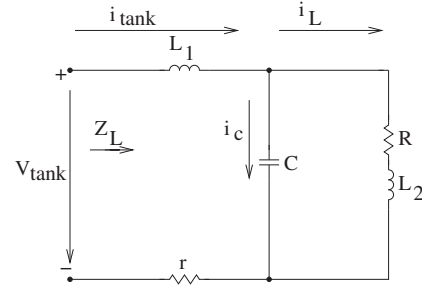
Fig. 9: Modified LLC load tank

3) Power transfer of optimized LLC topology: In high power IH systems, in order to achieve optimum power transfer to the load-tank, this implies a feedback from the load of the application to the controller circuit, which would be connected to the driver of the converter-switches. Usually, this controller requires a current transformer (CT) through which a feedback load tank current can be observed. Although there are modern CTs with good properties used efficiently in many applications, but they still suffers from some drawbacks, especially when used for high frequency applications [11]. Normally,they involve an internal transformer, which will interference with the inductance of the IH system and causes some deterioration change in the system impedance. Also using CTs will increase the size and cost of the system , besides their complexity [12], which is undesirable. Thus, they will affect the resonant state of the system and thus, decreasing the efficiency of IH system [4] [5] In order to measure and monitor the tank current without using the traditional CTs in high power super frequency IH systems, a proposed current sensor circuit is designed, which involves adding a small-value resistor in series with the load-tank, see Fig. 9. Considering the new design of Fig. 9, the impedance Z_L with additional current sensing resistor r will equal to

$$Z_L = r + j\omega L_1 + \frac{1}{j\omega C + \frac{1}{R + j\omega L_2}} \quad (18)$$

By rearranging Equation 18, into real amd imaginary parts, then Z_L will equal to

$$Z_L = \frac{R_T - (rL_2 C - RL_1 C)\omega^2 + j\omega\left(RrC + L_T - L_1 L_2 C\omega^2\right)}{(1 - L_2 C\omega^2) + jRC\omega} \quad (19)$$

Where

$$R_T = R + r \quad (20)$$

And

$$L_T = L_1 + L_2 \quad (21)$$

The magnitude of new overall load Z_L will equal to

$$|Z_L| = \frac{\sqrt{(R_T - (rL_2 C - RL_1 C)\omega^2)^2 + \omega^2\left(RrC + L_T - L_1 L_2 C\omega^2\right)}}{\sqrt{(1 - L_2 C\omega^2)^2 + (RC\omega)^2}} \quad (22)$$

208

And the phase shift angle, φ will equal to

$$\varphi = \arctan \frac{RrC\omega + L_1\omega + L_2\omega - L_1L_2C\omega^3}{R + r - rL_2C\omega^2 - RL_1C\omega^2} - \arctan \frac{RC\omega}{1 - L_2C\omega^2} \tag{23}$$

From transfer function of Equation 19, two pole-roots can be given, the first is due to parallel inductance only, this pole represents the resonant frequency at L_2 and expressed as

$$\omega_p = \frac{1}{\sqrt{L_2C}} \tag{24}$$

And the second pole-root is the series resonant frequency that represents the effect of series-parallel inductances, L_1 and L_2 together with the effect of the sensing resistor, r as well. Hence, the series resonant pole ω_o will equal to

$$\omega_o = \sqrt{\frac{Rr}{L_1L_2} + \frac{1}{L_{eq}C}} \tag{25}$$

Being

$$L_{eq} = \frac{L_1L_2}{L_1 + L_2} \tag{26}$$

Considering that, the sensing resistor, r is always chosen to be very close to zero value, in order to decrease the influence on the maximum power transfer to the load tank of the system, therefore the series pole, ω_o could be considered approximately to be equal to

$$\omega_o \approx \frac{1}{\sqrt{L_{eq}C}} \tag{27}$$

Then, substituting ω_o into the impedance Z_L of Equation 19, and considering that the reactive power is minimum with respect to the optimum power transfer to the load at resonant case (P_{max}), and the impedance will equal approximately the real part of the impedance of Equation 19, at this resonant point [8].

Therefore, the maximum power transfer from the MNPCI converter to the resonant load-tank at ω_o, will equal to the following formula

$$P_{max} = \frac{V_{tank}^2}{Z_L} = \frac{V_{tank}^2}{r + R\left(\frac{L_1}{L_2}\right)^2} = \frac{V_{tank}^2}{r + \beta^2 R} \tag{28}$$

4) Control circuit: It consists from two parts; the first is the zero current detector circuit (ZCD). It involves three components: the differential amplifier, the operational amplifier and the comparator. The output of this stage is a square wave that matches the zero current crossing point, which performs the soft switching mode of the MNPCI. The second part is the Pic18lf4553 processor that triggers the MNPCI MOSFET switches with four control signals that matches the four commutation modes of Table I, see Fig. 10.
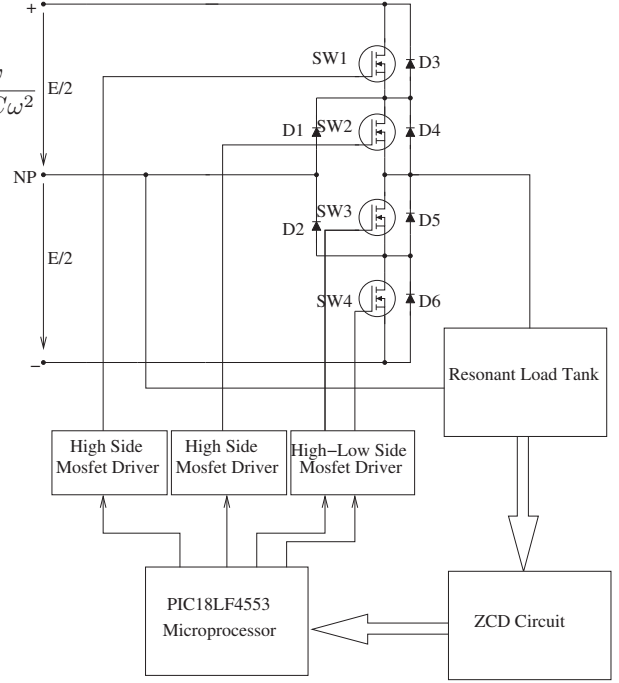
Fig. 10: Control circuit

TABLE II: Values of experimental prototype

Circuit parameter	Magnitude and unit
Series inductance, L_1	$100\mu H$
Parallel inductance, L_2	$100\mu H$
Equivalent resistance, R	$0.3K\Omega$
Series sensing resistor, r	0.2Ω
Parallel rosanant compensator, C	$11.8\mu F$
Voltage source capacitors, C_1 and C_2	$470\mu F$, $470\mu F$
Resonant frequency, F_r	$4.639KHz$
Classical impedance, $|Z|$	300Ω
Modified impedance, $|Z_L|$	300.2Ω
Classical maximum power transfer, P_{max}	$0.12W$
Modified maximum power transfer, P_{maxmod}	$0.1199W$

III. CALCULATION RESULTS AND DISCUSSION

Table II lists the values of circuit parameters of MNPCI prototype used in experimental work.

It can be deduced from experimental results given in Table II that, the maximum power transfer from the MNPCI inverter to the resonant load tank of both the classical and modified LLC systems are nearly the same, with very small variance between them. This difference is about 0.06%, which is because of the damping effect of the current sensing resistor r, as can be seen also from Equation 28.

But, the resonance state of maximum power delivery from MNPCI to the load tank in IH system will be more stable, as the prototype does not use CT in the feedback control circuit which affects the induction load which can be considered with highly inductive properties [4], especially when its inductance variates during the heating cycle. Besides, this CT cancellation will increase the efficiency and decrease the bulk size and

209
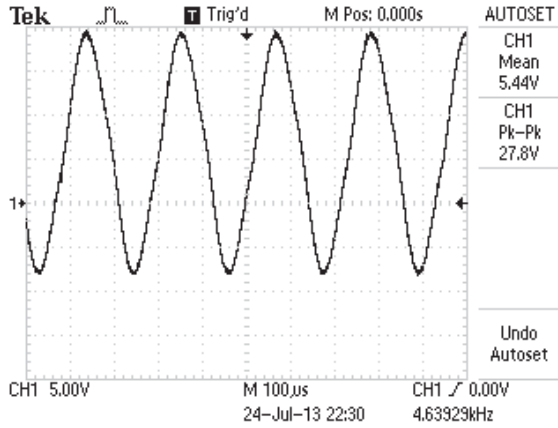
Fig. 11: Signal of equivalent resistor R
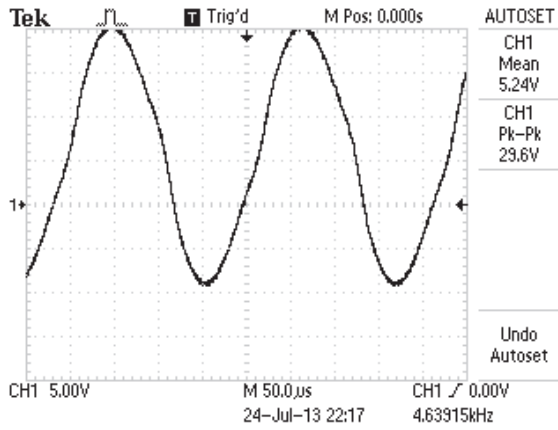
Fig. 12: Signal of parallel inductor L_2

overall cost of the industrial plant of IH system being designed.

Besides, the output signals of proposed experimental prototype across the equivalent resistor R and parallel inductor L_2 are of uniform ac waveform, as shown in Fig. 11 and Fig. 12, respectively. These waveforms matches the ZCS operation of MNPCI converter modes and the modified LLC resonant load tank being explained before.

Also, as the MNPCI topology is operating under zero current soft mode condition ($I_{MOSFET} = 0$), this implies that the switching losses will be kept mininum, due to the cancellation of MOSFET conduction losses, as in the following expression

$$P_{condlosses|_{ZCS}} = I^2_{MOSFET} R_{DS_{(ON)}} = 0 \qquad (29)$$

where:

$P_{condlosses|_{ZCS}}$ is conduction power losses of MOSFET semiconductor at zero current switching mode, I_{MOSFET} is MOSFET current and $R_{DS_{(ON)}}$ is MOSFET on-resistance.

Therefore, no heat rise being observed on MNPCI switches during experimental work.

IV. CONCLUSION

A novel IH power supply using mutilevel neutral point clamped inverter (MNPCI) is built and verified successfully. The new design shares the advantage aspects of both the VFI and CFI converters, therefore it can be considered as a hybrid VFI-CFI inverter (HVCFI) topology.

In order to improve the MNPCI control circuit, a zero current detector is built and tested. Its function is to control the processor Pic18lf4553, which triggers the MOSFET drivers and achieves the soft switching mode condition of MNPCI, with the aid of its operation under half the main DC rail voltage and thus, decreasing the switching losses and increasing the efficiency of the prototype design. Also, it compensates the effect of traditional current transformer (CT). Therefore, the size and cost of the IH system is decreased.

Finally, the IH resonant load tank is developed by introducing an optimized LLC topology. The new design involves adding a small current sensing resistor r in series with LLC resonant load tank to measure the current. This resistor has a very small damping effect on the maximum power transfer from the MNPCI to the optimized load tank of the proposed design of less than 0.1%, which is insignificant.

REFERENCES

[1] E. Laithwaite, "The influence of michael faraday on power engineering," *Power Engineering Journal*, vol. 5, no. 5, pp. 209–219, 1991.

[2] V. Rudnev, D. Loveless, R. Cook, and M. Black, *Handbook of Induction Heating*, ser. Manufacturing Engineering and Materials Processing. Taylor & Francis, 2002.

[3] N. Mohan, T. Undeland, and W. Robbins, *Power electronics: converters, applications, and design*, 2nd ed. Wiley, 1995.

[4] L. Jingang, Z. Yanru, and M. Xin, "Study on a new way of load-matched for voltage-source induction heating inverters," in *Industrial Electronics and Applications, 2006 1ST IEEE Conference on*, 2006, pp. 1–5.

[5] Z. Wang, Z. Lou, and H. Chen, "A novel dual-llc resonant soft switching converter for super high frequency induction heating power supplies," in *Power Electronics Specialists Conference, 2007. PESC 2007. IEEE*, 2007, pp. 2561–2566.

[6] G. Martin Segura *et al.*, "Induction heating converter's design, control and modeling applied to continuous wire heating," 2012.

[7] Z. Gao and Y. Zhou, "Research on switching losses for induction heating power supply with llc resonant load," in *Electronic and Mechanical Engineering and Information Technology (EMEIT), 2011 International Conference on*, vol. 5. IEEE, 2011, pp. 2474–2477.

[8] J. Espi Huerta, E. Dede Garcia Santamaria, R. Garcia Gil, and J. Castello Moreno, "Design of the l-lc resonant inverter for induction heating based on its equivalent sri," *Industrial Electronics, IEEE Transactions on*, vol. 54, no. 6, pp. 3178–3187, 2007.

[9] J. Davies and P. Simpson, *Induction heating handbook*. McGraw-Hill, 1979.

[10] D. Boian, C. Biris, R. Teodorescu, and M. Sztykiel, "Development of modulation strategies for npc converter addressing dc link voltage balancing and cmv reduction," in *Power Electronics for Distributed Generation Systems (PEDG), 2012 3rd IEEE International Symposium on*. IEEE, 2012, pp. 828–835.

[11] D. Douglass, "Current transformer accuracy with asymmetric and high frequency fault currents," *Power Apparatus and Systems, IEEE Transactions on*, vol. PAS-100, no. 3, pp. 1006–1012, 1981.

[12] A. Elhaffar and M. Lehtonen, "High frequency current transformer modeling for traveling waves detection," in *Power Engineering Society General Meeting, 2007. IEEE*, 2007, pp. 1–6.

210

A.2 The 11th IEEE International Conference on Power Electronics and Drive Systems (PEDS 2015) held in Sydney, Australia, from 9th - 12th June 2015.

"A Comprehensive Power Analysis of Induction Heating Power Supply System Using Multilevel Neutral Point Clamped Inverter With Optimum Control Algorithm" This paper was presented by the author in IEEE PEDS 2015.

A Comprehensive Power Analysis of Induction Heating Power Supply System Using Multilevel Neutral Point Clamped Inverter With Optimum Control Algorithm

Bashar Mohammed Flayyih [#1], Mohammed Zaki Ahmed [#2], Stuart MacVeigh [#3]

 # Mathematical and Computer Science, Plymouth University
Plymouth, UK
[1] bashar.flayyih@postgrad.plymouth.ac.uk
[2] M.Ahmed@plymouth.ac.uk
[3] stuart.macveigh@plymouth.ac.uk

Abstract—**A novel super frequency induction heating power supply using multilevel neutral point clamped inverter with optimum control algorithm using high performance STM32F4DISCOVERY board is introduced. The control strategy is to keep phase shift angle between voltage and current approximately zero at all load conditions to ensure maximum power transfer.**

Index Terms—**Induction heating, MNPCI topology, LLC design, phase shift, harmonic content.**

I. INTRODUCTION

Since its discovery by Michel Faraday(1831) [1]; the induction heating (IH) principle has begun to be utilized in many industrial applications like, surface hardening, annealing, brazing, metal melting or alloying. Therefore, the development of IH system has become a pressing need to improve the power transfer from power supply to the IH load of the application required, and due to variable characteristic of IH load workpiece during the melting cycle [2] [3], it is necessary to develop an IH system that operates using resonant inverters with switching frequency that changes according to changing load conditions during the IH application process, in order to keep tuning with natural resonant frequency of the system [4].

Therefore, a new IH system using hybrid MNPCI configuration [5] [6]. This design reduces the voltage tension applied to the MNPCI switches of the system to half the DC rail voltage with decreasing the switching losses and increasing the efficiency [6]. The control of variable load frequency is achieved by high performance STM32F4DISCOVERY board due to its accuracy and high speed. Its control strategy is to maintain the phase shift angle φ between voltage and current almost zero at all load conditions. The LLC equivalent circuit is chosen to model the IH load, due to its benefits such as ability for short-circuit handling and current gain [3], [7], [8].
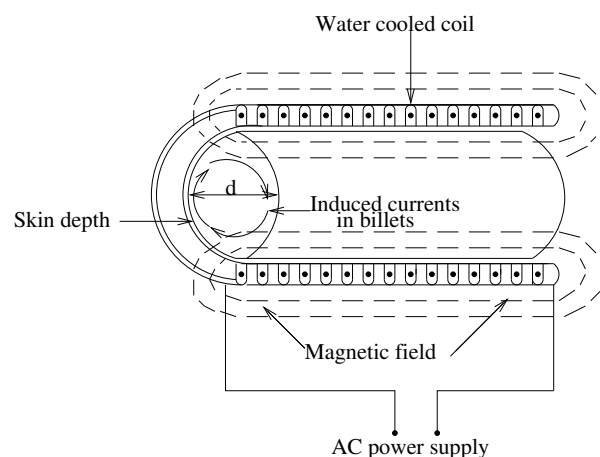
Fig. 1: IH System Principles
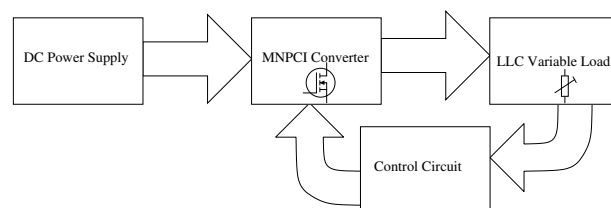
Fig. 2: IH Prototype Configuration System

II. INDUCTION HEATING PRINCIPLES

As can be seen in Fig. 1, the output of IH device consists mainly from a cooled hollow coil fed from a resonant IH power supply and surrounds the workpiece load to be heated. The basic concept of induction heating is similar to the transformer theory with the inductor as a primary and a single turn-short circuited secondary winding as the workpiece. Therefore, its current will be high and considerable losses will be developed. When the coil is excited, it produces an

Fig. 3: Hybrid MNPCI Configuration With Variable Load

TABLE I: MNPCI configuration operational states

	SW1	SW2	SW3	SW4	Output voltage
+ve Mode	1	1	0	0	$V = \frac{\pm E}{2}$
0 Mode	0	1	0	0	0
-ve Mode	0	0	1	1	$V = \frac{-E}{2}$
0 Mode	0	0	1	0	0

Fig. 4: LLC Equivalent Variable IH Load

alternating magnetic field. The variation in the field induces eddy currents along paths concentric with the axis and concentrate near the surface to form the skin (penetration) depth phenomena [9]. The magnetic field of eddy currents opposes the main field according to Lenz law. This energy dissipation mechanism is called Joule effect [8].

III. SYSTEM DESCRIPTION

The configuration diagram of proposed IH system using hybrid MNPCI converter can be shown in Fig. 2. It consists mainly from DC power supply to feed the switches of MNPCI converter with half the DC rail voltage due to two bulk voltage source capacitors, then the MNPCI output supplies a variable LLC load equivalent and controlled by high performance STM32F4DISCOVERY board. The various prototype elements will be illustrated in the following section:

A. Induction Heating MNPCI Converter

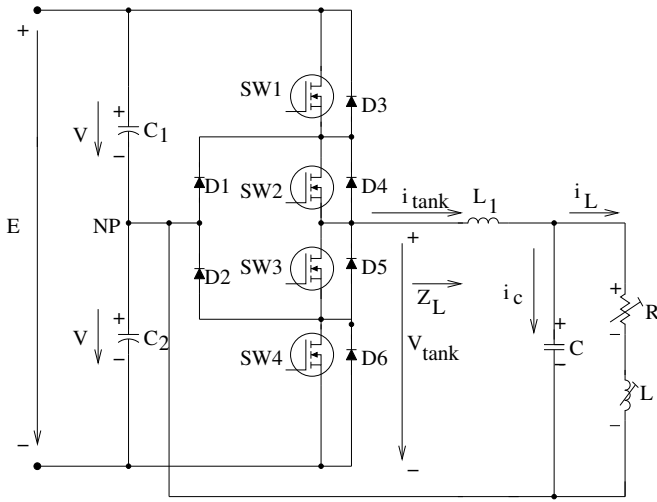The design of hybrid IH MNPCI configuration is shown in Fig. 3 [5] [6]. The MNPCI switches of the topology operates under maximum of half the DC rail voltage tension of magnitude $V = |\frac{E}{2}|$ by using two equal value voltage source capacitors $C1$ and $C2$, which maintains constant voltage delivery to the designed configuration like the voltage fed inverter (VFI) thus, it benefits from commercial devices and protection system [8].

The central point between the source capacitors called neutral point (NP). It splits the operational voltages into three levels $-\frac{E}{2}, 0$ and $\frac{E}{2}$, which facilitates the soft switching mode of the four operational modes of Mosfet switches of MNPCI topology shown in Table I, i.e, this will decrease the switching losses which in turn increase the efficiency.

B. IH Load Equivalent

As can be pointed from IH load configuration in Fig. 4, the inductor - workpiece load set will be moduled using variable
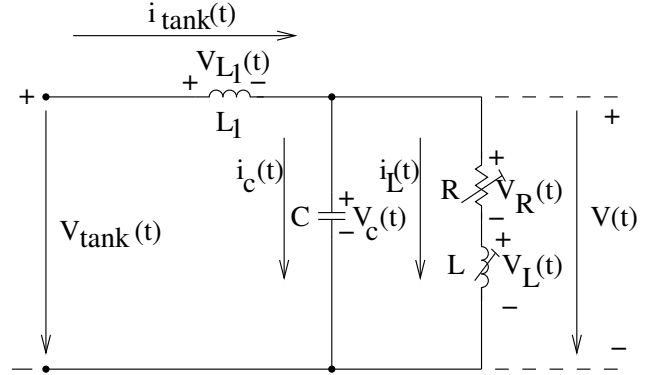
inductor - resistor equivalent of R and L, to represent the changeable characteristic of melting cycle, both connected in parallel with constant value compensating capacitor C, in order to reach the resonant state faster in spite of load variation.

Besides, It contains series connected inductance L_1, to form the LLC load equivalent circuit which has the following advantages of:

- Maintains constant current delivery to the IH load, thus the current flowing through the inductor i_L is greater than the current flowing through the converter semiconductor switches i_{tank} by Q times like the current fed inverter (CFI), therefore Equations 1,2 and 3 below are applied.
- Capability to absorb the undesired inductive parasitic components in IH system.
- Compensate the matching transformer absence at load side which decreases the cost and increases the efficiency.

The current gain of IH load configuration can be calculated from tank current i_{tank} which will be divided into inductor-resistance current i_L and capacitor current i_C as follows:

$$i(t)_{tank} = i_C(t) + i_L(t) \qquad (1)$$

Being, i_C is the compensator current which equal to

$$i_c(t) = (1 + jQ)i_{tank}(t) \qquad (2)$$

And, the inductor current i_L is equal to

$$i_L(t) = -jQi_{tank}(t) \qquad (3)$$

Where Q is quality factor.

213

Fig. 5: Control Circuit

C. Control circuit

The most important merit of IH system is its variable characteristics during the heating process which means that the control plan of the prototype should be adapted to achieve optimum algorithmic behaviour at all load equivalent conditions to ensure maximum power delivery from MNPCI power supply to IH load. The control strategy is designed to maintain the phase shift angle φ bet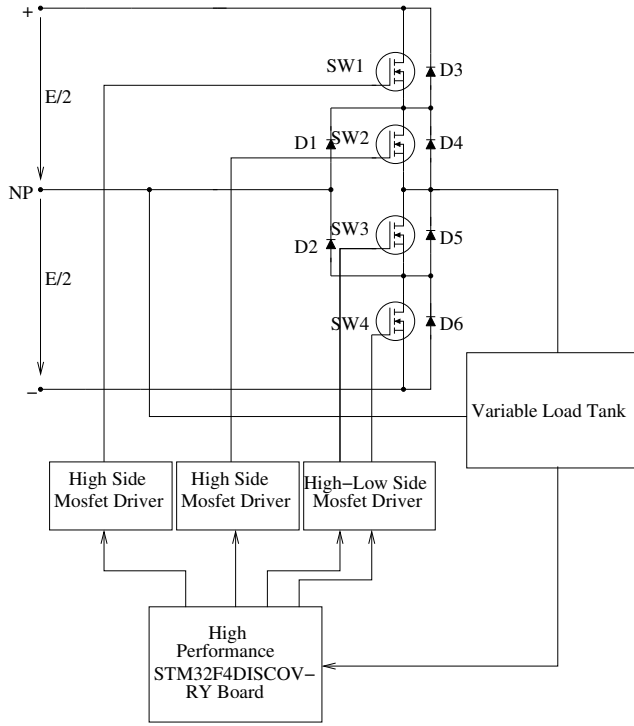ween voltage and current approximately zero at all load tested conditions, which facilitates capturing the resonant state and achieves soft switching mode of MNPCI mosfets of the prototype.

Considering that, the control circuit consists essentially from high performance STM32F4DISCOVERY (STM32) board, due to its high speed, better accuracy and more functionality than other pic-processors. The STM32 board used to trigger three mosfet drivers of two high-side and one high/low-side drivers. These will attenuates four mosfets of three high side and one low side switches with four modes shown in Table I , as shown in Fig. 5 above.

IV. EXPERIMENTAL RESULTS AND TRANSFER POWER CALCULATION

For better comprehension to the variations of IH load of the configuration design as been selected in Table II, there will be an extensive analysis to power transfer in terms of harmonic components of output voltage and current waveforms delivered from MNPCI topology to the IH load of captured values of $L1 = 105.7\mu H$, $R = 10.07\Omega$ and

$L = 33\mu H$, see Fig. 6.

TABLE II: Values of experimental prototype

Circuit parameter	Magnitude and unit
Series inductance, L_1	$105.7\mu H$
Parallel inductance, L	$22, 33, 47, 68, 100 (\mu H)$
Equivalent resistance, R	$3.37, 10.07, 15.07, 22.07 (\Omega)$
Parallel resonant compensator, C	$11.8\mu F$
Voltage source capacitors, C_1 and C_2	$470, 470 (\mu F)$

From practical point, it was found from analysing experimental results shown in Fig. 7 and Fig. 8 that there are three harmonic components of output voltage of (ω_1, ω_3 and ω_5), of frequencies f_1(main frequency), $f_3 = 3f_1$ and $f_5 = 5f_1$ respectively, and two harmonics of current of (ω_1 and ω_3) of frequencies f_1(main frequency) and $f_3 = 3f_1$, therefore for simplicity there will be three terms of voltage and current to represent the real and imaginary parts using Fourier Series, and the transfer power will equal to the average power through the resistor R, assuming ideal state and resonant mode, therefore the average power will be expressed as:

$$P_{Av} = P_R = \frac{1}{T}\int_0^T V_R(t)i_R(t)dt$$

$$= \frac{1}{T}\int_0^T \left(V(t) - L\frac{di_L(t)}{dt}\right)i_L(t)dt \quad (4)$$

The $V(t)$ and $i_L(t)$ are the time domain output voltage and current respectively, given from Fourier Series as follows:

$$V(t) = k_1 \cos\omega_1 t + k_2 \sin\omega_1 t + k_3 \cos\omega_3 t + k_4 \sin\omega_3 t$$
$$+ k_5 \cos\omega_5 t + k_6 \sin\omega_5 t \quad (5)$$

With,

$$i_L(t) = k_7 \cos\omega_1 t + k_8 \sin\omega_1 t + k_9 \cos\omega_3 t + k_{10} \sin\omega_3 t$$
$$+ k_{11} \cos\omega_5 t + k_{12} \sin\omega_5 t \quad (6)$$

And the derivative of $i_L(t)$ will given by

$$\frac{di_L(t)}{dt} = -k_7 \sin\omega_1 t + k_8 \cos\omega_1 t - k_9 \sin\omega_3 t + k_{10} \cos\omega_3 t$$
$$- k_{11} \sin\omega_5 t + k_{12} \cos\omega_5 t \quad (7)$$

By substituting Equations 5,6 and 7 into Equation 4, with taking the Laplace Transform then the Laplace Inverse of the equation gives the following expression:

$$P_{av} = \frac{1}{T}[p_o t + p_T$$
$$+ p_1 \sin 2\omega_1 t - p_2 \cos 2\omega_1 t$$
$$+ p_3 \sin 2\omega_3 t - p_4 \cos 2\omega_3 t$$
$$+ p_5 \sin 2\omega_5 t - p_6 \cos 2\omega_5 t$$
$$+ p_7 \sin(\omega_1 + \omega_3)t - p_9 \cos(\omega_1 + \omega_3)t$$
$$+ p_8 \sin(\omega_3 - \omega_1)t - p_{10} \cos(\omega_3 - \omega_1)t$$
$$+ p_{11} \sin(\omega_5 + \omega_1)t - p_{14} \cos(\omega_5 + \omega_1)t$$
$$+ p_{12} \sin(\omega_1 + \omega_5)t - p_{13} \cos(\omega_1 - \omega_5)t$$
$$+ p_{15} \sin(\omega_1 - \omega_3)t - p_{16} \cos(\omega_1 - \omega_3)t$$
$$+ p_{18} \sin(\omega_3 + \omega_5)t - p_{19} \cos(\omega_3 + \omega_5)t$$
$$+ p_{17} \sin(\omega_5 - \omega_3)t - p_{20} \cos(\omega_5 - \omega_3)t$$
$$+ p_{21} \sin(\omega_1 - \omega_5)t - p_{22} \cos(\omega_1 - \omega_5)t$$
$$+ p_{23} \sin(\omega_3 - \omega_5)t - p_{24} \cos(\omega_3 - \omega_5)t]$$

(8)

Where k_1, k_2, K_3, k_4, k_5 and k_6 are voltage constants and their values equal to,

$$\left.\begin{array}{l} k_1 = 0.328, k_2 \quad = -9.0, k_3 = 0.142 \\ k_4 = 0.978, k_5 \quad = -0.1963, k_6 = -0.498 \end{array}\right\}$$

(9)

And $k_7, k_8, k_9, k_{10}, k_{11}$ and k_{12} are current constants and their magnitudes would be as follow,

$$\left.\begin{array}{l} k_7 = -0.13, k_8 \quad = -0.75, k_9 = 0.1 \\ k_{10} = -3.185 * 10^{-3}, k_{11} \quad = 0, k_{12} = 0 \end{array}\right\}$$

(10)

The values of $k_1, k_2, k_3, ..., k_9, k_{10}$ and k_{12} are constants referred to the amplitudes of all real and imaginary harmonic components of output voltage and current signals, which can be found from Fast Fourier Transform (FFT) function with the aid of Matlab software.

The values of $p_o, p_T, p_1, p_2, p_3, ..., p_{22}, p_{23}$ and p_{24} can be derived from the voltage and current constants with abbreviation and rearranging of Equation 4, therefore their values will equal to the following general expressions:

$$\left.\begin{array}{l} p_0 = 15.853 * 10^{-3}, p_T = \dfrac{0.731 - 0.14\omega_1 L}{\omega_1} \\[2mm] p_1 = \dfrac{10.833 * 10^{-3} - 24.604 * 10^{-3}\omega_1 L}{\omega_1} \\[2mm] p_2 = \dfrac{0.3583 - 0.1345\omega_1 L}{\omega_1} \\[2mm] p_3 = \dfrac{1.488 * 10^{-3} + 0.165 * 10^{-3}\omega_1 L}{\omega_1} \\[2mm] p_4 = \dfrac{8.4 * 10^{-3} + 2.679 * 10^{-3}\omega_1 L}{\omega_1}, p_5 = 0 \\[2mm] p_6 = 0, p_7 = \dfrac{89.4186 * 10^{-3} + 38.386 * 10^{-3}\omega_1 L}{\omega_1} \\[2mm] p_8 = \dfrac{-0.187 - 58.21 * 10^{-3}\omega_1 L}{\omega_1} \\[2mm] p_9 = \dfrac{0.146 + 2.741 * 10^{-3}\omega_1 L}{\omega_1} \\[2mm] p_{10} = \dfrac{-5.754 * 10^{-3} - 8.474 * 10^{-3}\omega_1 L}{\omega_1} \\[2mm] p_{11} = \dfrac{49.632 * 10^{-3}}{\omega_1}, p_{12} = \dfrac{-28.769 * 10^{-3}}{\omega_1} \\[2mm] p_{13} = \dfrac{17.671 * 10^{-3}}{\omega_1}, p_{14} = \dfrac{-10.071 * 10^{-3}}{\omega_1} \\[2mm] p_{15} = \dfrac{-15.663 * 10^{-3} - 19.997 * 10^{-3}\omega_1 L}{\omega_1} \\[2mm] p_{16} = \dfrac{0.2327 - 3.4183 * 10^{-3}\omega_1 L}{\omega_1} \\[2mm] P_{17} = \dfrac{-4.686 * 10^{-3}}{\omega_1}, p_{18} = \dfrac{-1.3696 * 10^{-3}}{\omega_1} \\[2mm] p_{19} = \dfrac{-3.18365 * 10^{-3}}{\omega_1}, p_{20} = \dfrac{-13.047 * 10^{-3}}{\omega_1} \\[2mm] p_{21} = p_{22} = p_{23} = p_{24} = 0 \end{array}\right\}$$

(11)

By considering these values in Equation 8, the general form of average power transfer from MNPCI configuration to IH load will equal to the following mathematical expression:

$$P_{av} = \frac{1}{T}[p_o t + p_T$$
$$+ p_1 \sin 2\omega_1 t - p_2 \cos 2\omega_1 t$$
$$+ p_3 \sin 2\omega_3 t - p_4 \cos 2\omega_3 t$$
$$+ p_7 \sin(\omega_1 + \omega_3)t - p_9 \cos(\omega_1 + \omega_3)t$$
$$+ p_8 \sin(\omega_3 - \omega_1)t - p_{10} \cos(\omega_3 - \omega_1)t$$
$$+ p_{11} \sin(\omega_5 + \omega_1)t - p_{14} \cos(\omega_5 + \omega_1)t$$
$$+ p_{12} \sin(\omega_1 + \omega_5)t - p_{13} \cos(\omega_1 - \omega_5)t$$
$$+ p_{15} \sin(\omega_1 - \omega_3)t - p_{16} \cos(\omega_1 - \omega_3)t$$
$$+ p_{18} \sin(\omega_3 + \omega_5)t - p_{19} \cos(\omega_3 + \omega_5)t$$
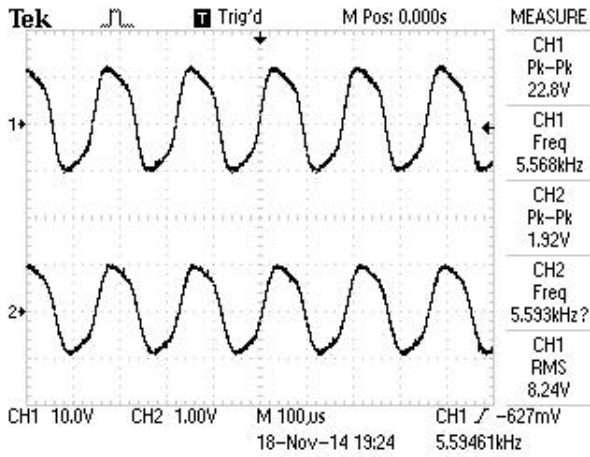$$+ p_{17} \sin(\omega_5 - \omega_3)t - p_{20} \cos(\omega_5 - \omega_3)t]$$

(12)

Fig. 6: Output Voltage (Ch1) and Current (Ch2) Signals of prototype values:$L1 = 105.7\mu H$, $R = 10.07\Omega$ and $L = 33\mu H$
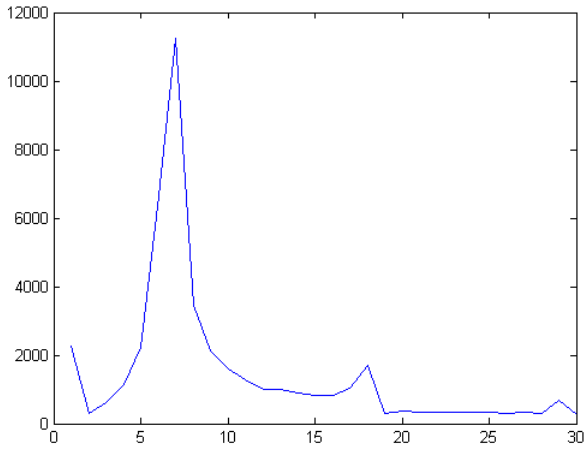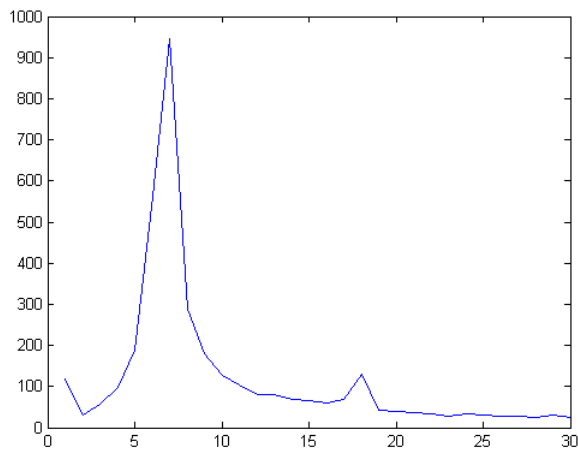

Fig. 7: Harmonic Components of Output Voltage

Fig. 8: Harmonic Components of Output Current

V. CONCLUSION

This paper is concerned with the development of induction heating system by building, investigating and testing a new prototype design configuration. These parts consist from IH power supply converter, control circuit and the resonant load tank oscillatory circuit.

The first development step is the DC/AC converter. A new mutilevel neutral point clamped inverter (MNPCI) is built and verified successfully, as part of IH power supply system. The new design shares the advantage aspects of both the VFI and CFI converters and therefore, it can be considered as a hybrid VFI-CFI inverter (HVCFI) topology.

Secondly is the improvement of the MNPCI control circuit strategy, by utilizing a high performance STM32F4DISCOVERY board to trigger the MOSFET drivers, due to its high speed, accuracy and functionality. The STM32 board achieves the soft switching mode condition with the aid of MNPCI operation under half the DC link voltage and thus, decreasing the switching losses and increasing the efficiency of the prototype to more than 85%. It maintains the phase shift angle between output voltage and current almost zero at all load conditions. The configuration design involves also using variable LLC equivalent of IH load to represent the changeable characteristics of induction heating system during the heating cycle.

REFERENCES

[1] E. Laithwaite, "The influence of michael faraday on power engineering," *Power Engineering Journal*, vol. 5, no. 5, pp. 209–219, 1991.

[2] Y. Ge, R. Hu, Z. Zhang, and Q. Shen, "Optimization control of induction hardening process," in *Mechatronics and Automation, Proceedings of the 2006 IEEE International Conference on*, June 2006, pp. 1126–1130.

[3] Z. Wang, Z. Lou, and H. Chen, "A novel dual-llc resonant soft switching converter for super high frequency induction heating power supplies," in *Power Electronics Specialists Conference, 2007. PESC 2007. IEEE*, 2007, pp. 2561–2566.

[4] I. Yilmaz, M. Ermis, and I. Cadirci, "Medium-frequency induction melting furnace as a load on the power system," *Industry Applications, IEEE Transactions on*, vol. 48, no. 4, pp. 1203–1214, 2012.

[5] D. Boian, C. Biris, R. Teodorescu, and M. Sztykiel, "Development of modulation strategies for npc converter addressing dc link voltage balancing and cmv reduction," in *Power Electronics for Distributed Generation Systems (PEDG), 2012 3rd IEEE International Symposium on*. IEEE, 2012, pp. 828–835.

[6] B. Flayyih, M. Ahmed, and M. Ambroze, "A novel hybrid votage-current fed induction heating power supply system using multilevel neutral point clamped inverter," in *Energy Conference (ENERGYCON), 2014 IEEE International*, May 2014, pp. 189–194.

[7] Z. Gao and Y. Zhou, "Research on switching losses for induction heating power supply with llc resonant load," in *Electronic and Mechanical Engineering and Information Technology (EMEIT), 2011 International Conference on*, vol. 5. IEEE, 2011, pp. 2474–2477.

[8] G. Martin Segura *et al.*, "Induction heating converter's design, control and modeling applied to continuous wire heating," 2012.

[9] J. Davies and P. Simpson, *Induction heating handbook*. McGraw-Hill, 1979.

A.3 The IEEE Transportation Electrification Conference and Expo Asia-Pacific (ITEC2016), Busan, Korea, from 1st - 4th June, 2016.

"An Optimum Harmonic Control of Induction Heating Power Supply System Using Multilevel Neutral Point Clamped Inverter"

This paper was presented by the author in ITEC2016 BUSAN.

An Optimum Harmonic Control of Induction Heating Power Supply System Using Multilevel Neutral Point Clamped Inverter

Bashar Mohammed Flayyih [#1], Mohammed Zaki Ahmed [#2], Marcel Ambroze [#3]

Mathematical and Computer Science, Plymouth University
Plymouth, UK
[1] bashar.flayyih@postgrad.plymouth.ac.uk
[2] m.ahmed@plymouth.ac.uk
[3] m.ambroze@plymouth.ac.uk

Abstract—**An Optimum Harmonic Control of a new induction heating power supply with multilevel neutral point clamped inverter is introduced. The proposed system achieves the soft switching mode for both current and voltage with low harmonic distortion and the capability to maximize the heating power by controlling the harmonics.**

Index Terms—**Induction heating, MNPCI topology, LLC design, Harmonic control.**

I. INTRODUCTION

The induction heating (IH) principle used in many industrial applications like, surface hardening, induction melting, tempering, annealing, brazing, metal melting or alloying. Due to the variable behaviour of IH load during the melting cycle [1], [2], the development of IH system to adapt these instantaneous load changes has become a great need to improve the power transfer from power supply to the IH load of the application required. Therefore, it is necessary to develop an IH system that operates using resonant inverters with switching frequency that changes according to the changing load conditions during the IH application process, in order to keep natural tuning of resonant frequency of the system at all load conditions,And due to these instantaneous changes , the IH system considered as a high harmonic distortion system [3].

Due to its capability for harmonic reduction, a new IH system using hybrid Multilevel Neutral Point Clamped Inverter (MNPCI) configuration with optimum harmonic control has being introduced in this paper [4]–[6]. The proposed design reduces the voltage tension applied to the MNPCI switches of the system to half the DC rail voltage which decreases the switching losses of the inverter [5]. With the achievement of zero current and voltage switching modes, its control strategy is to change the discharge time t_α of the prototype to an optimized value which achieves natural switching with lowest harmonic distortion and highest heating power efficiency. The LLC equivalent circuit is chosen to model the IH load, due to its benefits like its capability for short-circuit handling
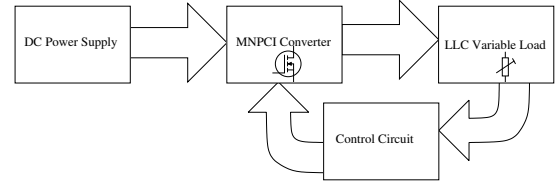
Fig. 1: IH prototype Configuration

and current gain, besides it allows the dispensing from the matching transformer which reduces the IH system harmonic distortion and decreases the cost [2], [7], [8].

II. INDUCTION HEATING PRINCIPLES

The IH device consists mainly from an induction coil fed from a resonant IH power supply and surrounds the material load to be heated. The basic concept of induction heating is similar to the transformer theory with the inductor as a primary and a single turn-short circuited secondary winding as the workpiece. Therefore, its current will be high and considerable losses will be developed. When the coil is excited, it produces an alternating magnetic field. The variation in the field induces eddy currents along paths concentric with the axis. The magnetic field of eddy currents opposes the main field according to Lenz law. This energy dissipation mechanism is called Joule effect [8], and it concentrates near the surface of the workpiece. The current density varies exponentially inside the workpiece, and when it falls to $(1/e = 0.368)$ of its surface value is usually called penetration (skin) depth phenomena [9].

The skin depth (δ) is related to electrical resistivity (ρ), reversely proportional with magnetic permeability (μ) of the workpiece, and switching frequency (f)

$$\delta = \sqrt{\frac{\rho}{\mu f \pi}} \qquad (1)$$

and

218

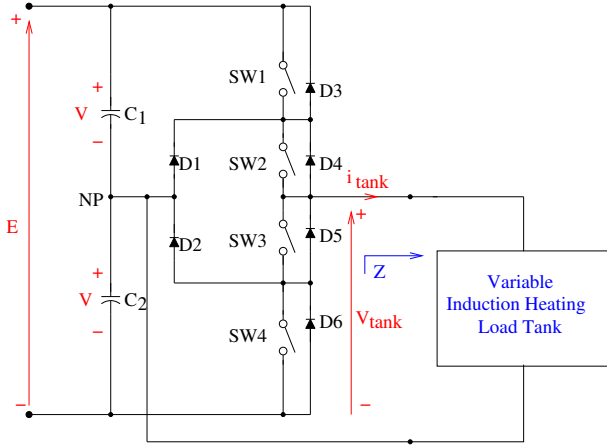Fig. 2: MNPCI prototype

•

$$\mu = \mu_o \mu_r \quad (2)$$

Where μ_o, is the absolute (vacuum) permeability equals $4\pi.10^{-7} H/m$ and μ_r, is the relative permeability.

In efficient induction heating system, it is proper to assume that $\delta \ll d$ (the diameter of the workpiece). Increasing the working frequency f will increase the power density, because P (workpiece supplied power) is proportional $\propto \sqrt{f}$ and this allows for much better induction heating process. [10]. As there should be more than one harmonic content (besides the fundamental) in the system output, then the Effective Heating Power $P_e(f)$ is proportional to:

$$P_e(f) \propto \sum_{n=1}^{N} I^2(f).\sqrt{f} \quad (3)$$

Where N referred to the number of harmonics, f is the natural-switching resonant frequency and $I(f)$ is the current at selected harmonic.

Which means the heating power is directly proportional to the summation of all individual harmonic currents squared, multiplied by the $\sqrt{f}$, assuming resonant state and pure resistive load.

III. SYSTEM DESCRIPTION

The general configuration of proposed IH system using hybrid MNPCI converter is shown in Fig. 1. It consists mainly from DC power supply feeding the switches of MNPCI converter through two bulk voltage source capacitors. It then supplies a variable load of LLC equivalent circuit. The basic prototype components is illustrated in this section

A. Induction Heating MNPCI Converter

The design of hybrid IH MNPCI configuration is shown in Fig. 2 [4] [5]. The MNPCI switches of the topology operates under maximum of half the DC rail voltage tension of magnitude $V = |\frac{E}{2}|$ by using two equal voltage source capacitors $C1$ and $C2$ ($C1=C2$) like the voltage fed
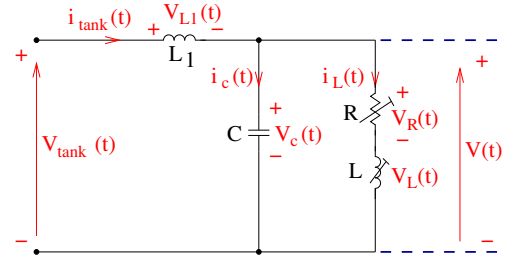

Fig. 3: Variable Load tank configuration

inverter (VFI), which maintains constant voltage delivery thus, it benefits from commercial devices and protection system [8].

The central point between the source capacitors called neutral point (NP). It splits the operational voltages into three levels $-\frac{E}{2}$,0 and $\frac{E}{2}$, which facilitates the soft switching mode of four operational modes of MNPCI switches being shown in Table I under tension of half the DC rail voltage, i.e, this will decrease the switching losses, together with the tendency property of MNPCI converter to reduce harmonic distortion in output signal, which in turn increase the heating power efficiency of IH system.

TABLE I: MNPCI topology operational modes

	SW1	SW2	SW3	SW4	Output voltage
(+ve) Mode	1	1	0	0	$v = \frac{+E}{2}$
(0) Mode	0	1	0	0	0
(−ve) Mode	0	0	1	1	$v = \frac{-E}{2}$
(0) Mode	0	0	1	0	0

B. IH load Equivalent

The LLC equivalent is used to model the IH load tank, with selecting a variable set of inductor-resistor group to represent the load variations during the heating cycle, both in parallel with a compensating capacitor to perform the resonant state, and then all connected to series inductance, as shown in Fig. 3.

Considering the above proposed load, the load tank current i_{tank} is divided into inductor-resistance current $i(t)$ and capacitor current $i_C(t)$ as follows

$$i_{tank}(t) = i_C(t) + i(t) \quad (4)$$

The existence of series connected inductance L_1 in the prototype has three advantages of:

• Maintains constant current delivery to the IH load especially during the 0-state complementary mode of both +ve and -ve cycles .
• The ability to absorb the undesired inductive parasitic components that may exist during experimental work in the proposed system.
• Compensate the matching transformer absence which decreases the harmonic distortion and increases the efficiency, with reducing the cost of the system.

219

IV. Power Harmonic Analysis

The output signal $v(t)$ produced from MNPCI prototype under the four operational modes of Table I is shown in Fig. 4. To analyse this signal as a periodic waveform obtained from experimental job in time domain, the Fourier Series is very essential at this point, in order to find the spectrum of the signal especially at any circuit operating point and to identify the harmonic content of the signal of the proposed system.

Starting from the general law of Fourier Series:

$$g(t) = a_o + \sum_{n=0}^{m}(a_n Cos(n\omega t) + b_n Sin(n\omega t)) \qquad (5)$$

Where, $g(t)$ is the Fourier Series equivalent function of $v(t)$ and,

$$\omega = 2\pi f \qquad (6)$$

With a_o a_n and b_n are Fourier Series amplitude coefficients and they are given by the following set of equations:

$$a_o = \frac{1}{T}\int_0^T v(t)dt \qquad (7)$$

$$a_n = \frac{2}{T}\int_0^T v(t)Cos(n\omega t)dt \qquad (8)$$

$$b_n = \frac{2}{T}\int_0^T v(t)Sin(n\omega t)dt \qquad (9)$$

above

The output voltage $v(t)$ equals to four succession segments over overall period from $0 \longrightarrow T$ interval,

$$v(t) = \begin{cases} V_p.Sin\left(2\pi f_n t\right) & \text{for } (0 < t \leq t_\alpha), \\ V_s.e^{-\frac{t-t_\alpha}{\tau}} & \text{for } \left(t_\alpha < t \leq \frac{T}{2}\right), \\ -V_p.Sin\left(2\pi f_n\left(t - \frac{T}{2}\right)\right) & \text{for } \left(\frac{T}{2} < t \leq \frac{T}{2} + t_\alpha\right), \\ -V_s.e^{-\frac{t-(\frac{T}{2}+t_\alpha)}{\tau}} & \text{for } \left(\frac{T}{2} + t_\alpha < t \leq T\right). \end{cases} \qquad (10)$$

Where, V_p is the peak voltage of $v(t)$, V_s is the switching voltage between sine and exponential modes at time t_α, f_n is natural switching frequency of MNPCI inverter, t_α is the discharge time or switching time from Sine to Exponential periods, τ is the time constant due to supply inductor $L1$, and T is the waveform total time period.

*The a_o coefficient stands for the mean value of Fourier Series of the function and it equals the average value of the area under the curve of $v(t)$ function, and as the two periods of operational modes are symmetrical for the +ve and -ve cycles over the time period of T, then the value of a_o equals zero.
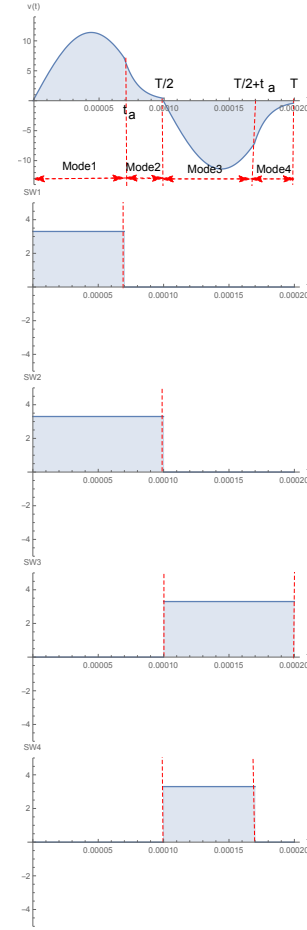
Fig. 4: Output Signal $v(t)$

By applying equation (10) in equation (8), then the a_n equals to the following expression:

$$a_n = \frac{1}{T}\left[\frac{V_p}{2\pi\left(n^2 f^2 - f_n^2\right)}\cdot\left[-(nf - f_n)Cos(2\pi(nf + f_n)t_\alpha)\right.\right.$$
$$+(nf + f_n)Cos(2\pi(nf - f_n)t_\alpha) - 2f_n$$
$$+(nf - f_n)Cos\left(\pi\left(2(nf + f_n)\left(\frac{T}{2} + t_\alpha\right) - f_n T\right)\right)$$
$$-(nf + f_n)Cos\left(\pi\left(2(nf - f_n)\left(\frac{T}{2} + t_\alpha\right) + f_n T\right)\right)$$
$$\left. +2f_n Cos\left(\pi n f T\right)\right]$$
$$+\frac{V_s\tau}{(4\pi^2\tau^2 n^2 f^2 + 1)}\cdot\left[(2i\pi\tau nf + 1)e^{-\left(\frac{\frac{T}{2}-t_\alpha}{\tau}\right)}\right.$$
$$\left(e^{2i\pi nfT} - e^{i\pi nfT}\right)$$
$$-(2i\pi\tau nf - 1)e^{-\left(\frac{\frac{T}{2}-t_\alpha}{\tau}\right)}\left(e^{-2i\pi nfT} - e^{-i\pi nfT}\right)$$
$$+(2i\pi\tau nf + 1)e^{2i\pi nft_\alpha}\left(1 - e^{i\pi nfT}\right)$$
$$\left.\left.-(2i\pi\tau nf - 1)e^{2i\pi nft_\alpha}\left(1 - e^{-i\pi nfT}\right)\right]\right]$$
$$(11)$$

And by substituting equation (10) in (9), the b_n formula equals:

$$b_n = \frac{1}{T}\left[\frac{V_p}{2\pi\left(n^2 f^2 - f_n^2\right)}\cdot\left[-(nf - f_n)Sin(2\pi(nf + f_n)t_\alpha)\right.\right.$$

$$+(nf + f_n)Sin(2\pi(nf - f_n)t_\alpha)$$

$$+(nf - f_n)Sin\left(\pi\left(2(nf - f_n)\left(\frac{T}{2} + t_\alpha\right) - f_n T\right)\right)$$

$$-(nf - f_n)Sin\left(\pi\left(2(nf + f_n)\left(\frac{T}{2}\right) - f_n T\right)\right)$$

$$-(nf + f_n)Sin\left(\pi\left(2(nf - f_n)\left(\frac{T}{2} + t_\alpha\right) + f_n T\right)\right)$$

$$\left.+(nf + f_n)Sin\left(\pi\left(2(nf - f_n)\left(\frac{T}{2}\right) + f_n T\right)\right)\right]$$

$$+\frac{V_s\tau}{(4\pi^2\tau^2 n^2 f^2 + 1)}\cdot\left[(2\pi\tau nf - i)e^{-\left(\frac{\frac{T}{2} - t_\alpha}{\tau}\right)}\right.$$

$$\left(e^{2i\pi nfT} - e^{i\pi nfT}\right)$$

$$+(2\pi\tau nf + i)e^{-\left(\frac{\frac{T}{2} - t_\alpha}{\tau}\right)}\left(e^{-2i\pi nfT} - e^{-i\pi nfT}\right)$$

$$+(2\pi\tau nf - i)e^{2i\pi nft_\alpha}\left(1 - e^{i\pi nfT}\right)$$

$$\left.\left.+(2\pi\tau nf + i)e^{-2i\pi nft_\alpha}\left(1 - e^{-i\pi nfT}\right)\right]\right]$$

$$\tag{12}$$

While, the magnitude of spectrum is given by

$$S_n = \sqrt{a_n^2 + b_n^2} \tag{13}$$

V. EXPERIMENTAL RESULTS AND POWER CONTROL ANALYSIS

For better understanding the control strategy of the configuration, there will be an extensive analysis to the efficient heating power in terms of harmonic components of output load voltage and current waveforms delivered from MNPCI topology to the IH load of captured values: $L1 = 105.7\mu H$, $R = 10.07\Omega$ and $L = 33\mu H$, as in experimental output voltage and current signals shown in Fig. 5, which clearly clarifies that the phase shift angle between $v(t)$ and $i(t)$ is approximately zero magnitude difference with performing soft switching mode condition.

It can be deduced from experimental result of frequency spectrum FS for MNPCI prototype shown in Fig. 6 that the harmonic content are the fundamental 1st , 3rd, 5th and finally the 7th harmonic. Therefore, the analysis concentrates mainly on those particular harmonics with comparing their amplitude values at different operational points.

Through comparing the FS and output voltage harmonic content of two different operational points at time $t_\alpha = 51.2\mu sec$ and $t_\alpha = 72.6\mu sec$, which are shown in Fig. 7, Fig. 8, Fig. 10 and Fig. 11 respectively, illustrates that the MNPCI configuration expresses harmonic content of approximately 1st, 3rd and 5th basic harmonics, with relatively low 7th harmonic oscillation (it can be neglected depending on the selected time t_α), which coincide with the FS shown in Fig. 6.
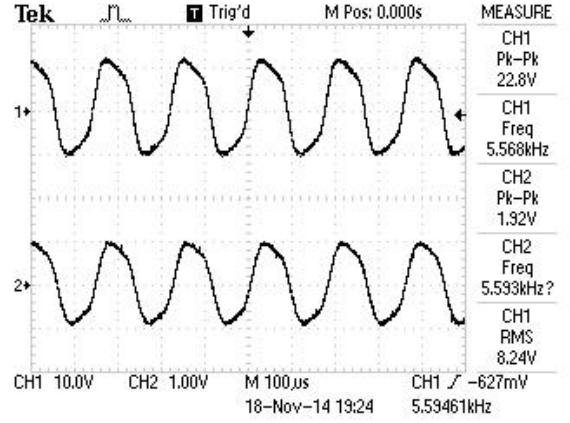

Fig. 5: Experimental results of Output Voltage, $v(t)$ (Ch1) and Output Current, $i(t)$ (Ch2) Signals of prototype values:$L1 = 105.7\mu H$, $R = 10.07\Omega$ and $L = 33\mu H$
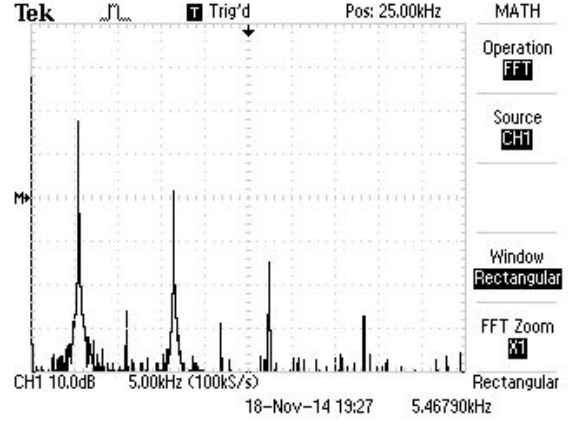

Fig. 6: Experimental Results of Frequency Spectrum Analysis of Output Voltage, $v(t)$ (Ch1) of prototype values:$L1 = 105.7\mu H$, $R = 10.07\Omega$ and $L = 33\mu H$ and $t_\alpha = 72.6\mu sec$

Therefore, a 21 operational points with equal step interval of ON switching time t_α are selected for comparison starting from $\left(\frac{1}{4f_n}\right) \longrightarrow \left(\frac{T}{2}\right)$ limit, which represents the estimated effective ON switching time range starting from minimum time of t_α with maximum harmonic distortion, then t_α rises up step by step until reaches its maximum ON time t_α, meanwhile the amplitude of harmonic distortion decreases until it reaches the minimum possible value, as can be seen in Fig. 11, although this graph seems to be nested that one can not recognize the interlinked lines, but this curve illustrates the operational band borders of harmonic amplitude change of the proposed MNPCI configuration. To show the curve of harmonic change more clearly, less points must be chosen for comparison as shown in Fig. 12.

To identify the optimum operational point, it is very important to determine the available power over the selected t_α points as in Fig. 13, which shows that the available power rises gradually from minimum value of 76.4% at $t_\alpha = 41.7\mu sec$ until it reaches an average value of about 95% at $t_\alpha = 63\mu sec$
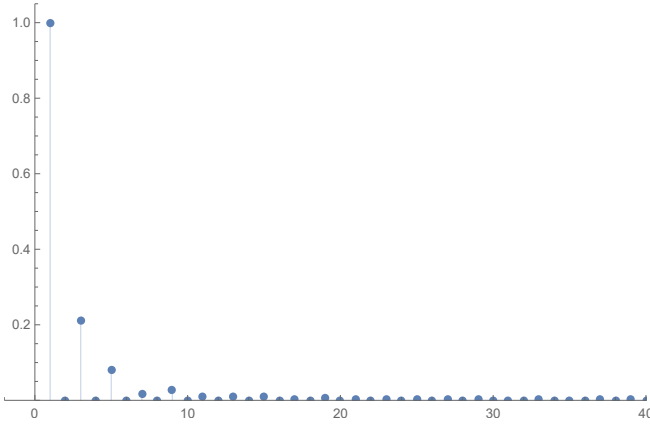
221

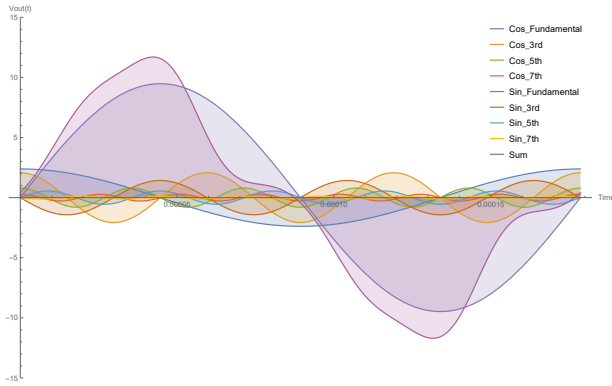Fig. 7: Frequency Spectrum at $t_\alpha = 51.2\mu sec$

Fig. 9: Frequency Spectrum at $t_\alpha = 72.6\mu sec$

Fig. 8: $v(t)$ with 1st,3rd,5th and 7th Harmonics at $t_\alpha = 51.2\mu sec$
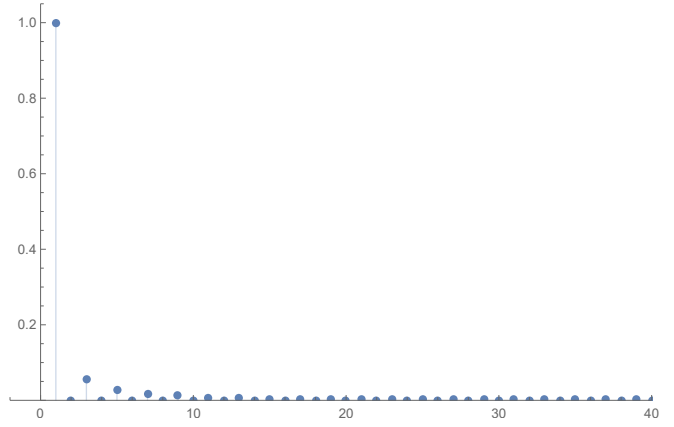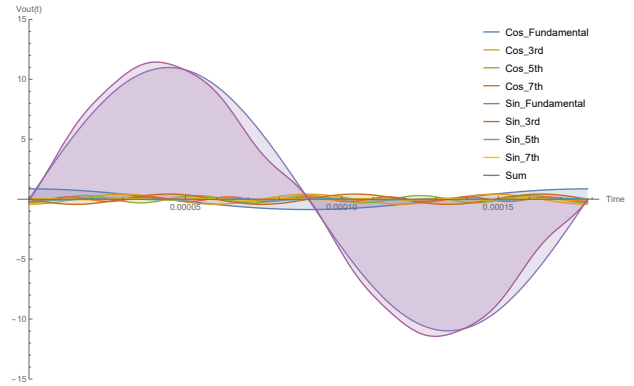

Fig. 10: $v(t)$ with 1st,3rd,5th and 7th Harmonics at $t_\alpha = 72.6\mu sec$

and then reaches the maximum of 96.8% at $t_\alpha = 72.6\mu sec$. While Fig. 11 shows the behaviour of 1st,3^{ed},5th and 7th current harmonics at different t_α values, in which the 1st Harmonic starts from 69% at $t_\alpha = 41.7\mu sec$, then rises gradually until it reaches the average value of 92% at $t_\alpha = 65.5\mu sec$ and then reaches the maximum value 93% at $t_\alpha = 72.6\mu sec$, meanwhile the 3^{ed} harmonic starts from maximum value of 23.6% at $t_\alpha = 41.7\mu sec$, but then it decreases until it reaches the minimum average value of 5% at $t_\alpha = 72.6\mu sec$. While, the 5th harmonic oscillates from minimum of 4% at $t_\alpha = 41.7\mu sec$ and then rises to 7% at $t_\alpha = 53.6\mu sec$, but then it falls down to 2.8% at $t_\alpha = 72.6\mu sec$.

Therefore, the resultant effective heating power of the system is shown in fig.13. It begins from minimum value of 43.6 at $t_\alpha = 41.7\mu sec$ and rises until reach the optimum of 65.24 at $t_\alpha = 72.6\mu sec$ and then drops a little to settle at average of 64.5. This curve gives a clear picture of the changing characteristic of heating efficiency, which can be controlled to the maximum value through setting the t_α to an optimum possible point.

This fact implies that, by setting the ON switching time t_α to a suitable value, the Total Harmonic Distortion THD of the system can be reduced to a minimum level, as a consequence; controlling the t_α performs maximum power transfer.

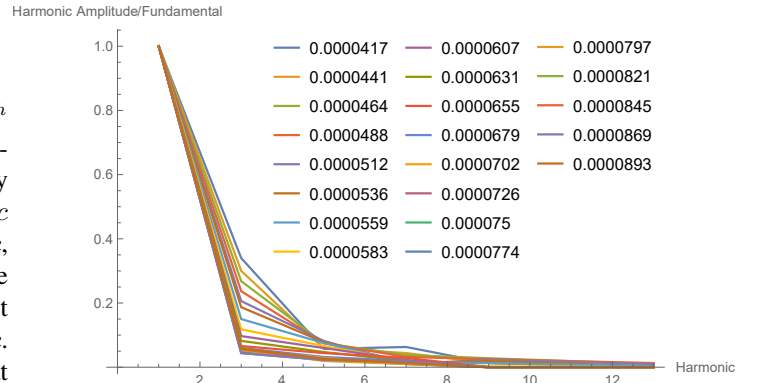And according to IEEE STD 519 Standards, the maximum

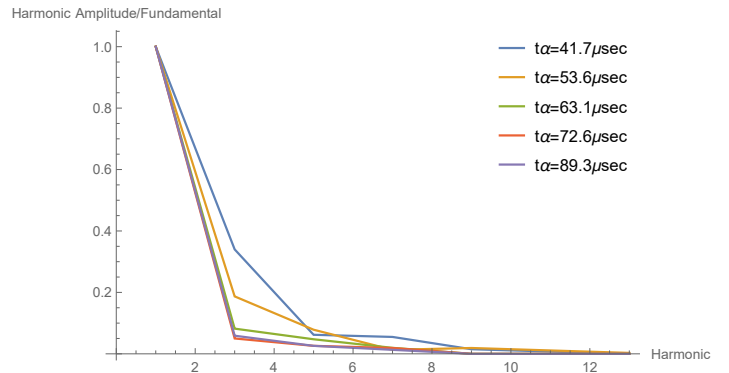Fig. 11: Frequency Spectrum of 21-Operational Points of ON-Switching Time t_α

Fig. 12: Frequency Spectrum of 5-Operational Points of ON-Switching Time t_α

accepted THD percentage of the inverter is 20%, therefore; through observing the THD curve of the proposed configuration shown in Fig. 16, it can be revealed that the accepted corresponding operational region begins from threshold ON time of $t_\alpha = 53.6\mu sec$, at this time, the maximum permissible THD is occurred, which represents about $\left(\frac{T}{3.3}\right)$ of the total signal time, therefore; the limits of acceptable operational region lies between $\left(\frac{T}{3.3} < t_\alpha < \frac{T}{2}\right)$ period, then after; the THD begins to decrease gradually until it reaches the minimum value of $THD = 6.5\%$ at $t_\alpha = 72.6\mu sec$, and then it settles on the average of $THD = 6.75\%$, which verifies the reliability of the proposed control strategy of the configuration, as it operates at $t_\alpha = 72.6\mu sec$ operational point, i.e, with minimum THD of 6.5%, which is much lower than the maximum threshold limit of IEEE STD 519 Standards.

VI. CONCLUSION

A new control method for induction heating system using Multilevel Neutral Point Clamped Inverter (MNPCI) is introduced and verified successfully. The strategy includes controlling the harmonic distortion content of output signal through changing the value of ON switching time t_α, in order to find the optimum operational point and hence; the maximum effective heating power and minimum Total Harmonic Distortion (THD) for proposed IH system. The reliability of MNPCI design is proved through operating under $THD = 6.75\%$, which is in the safe operational region according to IEEE STD 519 Standards.

REFERENCES

[1] Y. Ge, R. Hu, Z. Zhang, and Q. Shen, "Optimization control of induction hardening process," in *Mechatronics and Automation, Proceedings of the 2006 IEEE International Conference on*, June 2006, pp. 1126–1130.

[2] Z. Wang, Z. Lou, and H. Chen, "A novel dual-llc resonant soft switching converter for super high frequency induction heating power supplies," in *Power Electronics Specialists Conference, 2007. PESC 2007. IEEE*, 2007, pp. 2561–2566.

[3] I. Yilmaz, M. Ermis, and I. Cadirci, "Medium-frequency induction melting furnace as a load on the power system," *Industry Applications, IEEE Transactions on*, vol. 48, no. 4, pp. 1203–1214, 2012.

[4] D. Boian, C. Biris, R. Teodorescu, and M. Sztykiel, "Development of modulation strategies for npc converter addressing dc link voltage balancing and cmv reduction," in *Power Electronics for Distributed Generation Systems (PEDG), 2012 3rd IEEE International Symposium on*. IEEE, 2012, pp. 828–835.

[5] B. Flayyih, M. Ahmed, and M. Ambroze, "A novel hybrid voltage-current fed induction heating power supply system using multilevel neutral point clamped inverter," in *Energy Conference (ENERGYCON), 2014 IEEE International*, May 2014, pp. 189–194.

[6] B. Flayyih, M. Ahmed, and S. MacVeigh, "A comprehensive power analysis of induction heating power supply system using multilevel neutral point clamped inverter with optimum control algorithm," in *Power Electronics and Drive Systems (PEDS), 2015 IEEE 11th International Conference on*, June 2015, pp. 727–731.

[7] Z. Gao and Y. Zhou, "Research on switching losses for induction heating power supply with llc resonant load," in *Electronic and Mechanical Engineering and Information Technology (EMEIT), 2011 International Conference on*, vol. 5. IEEE, 2011, pp. 2474–2477.

[8] G. Martin Segura *et al.*, "Induction heating converter's design, control and modeling applied to continuous wire heating," 2012.

[9] J. Davies and P. Simpson, *Induction heating handbook*. McGraw-Hill, 1979.

[10] J. Davies, *Conduction and Induction Heating*, ser. IEE power engineering series. P. Peregrinus Limited, 1990.
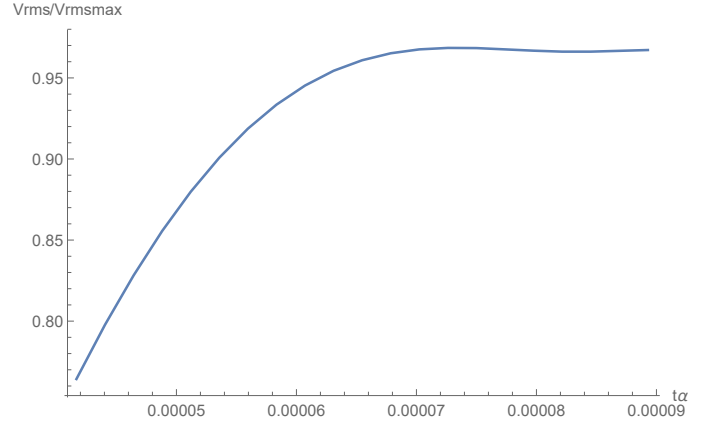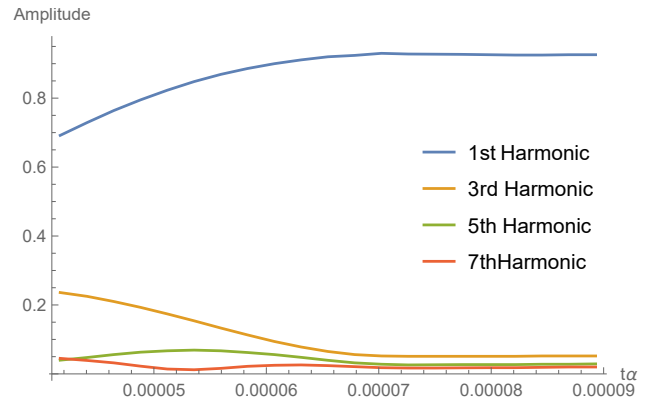
Fig. 13: Available Power

Fig. 14: Output Current Harmonics
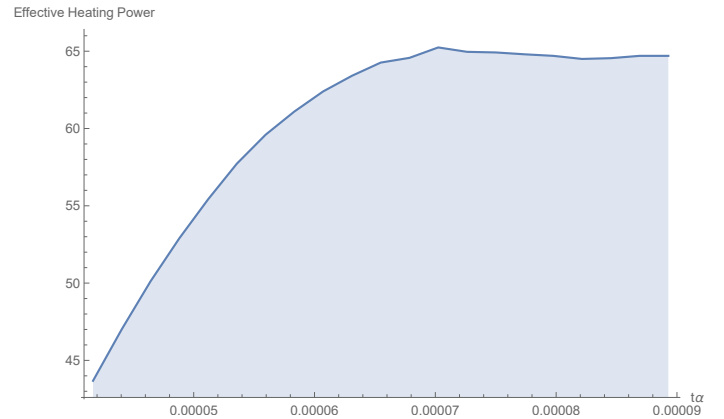
Fig. 15: Effective Heating power
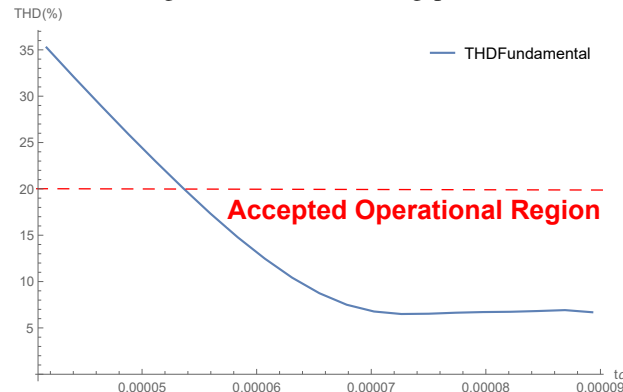
Fig. 16: Total Harmonic Distortion THD Versus ON Switching Time t_α

Appendix B

MNPCI Circuit Diagram

Multilevel Neutral Point Clamped Inverter Page 1 of 1

ICD1 — IRS21864SPBF
S1, Hin, Lin, VSS, na, COM, LO, Vcc, na, VB, HO, Vs, na, na
C3 1uF, C4 1uF Ceramic, C5 1uF, HiA, HiSA, D5 VS-10BQ015TRPBF, R5 10R, +12V, GND

ICD2 — IRS21864SPBF
S2, Hin, Lin, VSS, na, COM, LO, Vcc, na, VB, HO, Vs, na, na
C6 1uF, C7 1uF GND, C8 1uF Ceramic, HIB, HiSB, D4 VS-10BQ015TRPBF, R6 10R, +12V

ICD3 — IRS21864SPBF
S3, S4, Hin, Lin, VSS, na, COM, LO, Vcc, na, VB, HO, Vs, na, na
C11 1uF, C12 1uF GND, C13 1uF Ceramic, LOC, HIC, HISC, D1 VS-10BQ015TRPBF, R7 10R, +12V, LOCG

U2 LD1117v50
VI, VO, GND
C9 100nF, C10 10uF, GND, +12v, VCC

X1 4MHZ_RESONATOR
OSC1, OSC2
VCC, C14 100nF, GND

U1 PIC18F4550
RA0/AN0, RA1/AN1, RA2/AN2/VREF-/CVREF, RA3/AN3/VREF+, RA4/T0CKI/C1OUT/RCV, RA5/AN4/SS/LVDIN/C2OUT, RA6/OSC2/CLKO, OSC1/CLKI
RB0/AN12/INT0/FLT0/SDI/SDA, RB1/AN10/INT1/SCK/SCL, RB2/AN8/INT2/VMO, RB3/AN9/CCP2/VPO, RB4/AN11/KBI0/CSSPP, RB5/KBI1/PGM, RB6/KBI2/PGC, RB7/KBI3/PGD
RE0/AN5/CK1SPP, RE1/AN6/CK2SPP, RE2/AN7/OESPP, RE3/MCLR/VPP, VUSB
RC0/T1OSO/T1CKI, RC1/T1OSI/CCP2/UOE, RC2/CCP1/P1A, RC4/D-/VM, RC5/D+/VP, RC6/TX/CK, RC7/RX/DT/SDO
RD0/SPP0, RD1/SPP1, RD2/SPP2, RD3/SPP3, RD4/SPP4, RD5/SPP5/P1B, RD6/SPP6/P1C, RD7/SPP7/P1D
TX, RX, S1, S2, S3, S4, PGC, PGD
VCC, R8 10k, SW1 BUTTON, GND, J4 CONN-H6, PGD, PGC

+12V
C1 4.7uF, C2 4.7uF
D3 VS-10BQ015TRPBF, D2 VS-10BQ015TRPBF
R1 20R, R2 20R, R3 20R, R4 20R
HIA, HIB, HIC, LOC
HISA, HISB, HISC, LOCG
Q1 IRF540, Q2 IRF540, Q3 IRF540, Q4 IRF540
L1 100uH 20mm spacing
J1 TBLOCK-M2, J2 TBLOCK-M2, J3 TBLOCK-M2
LOCG
GND

FILE NAME: NPC.DSN
DESIGN TITLE: MNPCI
PATH: C:\Users\bmflayyih\Desktop\MNPCI Diagrams\NPC.DSN
BY: Bashar M Flayyih
DATE: 03/02/2016
PAGE: 2
REV: 1
TIME: 14:15:16

Appendix C

Zero Current Detector Circuit

V_{ref}

i_{tank}

+12v

AD629

r 0.2

V_o

−12v

A

10K

10K

+12v

OP1

OPO7

+

−12v

10K

R_v =100K

+12v

10K

OP2

OPO7

B

+

−12v

V_{ref}

10K

−

COP

LM393

+

+5v

+5v

10K

C

Pic18lf4553

+5v

10K

−

OP3

OPO7

+

V_{ref}

10K

+12v
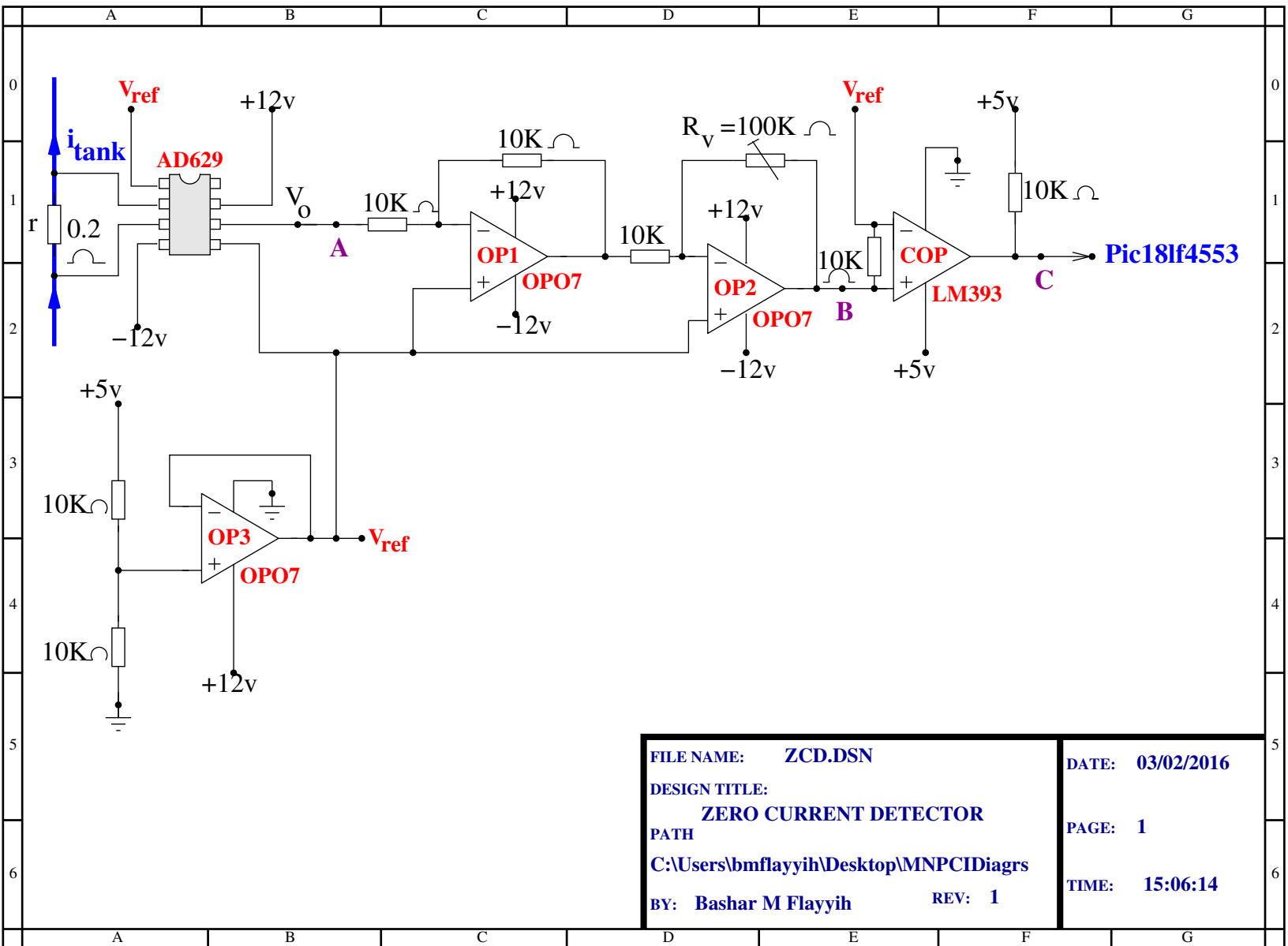
Appendix D

Programming Code

```c
#include <stm32f4xx.h>
#include "GPIO.h"
#include "TIMERS.h"
#include "IP.h"
#include "ADC.h"
#include "DMA.h"
#include <math.h>

#define Fs      130000
#define N               26
#define k               1

#define Fcy     168000000

#define T               4666
int Itank[N+1]={0};
int Vtank[N+1]={0};
int Iload[N+1]={0};
int Vload[N+1]={0};
int current=0, end=N;
unsigned int n=0;
float diff;
float ItankRe=0.0,ItankIm=0.0;
float VtankRe=0.0, VtankIm=0.0;
float IloadRe=0.0,IloadIm=0.0;
float VloadRe=0.0,VloadIm=0.0;
float cosLUT[N], sinLUT[N];
int Iphase,Vphase, tank_IVphase, load_IVphase;
unsigned short int adc_data[4];
unsigned short int switch_outputs[4]={0x3003,0x2002,0xc00c,0x4004};
unsigned short int switch_times[4]={T,T,T,T};
#define Itank_buf       adc_data[0]
#define Vtank_buf       adc_data[2]
#define Iload_buf       adc_data[1]
#define Vload_buf       adc_data[3]

void initLUT(void)
{
        unsigned int i;
        float omega;
        for(i=0; i<N; i++)
        {
                omega=2.0f*3.14159f*(float)(i*k)/(float)N;
                cosLUT[i]=cos(omega);
                sinLUT[i]=sin(omega);
        }
}

int main(void)
{
        initLUT();
        config_GPIOC();
```

229

```c
        config_GPIOD();

        config_TIM8();
        config_DMA2_S1();
        config_DMA2_S2();
        PSC8=0;
        PR8=switch_times[0];
        GPIOD_OUT=switch_outputs[0];
        TMR8=0;
        T8CCR1=PR8;
        start_timer8();


        config_ADC1();
        config_DMA2_S0();
        ADC1_START_REG();

        config_TIM2();
        PSC2=0;
        PR2=(Fcy/(2*Fs));
        TMR2=0;
        set_IP(TIM2IP,3);
        start_timer2();

        config_TIM3();
        PSC3=511;
        TMR3=0;
        PR3=164;                                        //1ms
        set_IP(TIM3IP,4);
        start_timer3();
        while(1);
}

void TIM2_IRQHandler(void)
{
        CLR_TIM2_IF();

        GPIOD_SET|=0x8000;
        Itank[current]=Itank_buf-2047;
        diff=(float)(Itank[current]-Itank[end]);
        ItankRe+=diff*cosLUT[n];
        ItankIm-=diff*sinLUT[n];

        Vtank[current]=Vtank_buf-2047;
        diff=(float)(Vtank[current]-Vtank[end]);
        VtankRe+=diff*cosLUT[n];
        VtankIm-=diff*sinLUT[n];

        Iload[current]=Iload_buf-2047;
        diff=(float)(Iload[current]-Iload[end]);
        IloadRe+=diff*cosLUT[n];
        IloadIm-=diff*sinLUT[n];
```

230

```
        Vload[current]=Vload_buf-2047;
        diff=(float)(Vload[current]-Vload[end]);
        VloadRe+=diff*cosLUT[n];
        VloadIm-=diff*sinLUT[n];

        current=end;
        if(--end<0)end=N;
        if(++n==N)n=0;
        GPIOD_CLR|=0x8000;
}

void TIM3_IRQHandler(void)
{
        CLR_TIM3_IF();
        GPIOD_SET|=0x2000;

        //PHASE INFORMATION FOR OUTPUT VOLTAGE AND CURRENT
        Iphase=(int)(atan2(ItankIm,ItankRe)*180.0f/3.14159f);
        Vphase=(int)(atan2(VtankIm,VtankRe)*180.0f/3.14159f);
        tank_IVphase=Iphase-Vphase;
        tank_IVphase+=0;                        //PHASE CORRECTION FACTOR BASED ON
CALIBRATION RESULTS - THIS IS TO COMPENSATE FOR PHASE ERRORS PRODUCED
BY SENSING HARDWARE
        if(tank_IVphase>180)tank_IVphase-=360;
        else if(tank_IVphase<(-180)) tank_IVphase+=360;

        //PHASE INFORMATION FOR INPUT VOLTAGE AND CURRENT
        Iphase=(int)(atan2(IloadIm,IloadRe)*180.0f/3.14159f);
        Vphase=(int)(atan2(VloadIm,VloadRe)*180.0f/3.14159f);
        load_IVphase=Iphase-Vphase;
        load_IVphase+=0;                //PHASE CORRECTION FACTOR BASED ON
CALIBRATION RESULTS - THIS IS TO COMPENSATE FOR PHASE ERRORS PRODUCED
BY SENSING HARDWARE
        if(load_IVphase>180) load_IVphase-=360;
        else if(load_IVphase<(-180)) load_IVphase+=360;
        GPIOD_CLR|=0x02000;
}
```